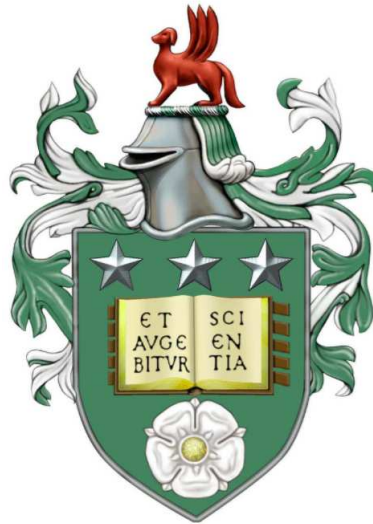


Multi-Mode Dielectric Resonator Filters



Saad Wasmi Osman Luhaib

Submitted in accordance with the requirements for the degree of
Doctor of Philosophy

The University of Leeds
School of Electronic and Electrical Engineering
Leeds, UK

February 2018

Declaration

The candidate confirms the work submitted is his own, except where work which has formed part of jointly-authored publications has been included. The contribution of the candidate and other authors to this work has been explicitly indicated below. The candidate confirms that appropriate credit has been given within the thesis where reference has been made to the work of others. Some portions of Chapter 4 of this thesis are based on the following published papers:

Mustafa S. Bakr, Saad W. O. Luhaib and Ian C. Hunter, "A Novel Dielectric-Loaded Dual-Mode Cavity for Cellular Base Station Applications", 2016 46th European Microwave Conference (EuMC), London, 2016, pp. 763-766.

The candidate (Saad Wasmi Osman Luhaib) suggested and simulated the coupling structure, the calculation of optimum size of the resonator and the filter coefficients and graphical presentation.

The co-author (Prof Ian Hunter) supervised the work, suggested the initial idea of the novel resonator, proofread the drafts and made suggestions and corrections to the draft paper.

Mustafa S. Bakr performed the experimental work, and suggested the way to insert TZs and write the initial paper draft.

This copy has been supplied on the understanding that it is copyright material and that no quotation from the report may be published without proper acknowledgement.

© 2018 The University of Leeds and Saad Wasmi Osman Luhaib

Acknowledgements

In the first place, I express my sincere gratitude and thanks to my primary supervisor, Prof. Ian Hunter, for his outstanding support and assistance during the research period.

I incessantly thank my PhD sponsors, namely the Ministry of Higher Education and Scientific Research in the Republic of Iraq.

I am grateful to Radio Design Limited for their technical support toward our research group at the University of Leeds.

My acknowledgement cannot be complete without recognising the effort of friends and colleagues.

My thanks as well go my secondary supervisor Dr. Nutapong Somjet and to Graham in the department workshop for fabricating the filers.

Lastly, I thank my family, my parents, brothers and sister, my wife, Ashwaq, my sons, Hudheefa and Qatada, and daughter, Zainb, for their endurance, emotional support and comfort rendered to me during the course of my research.

Abstract

Dielectric resonator (DR) filters are widely used in microwave communications due to their small size and high Q-factor. Multi-mode filters offer a further level of miniaturisation. A new multi-mode dielectric resonator filter is presented in this thesis. The $TE_{11\delta}$ dual-mode DR offers an 11% size reduction ratio compared with a coaxial air-filled filter with the same unloaded Q-factor (Q_u) and about 820 MHz spurious separation from the fundamental frequency 1.95 GHz. Two coupling techniques are applied in the $TE_{11\delta}$ filter configuration. These are: ceramic puck/probe in contact and etching holes through the ceramic puck for probe installation.

A 4th order Chebyshev filter dual-mode DR filter has been simulated and fabricated using each technique. The results show a good agreement between the simulation and measurement with half spurious-free window compared with non-loaded cavity. In the etching method, the spurious-free window and the Q_u improved compared with unpatterned ceramic puck. The inline structure filter provides an extra improvement in the spurious window base for the planar configuration.

Another approach to the dual-mode DR filter has been studied in this work. A HE_{11} dual-mode with ceramic puck placed at the base of the cavity presents a good size reduction ratio and acceptable spurious window. The mathematical model shows that transmission zeros (TZs) can be generated in all orientation cases of the inter resonator coupling hole. The control range of the TZs positions was from 40 MHz from the centre frequency. A good agreement was obtained between the simulation and the measurement results.

A triple-mode DR filter with two-piece of the ceramic puck in parallel has been presented. The one cavity approach offers a high Q-factor with 400 MHz suppression. A coaxial probe was used for the input/output coupling and the etching hole through the ceramic puck for inter-resonator coupling. A 3rd order Chebyshev DR filter was simulated and fabricated with two TZs on the upper side band. The practical results show prospects in application of the filter for miniaturised microwave communications.

Contents

Declaration	i
Acknowledgements	ii
Abstract	iii
1 Introduction	1
1.1 Microwave Filter Applications	1
1.2 Review of Dielectric Resonators	3
1.3 Aims and Objectives	4
1.4 Thesis Outline	5
2 Literature Review	7
2.1 Microwave Resonators	7
2.2 Coaxial TEM Resonator Filters	9
2.2.1 Compline Resonator Filter	9
2.3 Waveguide Resonators	11
2.4 Quality Factor	13

2.5	Microstrip and Superconducting Resonators	14
2.6	Dielectric Resonator Filters	16
2.6.1	Dual-Mode Dielectric Resonator Filters	17
2.6.2	Conductor Loading of Dielectric Resonators	21
2.6.3	Improvement of Spurious Performance	23
2.6.4	Triple-Mode Resonator Filter	24
2.7	Summary	26
3	Filter Design Methodology	27
3.1	Introduction	27
3.2	Transfer Function Approximation	28
3.2.1	Power Transfer Function and Characteristic Polynomials	28
3.2.2	Butterworth Approximation	30
3.2.3	Chebyshev Approximation	31
3.2.4	Generalized Chebyshev Approximation	33
3.3	Lowpass Prototype Filters and Elements	35
3.4	Frequency and Element Transformation	38
3.5	Introduction of Coupling Matrix	39
3.6	Circuit Model of the Dielectric Resonator	42
3.6.1	The Cohn Model	42
3.7	High Frequency Structure Simulator (HFSS)	44
3.8	Summary	45

4	Design and Implementation of a Novel $TE_{11\delta}$ Dual-Mode Dielectric Resonator Filter	46
4.1	Introduction	46
4.2	Configuration of the Proposed Resonator	47
4.3	Design of a Single Cavity Dual-Mode Filter	52
4.3.1	Input and Output Coupling	52
4.3.2	Coupling of Degenerate Modes	55
4.4	Implementation of the Second-order Filter	57
4.5	Implementation of the 4 th -order dual-mode filter	61
4.6	Fabrication and Measurement	65
4.7	Fourth-order Dual-Mode Filter with Strip Coupling	68
4.8	Summary	72
5	Dual-Mode Filter Implementation by Etching the Dielectric Resonator	73
5.1	Introduction	73
5.2	Configuration of the Proposed Resonator	74
5.3	Design of the 4 th -Order Chebyshev Dual-Mode Filter Planar Configuration	77
5.3.1	External Coupling	77
5.3.2	Inter-Resonator Coupling	78
5.3.3	Inter-Cavity Coupling	79
5.3.4	Simulation Results	80

5.4	Design of the Dual-Mode Filter Inline Configuration	83
5.5	Dual-Mode Loaded Cavity Filter with T-shape Coupling	86
5.6	Filter Design with T-shaped I/O Coupling	89
5.6.1	External Q factor	89
5.6.2	Inter-Resonator Coupling	91
5.6.3	Inter-Cavity Coupling	92
5.6.4	Filter Design with T-shaped Probe	93
5.7	Experimental Results	95
5.8	Summary	99
6	HE_{11} Dual-Mode DR Filters	100
6.1	Introduction	100
6.2	Configuration of the Proposed Resonator	101
6.2.1	Effect of the Resonator Dimensions	105
6.3	Coupling Technique	107
6.4	Design of the 4 th -order Dual-Mode HE_{11} Filter	111
6.5	Circuit Model for HE_{11} Dual-mode Resonator Filter	114
6.6	Filter with Transmission Zeros	118
6.7	Implementation of the HE_{11} dual-mode filter	121
6.8	Summary	126
7	Triple-Mode Filter with Splitted Dielectric Resonator Pucks	127
7.1	Introduction	127

7.2	Triple-Mode Resonator Cavity	128
7.3	The Coupling Mechanism	131
7.4	Simulation Result for One Cavity	134
7.5	Summary	138
8	Conclusions and future work	139
8.1	Conclusions	139
8.2	Future Work	141
	References	142

List of Tables

2.1	Comparison between Various modes of operation.	8
2.2	δ_s/λ values for various metals	14
3.1	Conversions from the normalized low-pass prototype to low-pass . . .	39
4.1	First three modes in proposed resonator cavity	51
5.1	Comparison of simulated resonance frequency, mode type and Q_u for the cavity resonator with unpatterned and vertically-etched structures	88
6.1	Q_u , the spurious-free window and the volume of HE_{11} dual-mode resonator with different dimension at resonant frequency equal 2 GHz.	103
6.2	Typical dimensions of 4 th order filter HE_{11} dual-mode.	112
6.3	TZs position at resonant frequency 1 Hz.	117
6.4	Comparison of HE_{11} dual-mode filter with the state-of-the arts. . .	125
7.1	Comparison of simulated resonance frequency (f_r), mode type and Q_u for the cavity resonator with unpatterned (UNP) and vertically- etched(V-E) structures in triple-mode cavity.	131
7.2	Typical dimensions of 3 rd order filter triple-mode.	136

List of Figures

1.1	RF front end of a mobile base station.	2
1.2	Typical dielectric resonator filter.	4
2.1	Insertion loss versus size for various RF resonators	8
2.2	(a) Interdigital filter, (b) Combline filter.	10
2.3	Air-filled combline resonator.	11
2.4	Circular and rectangular waveguide resonators.	12
2.5	Mode chart for circular waveguide resonators.	12
2.6	The theoretical Q-factors for a circular waveguide resonator at $\epsilon_r = 1$	14
2.7	The microstrip structure.	15
2.8	(a) Layout of the four-pole microstrip HTS bandpass filter on 0.508-mm-thick MgO (b) Measured performance of the four-pole filter.	16
2.9	Dielectric filter layout (a) Cut-off waveguide filter, (b) Planar filter.	17
2.10	Configuration of dual-mode DR filter	18
2.11	Canonical and longitudinal dual-mode dielectric resonator filter	19
2.12	Configuration of metallic strip coupling.	20
2.13	Dual-mode DR conductor-loaded filter configuration	21

2.14	Triple-mode DR conductor-loaded filter configuration	24
2.15	Compact triple-mode DR conductor-loaded filter.	25
3.1	Filter design procedure.	27
3.2	Doubly terminated lossless linear network.	28
3.3	Maximally flat filter responses for various filter orders N	31
3.4	Lowpass filter frequency response of Chebyshev type.	33
3.5	Generalized Chebyshev (or pseudo-elliptic) frequency response with two transmission zeros in the upper stopband.. . . .	35
3.6	Lowpass prototype filters for all-pole filters with (a) a ladder net- work structure and (b) its dual.	36
3.7	Impedance inverter with load Z_L	37
3.8	Inverter coupled generalized lowpass prototype filter.	37
3.9	Lumped-element immittance inverters (a) T-Section (b) π -Section.	38
3.10	A generalized lowpass prototype filter is represented by coupling matrix.	40
3.11	Cohn's second-order DR model.	42
3.12	Single mode equivalent circuit of Cohn's model for DR.	43
4.1	Configuration of dual-mode dielectric resonator: (a) 3D view, (b) side view.	47
4.2	Q-factor/volume and spurious-free window against the ratio of height of resonator/height above ceramic.	48
4.3	Q-factor against the ratio of resonator diameter to ceramic puck height.	49

4.4	Cohn model and HFSS simulation comparison for resonance frequencies.	50
4.5	Cohn model and HFSS simulation comparison for Q_u -factor.	51
4.6	Field distributions of $TE_{11\delta}$ dual-mode (a) E-field plot (b) H-field plot.	52
4.7	Externally coupled methods (a) Weak port, (b) One port, (c) Response of S_{21} and (d) Group delay for S_{11}	54
4.8	Variation of external quality factor (Q_e) against L_f	54
4.9	Inter-coupling dual-mode resonator (a) Dual-mode coupling configuration, (b) S_{21} of two coupled resonators showing two frequency peaks.	55
4.10	Inter-resonator coupling bandwidth varying with radius (re) and position of the etching hole (X_f).	57
4.11	2^{nd} order filter (a) Filter topology, (b) Normalized coupling matrix.	58
4.12	2^{nd} order filter (a) 3D structure view, (b) Top view.	59
4.13	Simulated of in-band frequency responses of 2^{nd} order filter.	59
4.14	Group delay of 2^{nd} dual-mode order filter.	60
4.15	Broadband simulation of the 2^{nd} order filter.	61
4.16	Configuration of a 4^{th} order filter in HFSS.	62
4.17	Variation of inter-cavity coupling bandwidth against L_{f1}	62
4.18	4^{th} order filter (a) Filter topology, (b) Normalized coupling matrix.	63
4.19	Simulation of in-band frequency responses of 4^{th} order filter.	64
4.20	Simulation of the wideband response 4^{th} order filter.	65

4.21	Fabricated 4 th degree dual-mode bandpass filter.	66
4.22	Measured and simulated results of the filter	67
4.23	Configuration of 4 th order filter in HFSS.	68
4.24	The external quality factor (Q_e) against length of strip L_{fe}	69
4.25	Variation of inter-cavity coupling (M_{23}) against L_{fe1}	70
4.26	Simulation of in-band frequency responses of 4 th order filter strip coupling.	71
4.27	Simulation of the wideband response 4 th order filter strip coupling. .	71
5.1	Configuration of dual-mode dielectric resonator: (a) 3D view, (b) side view.	75
5.2	Resonance frequencies and Q_u with varying hole radius (r_0).	75
5.3	Field distributions of $TE_{11\delta}$ dual-mode (a) E-field plot (b) H-field plot.	76
5.4	Variation of external quality factor (Q_e) against L_f	78
5.5	Inter-resonator coupling bandwidth varying with radius (re) and etching hole position (X_f).	79
5.6	Variation of inter-cavity coupling bandwidth (M_{23}) against L_{f1} . . .	80
5.7	Configuration of 4th order filter dual-mode in HFSS.	81
5.8	Simulated response of 4 th order planar filter.	82
5.9	Simulated wideband response of 4 th order planar filter.	82
5.10	Inline configuration of 4th order filter dual-mode in HFSS	83
5.11	Coupling bandwidth for two cavities against L_x and W_x	84

5.12	Simulated response of 4 th order inline filter..	85
5.13	Simulated wideband response of 4 th order inline filter.	86
5.14	Configuration of dual-mode dielectric resonator (a) 3D-View and (b) Top view.	87
5.15	Resonance frequencies and Q_u with varying radius of hole (L_x). . .	88
5.16	Field patterns (a)and (b) Electric field, (c) and(d)Magnetic field. . .	89
5.17	Configuration of input/output coupling in HFSS (a) 3D view and (b) Top view.	90
5.18	The external quality factor (Q_e) against L_m	90
5.19	Inter-resonator coupling bandwidth against X_f	91
5.20	Configuration of inter-cavity coupling in HFSS.	92
5.21	Inter-cavity coupling bandwidth against L_n	92
5.22	T shape coupling configuration of 4th order filter dual-mode in HFSS.	93
5.23	Simulated response of 4 th order T-shape coupling filter.	94
5.24	Simulated wideband response of 4 th order T-shape coupling filter. .	95
5.25	Fabricated of 4 th -order T-shaped coupling dual-mode bandpass fil- ter (a) with top lid, (b)without lid.	96
5.26	Measured response of the 4 th order T-shaped coupling filter.	97
5.27	Wideband response of the measured 4 th order T-shaped coupling filter.	98
5.28	Comparison of wideband response of measured T-shaped coupling filter	98
6.1	Diagram of DR in conducting cavity.	101

6.2	Mode chart against of H/h with frequency.	102
6.3	Mode chart for shorted dielectric against of H/h.	103
6.4	Field distributions of HE_{11} dual-mode (a) E-field plot (b) H-field plot.	104
6.5	Resonant frequencies and Q_u against the varying ga.	105
6.6	Resonant frequencies and Q_u against the varying ga with ceramic solder.	106
6.7	Resonant frequencies and Q_u against the varying b_a	107
6.8	Coupling mechanism for HE_{11} dual-mode (a) 3D view (b) side view.	108
6.9	External quality factor (Q_e) against t and ts.	108
6.10	Inter-resonator coupling for HE_{11} (a) metallic screw (b) circular hole.	109
6.11	Inter resonator coupling bandwidth against L_{c1}	110
6.12	Inter resonator coupling bandwidth varying with radius (re) and (X_f).	110
6.13	4^{th} order filter (a) Filter topology, (b) Normalized coupling matrix.	111
6.14	Configuration of HE_{11} dual-mode 4^{th} order filter in HFSS.	112
6.15	Simulated response of 4^{th} order HE_{11} dual-mode filter.	113
6.16	Broadband response simulated of 4^{th} order HE_{11} dual-mode filter.	113
6.17	E-field distributions of HE_{11} dual-mode.	114
6.18	Ring resonator with FIR coupling elements.	115
6.19	Equivalent circuit for ring resonator.	116
6.20	Equivalent circuit representation for the two-port network.	117
6.21	Simulation of 4^{th} order HE_{11} dual-mode filter with TZs.	118

6.22	Simulation of 4 th order HE_{11} dual-mode filter with TZs.	119
6.23	Control the TZs position by one tuning screw.	120
6.24	Control the TZs position by two tuning screws.	120
6.25	Fabricated 4 th degree HE_{11} dual-mode bandpass filter.	121
6.26	Simulated and measured response of 4 th order HE_{11} dual-mode filter at $\theta_1 = 225^0$ and $\theta_2 = 135^0$	122
6.27	Measured and simulation group delay for 4 th order HE_{11} dual-mode.	123
6.28	Broadband response simulated and measured for 4 th order HE_{11} dual-mode filter at $\theta_1 = 225^0$ and $\theta_2 = 135^0$	124
6.29	Control the TZ position by two tuning screws in measurement at $\theta_1 = 225^0$ and $\theta_2 = 135^0$	124
6.30	Simulated and measured response of 4 th order HE_{11} dual-mode filter at $\theta_1 = 315^0$ and $\theta_2 = 135^0$	125
6.31	Simulated and measured broadband response of 4 th order HE_{11} dual-mode filter at $\theta_1 = 315^0$ and $\theta_2 = 135^0$	126
7.1	Configuration of triple-mode DR (a) Top view, (b) Side view. . . .	128
7.2	Resonant frequencies against t_{rg}	129
7.3	E and H field pattern (a)and (b) E-field for EH_{11} (c) H-field for EH_{11} (d)and (e) E-field for $TE_{01\delta}$ (c) H-field for $TE_{01\delta}$	130
7.4	Triple-mode resonator with vertical etching from the side of the DRs.	131
7.5	I/O and inter-resonator coupling for triple-mode cavity (a) 3D view (b) top view.	132
7.6	External Q-factor varying with length of I/O coupling probe.	132

7.7	Resonant frequencies varying with length of I/O coupling probe. . .	133
7.8	Resonant frequencies varying with offset of hole (X_r).	134
7.9	Resonant frequencies varying with L_{TT}	135
7.10	Resonant frequencies varying against L_{TS}	136
7.11	Structure of triple-mode 3 rd order filter in HFSS.	137
7.13	Frequency response of triple-mode filter with tuning screws. . . .	137
7.12	Frequency response of triple-mode filter without tuning screws. . .	138

Chapter 1

Introduction

1.1 Microwave Filter Applications

Application of RF and microwave filters has grown enormously over the past few decades. Microwave filters are often used in many wireless communication such as satellite, navigation, cellular base station and radar [1, 2]. The filter allows the wanted signal at certain frequency to pass and rejects or attenuates the unwanted frequencies band. With the extensive growth in the communication system and the limitation in the electromagnetic spectrum, meeting the filter specification is becoming more difficult and challenging. The majority of the literature on microwave filters concentrates on filter design related to material and structure, filter synthesis related to transmission performance and rejection, and filter manufacturing, which relates to cost and size. Based on the passband signals, the microwave filters can be classified into lowpass, highpass, bandpass and bandstop. Electrical and mechanical performances play an important role in the design of microwave filters in communication systems. The optimum electrical performance of a filter refers to the low insertion loss, high return loss, small group delay and good selectivity, while mechanical performance relates to parameters such as small volume, low mass and good temperature stability. Figure 1.1 illustrates the block diagram of the mobile radio frequency (RF) front end for a typical mobile base station [3,4].

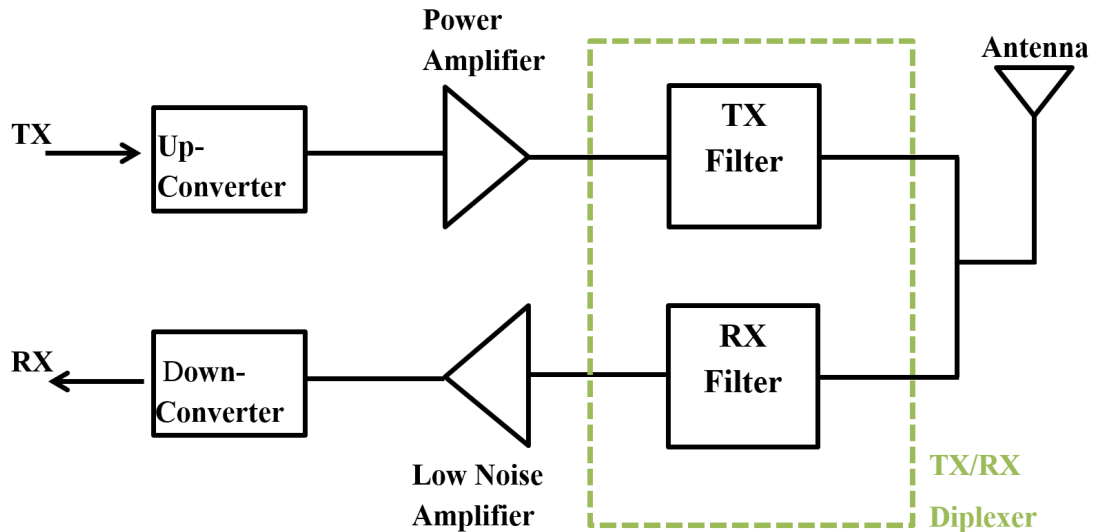


Figure 1.1: RF front end of a mobile base station [4].

The diplexer is required to ensure a high isolation between the transmitter (TX) and receiver (RX) channel and low insertion loss in the passband. To achieve this specification, transmission zeros (TZs) for the TX filter must be placed at inband of the RX filter and vice versa. Typically, microwave filters in base stations have the diplexers in the base mast and they are connected to the antenna by the coaxial cable. In this case, power losses will occur in the cable and need to be compensated by a power amplifier (PA) which may affect the filter and the PA. To avoid unnecessary dissipation of power, it is better to place the filter on the tower along with the antenna. Therefore, minimised microwave filters are required with low mass and small volume without compromising the electrical performance. This work aims to miniaturise the microwave filter for communication applications.

Typically, there are many configurations that are used for microwave filters. A waveguide filter has been used to achieve a high Q factor and high-temperature stability for wide and narrow bandwidth in the range of 900 MHz-100 GHz [3]. The drawback is its large volume and high cost. Microstrip filters have a small size, low Q and are easy to integrate with microwave circuits. They can be used in the high-frequency domain 100MHz-30GHz, but their disadvantage is their low Q, which usually needs to be compensated by a power amplifier or superconducting technology [5, 6]. The combine filter with an air-filled cavity is used in the

conventional cellular base station because of the good spurious window and ease of tuning. However, the Q-factor is nominal (<2000); this filter is also bulky and can not be easily miniaturised.

Dielectric resonators offer a high Q resonator with a low-loss solution. Significant size reduction can be achieved by these components to about $1/\sqrt{\epsilon_r}$ where ϵ_r is the permittivity of the material [7]. In addition, a multi-mode resonator filter can be used with dielectric resonators to achieve reduction in volume.

1.2 Review of Dielectric Resonators

The concept of the dielectric resonator was investigated by Richmyer in 1938, who obtained his idea by studying two shapes of the dielectric resonator, sphere and circular ring resonator [8]. However, the theoretical model became clear in the early 1960s [9]. During this time, modelling and experimentation had been conducted by researchers. Research was conducted on the characteristics of modes for various resonators to produce the first mode chart. Unfortunately, the development in this field suffered a setback because the dielectric material made at that time was unstable with temperature rise, which caused a shift in the operating frequency [10]. The dielectric resonator has an infinite number of operating modes similar to a metal cavity. The modes in the dielectric resonator can be classified into three distinct groups known as transverse electric (TE), transverse magnetic (TM) and hybrid electromagnetic (HE) modes [11]. An infinite range of individual modes has been found in each of these groups. The parameters that influence the type of modes present in the high relative permittivity (ϵ_r) puck are: the ratio of Length/Diameter (D/L), and the distance between the wall metal cavity and the puck, as shown in Figure 1.2. Where L/D is less than unity, $TE_{01\delta}$ becomes the lowest frequency mode which has a circular electric field and axial magnetic field distributions. A high electromagnetic energy is concentrated in the dielectric and a little current is induced in the cavity. As a result, the value of Q_u is close to

the Q of dielectric material. In this case, the dimension of the enclosure was twice the size of the largest dimension of the DR. For L/D more than one, the fundamental mode is $TM_{01\delta}$ which has a circular magnetic field and axial electric field distributions. HE modes have varying electric and magnetic fields in the azimuthal direction (Z). Mode charts for the cylindrical system in DR have been presented

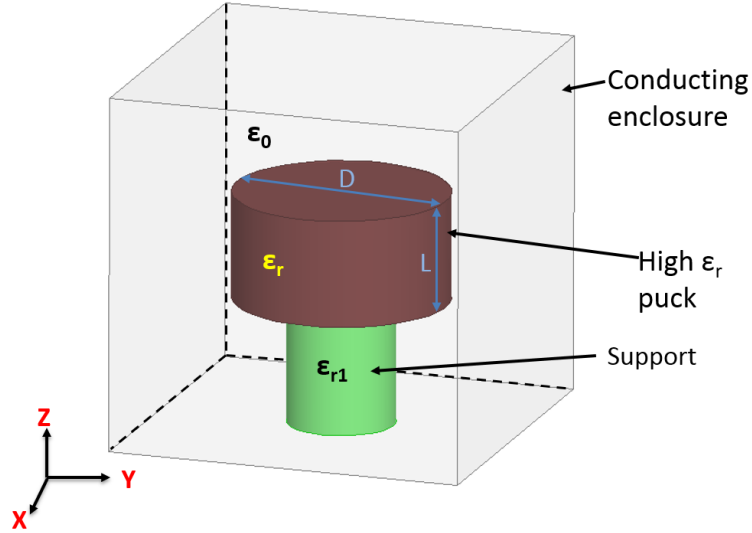


Figure 1.2: Typical dielectric resonator filter [4].

in literature [12, 13, 14]. A bandpass filter was also suggested by placing a $TE_{01\delta}$ mode dielectric rod resonator coaxially with a TE_{10} cut-off circular waveguide [15]. In the 1970s, Raytheon developed a barium tetratitanate ceramic material, which offers low loss and high temperature stability [16]. The first commercial DRs were presented by Murata Manufacturing Company with small variations in temperature coefficients of about $+10$ and -12 $ppm/^\circ C$, [17]. It was from this point that DRs developed dramatically in microwave filters [18].

1.3 Aims and Objectives

The aim of this thesis is to miniaturise the microwave filter without compromising the electrical performance using a multi-mode dielectric resonator technique. This work is phased to be conducted in stages covering the following:

1. Suggesting a novel $TE_{11\delta}$ dual-mode dielectric resonator filter with small

size compared with conventional filter, high Q-factor and wide spurious free window for cellular base station applications.

2. Investigating new coupling techniques and structures for the $TE_{11\delta}$ dielectric-loaded dual-mode filter to improve the spurious free window.
3. Investigating a new proposed of HE_{11} dual-mode dielectric resonator filter. Based on the resonant frequency, Q-factor, volume and the spurious-free window, optimization technique will be applied to give a good trade-off between the features of the filter.
4. Developing a mathematical model to understand the transmission zeros behaviour in dual-mode dielectric resonator filter.
5. proposing a triple-mode dielectric resonator filter with two-piece of ceramic puck in parallel with a good spurious-free window, high Q-factor and reduction size.

1.4 Thesis Outline

Chapter 1 provides an introduction to microwave filters, the need for miniaturisation in base station cellular systems and the objectives of the research.

Chapter 2 provides the literature review on the type of resonators used in base stations. It also provides details on the kind of multi-mode dielectric resonator with their structure and the advantages and disadvantages. The ways of coupling the multi-mode dielectric filter and the methods to improve the spurious window are also presented.

Chapter 3 gives the design procedure for the microwave filter and the approximation transfer function of the filter. This chapter further covers calculation of resonant frequency for the DR and the software used to verify the calculation and simulation model.

Chapter 4 provides the novel DR dual-mode filter with high reduction in size ratio and good spurious window. It also covers the 4th order Chebyshev filter that was implemented with a direct contact coupling probe, and comparison of the measurement and the simulation result. A discussion on the silver painting coupling technique is also presented.

Chapter 5 focusses on the new I/O coupling topology by etching through the DR design featured to improve the spurious window and the 4th order filter dual-mode inline structure. It proposes an iris structure to implement the two-cavity dual-mode which shows improvement in the spurious window.

Chapter 6 discusses a novel HE_{11} dual-mode grounded at the base of the DR in the cavity. It also covers the parametric study applied with the optimization method to obtain the best filter size. A new mathematical model is suggested to give the TZs behaviour. Two-cavity filter was simulated and fabricated with the ability to control the TZ position.

Chapter 7 provides the novel triple-mode filter with grooved ceramic, including the optimum dimensions chosen by HFSS software and MATLAB. Chapter 7 also features a method for the coupling technique and the simulation of a 3rd order filter.

Chapter 8 presents the summery of the thesis and the advantages and drawbacks of the multi-mode dielectric resonator filter, and the possibility to extend this work in the future.

Chapter 2

Literature Review

2.1 Microwave Resonators

Resonators are the base elements in filters and oscillators. The simplest form of resonator is one that connects inductors and capacitors (LC) in series or parallel, which enables the storage of electric and magnetic energy. Resonant frequency occurs when all energy is transferred to another section, i.e. when both inductance and capacitance cancel each other out. The frequency resonator can be determined from the values of L and C. There are many types of microwave resonator such as planar resonators, coaxial resonators, dielectric resonators and waveguide resonators whose resonator frequency can be calculated depending on their physical dimensions and characteristics. The main features when designing microwave resonators are their size, power handling, the unloaded Q-factor and spurious performance [3,4]. The Q value gives the losses of the resonator. Microwave resonators might have more than one mode at the same frequency [4]. However, the field patterns of these modes are different. In this case, the realization of multi-modes in one physical resonator is possible with a significant reduction in filter volume. Table 2.1 shows a comparison between different modes related to the properties of the resonator [3]. Figure 2.1 illustrates the relationship between size and insertion loss for the types of microwave filters at 5 GHz. It can be seen that the

Table 2.1: Comparison between Various modes of operation [3].

Parameter	Single Mode	Dual-Mode	Triple-Mode
Size	Large	Medium	Small
Spurious Performance	Good	Fair	Fair
Unloaded Q	High	Medium	Medium
Power-Handling capability	High	Medium	Medium
Design Complexity	Low	Medium	High

resonator configurations that can provide Q values greater than 4000 are dielectric and waveguide resonator. The significant factor in choosing the type of resonator is the application requirements of size, Q value and power-handling capability [19]. Nowadays, due to the expanding demand for wireless communication systems and

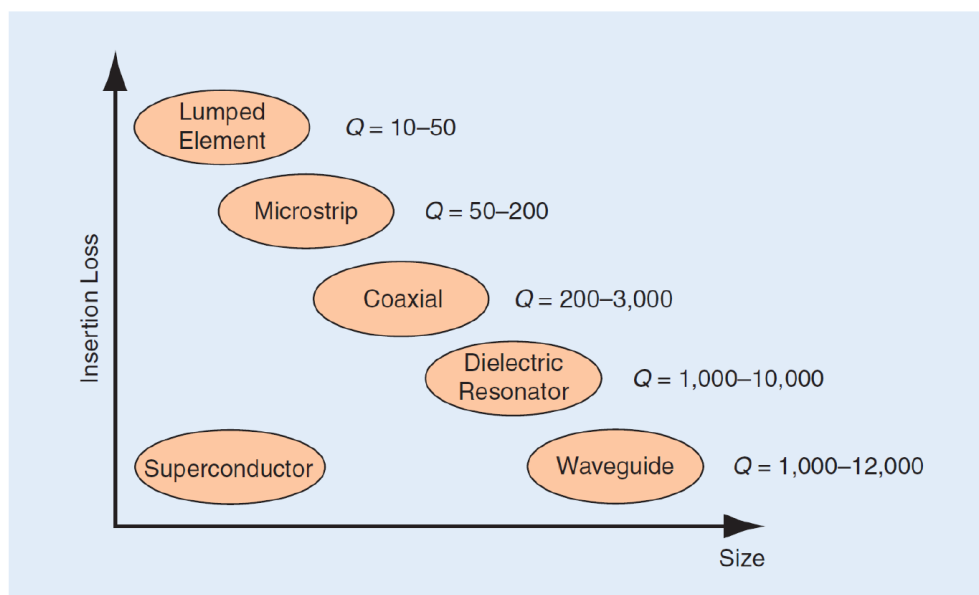


Figure 2.1: Insertion loss versus size for various RF resonators [19].

the crowded frequency spectrums, filter requirements are based on high Q values, small size, minimal insertion loss, greater return loss, low mass and larger spurious free window. For that, filters are designed to be small. At present, the types of filters often used in wireless base stations are coaxial cavity resonator filters and dielectric resonator filters [20]. Air-filled coaxial resonators are not suited for future miniaturised devices due to their large size, although they cost less to design with nominal Q (< 2000) and a good out-of-band rejection. Dielectric resonators have a good Q value with low loss and the size of the resonator is reduced significantly

by a factor of $1/\sqrt{\epsilon_r}$ and $1/2\sqrt{\epsilon_r}$ in dual-mode dielectric resonators. Therefore, they are often used as a solution to issues of space management.

2.2 Coaxial TEM Resonator Filters

Coaxial transverse electromagnetic (TEM) filters are widely used in the base station of mobile communications because of their unique characteristics. The filter consists of a cylindrical or square metallic cavity with a metallic rod placed in the centre of the cavity and short-circuited from one end and open at the other end. There are two structures for the coaxial TEM filter: interdigital and combline. The interdigital filters are used when the applications require a broad bandwidth, wide stopband and highly symmetrical frequency response. The combline filters are quite similar to interdigital filters but have their short circuit lines positioned at the same side and they are smaller in volume because of the capacitance loading on the resonators. In addition, 1-50% of the fractional bandwidth (FBW) can be designed by using combline filters [4, 20]. The configurations for combline and interdigital filter are given in Figure 2.2.

2.2.1 Combline Resonator Filter

Air-filled combline filters were introduced by G. Mitthaei in 1963 [21]. They are widely used in the base stations of mobile communications because of their ease of design, compactness and wide spurious free window. The length of the metallic rod in a combline resonator is equal to or less than $\lambda_g/4$. The capacitance between the resonator and the ground can produce a space filled by a dielectric material depending on the value of the capacitance. Figure 2.3 shows the standard combline resonator. The combline filters are viewed as coupled TEM-mode transmission lines. Selectivity of such a filter can be improved by increasing the electrical length of the resonators, but that causes it to decrease on the lower side

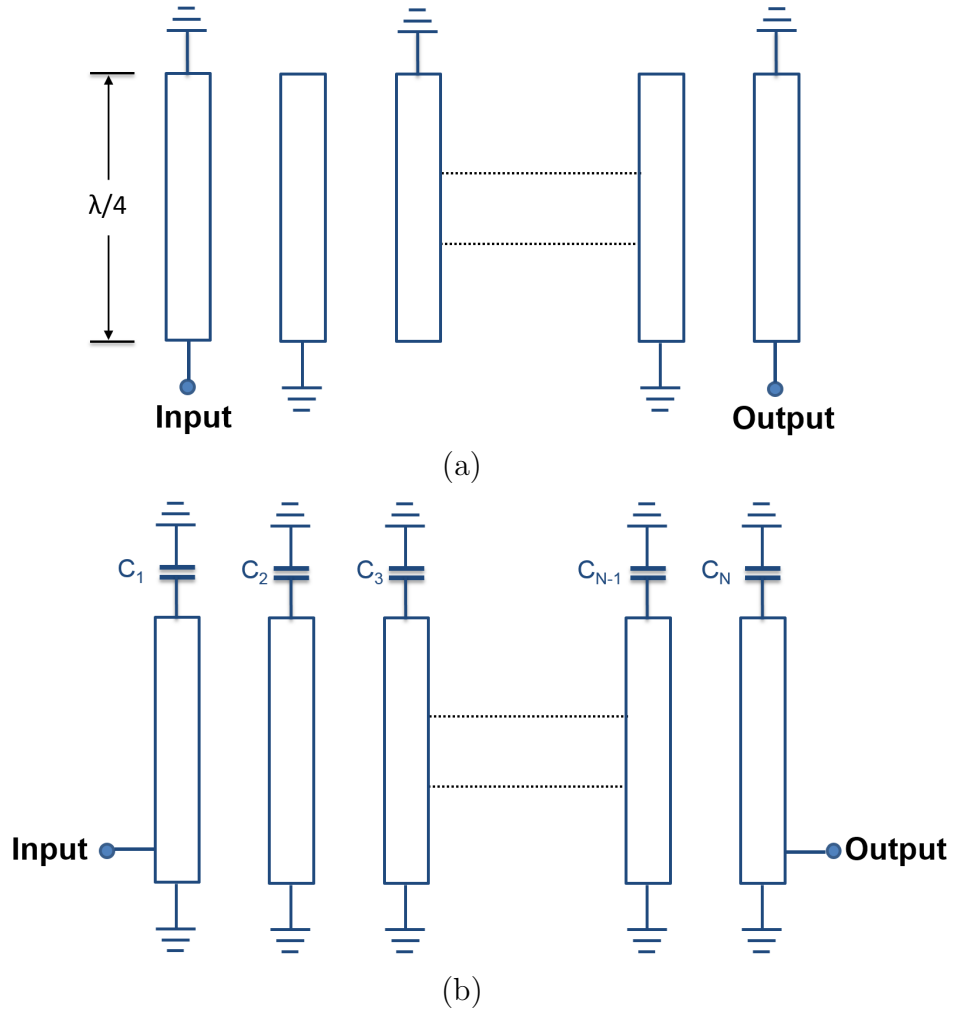


Figure 2.2: (a) Interdigital filter, (b) Comblin filter [4].

of the resonant frequency. Irises between resonators are needed to improve the selectivity by miniaturising the dimensions [22]. Due to the inner conductor, their Q factors are nominal (< 2000). Different techniques have been applied by [23] and [24] to increase the Q factor. A round base method [23] has a 5% increase in Q factor while about a 14.2% increase was achieved by using periodic six-disk inner conductor [24].

Replacing the metallic centre rod with a high permittivity dielectric rod is another way to decrease the losses in the comblin filter and improve the Q-factor. These types of filters are called dielectric comblin filters. The fundamental frequency depends on the length of the dielectric rod and is inversely proportional to dielectric permittivity. Whereas other modes are very sensitive to the diameter, the length/diameter ratio of more than 1 can give a good spurious-free performance.

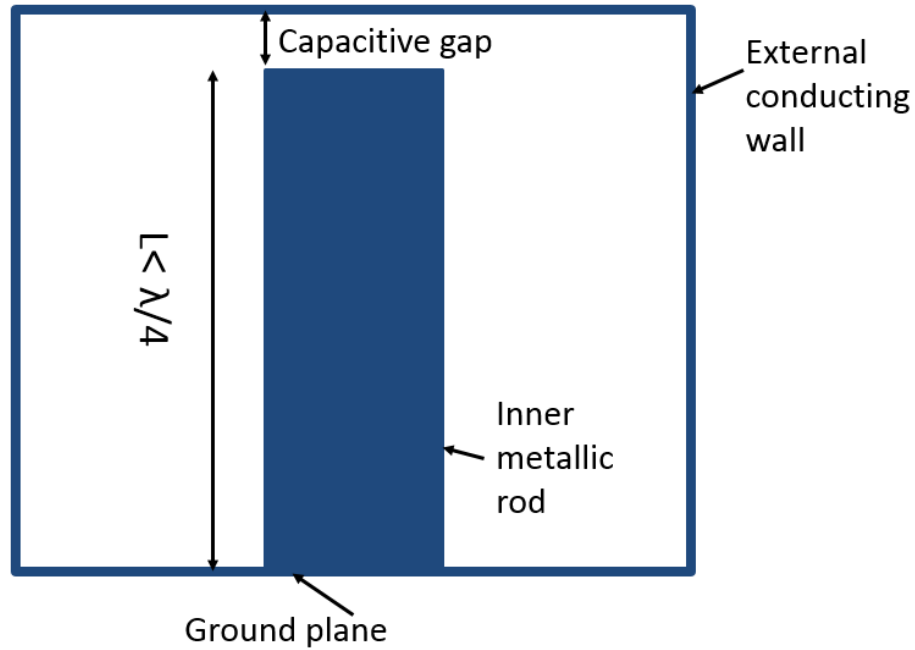


Figure 2.3: Air-filled combline resonator.

The dielectric combline resonator filter was studied by [20, 25, 26]. Findings show that dielectric combline resonator filters have the same advantages of coaxial combline filters, such as simple design, low cost, wide tuning and wide spurious performance. They offer a 50% increase in unloaded Q while maintaining the overall size, and the same applies to the air-filled coaxial combline resonators.

2.3 Waveguide Resonators

A waveguide is a hollow conductive structure used to propagate the electromagnetic energy from point to point. The two most common types of waveguide are rectangular and circular waveguides. It can behave as a resonator when cut at half guide wavelength section and shorted from each side. Although waveguides can support a high Q factor of up to 50,000, they suffer from a big size at the lower frequency which is generally used in mobile communications. There are three types of modes supported by waveguide resonators: $TE_{\ell,m,n}$, $TM_{\ell,m,n}$ and hybrid modes, where ℓ, m and n are the numbers half-period variations of E and H along x, y and Z respectively in the rectangular waveguide resonator. They relate to ϕ, r

and z respectively in the circular waveguide resonator, as shown in Figure 2.4. The dominant modes in rectangular and circular waveguides are usually TE_{01} and TE_{11} respectively [4, 27]. The volume of an air-filled waveguide resonator can be reduced by the factor $1/\sqrt{\epsilon_r}$ if the air is replaced by dielectric permittivity [7]. Mode charts for resonators are conveniently used to calculate and check the frequencies that might exist in the resonator. Figure 2.5 illustrates the mode chart for the circular waveguide resonator.

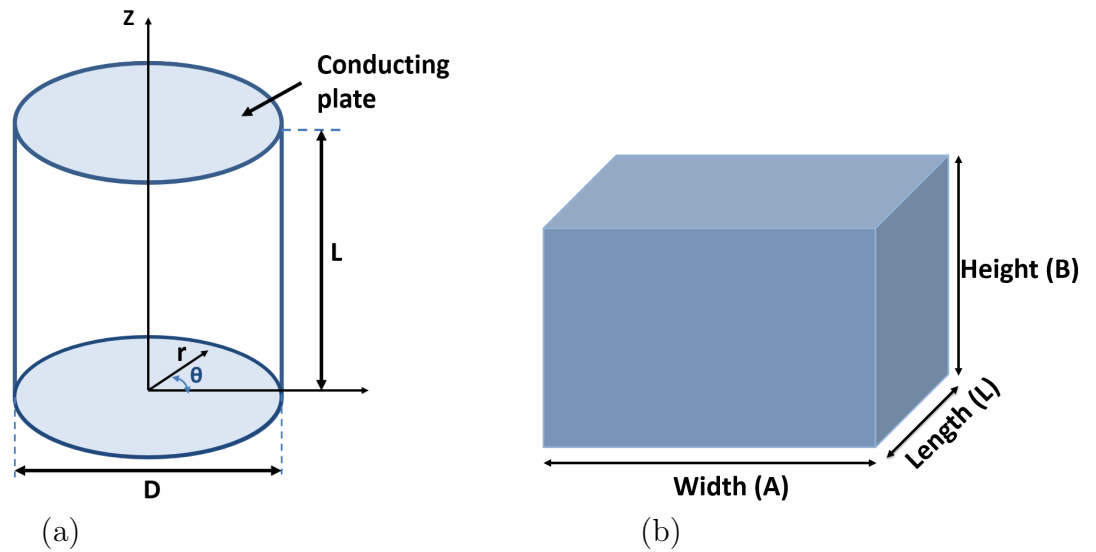


Figure 2.4: Circular and rectangular waveguide resonators.

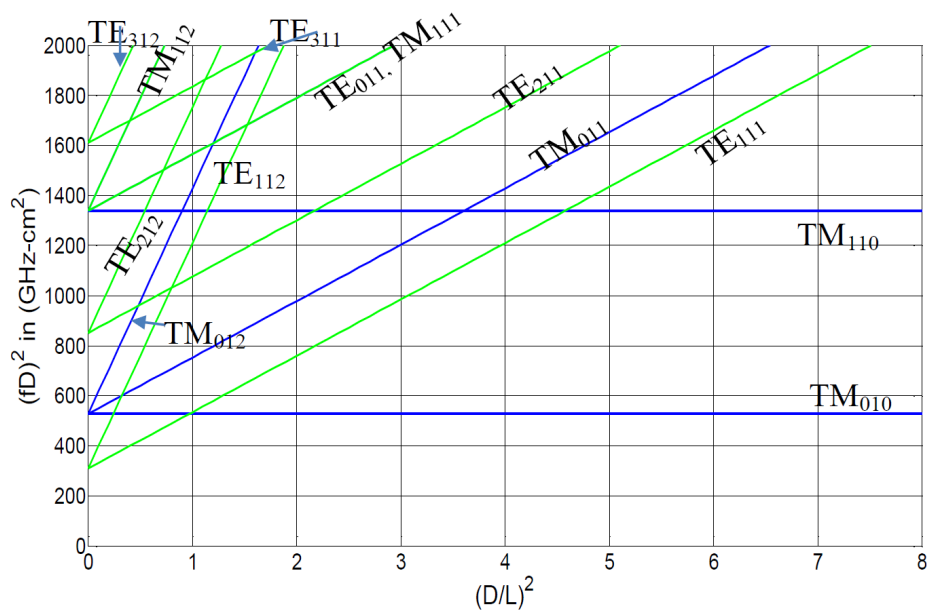


Figure 2.5: Mode chart for circular waveguide resonators.

2.4 Quality Factor

Practical filter components have a finite resistance which causes degradation in the filter performance. Q-factor indicates the quantity of losses in the filter, which is defined as

$$Q = \omega \frac{(\text{average energy stored})}{(\text{energy loss/second})} \quad (2.1)$$

where ω is the angular frequency (rad/sec). There are three types of Q factors:

- Unloaded Q factor Q_u .
- External Q factor Q_e .
- Loaded Q factor Q_L .

The unloaded Q_u accounts for internal losses of the resonator while the external Q_e determines the external losses when the resonator is connected to an external circuit. The loaded Q_L accommodates both internal losses and external losses. The unloaded Q factor can be introduced as [28]:

$$\frac{1}{Q_u} = \frac{1}{Q_d} + \frac{1}{Q_c} + \frac{1}{Q_r} \quad (2.2)$$

Where Q_c , Q_r , Q_d represent conduction, radiation and dielectric losses of resonator respectively. When there is no loss by the external field (conduction, radiation), their values are insignificant and can be neglected. The unloaded Q_u can be written as:

$$Q_u = \frac{1}{\tan\delta} \quad (2.3)$$

Where $\tan\delta$ is the loss tangent of the resonator [29]. The theoretical Q-factors for circular waveguide resonator are shown in Figure 2.6 and can be given by the equation form [7]. A term D/L is the ratio of diameter to length of the circular waveguide, while $\frac{\delta_s}{\lambda}$ is the ratio of the skin depth of the conductor to free space wavelength at the resonant frequency. It depends on frequency and type of materials used, as shown in Table 2.2.

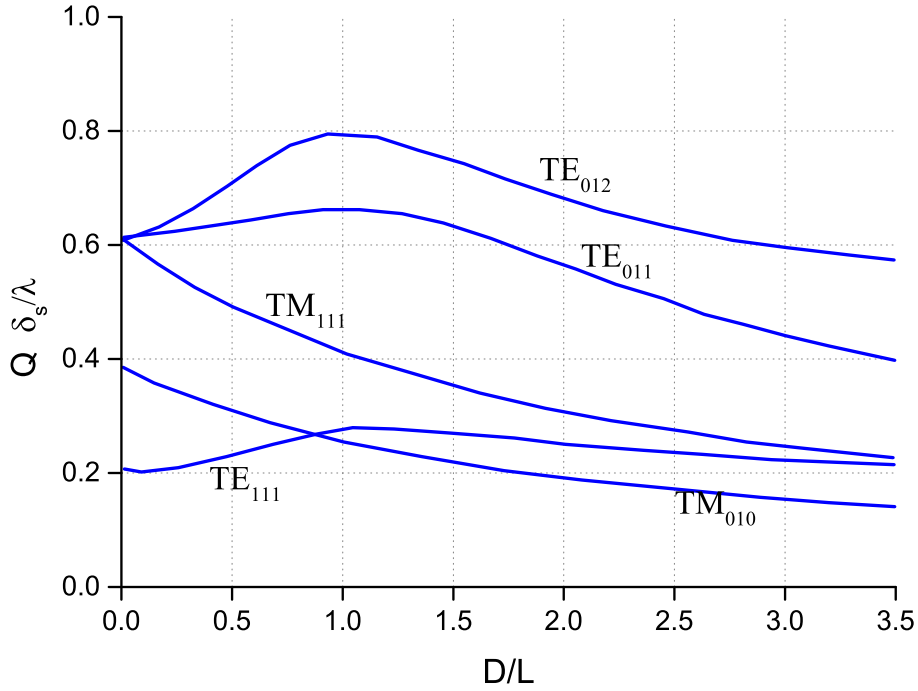


Figure 2.6: The theoretical Q-factors for a circular waveguide resonator at $\epsilon_r = 1$.

Table 2.2: δ_s/λ values for various metals [1].

Metal	δ/λ
Silver	$6.76 \times 10^{-6} \sqrt{f_{GHz}}$
Copper	$6.95 \times 10^{-6} \sqrt{f_{GHz}}$
Aluminium	$8.7 \times 10^{-6} \sqrt{f_{GHz}}$
Brass	$13.4 \times 10^{-6} \sqrt{f_{GHz}}$

2.5 Microstrip and Superconducting Resonators

The general structure of the microstrip transmission line is shown in Figure 2.7. A conductive strip with a thickness \mathbf{t} and width \mathbf{w} is positioned on the top of a dielectric substrate ϵ_r with height \mathbf{h} while the bottom side is grounded. A quasi-TEM wave is the common mode of propagation in the microstrip line. The planar configuration filter can be implemented in several ways, for example, with the photolithography process or thin-film and thick-film technology. Microstrip filters are preferred due to their ease of design, analysis, fabrication, low loss, small size and light weight, high frequency and good spurious-free window [30]. A multi-mode filter can be employed to reduce the size to 50% including the square loop [31],

circular ring [32], open-loop resonator [33] and patch-based resonators [34]. Moreover, the spurious-free window is good in this configuration and can be improved by stepped impedance resonator (SIR) [35, 36]. However, the losses in the microstrip are high, making it unsuitable for high power-handling like in the base station application.

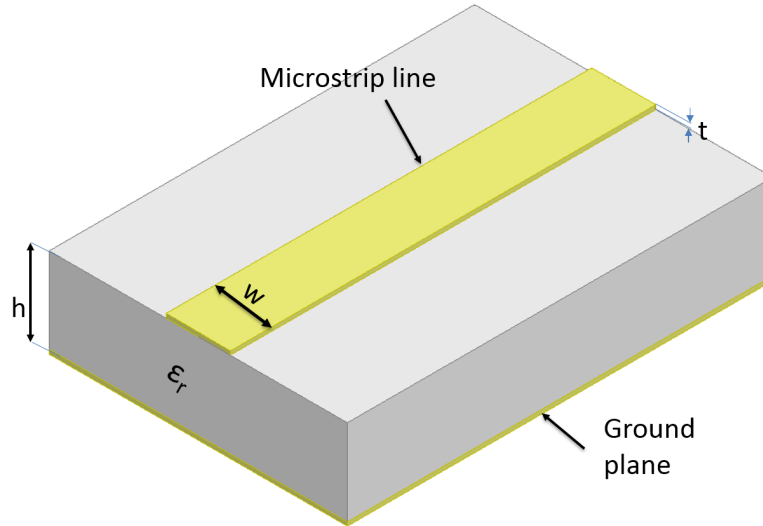


Figure 2.7: The microstrip structure.

In order to fabricate a high-order filter at low frequency range of a few hundred megahertz with low insertion loss and small size, high-temperature superconductor (HTS) filters could be utilised [6]. Figure 2.8 presents the cross-shaped spiral resonator filter operating at 408-MHz band [5]. The circuit with an overall dimension of 20×20.6 mm was made using a gold plate on MgO substrate with a dielectric relative permittivity of 9.64. Even though HTS technology provides a good trend in realizing small size and less loss, it requires a cooling system to drop the temperature below 150 K. In superconductors, the surface resistance for the stripline is dependent on the applied field. Under high field conditions, the surface resistance leads to non-linearities and generation of intermodulation products. The non-linear effect diminishes the power-handling capability of microwave superconductive devices [37, 38].

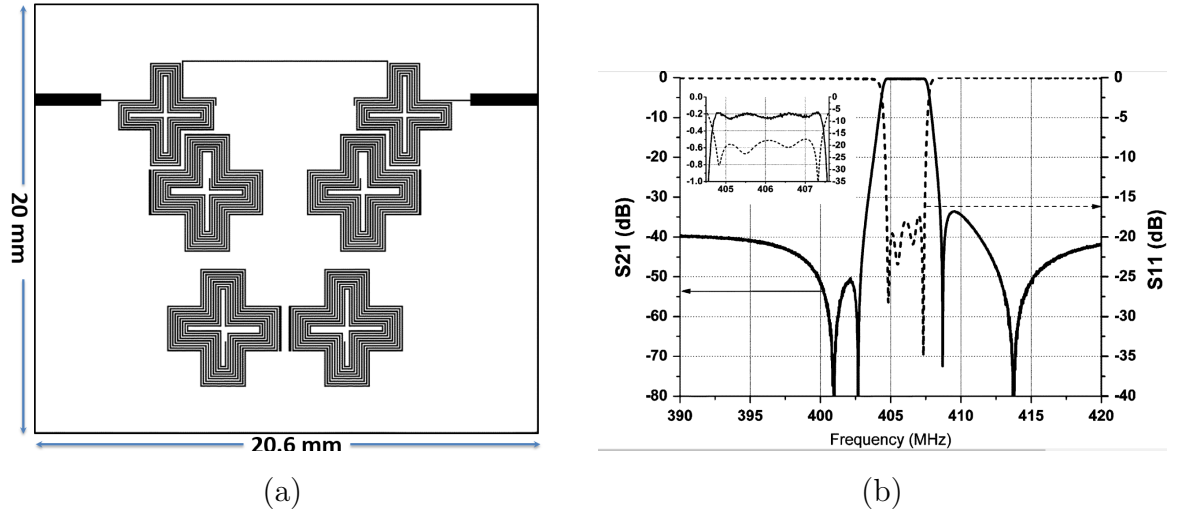
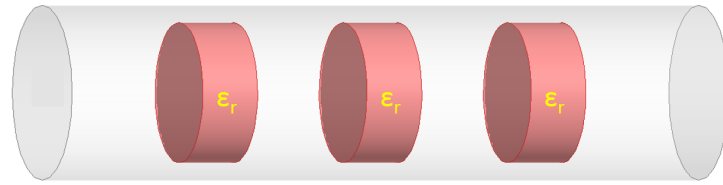


Figure 2.8: (a) Layout of the four-pole microstrip HTS bandpass filter on 0.508-mm-thick MgO (b) Measured performance of the four-pole filter [5].

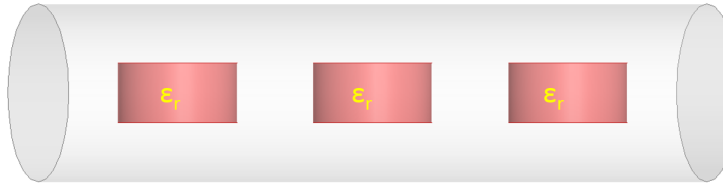
2.6 Dielectric Resonator Filters

Dielectric resonator (DR) filters play an essential role in mobile and satellite communication. Generally, the structure of DR filters consists of some dielectric resonators placed inside metallic enclosure cavities. According to the position of the dielectric resonator inside, the filter can be classified into two types: DRs can be aligned axially or transversally in the cut-off waveguide and individual resonators placed in the planer configuration, as shown in Figure 2.9. Input and output electromagnetic energy can be coupled by probes and irises, which are usually used to couple the inter-cavity resonator.

There are two kinds of dielectric resonator filters, which can be used depending on the number of operating modes (i.e. single-mode DR and multi-mode DR). Single-mode DR filter refers to the principle of realizing all resonators operating at the same operating mode. On the other hand, the multi-mode dielectric resonator filter has the property of operating more than one degenerative mode in the same cavity. Further details will be provided in the next section.

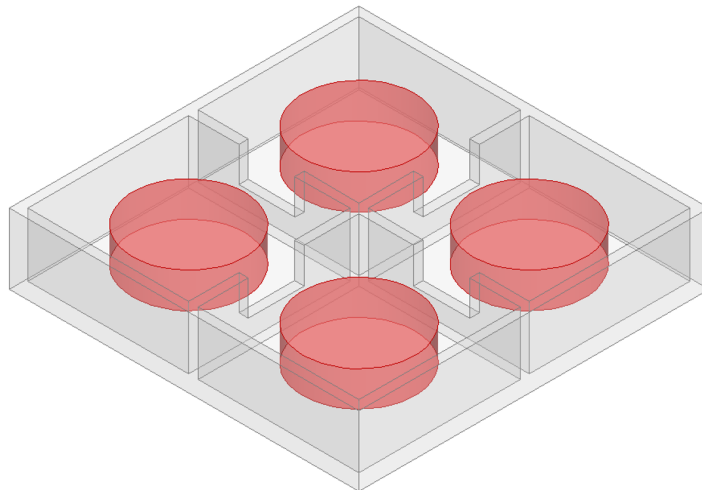


Longitudinal layout



Transversal layout

(a)



(b)

Figure 2.9: Dielectric filter layout (a) Cut-off waveguide filter, (b) Planar filter.

2.6.1 Dual-Mode Dielectric Resonator Filters

Fiedziuszko reported the first dual $HE_{11\delta}$ dual-degenerate mode in a dielectric loaded cavity filter in 1982 [39]. Figure 2.10 presents the configuration of the first dual-mode filter. This filter has 8th order and operates in C-band. The number of cavities is only half what is usually needed by using a single mode filter. It offers a low volume of about 8.3% reduction ratio in comparison with the standard TE_{111} metal wall cavity. Coupling between modes within a single cavity is achieved via a

mode-coupling screw with an angular location of 45° with respect to perpendicular tuning screws. Cross slots between two cavities were used to provide inter-cavity coupling. In this case, both resonators can be coupled to each other in adjacent cavities.

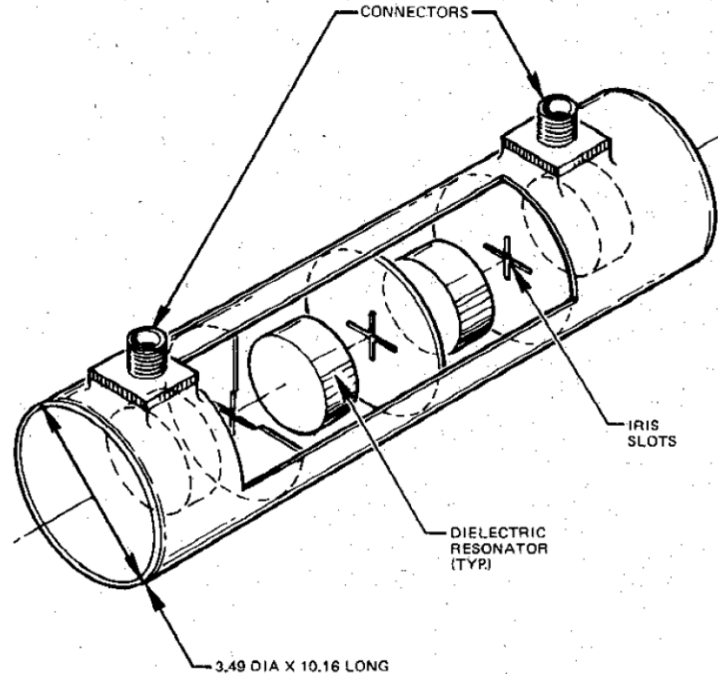
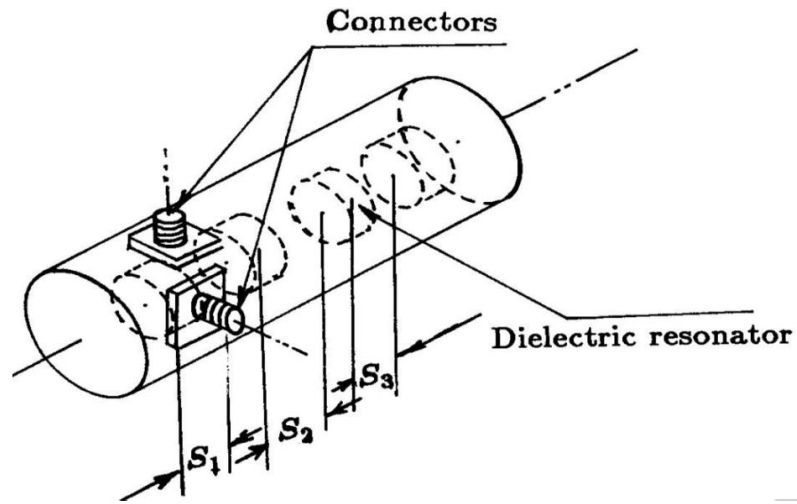
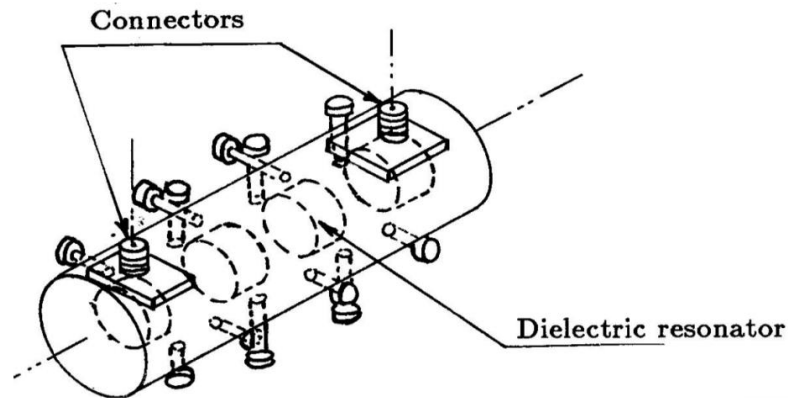


Figure 2.10: Configuration of dual-mode DR filter [39].

These bandpass filters are typically used in mobile base stations and satellite communications due to their small size, high Q_u of about 8000 and low loss compared to single-mode filter realization. New inter-cavity coupling has been suggested by Zaki [40] and Kobayash [41] for $EH_{11\delta}$ mode, as shown in Figure 2.11a. It uses coaxial probes for input and output ports and the irises are replaced by screws for easily tuneable coupling over a wide range of coupling [42]. That means all adjustment coupling can be done by screws, which increases the insertion loss in the mid-band because the conduction currents are eliminated by use of the iris. Furthermore, an elliptic function response can be produced by this type of filter because the tuning screws are able to control the position of transmission zeros. The unloaded Q-factor was 6000 while insertion losses were 0.4dB. The longitudinal dual-mode dielectric resonator filter without iris reported by Zaki, [43] in 1987 is illustrated in Figure 2.11b. The screws were placed in a mid-way position



(a)



(b)

Figure 2.11: Canonical and longitudinal dual-mode dielectric resonator filter without iris [43].

between two pairs of modes used to adjust the coupling and higher out-of-band isolation was achieved between the input and output compared to the canonical configuration. Moreover, the bandwidth has been increased with respect to the canonical structure.

The dielectric-loaded rectangular cavity resonator in stacked and planar form has been studied by Mirshekar et al. [44], who were able to control the non-adjusting coupling. Through their result, it can be seen that the stacked configuration has low loss compared with the planar, 0.14 dB and 0.32 dB respectively, even though the unloaded Q factors are the same. Figure 2.12 shows a novel coupling structure for a dual-mode dielectric resonator that was proposed in the literature [45, 46].

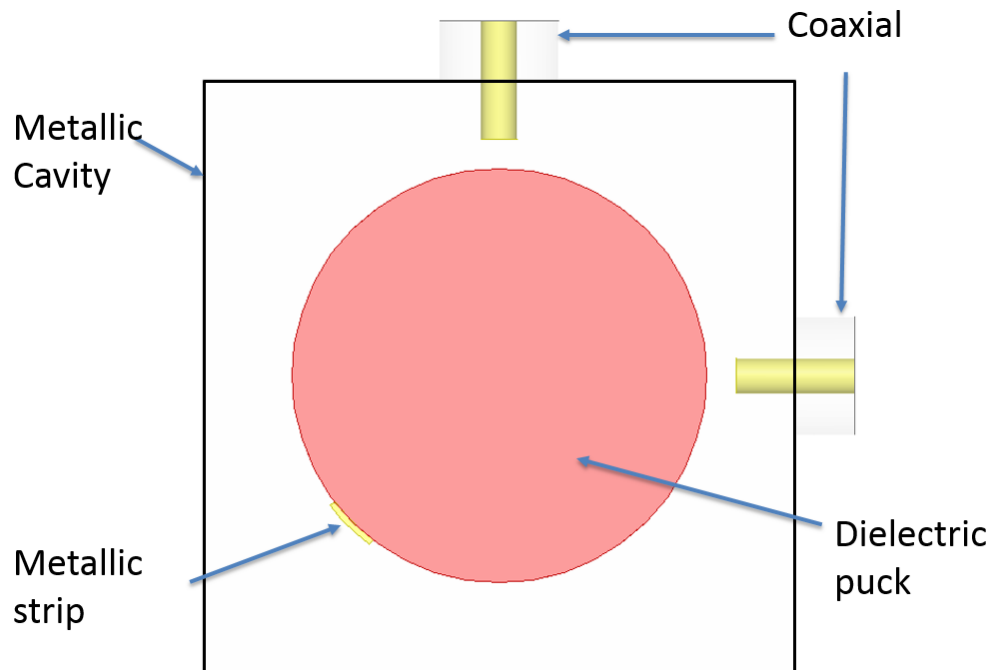


Figure 2.12: Configuration of metallic strip coupling [45].

A dual-mode resonator can be achieved by positioning a metal strip on the inner or outer dielectric ring resonator at 45° with respect to the two polarization axes. At the resonant frequency of 2.34 GHz, the bandwidth coupling is less than 10 MHz and the unloaded Q-factor is 11,000. The disadvantages of this design are that there is no way to increase the bandwidth and the insertion loss is high in comparison to other coupling methods. IL was 1.33 dB and the maximum spurious-free window was 250 MHz. The coupling between the two degenerate modes was achieved by introducing a slot at 45° without the need for a metallic strip [47]. A four pole dual-mode elliptic filter was developed by using this technique with a central frequency of 5.5 GHz, the -3 dB bandwidth was 55 MHz and the metallic cavity dimensions are 22.4×31 mm. A dual-mode filter with split grooved ceramic resonator was presented by Accatino et al. in 2002 [48]. Their findings show that a resonator with unloaded Q factor of 9000 and a spurious ratio of 1.34 has been obtained. An eight-pole filter was tested with probes for input and output coupling and iris for inter-cavity coupling. An advantage of this configuration in one cavity is that the coupling is widely controllable to achieve the optimum coupling when the field is strong.

2.6.2 Conductor Loading of Dielectric Resonators

All the aforementioned dielectric resonator structures reveal very high Q_u and bulky hardware which can be used in many applications, especially in the cellular base station market [49]. The direct contact between a metallic enclosure cavity and a ceramic resonator was used to reduce the size of resonator with high Q_u and a significant improvement in the power handling of the filter [50,51]. Engine-block or planar-type filter was developed [52], as shown in Figure 2.9b. This configuration is easy to assemble for in-line cavities. Realization of non-adjacent couplings is difficult, but can be obtained, for instance, by a combined probe and iris coupling through the cavity wall. A 50% weight reduction was achieved in C band 8 order compared with in-line filters. A loaded dielectric resonator was reported by Hunter et al. [53], who placed the DR on the base of the metal cavity with conductive discs positioned on the top of each resonator. Tangential electric fields E are reduced at both the bottom and top due to the loading of the DR with conductors at these positions. This was achieved by using a simple model as TM_{110} for analysing the

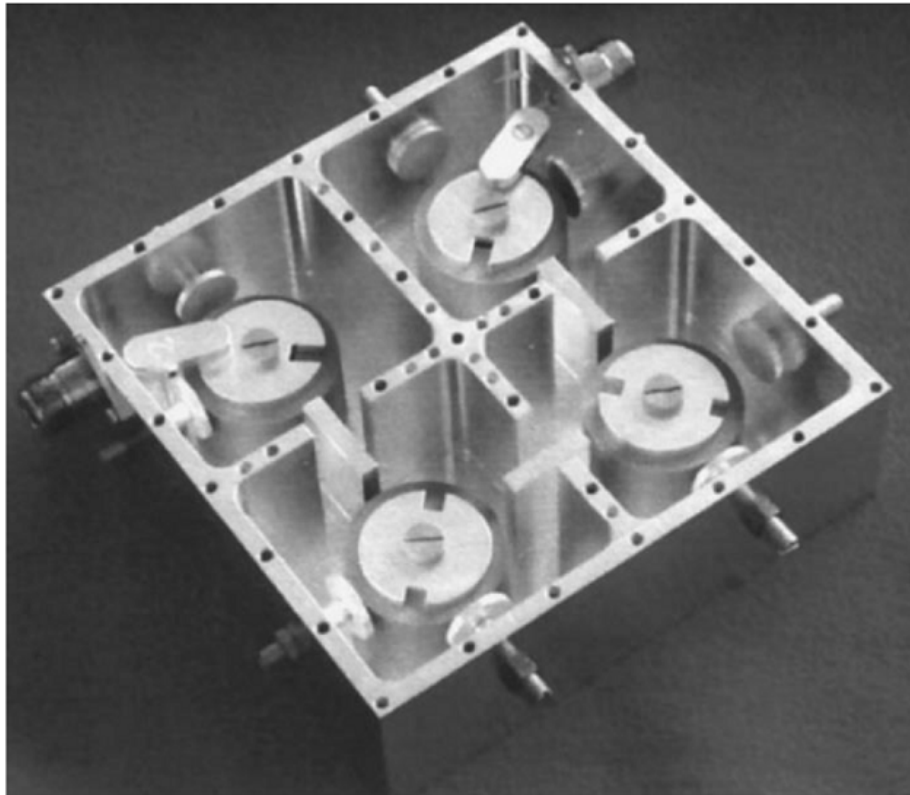


Figure 2.13: Dual-mode DR conductor-loaded filter configuration [53].

resonant frequency and theoretical Q . For this type, a typical dual-mode resonator achieved a Q_u of 6300 at 900 MHz with internal dimensions cavity of $6.5 \times 6.5 \times 6.5$ cm, as shown in Figure 2.13. The reduction in volume was half compared with an equivalent coaxial filter. However, placing these conductors on the top of DR creates a drift in the fundamental frequency with no significant effect on the first spurious mode, a usual problem in this type of filter.

Another way to load the dielectric resonator was proposed by Hu et al. [54] in which a cylindrical dielectric rod with relative permittivity $\epsilon_r = 20.5$ was in contact with the top and bottom walls of a metal cavity. Holes were drilled through the rod along the axis in order to realize a self-coupling for orthogonal modes, with the use of a loop to control the inter-cavity coupling. All tuning screws were placed on the top; with no screws on the sidewall. The insertion loss was 0.5 dB at centre frequency 1.948 GHz, Q_u 3000 with $41 \times 41 \times 14$ mm. This design has upper and lower spurious frequencies of about 1.25 GHz and 2.55 GHz respectively. High power handling and wide operating temperature range are very important in many applications, especially in satellite payloads. A novel configuration for dielectric resonator filter operation in the Ku-band was suggested by Panariello et al. [55]. The resonator has a double T cross section, which allows mechanical mounting. Screws and irises were used to adjust the self- and inter-cavity coupling. At a centre frequency of 11.52 GHz and bandwidth of 37 MHz, the design offered better spurious performance, 70% weight saving, over 50% footprint reduction and stability of the Q -factor over temperature of about 10% compared with the conventional TE_{114} mode. The majority of the loss is concentrated on the metal cavity. Mono-block of ceramic were employed for the implementation of a TM_{11} dual-mode resonator. Y-shaped mono-block ceramic was achieved by Höft [56]. Irises and screws were used to adjust the coupling. A Q_u 4000 at 2 GHz with a small ($40 \times 40 \times 25$ mm) metal cavity for the filter has been realized; however, the unit is large compared to conventional filter and needs many tuning screws with difficult shape for coupling.

2.6.3 Improvement of Spurious Performance

One of the major disadvantages of the DRs is that the spurious performance is poor when compared with metal filters [57]. Therefore, a low pass filter with high selectivity is required to clean up the undesired spurious-free window in the stop-band region. Consequently, the filter's total size and passband insertion loss will be increased. Altering the shape of the DR to improve the spurious performance in the hybrid mode has been demonstrated in the literature [58,59]. By creating a hole in the centre of the DR, the spurious ratio can be improved to 1.5:1 compared with a DR with no hole. Two orthogonal hollow cylindrical or cross-shaped DRs were reported by [60,61] to improve the spurious response in a dual-mode TE_{01} . However, this method has only a limited effect. The best ratio reported was 1.24 in [60] and 1.164 in [49], adding complexity and cost to the manufacturing process. The spurious behaviour can be improved by mixing the type of resonators in the same filter. In [62] a new method was applied to achieve a good spurious-free window of the dielectric ring TE_{01} single-mode using the advantages of the dual-mode HE_{11} . The filter slightly changed in volume compared with the size of the completely built HE_{11} dual-mode because the cavity size for the TE_{01} was smaller than that of the HE_{11} . All modes were close to HE_{11} having been suppressed below -50 dB by this technique. In another method, the DR single mode TE_{01} was replaced by a conductor loaded resonator filter. Significant improvement was achieved while the unload Q factor was slightly decreased because the conductor loaded resonator has less Q than the dielectric resonator [57]. A semi-cut dielectric puck was successfully applied as a dual-mode filter for S-band application in the work by Memarian et al. [63]. The operation modes were HEH_{11} for cavity 1 and HEE_{11} for cavity 2, which were coupling by vertical irises. In addition, the spurious-free window was improved by making a vertical and horizontal slot in the ceramic.

2.6.4 Triple-Mode Resonator Filter

A triple-mode DR filter was proposed by Walker et al [64]. A cube of ceramic material with relative permittivity 44 was placed in the centre of an aluminium enclosure cavity cube to operate at $TE_{01\delta}$ triple-mode as shown in Figure 2.14. The disc was used to decrease mode 2 but it affected the other mode to similar degree. The inter-cavity coupling has been realized by the chamfers along three axis of the ceramic cube. It offered reduction ratio of about 2 compared with the single-mode at 2 GHz. However, the tuning screws caused a significant decrease in the Q_u , about 15%, and the bandwidth was quite narrow, about 5 MHz. Lye

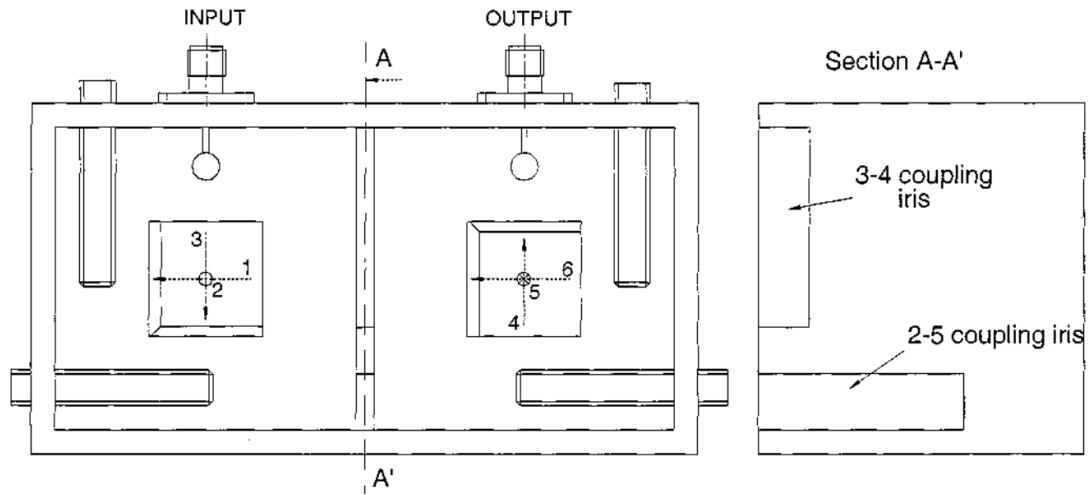


Figure 2.14: Triple-mode DR conductor-loaded filter configuration [64].

et al. [65] were presented a $TM_{11\delta}$ triple-mode which consist a cubic ceramic in the centre of the metallic cubic cavity. Three TZs were achieved with bandwidth of about 51 MHz where the size was larger than in [64] and the permittivity was less when a metal screw was used to adjust the frequency and the coupling bandwidth. A new TM triple-mode was presented by [66]. The filter consisted of a cross-shaped mono-block of ceramic $\epsilon_r=38$ in contact with the side wall of a square metallic cavity. The filter was designed on a resonant frequency of 850 MHz and bandwidth of about 21 MHz. The gain in size reduction was 1/5 compared with a conventional air cavity resonator; the Q-factor was 3000 with the metallic tuning screw. A compact triple-mode filter has been designed by Hendry [67]. The

novelty was the coupling technique that used a microstrip substrate to achieve all coupling requirements with a size of about 5.3 cm^3 at 1.8 GHz, as shown in Figure 2.15. Three TZs were implemented on one side with the ability to convert to the other side. The Q_u was about 2000 and the spurious-free window was 400 MHz, as shown in Figure 2.15.

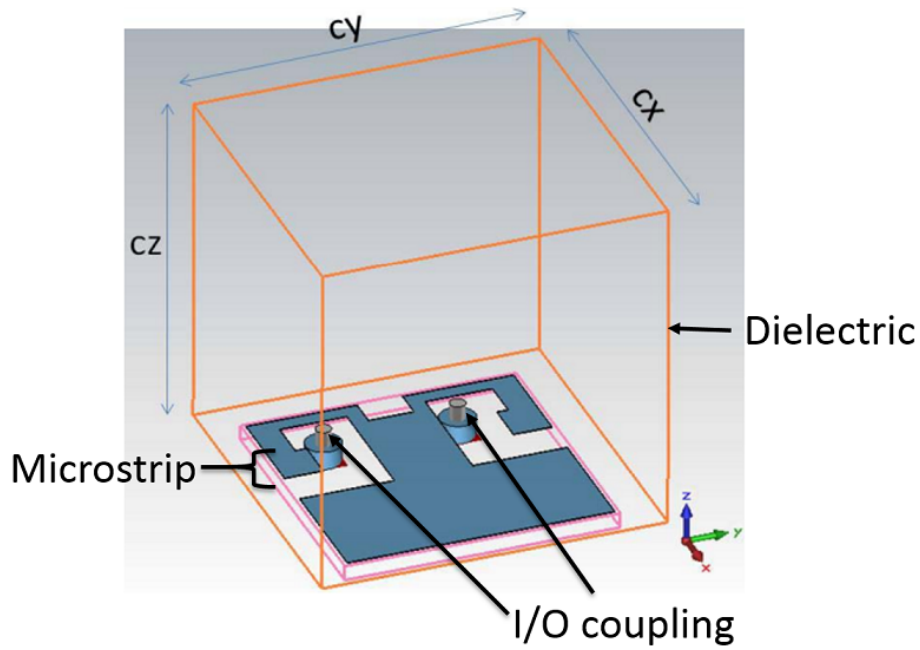


Figure 2.15: Compact triple-mode DR conductor-loaded filter [67].

A spherical dielectric resonator can be utilised as a triple-mode filter [68]. A high Q-factor of 32,000 was implemented by placing a spherical DR with relative permittivity 46 inside a sphere of a metallic cavity with radius 45 mm which operates at 850 MHz. However, the I/O coupling was complex and unable to achieve bandwidth greater than 15 MHz. The size reduction was about 1/3 and the spurious-free window was poor, about 150 MHz. Work by [69] proposed a triple-mode DR filter using a cylindrical-shaped ceramic inserted into the middle of the metal cylinder cavity. A pair of HE and TM mode were used to present a triple-mode filter. The length of I/O probes were used to generate the coupling between the hybrid mode and the others. The filter was fabricated without any tuning screws and the poor spurious-free window was about 230 MHz.

2.7 Summary

This chapter has provided a literature review of the types of resonators, such as coaxial TEM, microstrip, superconducting, waveguide and DR with single, dual and triple-modes. Each resonator has advantages and disadvantages based on the cost, size, loss and power-handling. Coaxial TEM and DR filters are used in the cellular base station. because they provide a have wide tuning range, low cost, and excellent spurious-free window, while microstrip, superconducting and waveguide filters are not used based on their drawbacks, like loss and power-handling, size and power-handling, and size respectively. Multi-mode DR filters offer a high Q factor and small size compared to the conventional air-filled coaxial resonator, and different shapes and topologies can be built. Etching through the DR and hybrid resonators topology can be used to improve the spurious-free window.

Chapter 3

Filter Design Methodology

3.1 Introduction

Microwave filters are important in extracting the desired frequency spectrum from a wide variety of electrical signals. According to passbands, the filters can be classified as: lowpass (LPF), highpass (HPF), bandpass (BPF), bandstop (BSF) and multiband. Filter design requires a robust methodology and therefore poses a complex engineering challenge. In general, the filter design procedure begins from specification of the filter and progresses in the steps shown in Figure 3.1. In next sections, the steps of filter design will be discussed.

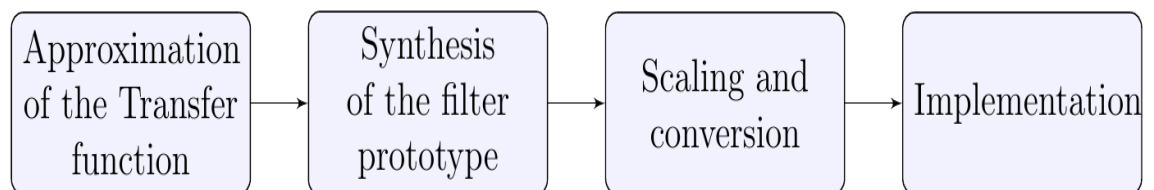


Figure 3.1: Filter design procedure [27].

3.2 Transfer Function Approximation

Filter design usually starts with a transfer function of the filter that satisfies a given filter specification. It is convenient to use complex variables for the analysis of the circuits in the frequency domain because the physical processes in the electrical circuit are represented as derivatives and integrals of currents and voltages. The transfer function can be presented mathematically as a ratio of two polynomials of complex frequency $s = \sigma + j\omega$. The analytical expression of the transfer function reflects the relationships between the initial specification and a lowpass filter prototype with its cut-off frequency normalized to unity [3,4].

3.2.1 Power Transfer Function and Characteristic Polynomials

Figure 3.2 shows a doubly terminated lossless transmission network which can represent the lossless filter. Assume that P_{in} is the input power that will transmit through the lossless circuit and P_{out} is the output power available at the load, while $P_{ref_{in}}$ and $P_{ref_{out}}$ are the reflection powers from source and load respectively caused by mismatch. It is relevant here to point out that P_{out} cannot be greater than P_{in} in passive circuits [27].

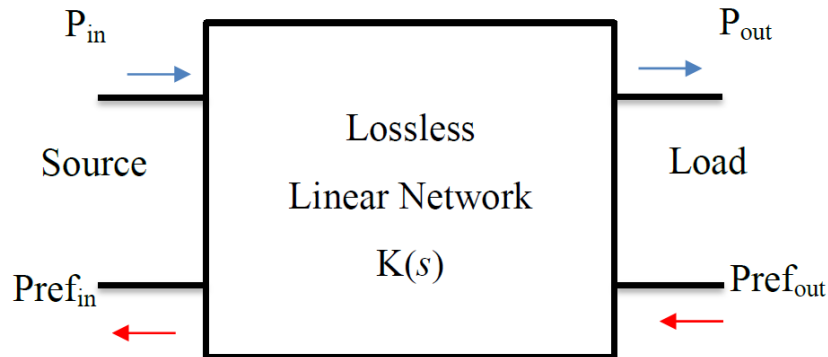


Figure 3.2: Doubly terminated lossless linear network.

$$\frac{P_{in}}{P_{out}} = 1 + |K(s)|_{s=j\omega}^2 \quad (3.1)$$

Where $K(s)$ is a rational function in s with real coefficients. Furthermore, the ratio of inverted power from equation 3.1 is a squared magnitude of the transmission coefficient; in transmission line theory, this is called the scattering parameter $S_{21}(s)$:

$$|S_{12}(s)|_{s=j\omega}^2 = \frac{1}{1 + |K(s)|_{s=j\omega}^2} \quad (3.2)$$

Reflected power is introduced by the reflection coefficient, or scattering parameter $S_{11}(s)$, which is related (for lossless networks) to $S_{21}(s)$ through:

$$|S_{12}(s)|^2 + |S_{11}(s)|^2 = 1 \quad (3.3)$$

It is clear that $S_{11}(s)$ can be represented as a ratio for linear time-invariant networks as equation 3.40:

$$S_{11}(s) = \frac{F(s)}{E(s)} \quad (3.4)$$

Thus, equation 3.3 will take into account for $s = j\omega$ it implies that:

$$S_{12}(s) = \frac{P(s)}{\epsilon \cdot E(s)} \quad (3.5)$$

$$P(s)P(-s) = E(s)E(-s) - \epsilon^2 \cdot F(s)F(-s) \quad (3.6)$$

Polynomials $E(s)$, $F(s)$ and $P(s)$ are referred to as characteristic polynomials; their coefficients are determined from the given specification which poses an approximation problem. Characteristic function $K(s)$ can be derived from the characteristic polynomials used in equation 3.7:

$$K(s) = \epsilon \frac{F(s)}{P(s)} \quad (3.7)$$

The ripple constant in equation 3.7, ϵ , is employed with a view to normalizing the maximum amplitude of the filter in the passband. In all synthesis procedures, each polynomial is normalized. For that, their highest coefficient is unity and the constant resultant factor is engaged in the ripple constant. In general, different characteristic functions are available for approximation; however, many classical functions are conventionally noted. These are Butterworth, or maximally flat;

Chebyshev and Generalized Chebyshev. Features and properties of these characteristic functions are discussed in sections 3.2.2 to 3.2.4.

3.2.2 Butterworth Approximation

Butterworth, or maximally flat, is the simplest approximation for an ideal lowpass filter. The approximation is defined by:

$$K(\omega) = \omega^N \tag{3.8}$$

where N is the degree of the filter prototype network. This suggests that $P(s) = 1$ and $F(s) = s^N$. S-parameters of the filter prototype are determined as:

$$|S_{12}(s)|^2 = \frac{1}{1 + \omega^{2N}} \tag{3.9}$$

$$|S_{11}(s)|^2 = \frac{\omega^{2N}}{1 + \omega^{2N}} \tag{3.10}$$

The insertion loss is given by:

$$L_A = 10 \log_{10}(1 + \omega^{2N}) \tag{3.11}$$

If $\omega < 1$, ω^{2N} , rapidly becomes very low. For $\omega > 1$, becomes very large and therefore is termed to be maximally flat. Consequently, the unknown coefficients of the polynomial $E(s)$ can be obtained from [4]:

$$S_k = \begin{cases} e^{[\frac{j\pi}{2N} (2k-1)]} & N = \text{even} \\ e^{(\frac{j\pi k}{N})} & N = \text{odd} \end{cases} \tag{3.12}$$

where $k = 1, 2, \dots, 2N$.

Figure 3.3 shows the maximally flat filter response with different N values, where N is the order of filter. It is essential to calculate the order of filter degree N as shown in equation 3.13 in order to meet the specification given:

$$N \geq \frac{L_R + L_R}{20 \log_{10}(S)} \tag{3.13}$$

where

$$S = \frac{\omega_s}{\omega_p} \geq 1 \tag{3.14}$$

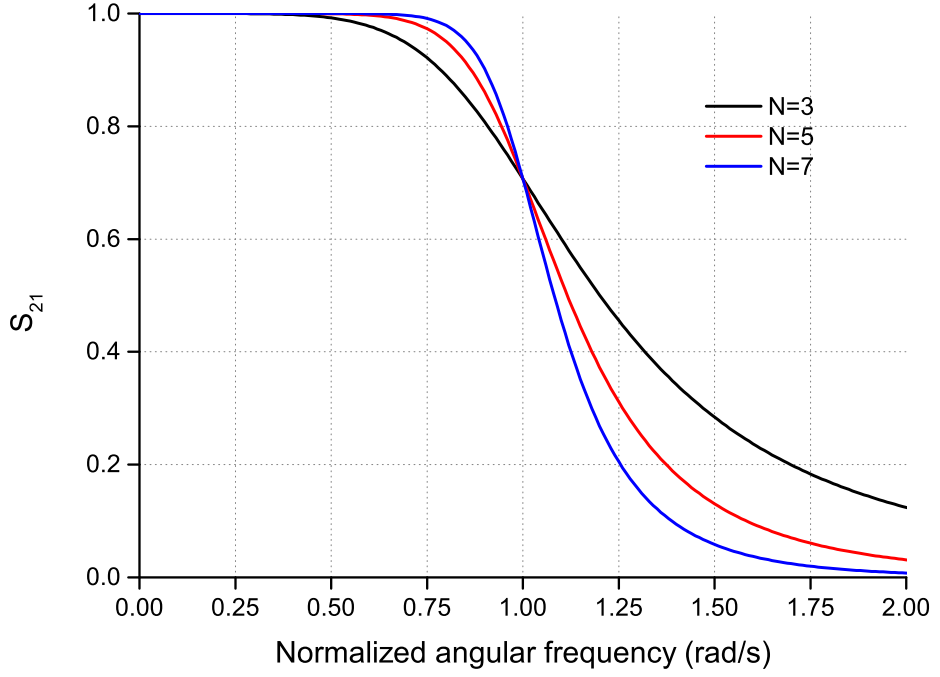


Figure 3.3: Maximally flat filter responses for various filter orders N .

ω_p represents the passband frequency bandwidth of the filter, ω_s represents the stop band frequency and L_R is the return loss where $\omega < \omega_p$. To determine the element values of N th order, a Butterworth prototype with impedance inverter is shown in Figure 3.8 [4].

$$g_r = 2 \sin \left[\frac{(2r-1)\pi}{2N} \right] \quad (r = 1, 2, \dots, N) \quad (3.15)$$

$$g_r = L_r \quad \text{or} \quad C_r \quad (3.16)$$

$$K_{r,r+1} = 1 \quad (r = 1, 2, \dots, N-1) \quad (3.17)$$

3.2.3 Chebyshev Approximation

The Chebyshev approximation that reveals the equal-ripple passband and maximally flat stopband is described in equation 3.40. It provides a sharper slope for lower filter order N , in comparison with the maximally flat approximation [1, 4]. Characteristic function for Chebyshev approximation is defined as:

$$K(\omega) = \epsilon T_N(\omega) \quad (3.18)$$

where $T_N(\omega)$ is a Chebyshev polynomial of degree N and ϵ is the ripple factor. Thus, $P(s) = 1$, $F(s) = T_N(s/j)$ and expressions for S-parameters yield:

$$|S_{12}(\omega)|^2 = \frac{1}{1 + \epsilon^2 T_N^2(\omega)} \quad (3.19)$$

$$|S_{11}(\omega)|^2 = \frac{\epsilon^2 T_N^2(\omega)}{1 + \epsilon^2 T_N^2(\omega)} \quad (3.20)$$

It can be defined using the Chebyshev polynomial recursion relationship:

$$T_{N+1}(\omega) = 2\omega T_N(\omega) - T_{N-1}(\omega) \quad (3.21)$$

where $T_0(\omega) = 1$ and $T_1(\omega) = \omega$. On the other hand, a trigonometric expression can be used:

$$T_N(\omega) = \cos(N \cdot \cos^{-1}(\omega)) \quad (3.22)$$

A product of the left half-plane roots can be derived for the characteristic polynomial $E(s)$ (i.e. with $\sigma_k < 0$) $\sigma_k = \sigma_k + j\omega_k$, where:

$$\sigma_k = \pm \sinh\left(\frac{1}{N} \sinh^{-1} \frac{1}{\epsilon}\right) \sin\left(\frac{\pi}{2} \frac{2k-1}{N}\right) \quad (3.23)$$

$$\omega_k = \cosh\left(\frac{1}{N} \sinh^{-1} \frac{1}{\epsilon}\right) \cos\left(\frac{\pi}{2} \frac{2k-1}{N}\right) \quad (3.24)$$

where $k = 1, 2, 3, \dots, 2N$.

The insertion loss of this filter at ripple level becomes:

$$IL = 10 \log_{10}(1 + \epsilon^2) \quad (3.25)$$

while

$$\epsilon = \frac{1}{\sqrt{10^{\frac{L_R}{10}} - 1}} \quad (3.26)$$

The degree N^{th} of the filter that is needed to achieve a specification is given as:

$$N \geq \frac{L_A + L_R + 6}{20 \log[S + \sqrt{S^2 - 1}]} \quad (3.27)$$

Where L_R is the return loss in the passband, L_A is the stopband attenuation and S denotes the ratio of stopband to passband frequencies. The equations to determine the element values of the N th order Chebyshev filter prototype with impedance

inverter as shown in Figure 3.8 are given below as [4]:

$$K_{r,r+1} = \frac{[\eta^2 + \sin^2(\frac{r\pi}{N})]^{\frac{1}{2}}}{\eta} \quad (3.28)$$

and

$$L_r \quad \text{or} \quad C_r = \frac{2}{\eta} \sin \left[\frac{(2r-1)\pi}{2N} \right] \quad r = 1, 2, \dots, N \quad (3.29)$$

While the parameter is defined as:

$$\eta = \sinh \left[\frac{1}{N} \sinh^{-1} \left(\frac{1}{\epsilon} \right) \right] \quad (3.30)$$

Figure 3.4 illustrates a typical frequency response of the Chebyshev filter prototype.

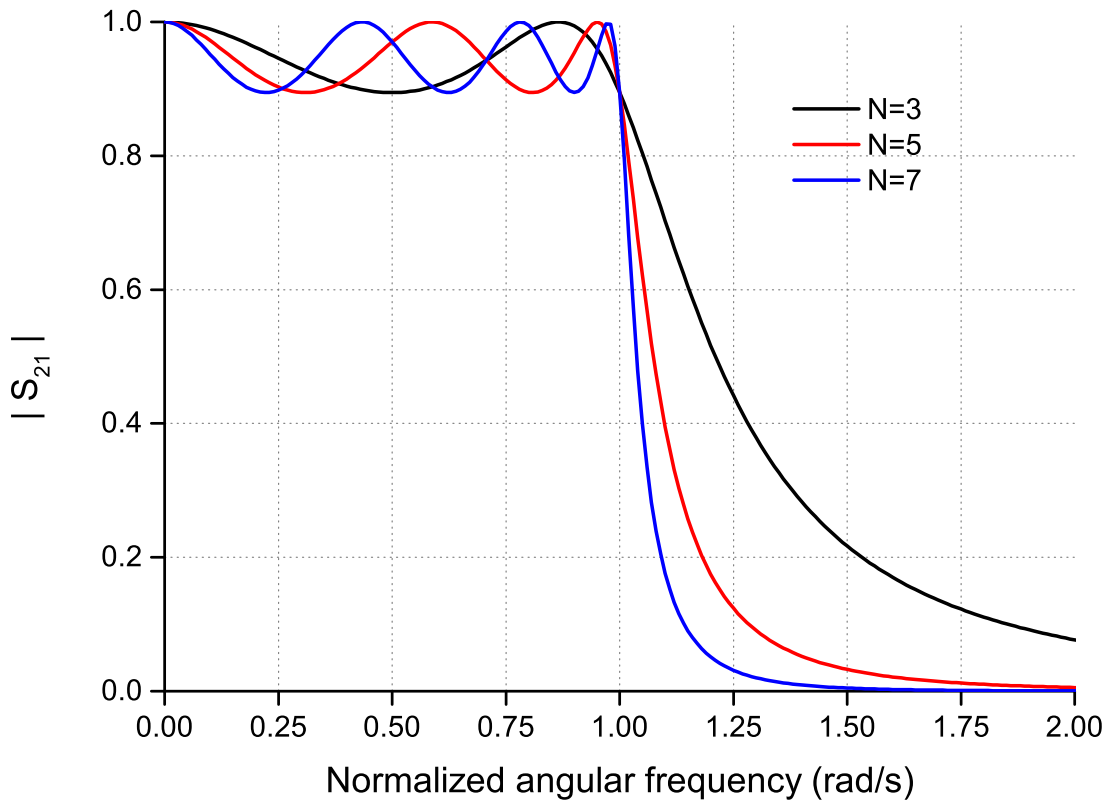


Figure 3.4: Lowpass filter frequency response of Chebyshev type.

3.2.4 Generalized Chebyshev Approximation

The generalized Chebyshev (or pseudo-elliptic) approximation offers the possibility to realize the filters with equally ripple insertion loss in passband and arbitrary

placed transmission zeros in the stopband. As the attenuation pole can be positioned arbitrarily at any finite frequency, synthesized high-selectivity filters are enabled with sharp slopes and asymmetrical frequency responses. This is required in certain applications, for example, base station transmit filters. The location of transmission zeros is not restricted to being at real frequencies only, but may also be of complex values [4]. The generalized Chebyshev approximation is defined as:

$$K(\omega) = \epsilon.C_N(\omega) \quad (3.31)$$

where

$$C_N(\omega) = \cosh \left(\sum_{i=1}^N \cosh^{-1}(x_i) \right) \quad (3.32)$$

$$x_i = \frac{\omega - 1/\omega_{TZi}}{1 - \omega/\omega_{TZi}} \quad (3.33)$$

Here, ω is the angular frequency variable and ω_{TZi} is the location of the i^{th} transmission zero to be realized. Therefore, the transmission coefficient is expressed as follows [70]:

$$|S_{12}(\omega)|^2 = \frac{1}{1 + \epsilon^2 C_N^2(\omega)} \quad (3.34)$$

With regard to equation 3.7, the filtering function $C_N(\omega)$ can be rephrased as a ratio of two polynomials:

$$C_N(\omega) = \epsilon \frac{F_N(\omega)}{P_N(\omega)} \quad (3.35)$$

The denominator will be composed directly of the transmission zeros:

$$P_N(\omega) = \prod_{i=1}^N (\omega - \omega_{TZi}) \quad (3.36)$$

while the numerator $F_N(\omega)$ is determined using a recursive technique [70]:

$$F_n(\omega) = \frac{1}{2} \left[G_N(\omega) + G'_N(\omega) \right] \quad (3.37)$$

$$G_N(\omega) = \prod_{i=1}^N \left[\left(\omega - \frac{1}{\omega_{TZi}} \right) + \omega' \sqrt{1 - \frac{1}{\omega_{TZi}^2}} \right] \quad (3.38)$$

$$G'_N(\omega) = \prod_{i=1}^N \left[\left(\omega - \frac{1}{\omega_{TZi}} \right) - \omega' \sqrt{1 - \frac{1}{\omega_{TZi}^2}} \right] \quad (3.39)$$

where $\omega' = \sqrt{\omega^2 - 1}$. An alternative recursive technique in [71] for obtaining the characteristic polynomials can be found. Figure 3.5 shows the frequency response

of the generalized Chebyshev filter prototype.

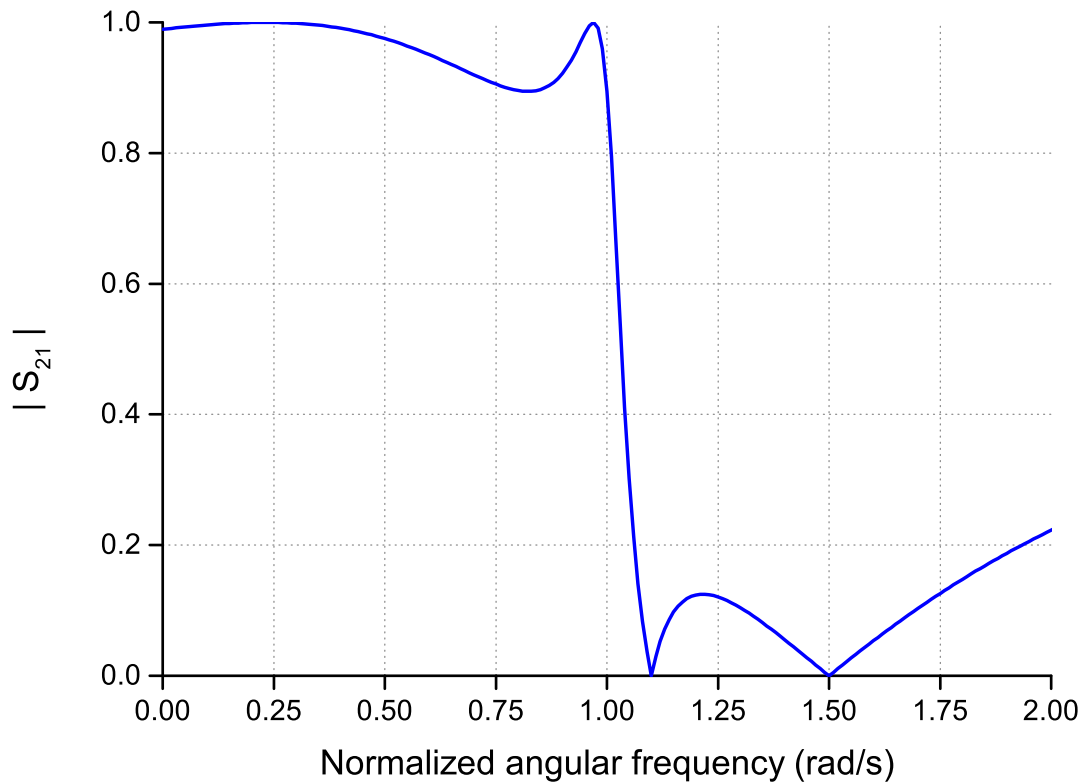


Figure 3.5: Generalized Chebyshev (or pseudo-elliptic) frequency response with two transmission zeros in the upper stopband..

3.3 Lowpass Prototype Filters and Elements

Filter synthesis in all filter types starts with the use of a normalized lowpass equivalent circuit prototype. It can give the transfer function derived as a result of the approximation process. Therefore, it is easy to convert this type of filter to another by applying a frequency and element transformations procedure. A lowpass prototype filter can be defined as a two-port passive network with source and load impedance equal to 1Ω , denoted by $g_0=1$, and angular cut-off frequency $\omega_c=1$ rad/sec. The total number of reactive elements determines the order of the filter, which is directly proportional to the selectivity in the filter. The low pass prototype filter can be realized by a cascade of ladder network composed of inductors in series and shunt capacitors [30,72], as featured in Figure 3.6. Impedance inverters

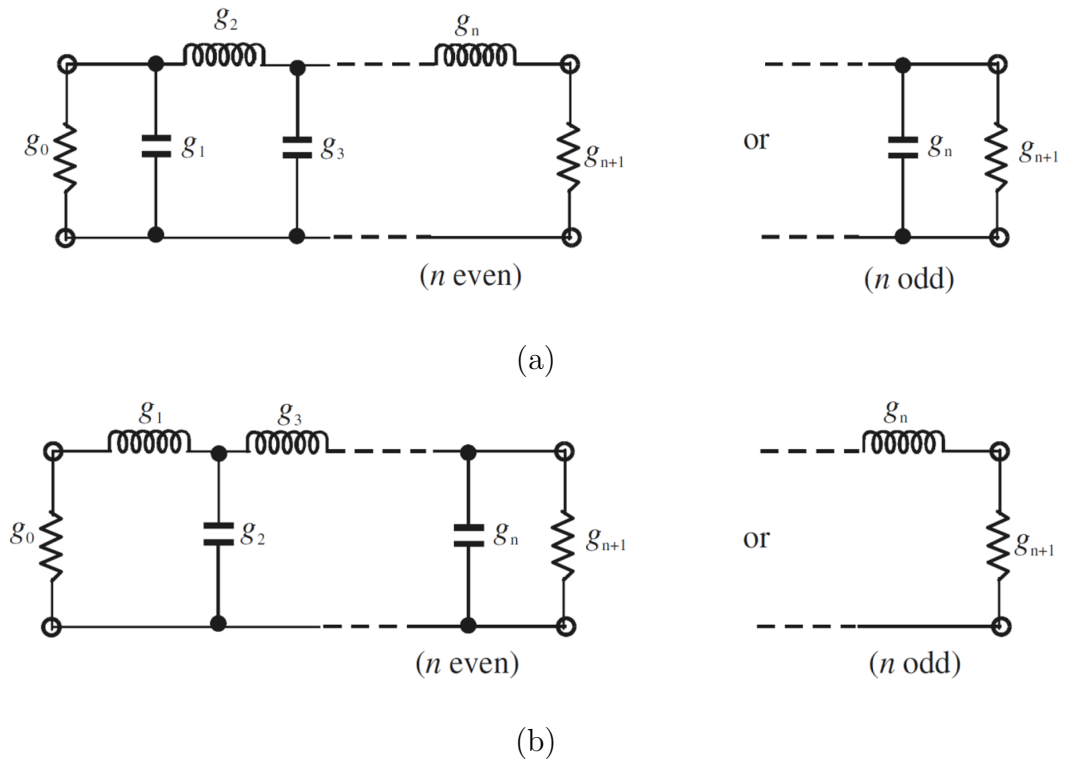


Figure 3.6: Lowpass prototype filters for all-pole filters with (a) a ladder network structure and (b) its dual [30].

are also used to realize a ladder network. An inverter is a lossless, reciprocal and two-port network which operates like a quarter-wavelength line at all frequencies. Usually, the inverter is defined by its transfer matrix, which is suitable for analysis of filter circuits.

$$[T] = \begin{bmatrix} 0 & jK \\ j/K & 0 \end{bmatrix} \quad (3.40)$$

Where K is characteristic impedance or admittance of the inverter. The relationship between the input impedance and output impedance where the inverter is connected can be written as:

$$Z_{in} = \frac{K^2}{Z_L} \quad (3.41)$$

Where Z_{in} and Z_L are the input and output impedance of the inverter (see Figure 3.7). A low pass prototype network can be realized by using either a capacitor or inductor with impedance or admittance inverters, as in Figure 3.8 below. As featured above, the impedance inverters are like ideal quarter-wave transformers.

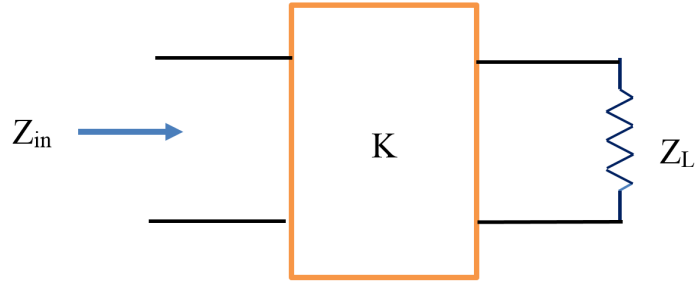


Figure 3.7: Impedance inverter with load Z_L .

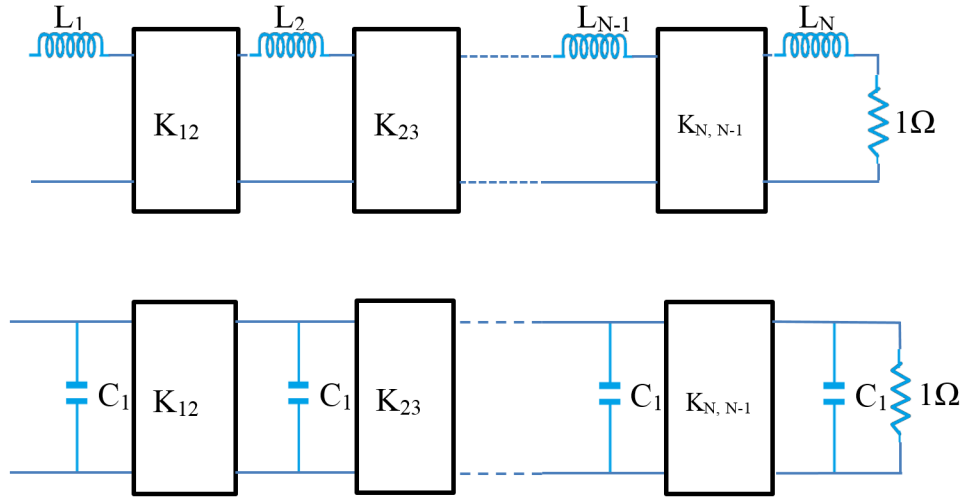


Figure 3.8: Inverter coupled generalized lowpass prototype filter.

There are no theoretical differences in their inverting properties. An impedance inverter with characteristic impedance K is identical to an admittance inverter with characteristic admittance $J = 1/K$. Besides a quarter-wavelength line, there are some other circuits that operate as inverters. Some useful K -inverters are shown in Figure 3.9. It can be observed that some of the inductors and capacitors have negative values. Although it is not practical to realize such components, they will be absorbed by adjacent resonant elements in the filter, as discussed in the following sections. It should also be noted that, since the inverters shown here are frequency sensitive, they are best suited for narrowband filters [1, 4, 30].

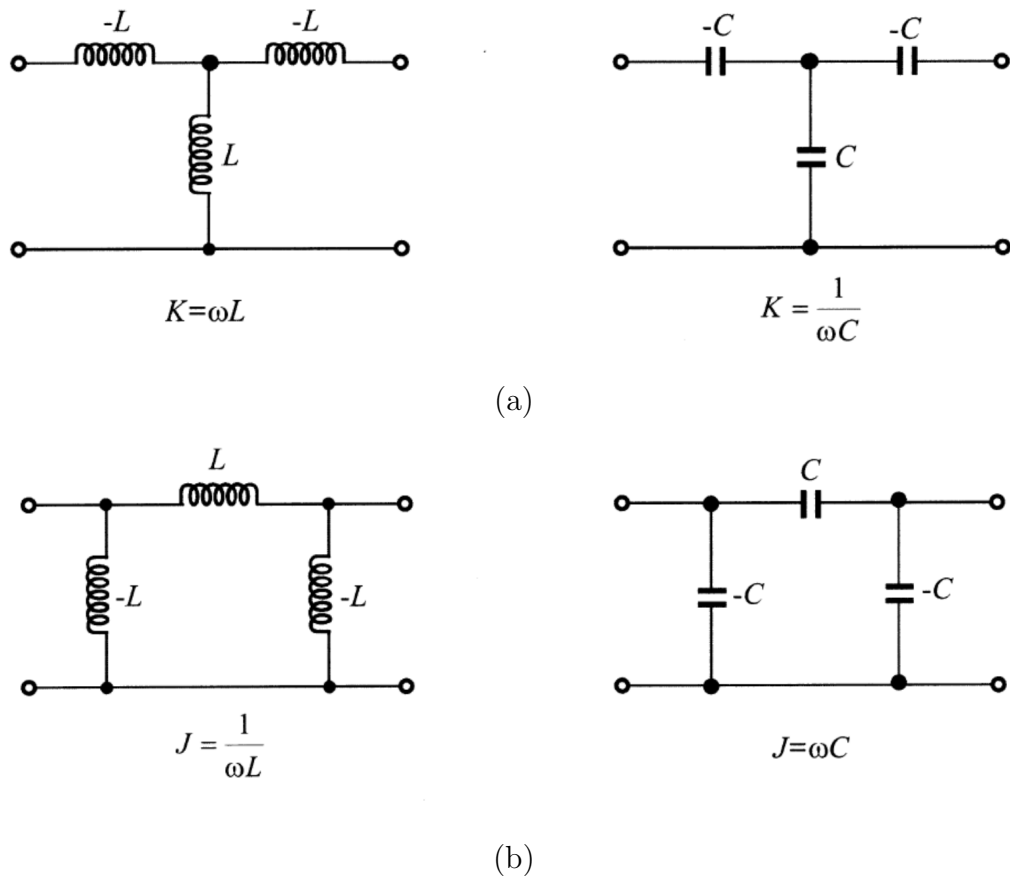
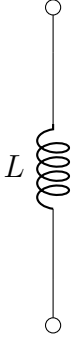
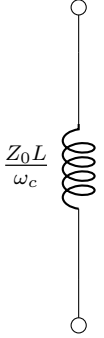
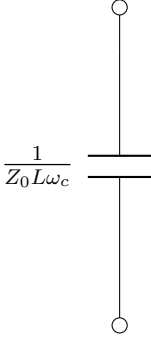
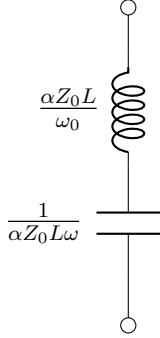
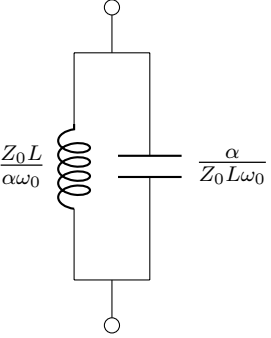
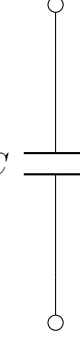
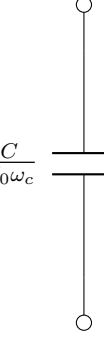
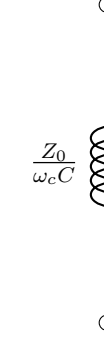
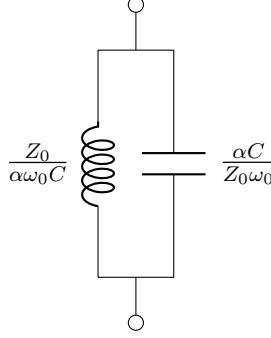
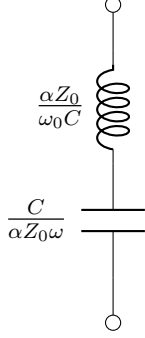


Figure 3.9: Lumped-element immittance inverters (a) T-Section (b) π -Section [30].

3.4 Frequency and Element Transformation

The lowpass filter prototype networks have been considered in this chapter, where the values for source and load impedance are normalized and cut-off frequency $\omega_c = 1$. However, these boundaries are noticeably impractical for use in real applications. Consequently, transformation and scaling of elements in the lowpass prototype should be performed to provide acceptable solutions for certain specifications [4]. In real a filter, a source resistance of R_0 is scaled to a low pass prototype. This can be found by multiplying or dividing all the impedances of the prototype design by R_0 depending on the type of filter and the components. The cut-off frequency of a low-pass prototype can be transformed from unity to ω_c , meaning the frequency dependence of the filter will be multiplied by the factor $1/\omega_c$, which is completed by replacing ω by ω/ω_c . Table 3.1 shows all transformations between different type of filter from the prototype LPF [4, 27, 30].

Table 3.1: Conversions from the normalized low-pass prototype to low-pass, high-pass, band-pass and band-stop filters.

Ne	LPF	HPF	BPF	BSF
				
				

3.5 Introduction of Coupling Matrix

In narrow frequency band, a cavity can be represented as single resonator with multi-couplings to other cavities. The resonator in a generalized lowpass filter is represented by capacitance $1F$ and the multi-couplings are represented by inductance coupling $M_{i,j}$ [73, 74, 75] as shown in Figure 3.10. The cavities are tuned to the same resonant frequency, $\omega_0=1$ rad/sec. The loop current equations in the Figure 3.10 can written as 3.42

$$\left[R_1\delta_{1i} + R_n\delta_{ni} + j \left(\omega - \frac{1}{\omega} \right) \right] I_i + j \sum_{\substack{k=1 \\ k \neq i}}^n M_{ik} I_k = e_1\delta_{1i} \quad (3.42)$$

$$i = 1, 2, 3, \dots, n$$

Where R_1 , R_n , I_k , e_1 and δ_{1i} are source resistance, load resistance, current cavity, input voltage and Kronecker delta respectively. The admittance parameter in two port network can be defined as 3.43.

Y_{11} and Y_{21} can be determined as in equation 3.45 where $[I]$ is an identity matrix

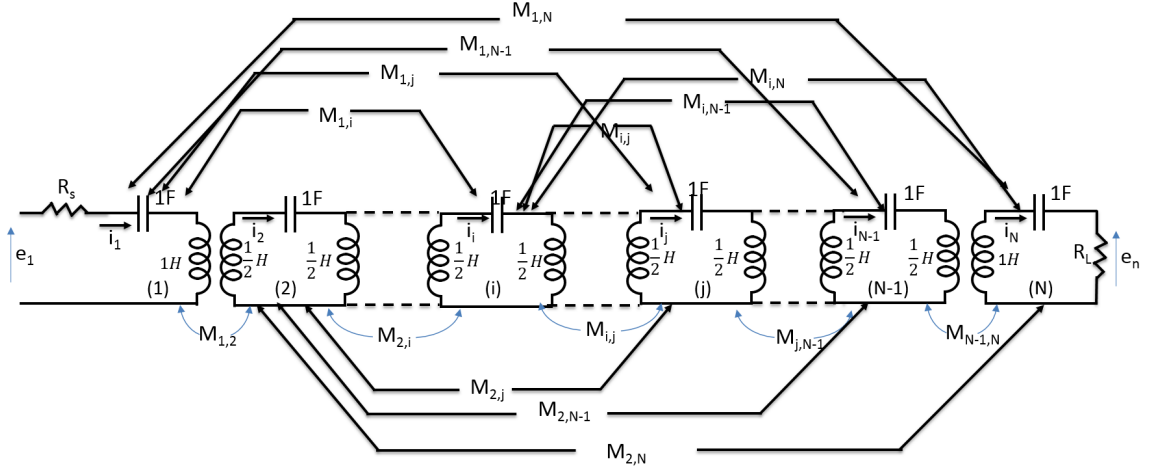


Figure 3.10: A generalized lowpass prototype filter is represented by coupling matrix [73].

$(N \times N)$ and $[M]$ is the coupling matrix; when $V_2=0$ and can be related to the loop current and voltage of the last and first section of the network in Figure 3.10.

$$I_1 = Y_{11}V_1 + Y_{12}V_2 \quad (3.43)$$

$$I_2 = Y_{21}V_1 + Y_{22}V_2 \quad (3.44)$$

$$Y_{11} = \frac{i_1}{e_1} = y_{11} = [sI + jM]_{11}^{-1} \quad (3.45)$$

$$Y_{21} = \frac{i_n}{e_1} = y_{n1} = [sI + jM]_{n1}^{-1} \quad (3.46)$$

Due to the filter network definition, the matrix M is real and reciprocal. That means, all eigenvalue of M is real and can be diagonalized ($[\Lambda]$) as equation 3.47 and the orthogonal eigenvector matrix T is written as 3.48.

$$\Lambda = \begin{bmatrix} \lambda_1 & 0 & \dots & 0 \\ 0 & \lambda_2 & \dots & 0 \\ \vdots & \vdots & \vdots & \vdots \\ 0 & 0 & \dots & \lambda_n \end{bmatrix}, TT^t = I \quad (3.47)$$

$$M = T\Lambda T^t \quad (3.48)$$

By substitution eq. 3.48 in the admittance Y_{11} and Y_{21} in eq. 3.45, we will find as shown in 3.49-3.52.

$$[y_1] = [z_1]^{-1} = [sI + jM]^{-1} = [sI + jT\Lambda T^t]^{-1} \quad (3.49)$$

$$\begin{bmatrix} T_{11} & \dots & T_{1n} \\ \vdots & \vdots & \vdots \\ T_{n1} & \dots & T_{nn} \end{bmatrix} \begin{bmatrix} \frac{1}{s+j\lambda_1} & \dots & 0 \\ \vdots & \ddots & \vdots \\ 0 & 0 & \frac{1}{s+j\lambda_n} \end{bmatrix} \begin{bmatrix} T_{11} & \dots & T_{n1} \\ \vdots & \vdots & \vdots \\ T_{1n} & \dots & T_{nn} \end{bmatrix} \quad (3.50)$$

$$Y_{11} = \frac{T_{11}^2}{s + j\lambda_1} + \frac{T_{12}^2}{s + j\lambda_2} + \frac{T_{1n}^2}{s + j\lambda_n} = \sum_{k=1}^N \frac{T_{1k}^2}{s + j\lambda_k} \quad (3.51)$$

$$Y_{21} = \frac{T_{11}T_{n1}}{s + j\lambda_1} + \frac{T_{12}T_{2n}}{s + j\lambda_2} + \frac{T_{1n}T_{nn}}{s + j\lambda_n} = \sum_{k=1}^N \frac{T_{1k}T_{nk}}{s + j\lambda_k} \quad (3.52)$$

According to polynomial of S parameter , the admittance can be derived as 3.53

$$Y_{21}(s) = \frac{-2P(s)}{E(s) + F_{11}(s) + F_{22}(s) - V(s)} \quad (3.53)$$

$$Y_{21}(s) = \frac{E(s) - F_{11}(s) + F_{22}(s) + V(s)}{E(s) + F_{11}(s) + F_{22}(s) - V(s)} \quad (3.54)$$

$$V(s) = E(s)(S_{12}(s)S_{21}(s) - S_{11}(s)S_{22}(s)) = (-1)^{N+1}(E(s))^* \quad (3.55)$$

By applying a partial expansion on Y parameters as in 3.56. As comparing equation 3.52 with 3.56, the λ_k can be determined from the poles of Y parameters, while the residues of Y parameters can be used to calculate T_{1k} and T_{nk} .

$$Y = \begin{bmatrix} Y_{11} & Y_{12} \\ Y_{21} & Y_{22} \end{bmatrix} = \sum_{k=1}^N \frac{1}{s - p_k} \begin{bmatrix} r_{11} & r_{12} \\ r_{21} & r_{22} \end{bmatrix} \quad (3.56)$$

To synthesis of coupling matrix(CM)where the resonator of cavity represents as shunt capacitance ($C_k=1$) in parallel with FIR (jB_k), which calculates as 3.57.

$$\begin{aligned} C_k &= 1, & B_k(\equiv M_{kk}) &= -\lambda_k \\ M_{Lk}^2 &= r_{22k}, & M_{Sk}M_{Lk} &= r_{21k} \\ M_{Lk} &= \sqrt{r_{22k}} = T_{nk} \\ M_{Sk} &= r_{21k}/\sqrt{r_{22k}} = T_{1k}, & k &= 1, 2, 3, \dots, n \end{aligned} \quad (3.57)$$

3.6 Circuit Model of the Dielectric Resonator

This section will discuss one of the circuit models used to calculate the resonant frequency of the DR.

3.6.1 The Cohn Model

Cohn's model is one of the simple mathematical models mostly used in DR models [10], which is used to improve the accuracy of the computed resonant frequency and fields. The model assumes that the DR is contained in a contiguous perfect magnetic-wall (PMC) waveguide, as shown in Figure 3.11. The field components

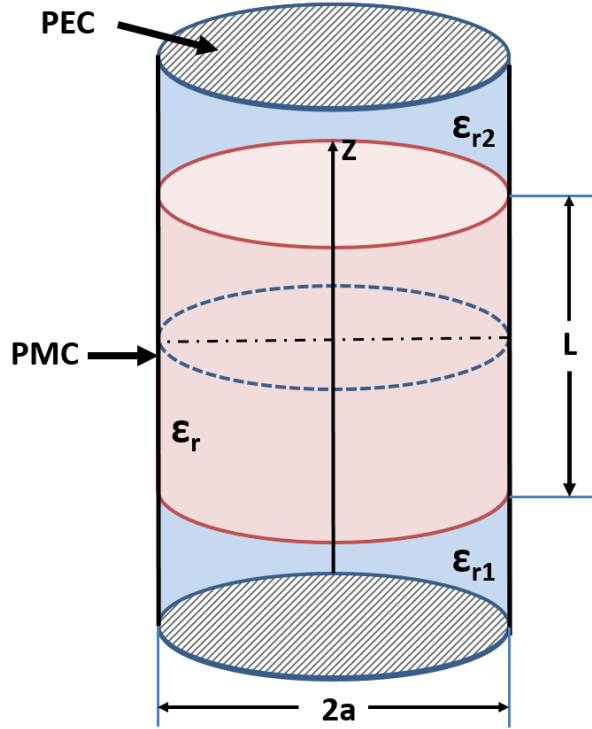


Figure 3.11: Cohn's second-order DR model.

for TE modes in a circular waveguide are given by:

$$H_z = H_0 J_n(k_c r) \cos(n\phi) e^{\pm\gamma z} \quad (3.58)$$

$$E_r = Z_{TE} H_\phi = \frac{j\omega\mu n}{k_c^2 r} H_0 J_n(k_c r) \sin(n\phi) e^{\pm\gamma z} \quad (3.59)$$

$$E_\phi = -Z_{TE} H_r = \frac{j\omega\mu}{k_c r} H_0 J'_n(k_c r) \cos(n\phi) e^{\pm\gamma z} \quad (3.60)$$

with

$$Z_{TE} = \frac{j\omega\mu}{\gamma} \quad (3.61)$$

and γ is the propagation constant. The radial propagation constant of the mode is fixed by the PMC wall at $r = a$, and for $TE_{11\delta}$ to be solved,

$$H_z = 0|_{r=a} \quad (3.62)$$

Hence

$$J_n(K_c a) = 0 \quad (3.63)$$

or

$$K_c = \frac{\chi_{nm}}{a} \quad (3.64)$$

and

$$K_c^2 = \gamma^2 + \omega^2\mu\epsilon \quad (3.65)$$

for the propagation modes in the lossless waveguide, γ is purely imaginary and

$$\gamma = j\beta \quad \beta = \sqrt{\omega^2\mu_0\epsilon_0\epsilon_r - \left(\frac{\chi_{nm}}{a}\right)^2} \quad (3.66)$$

for the cut-off mode, γ is real:

$$\gamma = \alpha = \sqrt{\left(\frac{\chi_{nm}}{a}\right)^2 - \omega^2\mu_0\epsilon_0\epsilon_r} \quad (3.67)$$

Cohn's model can be represented by sections of cut-off waveguide terminated in short circuits with a propagating waveguide section placed in the middle, as shown in Figure 3.12 [4], where the wave impedance for the propagating mode is:

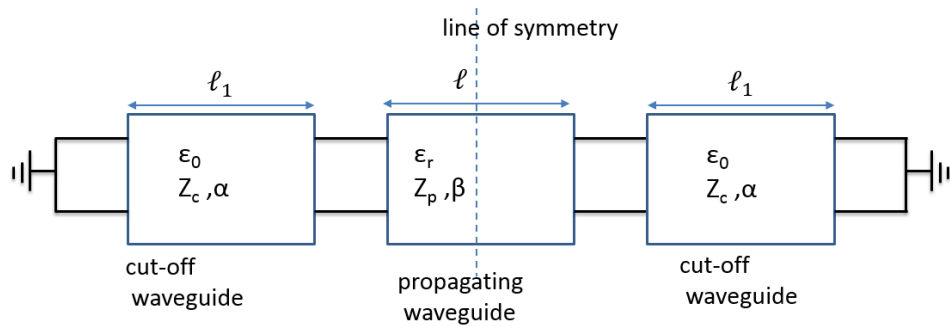


Figure 3.12: Single mode equivalent circuit of Cohn's model for DR [4].

$$Z_{TE} = Z_p = \frac{\omega\mu}{\beta} \quad (3.68)$$

and for non-propagating modes:

$$Z_{TE} = Z_c = \frac{j\omega\mu_0}{\alpha} \quad (3.69)$$

The transfer matrix of the propagating guide, looking into the circuit at the line of symmetry, is:

$$[T] = \begin{bmatrix} \cos(\beta\ell) & \frac{j\omega\mu}{\beta} \sin(\beta\ell) \\ \frac{j\beta}{\omega\mu} \sin(\beta\ell) & \cos(\beta\ell) \end{bmatrix}$$

The input impedance of the short-circuited section of the cut-off guide which is terminated in an impedance Z_L is given as:

$$Z_L = \frac{j\omega\mu_0}{\alpha} \tanh(\alpha\ell_1) \quad (3.70)$$

The circuit is terminated at both ends in short circuits so resonance occurs when the input impedance at the line of symmetry is infinite. The input impedance is:

$$Z_{in} = \frac{AZ_L + B}{CZ_L + D} \quad (3.71)$$

Resonance occurs when the denominator of 3.71 is zero, when:

$$\frac{\beta}{\alpha} \tan\left(\frac{\beta\ell}{2}\right) \tan(\alpha\ell_1) = 1 \quad (3.72)$$

This is the resonance equation for the $TE_{01\delta}$ mode. Since $\tanh(\alpha\ell_1)$ is positive, $\beta\ell/2$ must be less than 90° .

3.7 High Frequency Structure Simulator (HFSS)

The HFSS is a high performance software package that is used for modelling and analysing 3D passive devices by using the finite element method (FEM) which is used to solve Maxwell's equation with different levels of resolution. It has a good graphical user interface (GUI) with a library of material; also, users can insert new material to parameters all its specific such as permittivity, permeability, conductivity and dielectric loss tangent. Resonant frequencies, S-parameters and

field patterns for any arbitrary three dimensional design with irregular shapes can be solved by Ansoft HFSS. The three common solutions are: driven modal, driven terminal and eigenmode. For a driven modal, an external source of energy should be applied at the input and output ports to calculate the S-parameters for any geometry. A scattering matrix will be calculated in each modes and in all frequency points in the wanted spectrum. The major factor of the convergence criteria is the delta S that gives the maximum error between two consecutive passes in the S matrix and should be designed at the minimum value, if the calculation of delta S is less than the designed tolerance value, the number of meshes will need to increase to obtain an accurate solution. The eigenmode is used to solve a source-less problem when all planes of the designed shape are short-circuited for calculating resonant frequencies and Q-factor. It can also draw field patterns. The driven terminal is used to determine the S-parameters for transmission line ports. The HFSS solver can be calculated the electromagnetic fields of a 3D structure with high accuracy by sing FEM method [76].

3.8 Summary

The first step in the design procedure for any type of filter is to use the approximation of the transfer function that describes the filter specifications. From the transfer function, a normalized low pass filter can be synthesized by using lumped elements connected as a ladder network. The values of the prototype should be scaled to characteristic impedance and resonant frequency which was designed and then convert the LPF to the desired filter. The implemented filter depends on the application that determined the physical resonator technology. The Cohn model can be used to calculate the resonance frequency for DR in certain cases. HFSS software can be used to simulate the filter in any 3D shape.

Chapter 4

Design and Implementation of a Novel $TE_{11\delta}$ Dual-Mode Dielectric Resonator Filter

4.1 Introduction

A dielectric resonator (DR) bandpass filter is described in chapter 2 which offers a high Q, better performance, small volume and less weight compared to conventional air-filled cavity filters. These benefits are due to the dimensions of the filter being reduced by a square root of relative permittivity ($1/\sqrt{\epsilon_r}$) [77]. In this chapter, A novel $TE_{11\delta}$ dual-mode DR filter with a significant volume reduction compared with air filled filter will be described. The DR structure considers a dielectric puck situated in the middle of a metallic cavity with the same air space below and above the ceramic puck and shorted by the sides. The HFSS simulation was used to determine the resonance frequency with unloaded Q-factor and generate field patterns for this resonator and to analyse the frequency response. A 50 Ω probe in contact with the top surface of the ceramic puck is used for the input and output coupling. The length of the probe controls the amount of coupling and

vertical etching hole through the ceramic puck at 45° with respect to mode 1 or 2 controls the coupling between two generated modes. Two fourth-order Chebyshev filter were designed by using probe and strip-line coupling technique. A 4^{th} order dual-mode filter was fabricated and the response of the practical filter is compared with an EM simulation.

4.2 Configuration of the Proposed Resonator

A novel $TE_{11\delta}$ dual-mode loaded cavity filter is proposed. The proposed resonator consists of a ceramic puck of high permittivity placed in the middle of a cylindrical metallic housing where the resonator side-walls are in direct contact with the cylindrical metallic enclosure, as shown in Figure 4.1. D , L are the diameter and length of the ceramic puck respectively, while L_a is the distance above and below the puck filled with air. In order to choose the cavity dimensions, there is a need to specify the resonant frequency and trade-off between the Q-factor, the spurious-free frequency window and the volume. An initial EM eigenmode solver in HFSS software calculates the resonant frequency modes for a dielectric puck made from barium titanate with relative permittivity of $\epsilon_r = 43$; loss tangent is 4×10^{-5} and

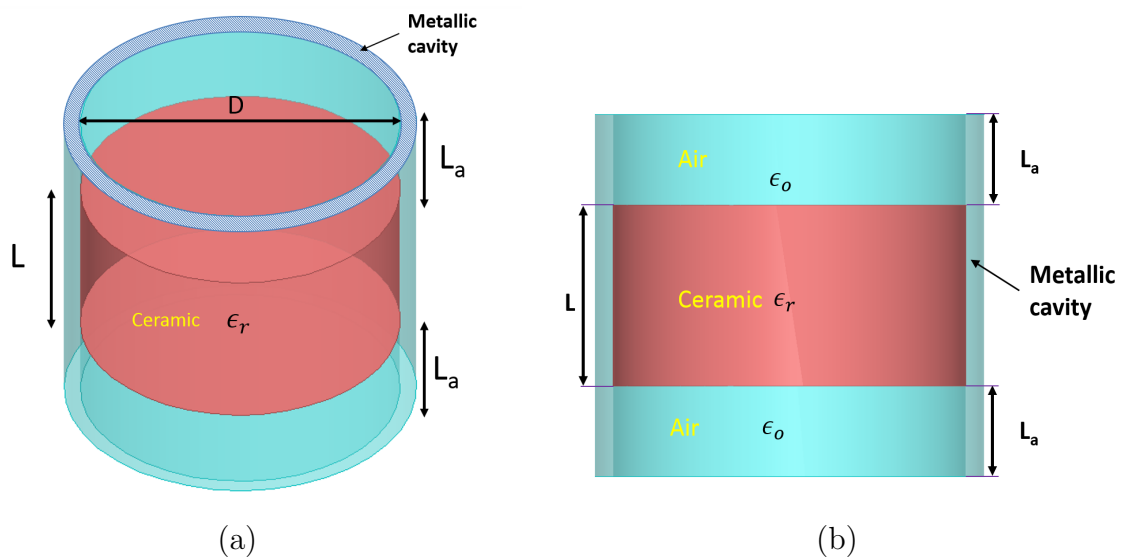


Figure 4.1: Configuration of dual-mode dielectric resonator: (a) 3D view, (b) side view.

the conductivity of the copper metal cavity walls is 4×10^7 S/m.

Figure 4.2 illustrates the relationship between the ratio of the height of the ceramic to the height of the air above it against the unloaded Q-factor per volume for the left axis and spurious-free window for right axis at the dual-mode resonance frequency of 2 GHz. Q_u/V is a reliable term for indicating a high unloaded quality factor (Q_u) and small volume of the resonator. It is worthy noting that, at a height where the resonator length (L) is equal to 7.5 mm, there is no data on the graph under L_a/L less than 0.7; this happened because the resonant frequency at these dimensions is more than 2 GHz. The Q_u/V ratio (0.7-1) decreased slightly from 680 to 640, and there was a 150 MHz increase in the spurious-free window at the same range. For a dielectric height of 10 mm, Q_u/V increased towards the lid near to the dielectric puck until it reached a maximum value of 850 at L_a/L of 0.4; it, however, lowers with a linear gradient when L_a is rising, but the spurious-free window is still increased. The maximum value for the spurious-free window for all conditions of L is 10 mm, which is about 100 MHz higher than the other

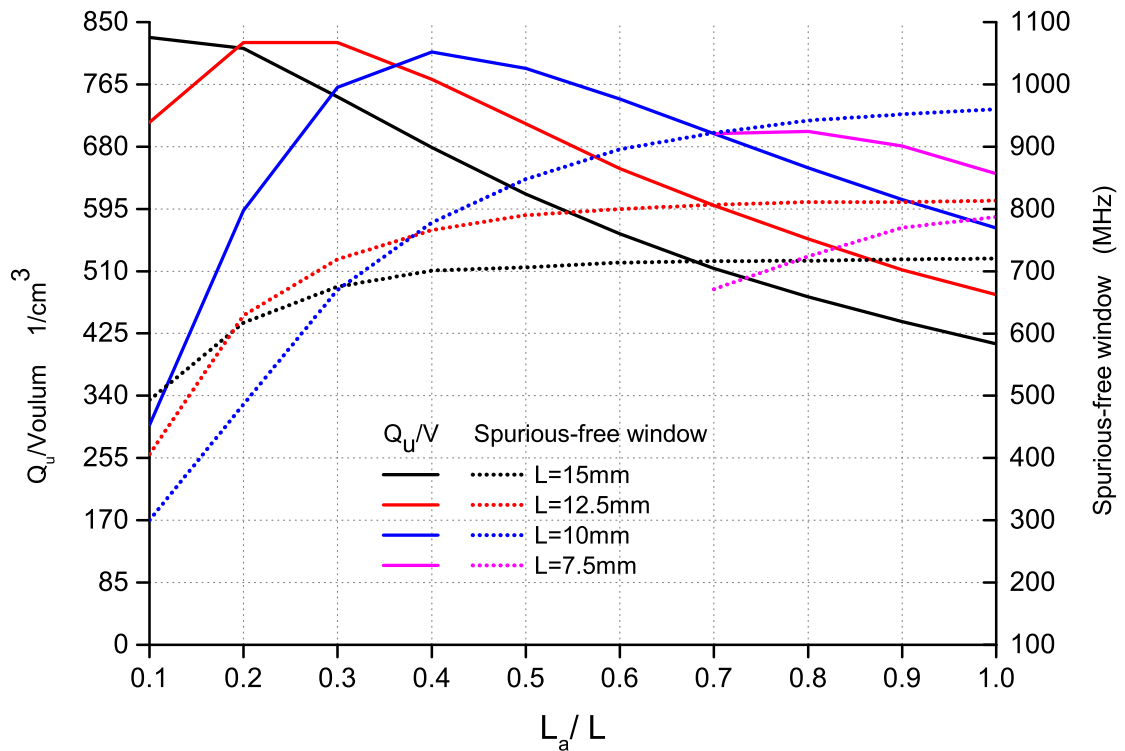


Figure 4.2: Q-factor/volume and spurious-free window against the ratio of height of resonator/height above ceramic.

dimensions. The maximum points of Q_u/V occurred at the small L_a when the height of ceramic L increased, with the optimum dimensions at a range of 0.4-0.6, which gives a good value for the Q_u -factor, volume and spurious-free window.

Figure 4.3 shows the relationship of ratio L_a/L to Q_u (dashed line) for the left axis and the ratio of diameter to ceramic height D/L (solid line) on the right axis. As mentioned earlier for a range of optimum values 0.4-0.6, it can be seen that the ratio of D/L and the frequency spurious-free window are 1.87-2 and 1.4-1.375 respectively. The range of Q-factor at the optimum dimensions is about 4250. According to the previous result, the optimum dimensions of this resonator are $D = 20mm, L = 10mm, L_a = 5mm$. A significant volume reduction was recorded of about 11% compared with the air-filled coaxial filter. Figure 4.4 presents the

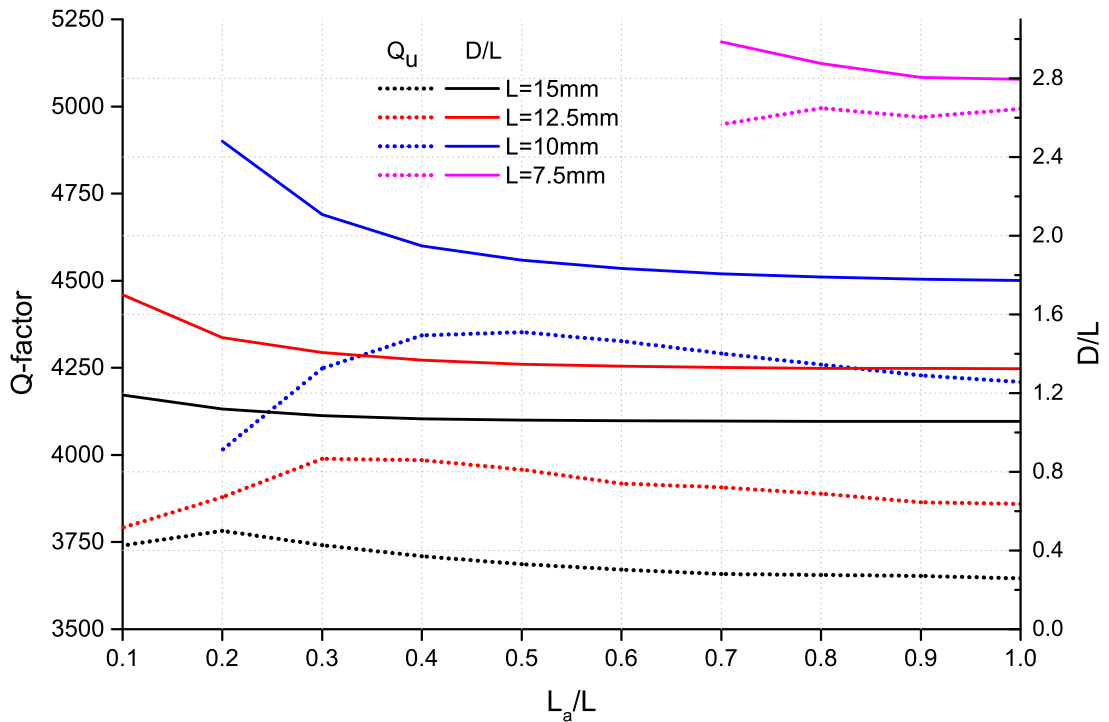


Figure 4.3: Q-factor against the ratio of resonator diameter to ceramic puck height.

resonant frequencies for the first and second modes against the ratio (D/L) using calculation by the Cohn model and HFSS software. The equation has been used to calculate the resonant frequency by the Cohn model, as described in section 3.6. The result is in agreement with the Cohn model with first dual-mode and eigenmode HFSS solver with a few MHz difference for the second dual-mode. In

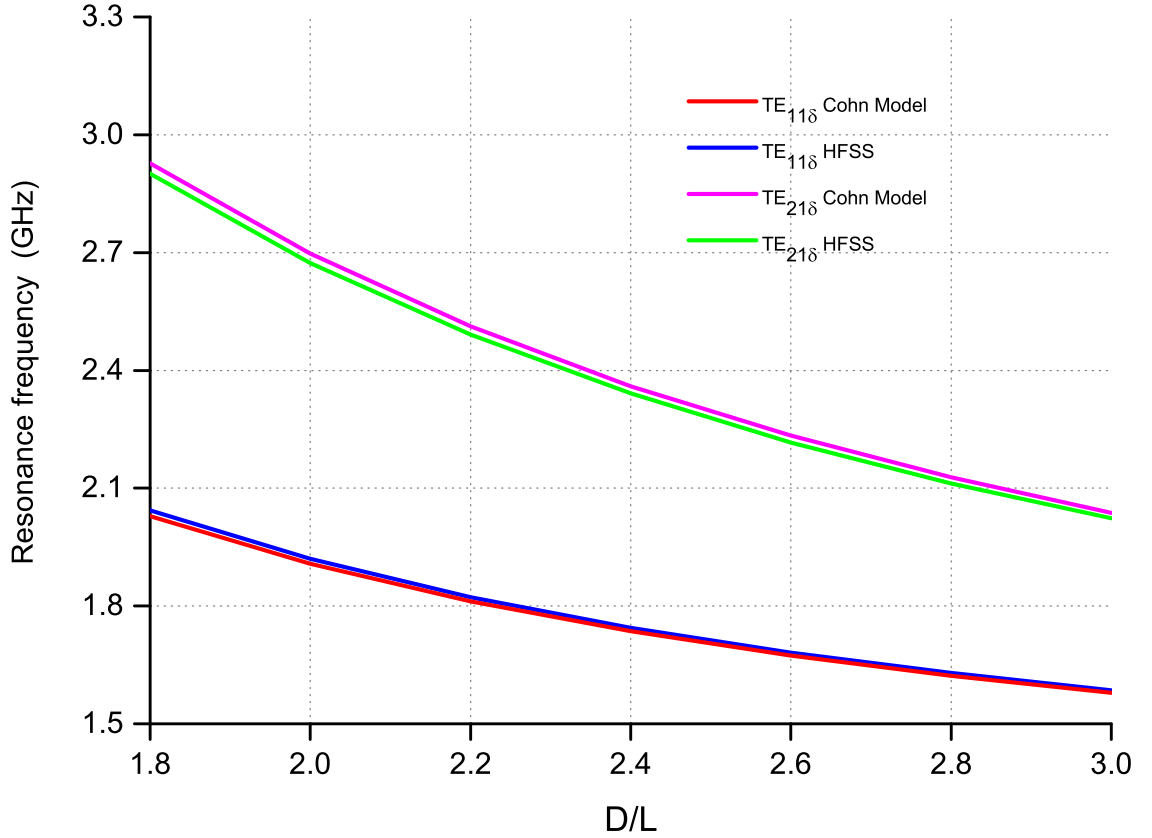


Figure 4.4: Cohn model and HFSS simulation comparison for resonance frequencies.

addition, the resonant frequencies decrease with the increasing of D/L . Figure 4.5 shows the Q_u factor for the first and second modes against the ratio (D/L) based on calculation by the Cohn model and HFSS software. A reasonable agreement is observed between the Cohn model and HFSS solver with some difference in Q -factor of about 50 for the fundamental mode and about 300 for the second dual-mode where D/L is less than 2.2 after reaching 500. Differences observed were from the approximation in the Cohn model that assumes there is no field outside the ceramic puck. Additionally, the Q_u factor has been increased by increasing the D/L ratio. The eigenmode solver was used to simulate the resonant frequencies of the first three modes of the dielectric resonator, the dimensions of $D=20$ mm, $L=10$ mm, $L_a=5$ mm, ceramic puck relative permittivity $\epsilon_r = 43$, $\tan \delta = 4 \times 10^{-5}$ and metal conductivity 4×10^7 S/m, as seen in Table 4.1. It is clear that $TE_{11\delta}$ and $TE_{21\delta}$ are both dual-modes with spurious-free window about 777 MHz and the Q_u are 3842 and 3500 respectively. The $TM_{01\delta}$ is a single-mode with a 5200 Q -factor.

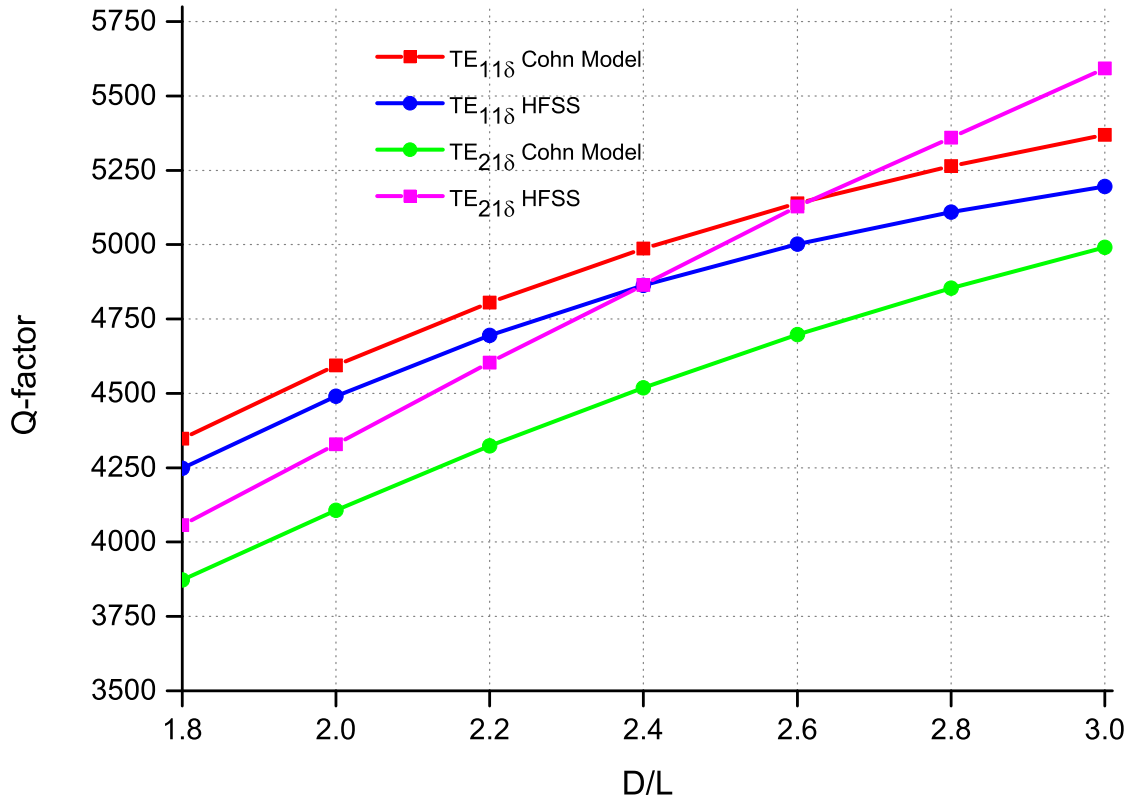


Figure 4.5: Cohn model and HFSS simulation comparison for Q_u -factor.

Figure 4.6 presents the pattern fields of the proposed cavity for the fundamental mode 1.92 GHz. From the figure, it can be noticed that most of the E-fields exist inside the dielectric puck, with small E-fields outside the ceramic puck until these vanished to the top/bottom lids. The maximum H-field is tangential to the side of the puck, but not in all sides: it is in the limited area.

Table 4.1: First three modes in proposed resonator cavity

Modes	Frequency (GHz)	Q-factor	Type
$TE_{11\delta}$	1.92	3845	Dual
$TE_{21\delta}$	2.697	3500	Dual
$TM_{01\delta}$	2.85	5200	single

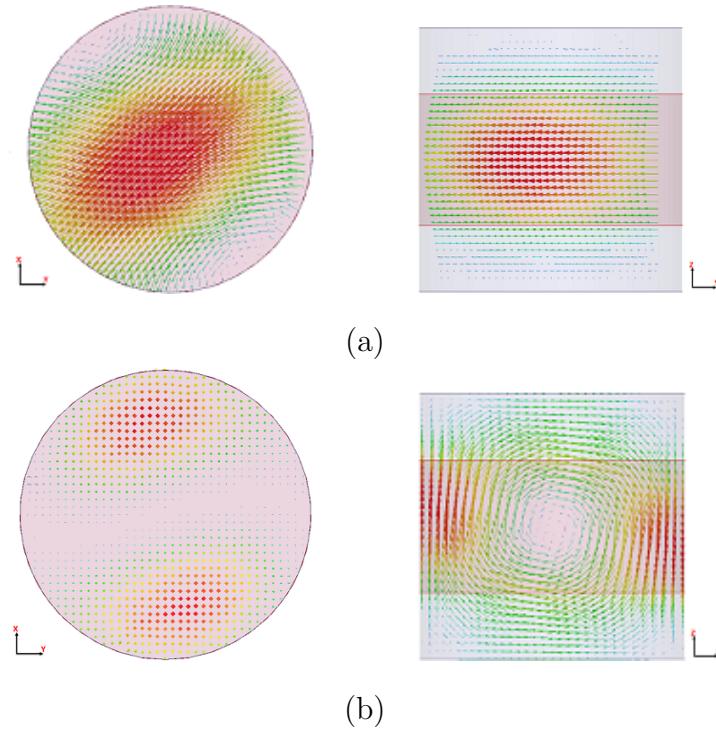


Figure 4.6: Field distributions of $TE_{11\delta}$ dual-mode (a) E-field plot (b) H-field plot.

4.3 Design of a Single Cavity Dual-Mode Filter

To design a filter, we need to follow a several steps as shown below:

1. Obtain the specification of the filter (resonance frequency f_r , Bandwidth (Bw), reflection loss (L_R)).
2. Calculate all coupling types as function to physical dimensions.
3. Choose the appropriate topology of the filter.
4. Generate the coupling matrix of the filter.
5. Extract the coupling values.
6. Realization of the dimensions.

4.3.1 Input and Output Coupling

Calculation the coupling vales is important step to design a filter as mentioned in section 4.3. Therefore, the external quality factor of a single resonator can be

found by two methods:

1. Simulating $|S_{21}|$ response with one port weakly coupled.
2. Simulating one port and measuring the group delay of $|S_{11}|$.

Figure 4.7(a) shows an example of a dual-mode cavity that is externally coupled to the input port via a probe with length (L_f) in mm and direct contact with the top or bottom surface of the dielectric disc and weakly coupled to the output port. The external quality factor Q_e can then be calculated from the simulated S_{21} response using equation 4.1 [30]:

$$Q_e = \frac{\omega_0}{\Delta\omega_{\pm 3dB}} \quad (4.1)$$

Where ω_0 is the resonant angular frequency of the loaded resonator and $\Delta\omega_{\pm 3dB}$ is the 3 dB angular bandwidth, as shown in Figure 4.7(c). Another method for calculating the Q_e , is to simulate just one port by the group delay of S_{11} response using equation 4.2 [78]:

$$Q_e = \frac{\omega_0\tau_d}{4} \quad (4.2)$$

Where τ_d is the group delay in second as shown in Figure 4.7(d).

Figure 4.8 shows the external quality factors Q_e against the length of input/output probe(L_f). It can be seen that the Q_e of the $TE_{11\delta}$ mode has been decreased with increasing the L_f . The value of Q_e when L_f is less than 7 mm is not suitable for filters that require high bandwidth; for example, a 2^{nd} order filter with bandwidth (Bw) less than 12 MHz can be achieved at this length. L_f greater than 7 mm is used to achieve higher Bw. The E-field of $TE_{11\delta}$ is concentrated in the middle of the ceramic disc, which produces a high external quality factor when the length of the probe approaches the centre.

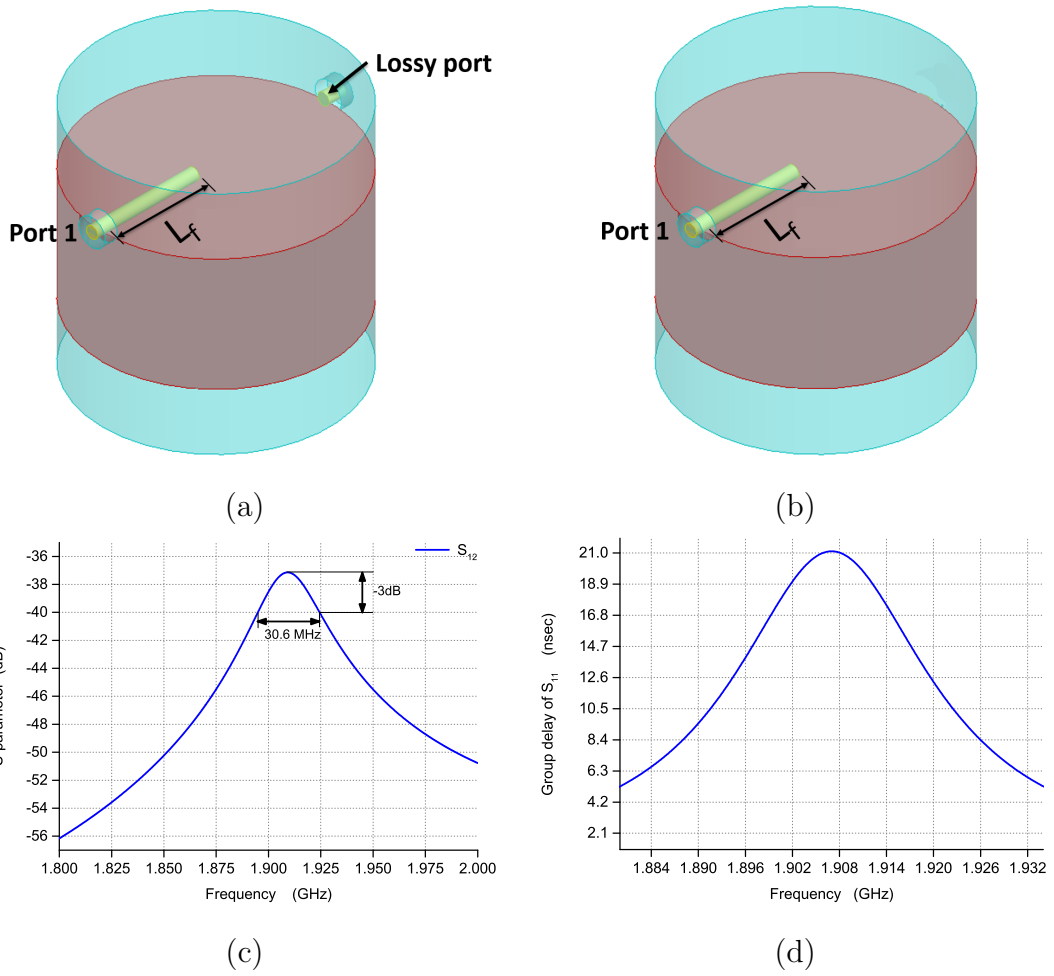


Figure 4.7: Externally coupled methods (a) Weak port, (b) One port, (c) Response of S_{21} and (d) Group delay for S_{11} .

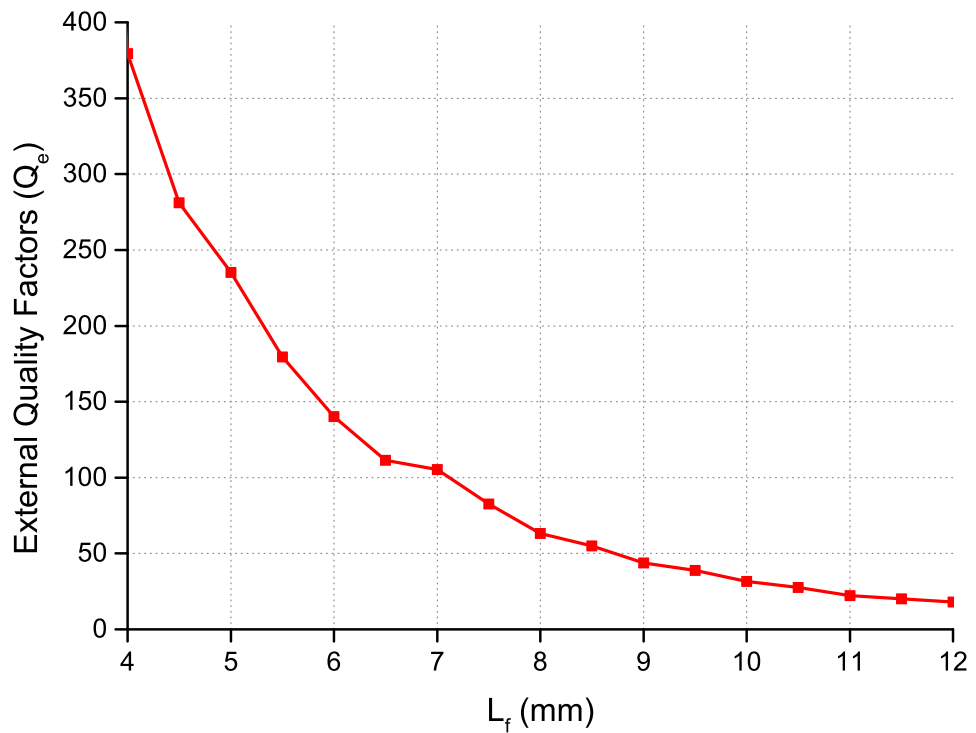


Figure 4.8: Variation of external quality factor (Q_e) against L_f .

4.3.2 Coupling of Degenerate Modes

The working principle of the dual-mode resonator is that energy is coupled from the first mode to its degenerate mode within the same resonator. Hence, the coupling and tuning structure is essential to the dual-mode filter design. Ideally, metallic screw, corner cuts and through holes at 45° with respect to the polarisation axis are utilised to couple the two orthogonal modes. To extract the coupling coefficient of two asynchronously coupled resonators, a general formula that applies to any type of resonators is used [78],

$$M = \pm \frac{1}{2} \left(\frac{\omega_{02}}{\omega_{01}} + \frac{\omega_{01}}{\omega_{02}} \right) \times \sqrt{\left(\frac{\omega_2^2 - \omega_1^2}{\omega_2^2 + \omega_1^2} \right)^2 - \left(\frac{\omega_{02}^2 - \omega_{01}^2}{\omega_{02}^2 + \omega_{01}^2} \right)^2} \quad (4.3)$$

where ω_{01} and ω_{02} are the resonant frequencies of the two coupled resonators, ω_1 and ω_2 are the lower and higher frequencies in the magnitude of S_{21} response of the two coupled resonator structures when ports are very weakly coupled to the resonators. The characteristic parameters ω_{01} , ω_{02} , ω_1 and ω_2 can be determined using full-wave EM simulations. Figure 4.9(a) shows an example of a dual-mode cavity coupling structure that is weakly coupled to the ports, and Figure 4.9(b) depicts the simulated S_{12} response showing the frequency peaks ω_1 and ω_2 . The

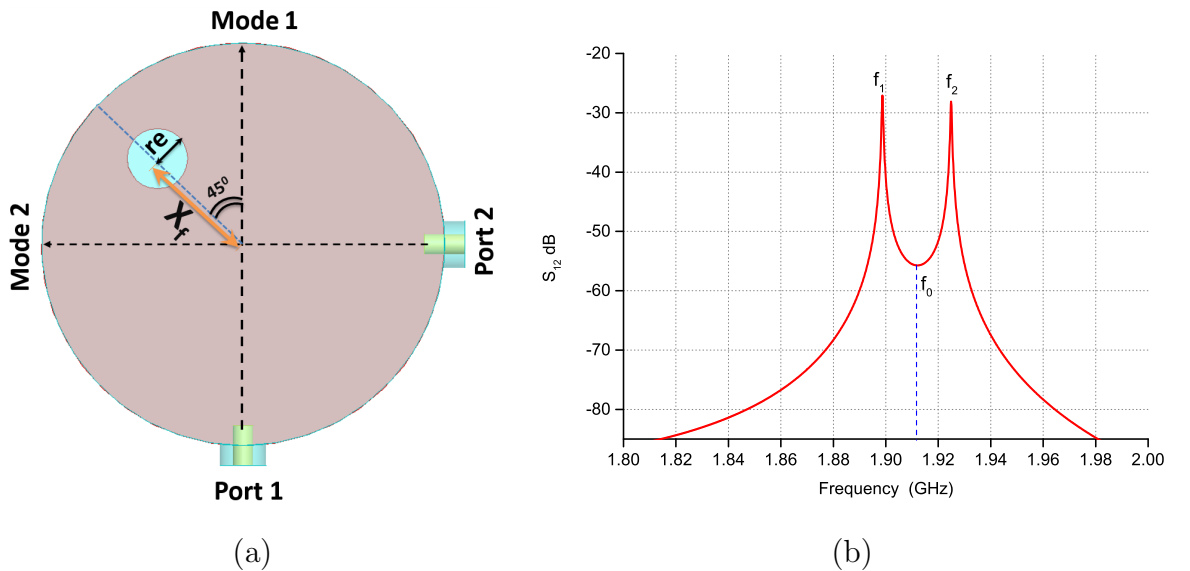


Figure 4.9: Inter-coupling dual-mode resonator (a) Dual-mode coupling configuration, (b) S_{21} of two coupled resonators showing two frequency peaks.

formula in equation 4.3 is applicable for synchronously coupled resonators, and in

this case it is simplified to equation 4.4 [78],

$$M = \pm \frac{\omega_2^2 - \omega_1^2}{\omega_2^2 + \omega_1^2} \quad (4.4)$$

Coupling coefficient usually corresponds to either a magnetic coupling or an electric coupling. These two types of coupling exhibit opposite signs for the coupling coefficient.

Figure 4.10 shows the coupling bandwidth of the dual-mode resonator against the position of the hole (X_f) with respect to the centre of the ceramic puck with variations in the hole radius (r_e). It is clear that the two main factors that have a significant influence on the coupling bandwidth are the position of the hole (X_f) and the hole radius (r_e) for the resonator in Figure 4.9a. Regarding X_f , there are two distinguishing regions shown in Figure 4.10, below and above 7 mm. In the first region, the coupling bandwidth has been increased with the increasing of X_f while it has a reverse relationship in the case of region two. All maximum points have occurred at 7 mm. Furthermore, the coupling bandwidth has a direct proportional relationship with the radius of the hole r_e . A wide range of bandwidth can be implemented by these configurations, from the narrow to the wide (some hundred of MHz).

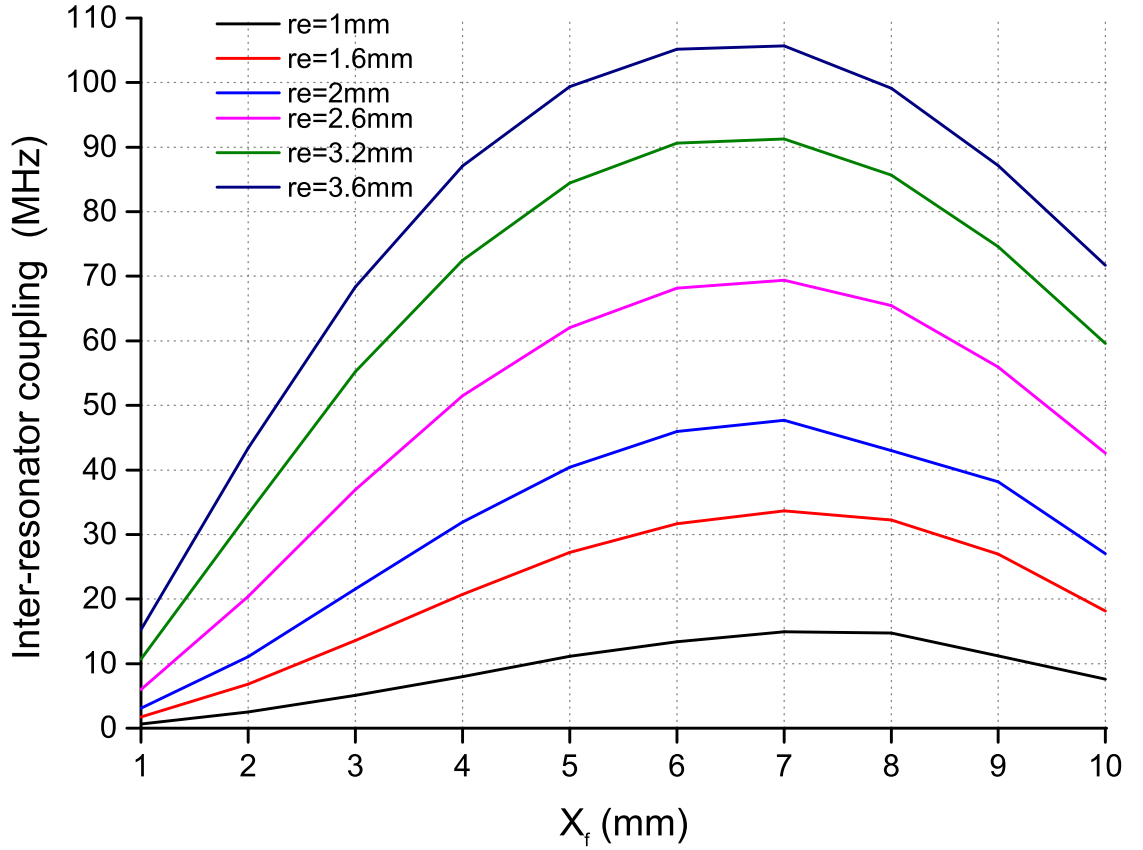


Figure 4.10: Inter-resonator coupling bandwidth varying with radius (r_e) and position of the etching hole (X_f).

4.4 Implementation of the Second-order Filter

The design of a dual-mode filter, one cavity or any type of filter, can be performed in two steps. Design step 1: coupling matrix synthesis

The coupling matrix values give the exact coupling for a filter operating at certain specifications. Coupling Matrix Synthesis (CMS) software can be used to extract the coupling value at reflection loss (L_R) = 20 dB as illustrated in Figure 4.11.

Design step 2: filter specifications

The type of application determines the filter specifications, which are the filter order, insertion loss (IL), f_0 and the bandwidth. For example, the filter can be designed as a Chebyshev filter with a centre frequency of 1.95 GHz, bandwidth of 50 MHz and reflection loss (L_R) of 20 dB at the passband. According to Figure 4.11(b), the I/O external quality factors and the coupling coefficients are computed

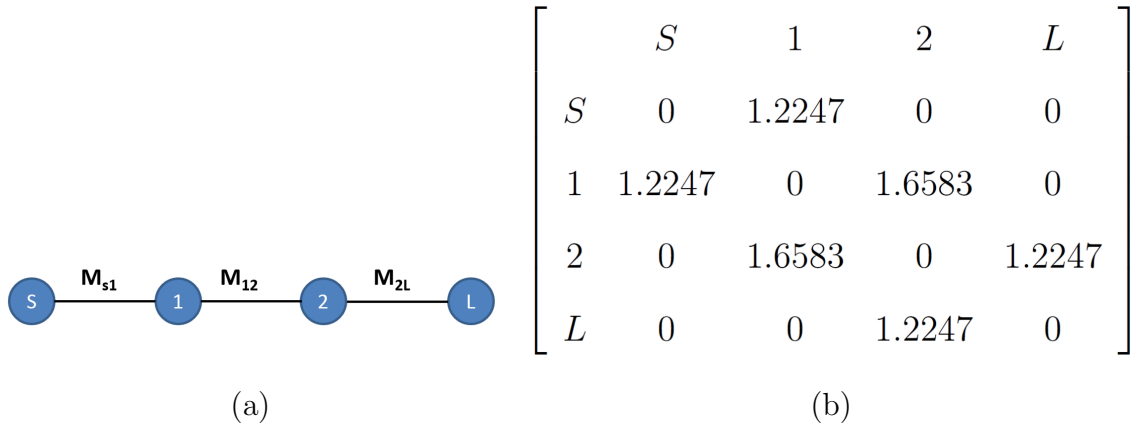


Figure 4.11: 2^{nd} order filter (a) Filter topology, (b) Normalized coupling matrix.

for $FBW=2.61\%$, and found to be $Q_e=26$ by using equation 4.5 [79] and $M_{12}=83$ MHz.

$$Q_e = \frac{f_0}{BW * M_{S1}^2} \quad (4.5)$$

where M_{S1} is the I/O normalized coupling from coupling matrix.

The filter has been implemented using a DR dual-mode cavity whose 3D structure is shown in Figure 4.12. The configuration consists of a dielectric puck inserted in the metal cavity made from copper for a better contact and high Q factor. A hole is made in the DR at 45^0 relative to input coupling while the I/O probes are orientated at 90^0 . The dimensions of the cavity are 20 mm for the diameter and height with conductivity of $\sigma = 4 \times 10^7 S/m$. The dielectric resonator dimensions are $\epsilon_r = 43$, $\tan \delta = 4 \times 10^{-5}$, $D=20$ mm and $L=10$ mm. Referring to Figure 4.8, the length of the I/O probes to obtain an external quality factor of 26 is 11 mm for copper where the internal coupling is about 83 MHz. From Figure 4.10, the hole diameter is 3.2 mm and it is placed 8.5 mm from the centre of the dielectric puck. The simulation model in HFSS for the Chebyshev two-pole filter can be seen in Figure 4.13. The cavity resonates at the frequency 1.95 GHz and the bandwidth of the filter at L_R 18 dB is 50 MHz. According to the same figure, the value of the ripple level is 0.15 dB. Therefore, the unloaded Q-factor can be extracted from equation 4.6 [1],

$$Q_u = \frac{4.434 \omega_0 T_d}{L_{A(f0)} - L_{A(\infty)}} \quad (4.6)$$

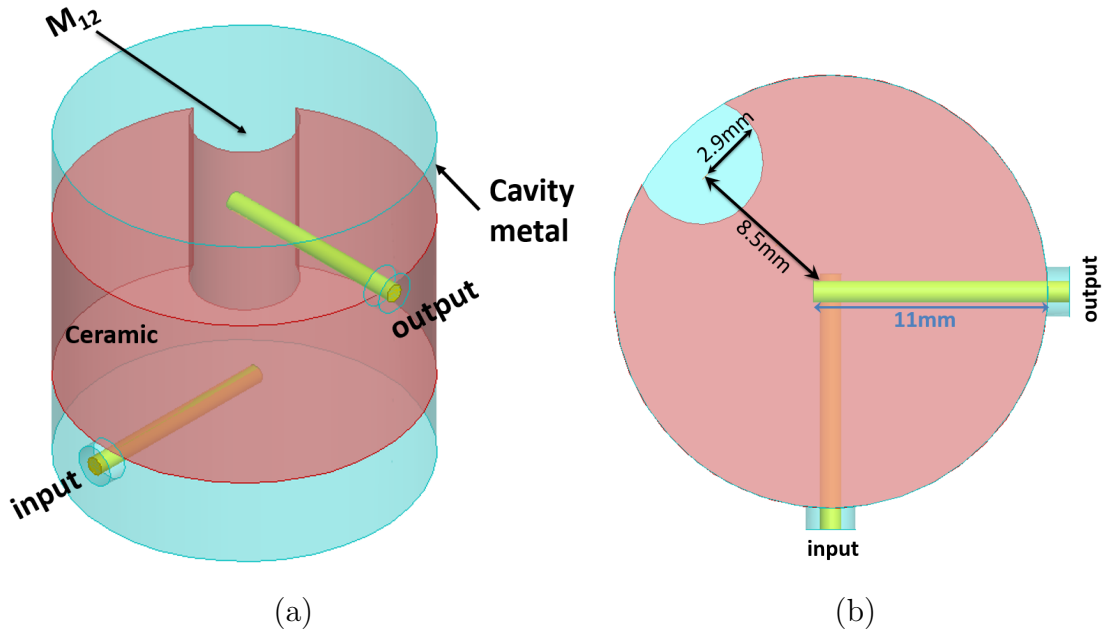


Figure 4.12: 2nd order filter (a) 3D structure view, (b) Top view.

where T_d , $L_A(f_0)$ and $L_A(\infty)$ are the group delay in seconds, insertion loss at resonant frequency in dB and insertion loss at resonant frequency in dB when the filter is lossless. From Figure 4.13 and Figure 4.14, the calculated unloaded Q factor is about 3200, with coupling loss of about 600, which means that this cavity is suitable to work in a cellular base station.

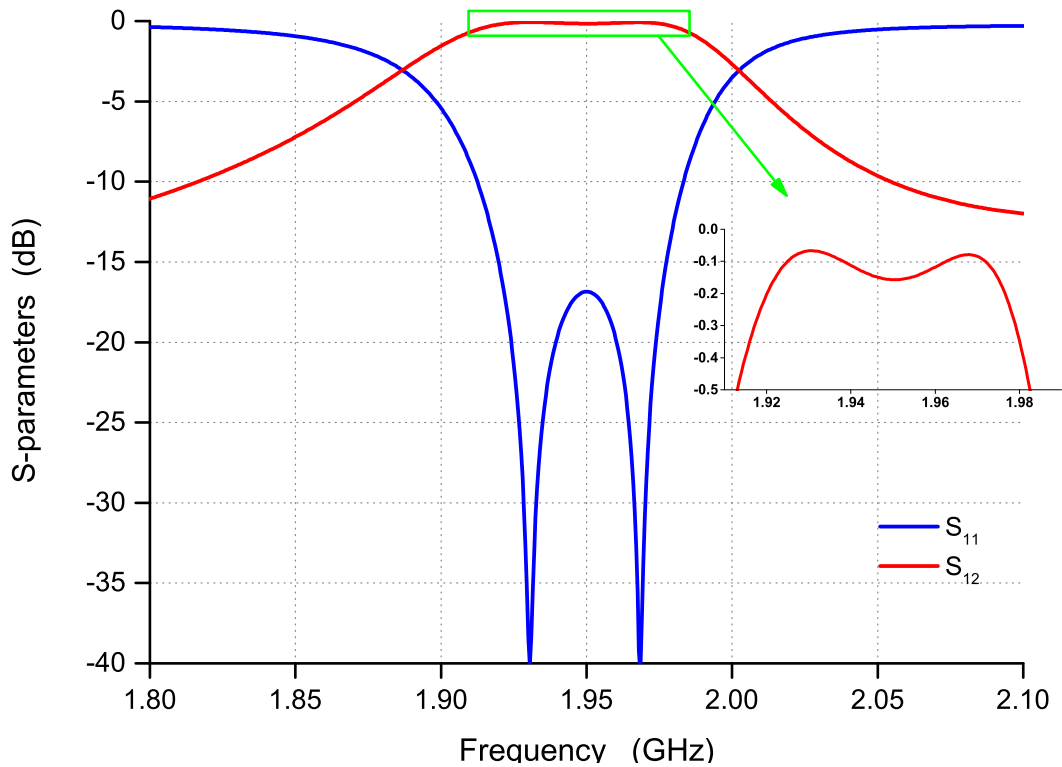


Figure 4.13: Simulated of in-band frequency responses of 2nd order filter.

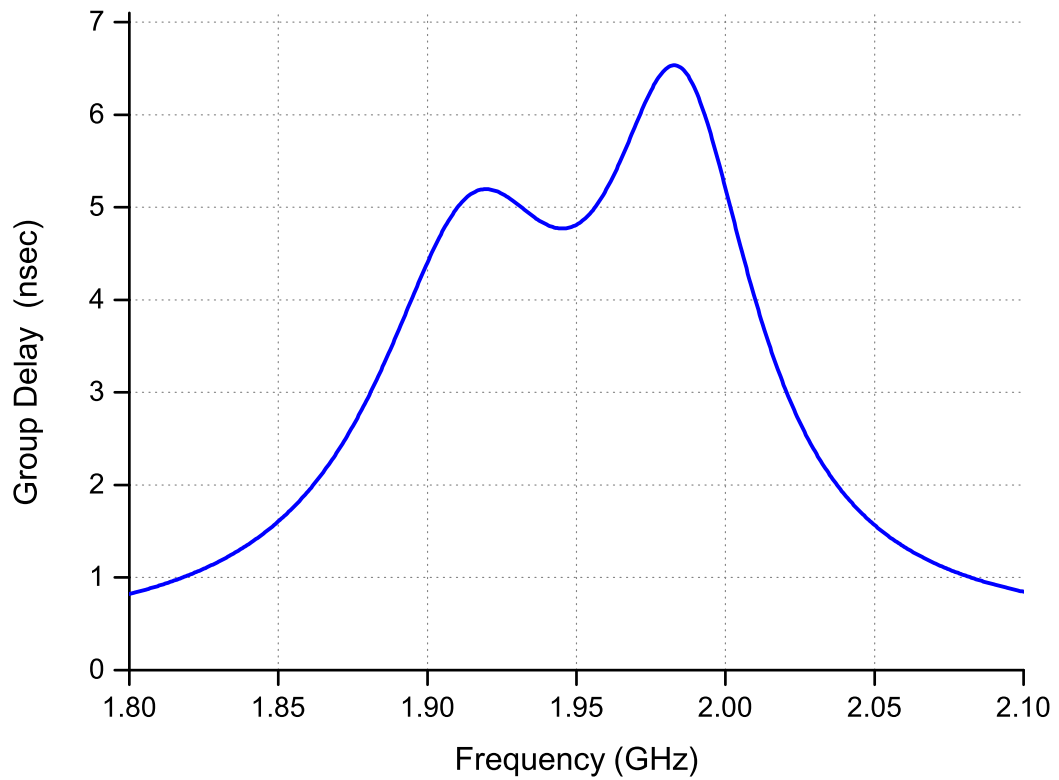


Figure 4.14: Group delay of 2^{nd} dual-mode order filter.

Figure 4.15 shows the response of a 2^{nd} order filter in wideband performance. It is observed that the first spurious mode occurs at 2.73 GHz. Also, there is a spurious-free window of 748 MHz, which is lower than the eigen-mode solution. However, the TE_{210} mode was excited by high inter-resonator coupling and not enough I/O coupling, which causes the distortion in the second mode. Moreover, the bandwidth at 3 dB is about 150 MHz starting from 2.55 GHz.

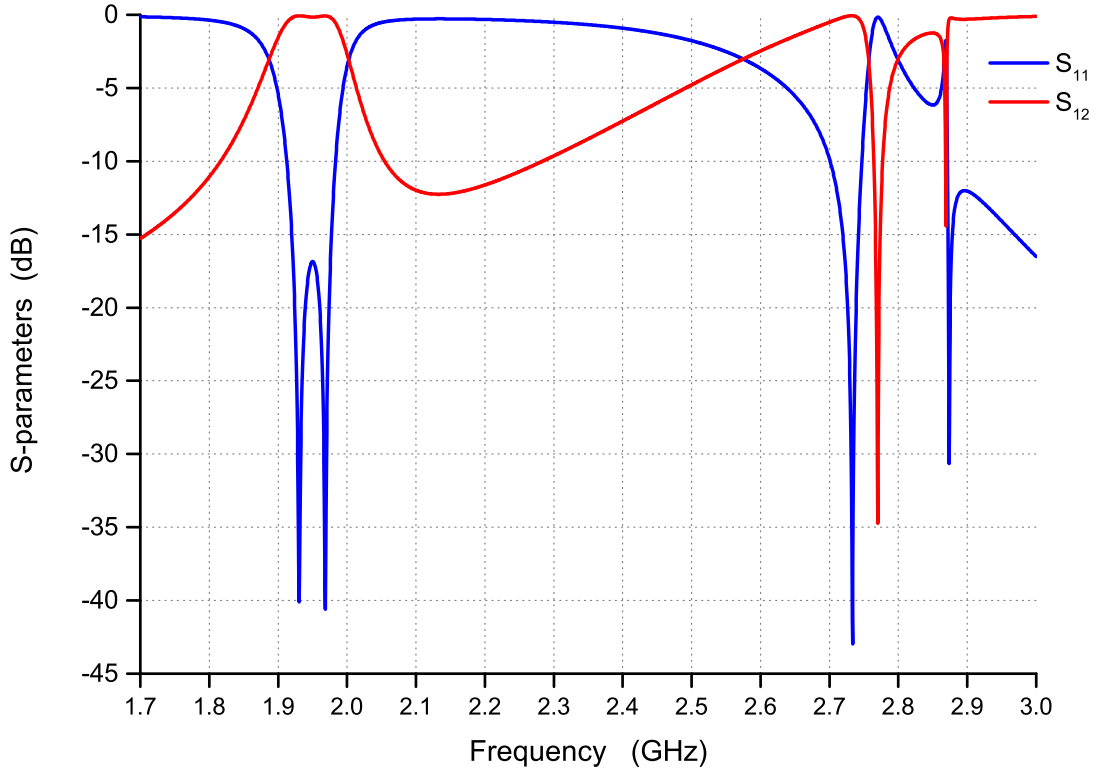


Figure 4.15: Broadband simulation of the 2nd order filter.

4.5 Implementation of the 4th-order dual-mode filter

Figure 4.16 shows the configuration of the four-pole filter in HFSS having similar materials as the 2nd pole filter. The filter has been implemented using a DR dual-mode, which has a two pieces of ceramic inserted in the middle of a copper cavity and I/O probes connected in the bottom of the DR and the inter-cavity probe connected to the top. The two cavities in the filter are similar to the single cavity design, as the same dielectric puck and coupling elements were used. The inter-cavity coupling is simulated by weak coupling for I/O and probe with length (L_{f1}) joining two cavities which are in direct contact with the top or bottom of the surface of the DR. A L_{f1} is measured on each cavity and has the same material and diameter as the I/O coupling probes. Figure 4.17 illustrates the inter-cavity coupling bandwidth against the length of the probe (L_{f1}). It is observed that the

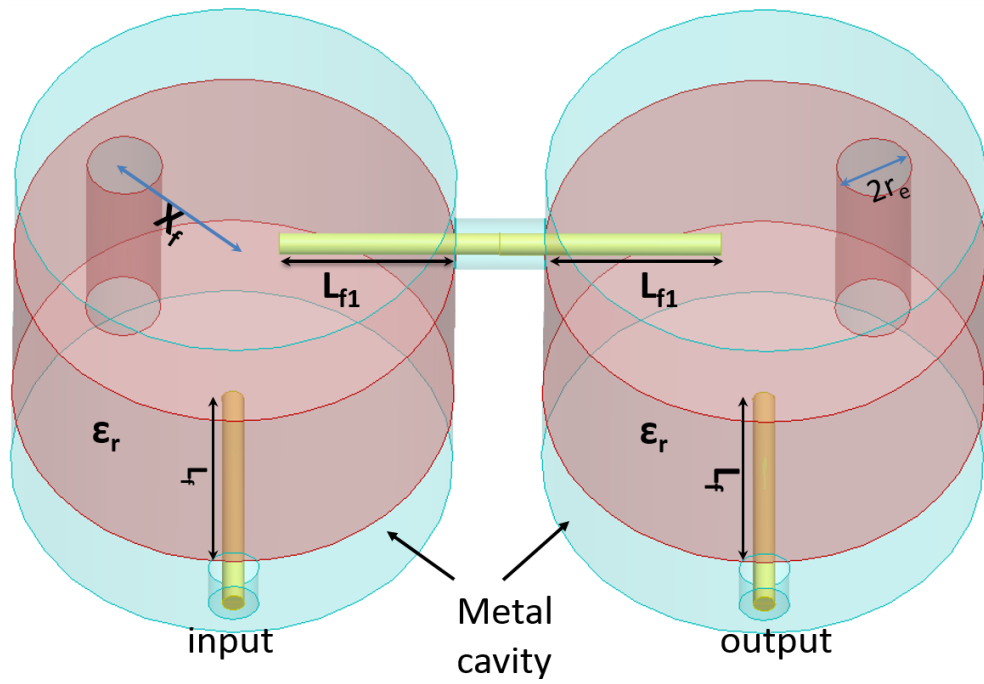


Figure 4.16: Configuration of a 4th order filter in HFSS.

coupling is increase with the L_{f1} , which rises gradually in the range of L_{f1} from 4 mm to 6 mm, recording 4 MHz to 18 MHz. Increasing rapidly from 6 mm to 8 mm recorded about an 80 MHz positive sloping. High accuracy is required when fabricating this filter at high bandwidth. The 4th order Chebyshev dual-mode fil-

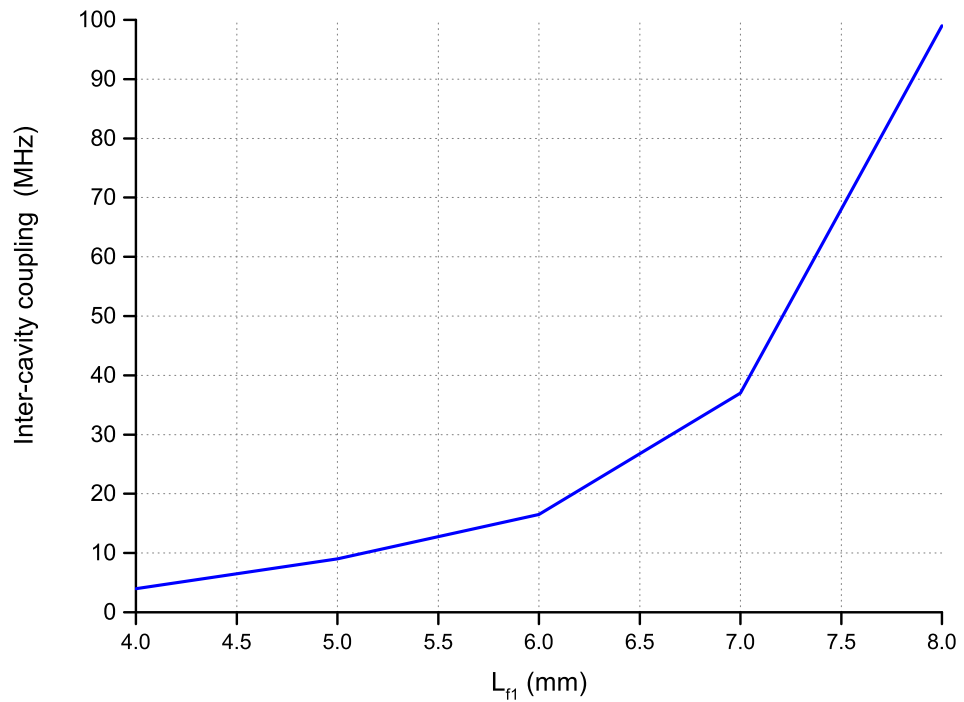


Figure 4.17: Variation of inter-cavity coupling bandwidth against L_{f1} .

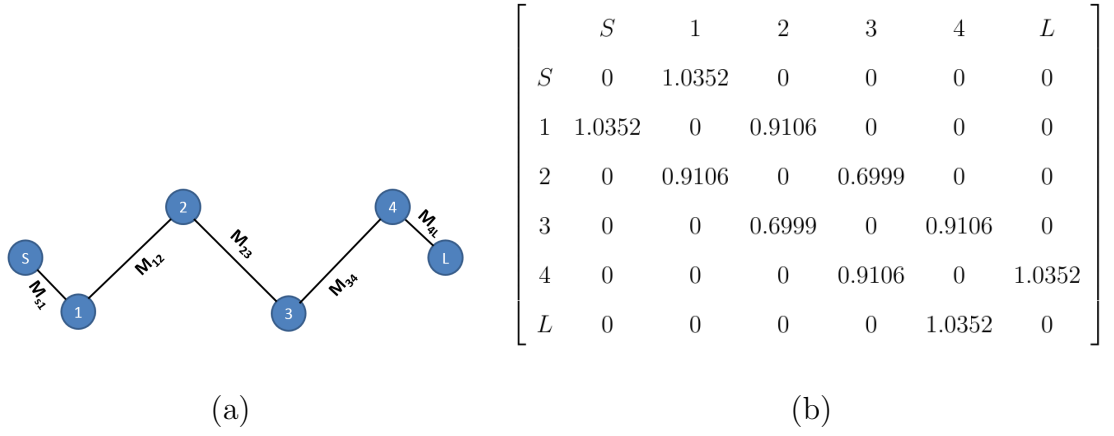


Figure 4.18: 4th order filter (a) Filter topology, (b) Normalized coupling matrix.

ter is designed with a centre frequency of 1.931 GHz, bandwidth of 50 MHz and return loss (L_R) of 20 dB in the passband. The coupling matrix and Chebyshev topology are shown in Figure 4.18 at FBW=2.61%. The external quality factor and the coupling coefficients are computed using CMS software. The true coupling bandwidth values are $M_{12}=M_{34}= 45.53$ MHz, $M_{23}=35$ MHz and $Q_e=36.4$. Referring to Figure 4.8, the length of the I/O probe required to achieve external quality factor 36.4 is 10 mm, where the internal coupling is about 45 MHz. From Figure 4.10, the dimensions of the hole are 3.4 mm and 7 mm for the diameter X_f respectively with M_{23} equal to 35 MHz, as derived from Figure 4.17 and $L_{f1}=8$ mm.

Figure 4.19 presents the S-parameter response for the 4th order Chebyshev filter. It can be observed that the bandwidth of the filter at -18 dB is 50.5 MHz based on the cellular system. The insertion loss at the resonant frequency (1.931GHz) is less than 0.3 dB and the extracted unloaded Q factor is slightly more than 3000. It is clear that the filter losses have increased compared with reduce Q_u by 200. The ripple in the passband of the filter is not equal because the probe lengths have a high sensitivity to the coupling especially when the bandwidth filter is designed at more than 20 MHz. The L_A at 2.05 GHz is 38 dB with a 2 dB difference to the designed value. It is worth mentioning that the total volume of the prototype filter is less than 8.75 times the conventional coaxial cavity filter at $\sqrt{\epsilon_r}Z_0$ is about 77 Ω with a comparable unloaded Q-factor value.

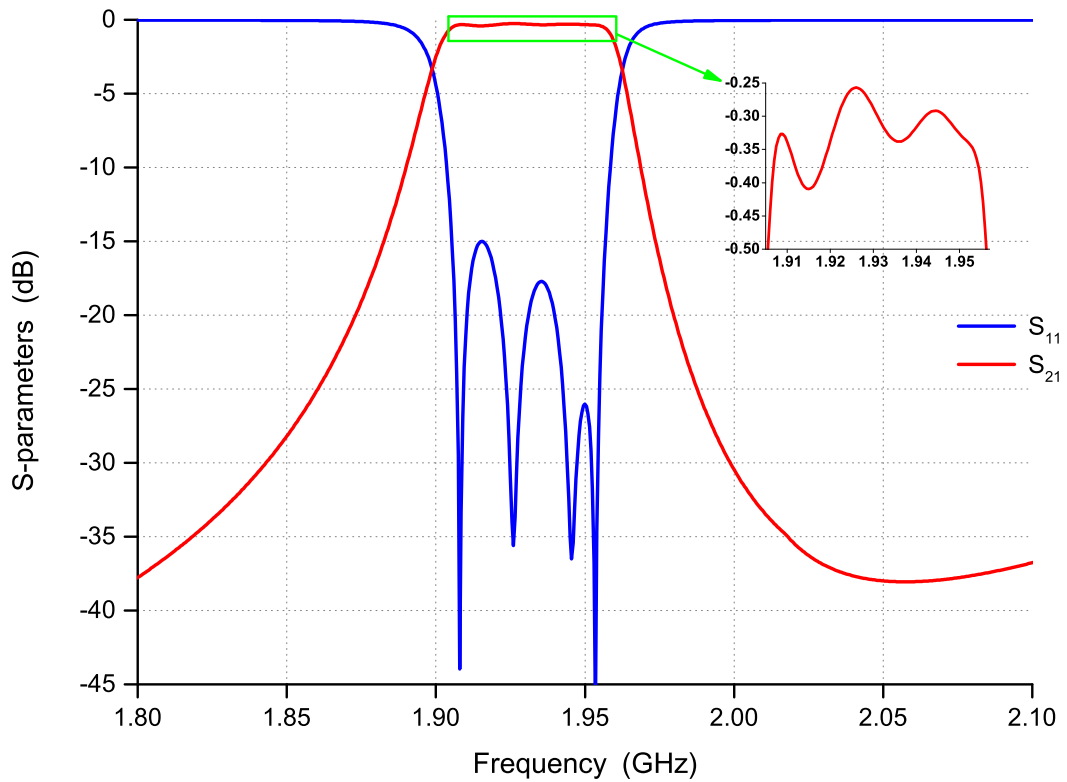


Figure 4.19: Simulation of in-band frequency responses of 4th order filter.

Figure 4.20 shows the broadband response of the 4th order Chebyshev filter. It can be seen that the lower spurious mode is about 2.38 GHz and the higher spurious mode is above 2.71 GHz. The first spurious mode appears in the frequency even though it does not exist in eigen-mode analysis and one-cavity simulation. This may be due to non-perfect coupling from I/O coupling to the first spurious mode, which is the dual-mode $TE_{21\delta}$ type. Furthermore, the notch through the dielectric puck is coupling the degenerated fundamental mode ($TE_{11\delta}$) in either coupling $TE_{21\delta}$ with high coupling value compared with the fundamental. The filter performs like parallel connected filters with different frequencies and the bandwidths. Finally, the coupling between cavity one and cavity two for the first spurious mode is not perfect, which creates a peak at 2.38 GHz. The simulation result shows that the spurious suppression occurred about 400 MHz from the fundamental frequency.

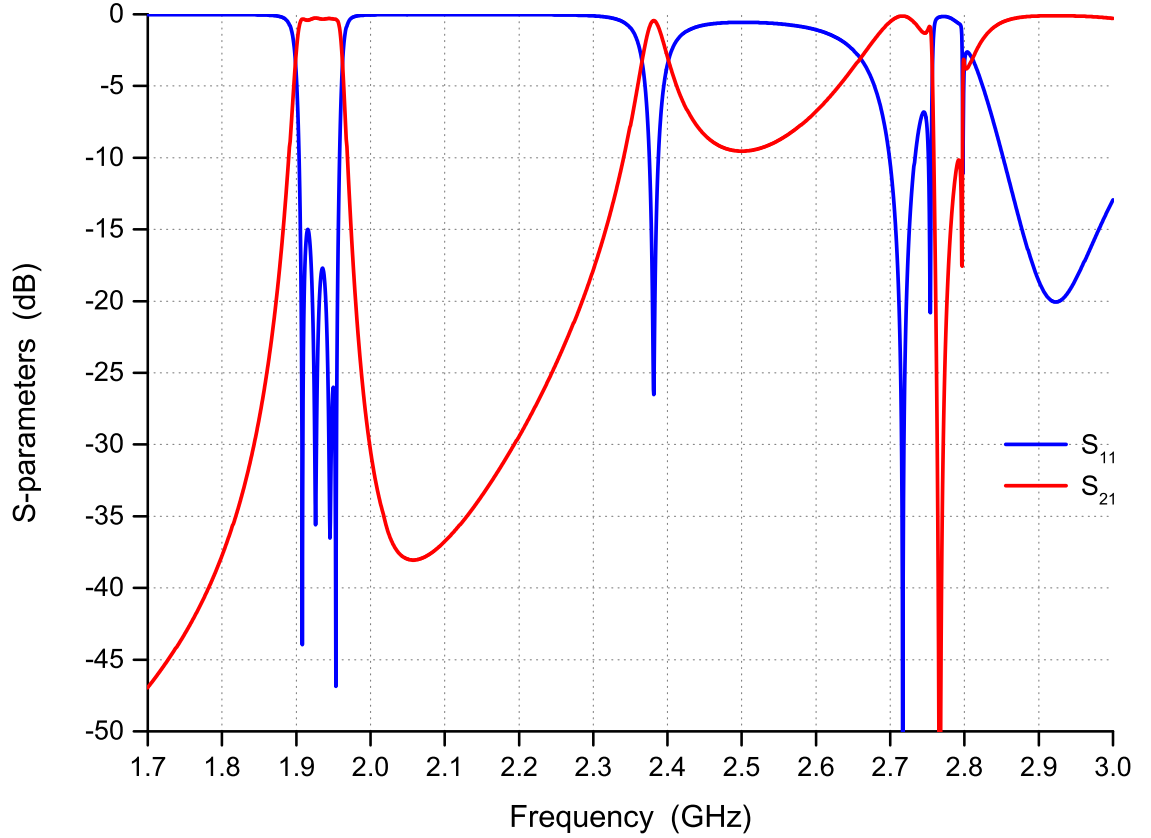


Figure 4.20: Simulation of the wideband response 4th order filter.

4.6 Fabrication and Measurement

A novel 4th order Chebyshev dual-mode DR filter has been fabricated; a photograph of the filter is shown in Figure 4.21. The metal cavity is made from aluminium ($\sigma = 2.6 \times 10^7 S/m$) with dimensions $55mm \times 30mm \times 28mm$, and the dielectric puck was chosen with ceramic material $\epsilon_r = 43$ and tangent loss of 4×10^{-5} . M2 tuning screws were provided on the top lid of the cavity for controlling the coupling. The probes are made of copper with a diameter of 1.27 mm. The filter is designed at $f_0=1.92$ GHz with a bandwidth of 41 MHz and Q_u of about 3200 for an aluminium cavity in eigen mode analysis. Additionally, the dimensions of the filter at this specification are $L_f=9$ mm, $L_{f1}=8$ mm, $X_f=7$ mm and $re=1.7$ mm.

S-parameter measurement is achieved by using an Agilent E5071C Network Analyzer. Two-port calibration is performed by using an Agilent N4431-60006 Electronic Calibration Module prior to the measurement.

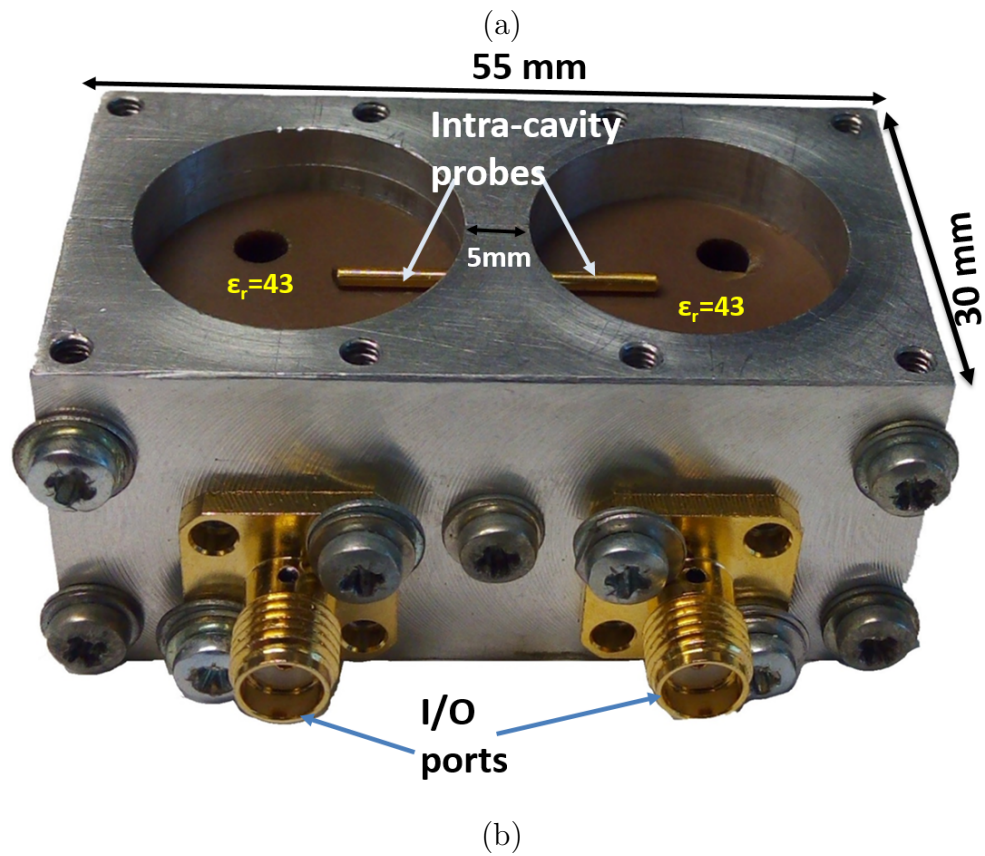
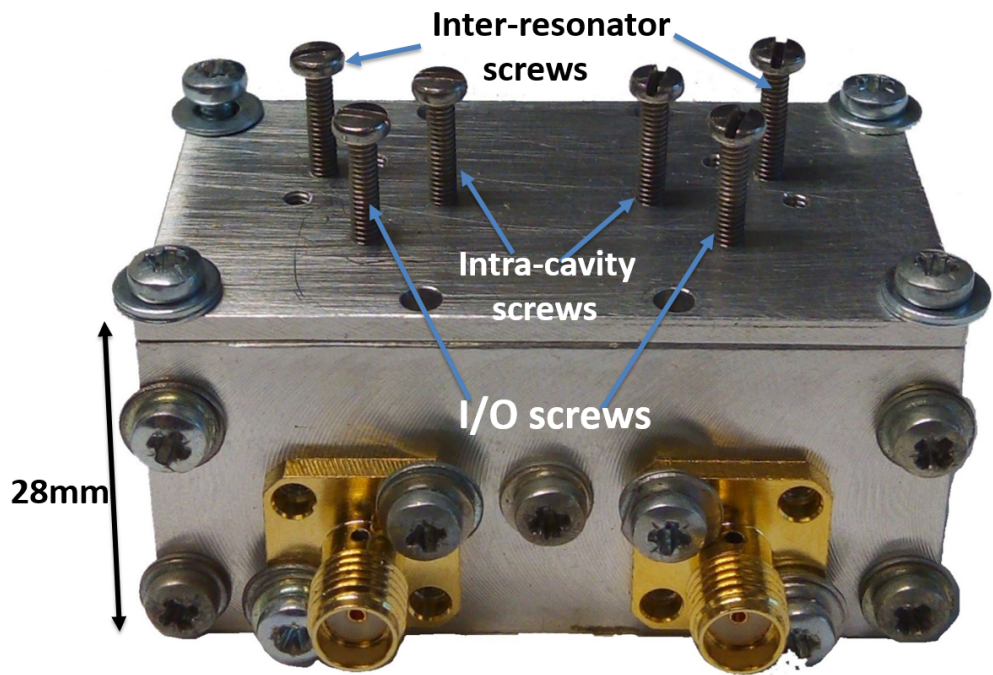


Figure 4.21: Fabricated 4th degree dual-mode bandpass filter.

The simulated and measured results of the filter are depicted in Figure 4.22. The experimental result shows that the maximum return loss within the passband is 8 dB and the minimum insertion loss is 2 dB. The bandwidth of the measured response is slightly higher than the simulated response and the centre frequency is

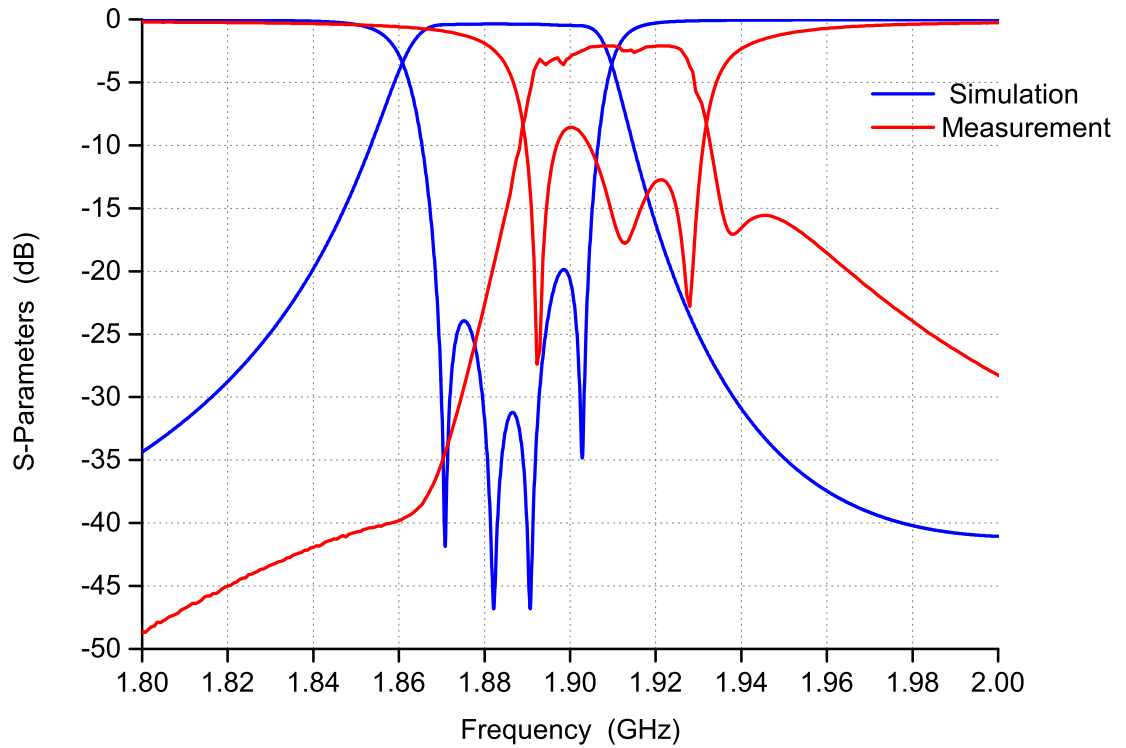


Figure 4.22: Measured and simulated results of the filter

shifted up about 20 MHz. There are many reasons for high losses in the fabricated filter and the shift in frequency. Firstly, the gap between the dielectric puck and the metal cavity is a significant factor in pushing the resonant frequency of the resonator up. Secondly, the dimension and orientation of the holes through the ceramic puck and the probes are not very precise, which could affect the coupling coefficients of the filter as shown in Figure 4.8 and Figure 4.17. Finally, the gaps between all probes and the DR should be zero to give a designed coupling, otherwise the coupling will be too weak. To sort out this problem, a Teflon disc was attached to all probes to make a good contact between them, and also to maintain high losses in the filter.

4.7 Fourth-order Dual-Mode Filter with Strip Coupling

The practical coupling issue in the filter in section 4.6 was indirect contact between the probe and the surface of the DR. To sort out this problem, a strip line coupling technique has been suggested. The design of a 4th order dual-mode filter with strip coupling is similar to that in section 4.6. The same dielectric puck and coupling elements for inter-resonators were used. Figure 4.23 shows the configuration of the 4th order DR dual-mode filter in HFSS. The I/O coupling is made

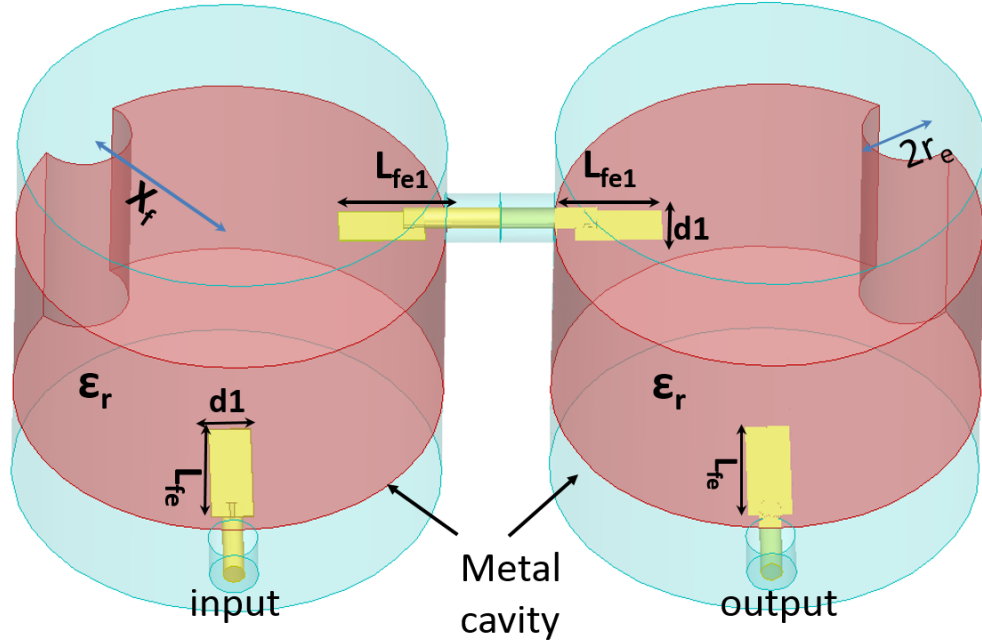


Figure 4.23: Configuration of 4th order filter in HFSS.

from silver paint on the ceramic with rectangular shape, length (L_{fe1}), width ($d1$) 2 mm, and the thickness of the paint is about 15 μm , which has a conductivity of $2 \times 10^7 S/m$. Figure 4.24 illustrates the external quality factor for the I/O single cavity against L_{fe} . It can be seen that the Q_e declined when the L_{fe} is increased, which allows for varying bandwidth. Also, L_{fe} has a significant effect on the Q_e , which is reduced to 10% when the length is doubled. The inter-resonator coupling is exactly the same as Figure 4.10 because the structure does not change.

The inter-cavity coupling has been simulated by varying the length of the strip

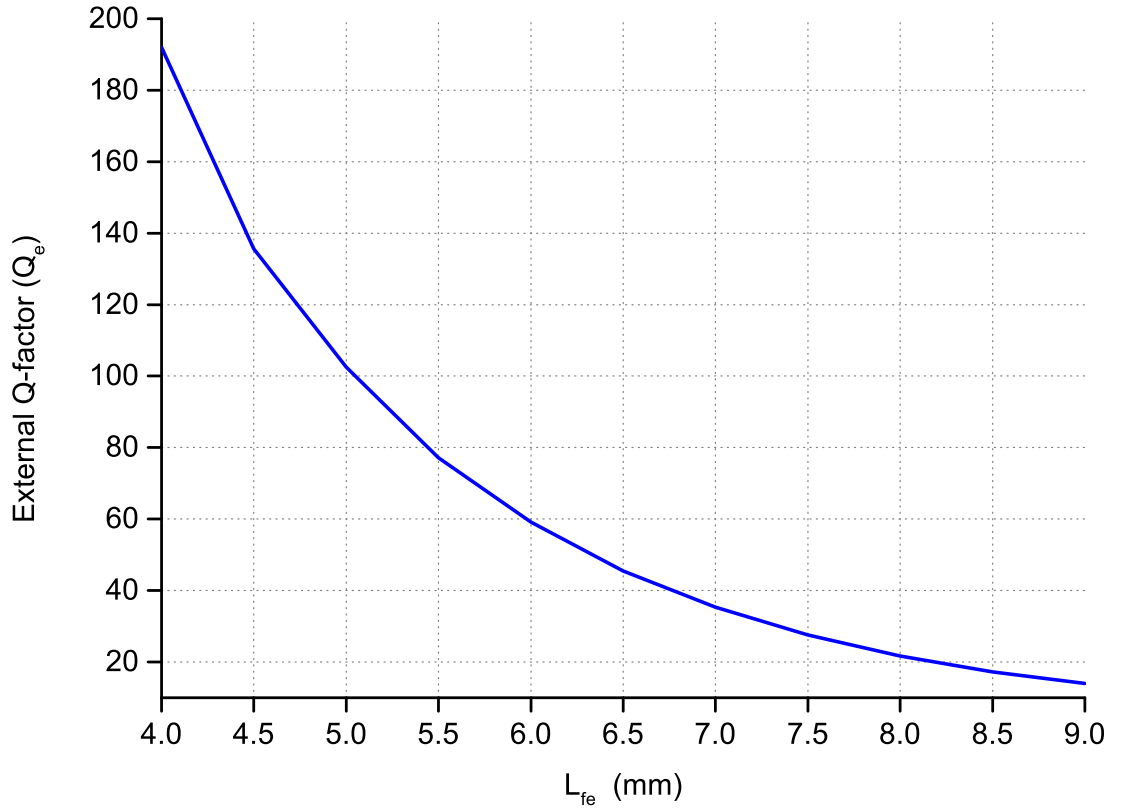


Figure 4.24: The external quality factor (Q_e) against length of strip L_{fe}

(L_{fe1}), as shown in Figure 4.25. It is observed that the coupling bandwidth increased with L_{fe1} . Also, a 1.5 mm change in length recorded a 60 MHz increment. A 4th order Chebyshev dual-mode filter is designed with a centre frequency of 1.931 GHz, bandwidth of 50 MHz and return loss (L_R) of 20 dB at the passband. The coupling matrix and filter topology is the same as Figure 4.18. Regarding Figure 4.24, the length of the I/O probe to obtain an external quality factor of 36.4 is 6.2 mm, where the internal coupling is about 45 MHz.

Referring to Figure 4.10, the diameter of the hole is 2.25 mm and is placed at 9.5 mm from the centre of the dielectric puck, $M_{23}=35$ MHz and $L_{f1} =4$ mm.

Figure 4.26 presents the S-parameter for the fourth-order dual-mode filter at the designed values. It can be observed that the resonant frequency (1.953GHz) bandwidth of the filter at -16 dB is equal to 50 MHz and the insertion loss is 0.427 dB. There is a 22 MHz shift in the resonant frequency and the maximum return loss is 10 dB, while the extracted unloaded Q factor is about 3000.

Figure 4.27 presents the broadband response of the 4th-order Chebyshev filter with

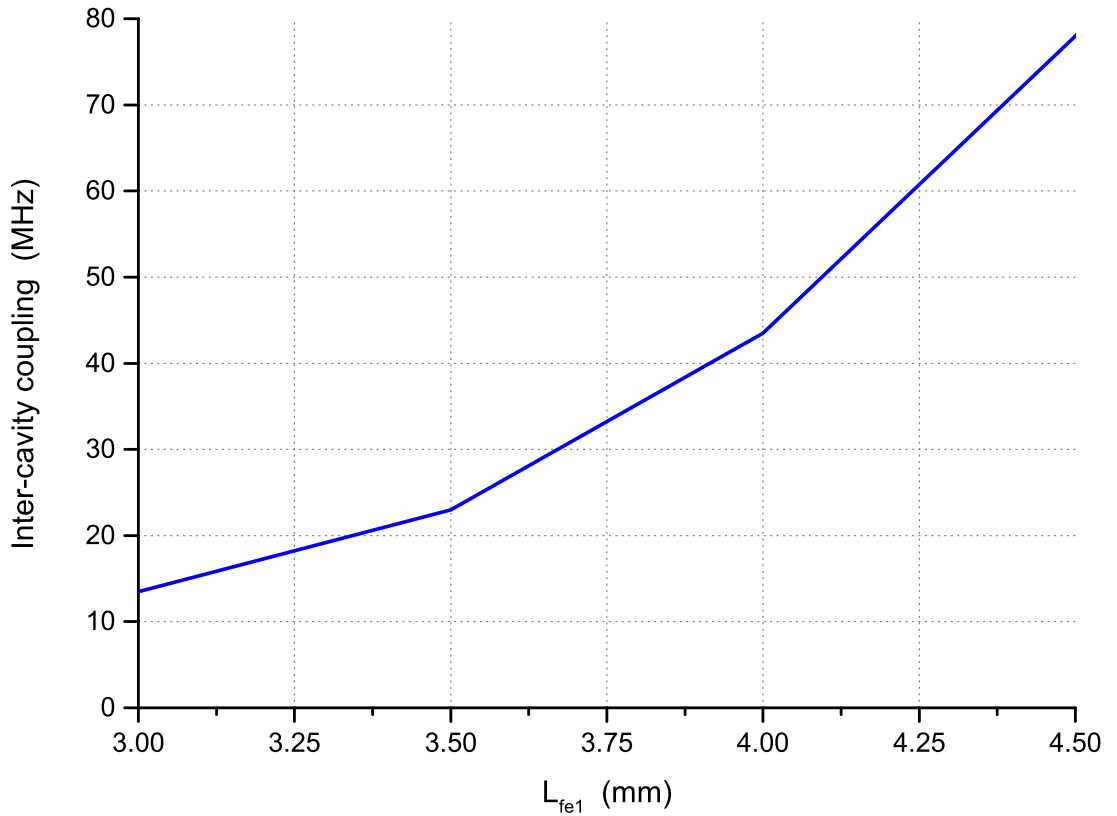


Figure 4.25: Variation of inter-cavity coupling (M_{23}) against L_{fe1} .

strip coupling. The lower spurious mode is about 2.3 GHz and the higher spurious mode is above 2.75 GHz. The first spurious mode is less than about 80 MHz compared with the probe coupling filter. As mentioned before, the main reason for this is a non-perfect coupling from I/O and inter-cavity coupling. Moreover, the sensitivity of the inter-cavity coupling when varying the length of the strip is also an important factor. The overall spurious-free window is 350 MHz and agrees with the majority of multi-mode DR filters.

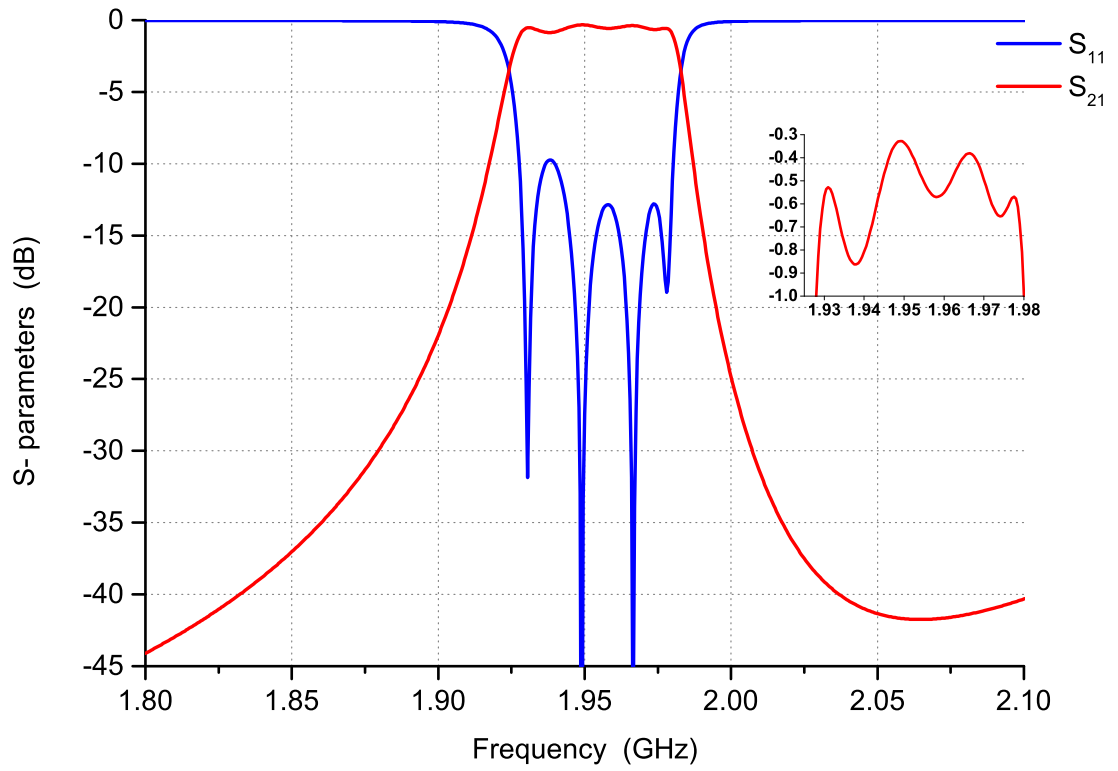


Figure 4.26: Simulation of in-band frequency responses of 4th order filter strip coupling.

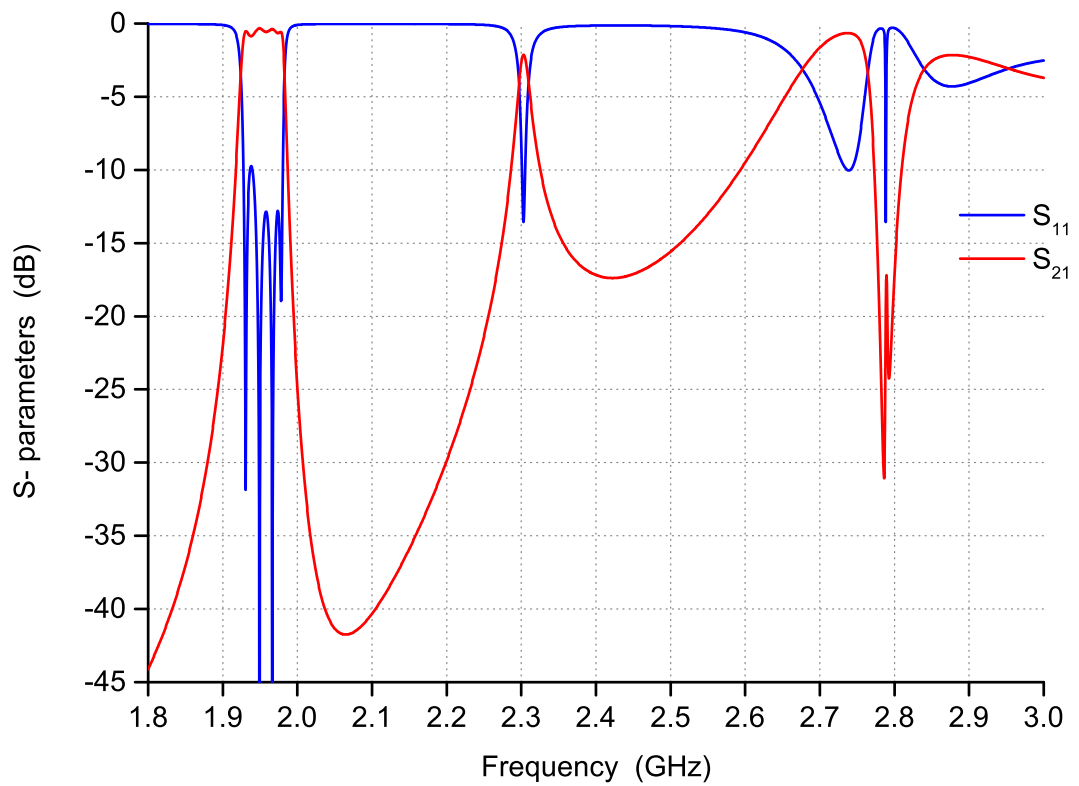


Figure 4.27: Simulation of the wideband response 4th order filter strip coupling.

4.8 Summary

A novel $TE_{11\delta}$ dual-mode DR filter was designed and fabricated with two different coupling techniques. A significant volume reduction ratio of 11% compared to an air filled coaxial filter was demonstrated. For the first filter, the input, output and inter-cavity coupling were achieved by using a coaxial probe in contact with the top or the bottom face of the ceramic puck. The length of the probe controls the amount of coupling and the inter-resonator coupling was achieved by cutting a hole in the ceramic at 45° with respect to the modes. The metallic cavity was made from aluminium. The practical result shows high losses in the filter with a 15 MHz shift in the resonant frequency and the spurious-free window was reduced by about 400 MHz compared with eigen-mode analysis. The coupling mechanism for the second filter was achieved by a silver-painted strip while the inter-resonator coupling was maintained. The simulation result indicates that the losses and spurious-free window of the filter were worse compared with the first one and also the sensitivity to the changes in dimension was higher.

Chapter 5

Dual-Mode Filter Implementation by Etching the Dielectric Resonator

5.1 Introduction

In microwave filter design, the coupling techniques are essential factors and configurations should be feasible and fixable. There are two types of coupling topology, inductive and capacitive, and each one depends on the size of the filter and the field pattern. As mentioned in Chapter 4, there are many technical problems in practical prototype. The major issues are the probes and strips which are used in input/output and inter-cavity coupling. These are unable to give a good contact with the DR to excite the resonator over the designed coupling bandwidth. The small size of the filter and the type of mode is a big challenge in obtaining an effective coupling configuration. In this chapter, a novel dual-mode Dielectric Resonator (DR) bandpass filter with a new coupling technique is described which offers a high Q , better performance, small volume and less weight compared to conventional air-filled cavity filters. Realisation processes are highlighted from

EM simulations to fabrication. The DR structure considers a dielectric puck situated in the middle of a metallic cavity with some air space below and above the ceramic puck and short-circuited by the sides. $TE_{11\delta}$ is the fundamental resonance for the dual-degenerate mode and HFSS simulations have been used to generate field patterns for this resonator and perform frequency response. Holes were provided through the middle side of the dielectric puck for the coupling I/O because the E-field was concentrated in the middle. Two fourth-order Chebyshev filter were designed by using planar and inline structures. A 50Ω probe in the middle side of the puck is used for the input and output coupling, the length of the probe controls the amount of coupling. Notching the ceramic puck at 45° with respect to the mode controls the coupling between the two generated modes. Vertical etching holes and slots the ceramic puck for coupling is designed with the fourth-order filter. The response of the practical filter is compared with the EM simulation which gives a shift in frequency resonance and more loss due to the gap between the ceramic puck and the cavity.

5.2 Configuration of the Proposed Resonator

Figure 5.1 shows the configuration of the $TE_{11\delta}$ dual-mode DR. This consisted of a circular ceramic puck of high dielectric constant that had two perpendicular cylindrical holes bored in-plane with the cylindrical face in the middle of the cavity. The puck was suspended in the middle of a cylindrical metallic enclosure and short-circuited to the sidewalls, effectively miniaturizing the filter size while maintaining a good electrical performance. In the schematic, D and L are the diameter and length of the DR respectively and L_a is the distance above and below the ceramic puck and is filled with air. The term r_0 is the diameter of the holes cut through the dielectric, which is done to improve the Q factor and make a good space for input/output coupling. The ceramic material used was barium titanate which has a relative permittivity of 43 and a loss tangent of 4×10^{-5} . This was placed

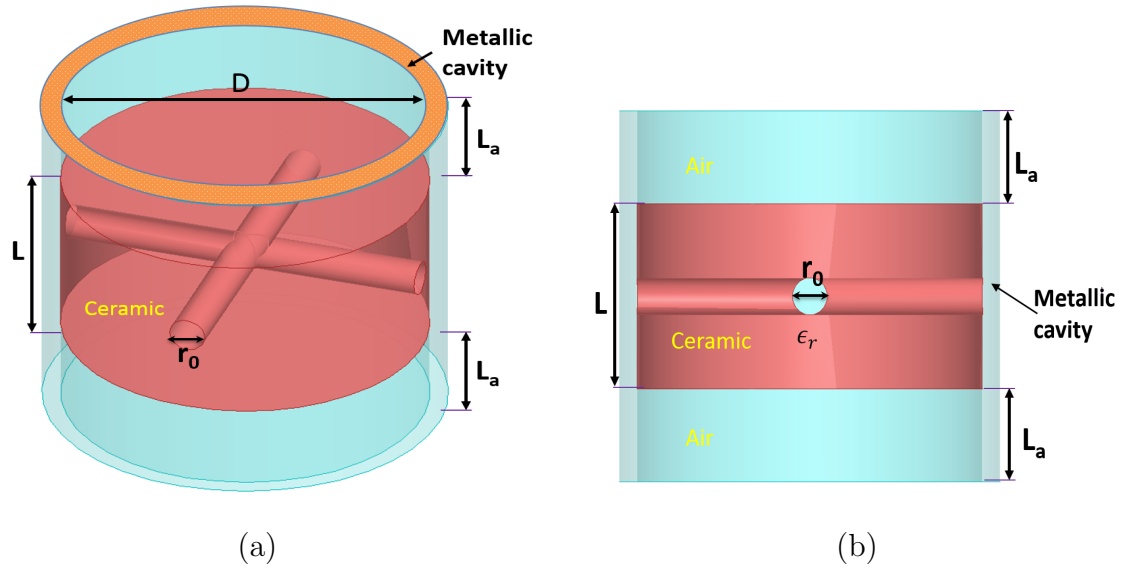


Figure 5.1: Configuration of dual-mode dielectric resonator: (a) 3D view, (b) side view.

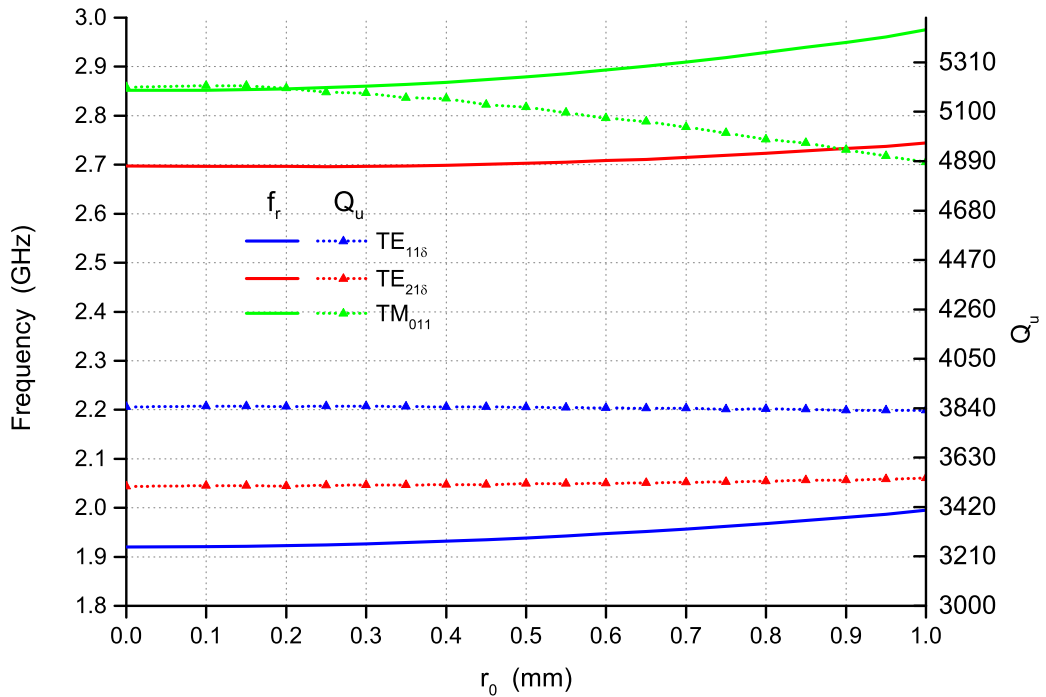


Figure 5.2: Resonance frequencies and Q_u with varying hole radius (r_0).

in the metal cavity and short-circuited on the side walls which had conductivity 4×10^7 S/m, while $D=20$ mm, $L=10$ mm and $L_a=5$ mm, which are given the optimum value. The eigen-mode solver in HFSS software was used to calculate the resonant frequency and unloaded Q factors for the DR proposed. Figure 5.2 illustrates the variation of the resonant frequency and Q factor of the first three modes against the radius of the hole r_0 . $TE_{11\delta}$ and $TE_{21\delta}$ are dual-mode. It can be seen that there is

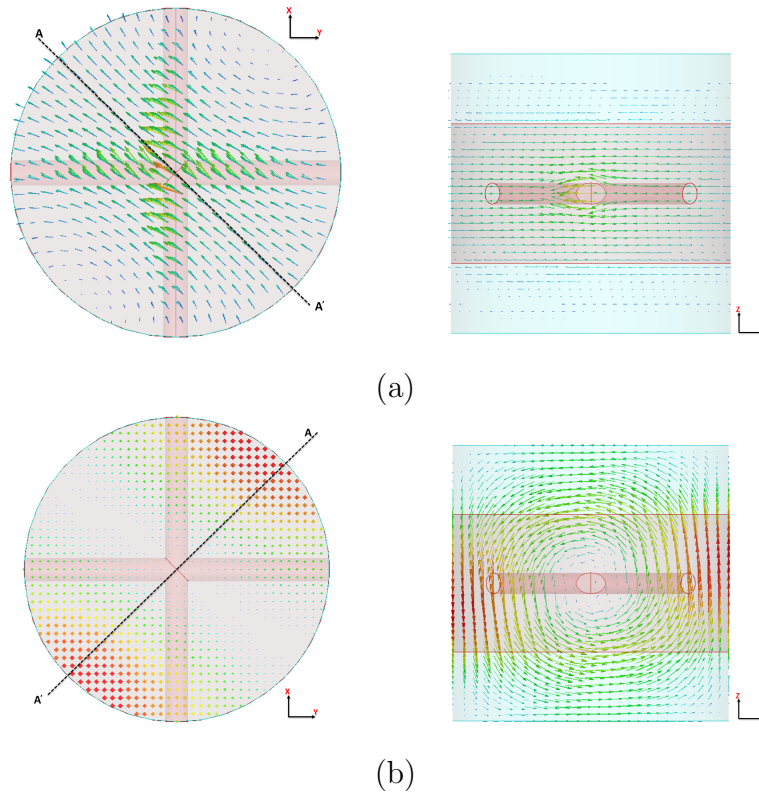


Figure 5.3: Field distributions of $TE_{11\delta}$ dual-mode (a) E-field plot (b) H-field plot.

a slight increase in resonance frequency with an increase in r_0 . The maximum drift in frequency at mode $TE_{11\delta}$ is about 76 MHz and is doubled at the $TM_{01\delta}$ mode. Furthermore, the spurious-free window is 780 MHz and still constant. For the same value of r_0 the Q factor does not affect the change in geometry for the second two modes, whilst mode $TM_{01\delta}$ has been gradually decreased. It is clear that the TE mode was not affected by the size of the hole through the ceramic puck because it is parallel with the direction of the E-field. Figure 5.3 illustrates the pattern fields of the proposed cavity for the fundamental mode (1.96 GHz). From Figure 5.3, it can be observed that most of the E-field exists inside the dielectric puck surface which is distributed around the hole. Furthermore, the z-component of the E-field near to the hole could be used to control the coupling because the E-field is concentrated in the centre of the puck. The maximum H-field is distributed tangentially to the side of the puck, and shows the same performance in the dielectric with or without the added hole. The H-field was not significantly affected by the holes.

5.3 Design of the 4th-Order Chebyshev Dual-Mode Filter Planar Configuration

The procedure required to design a filter is as follows:

1. Obtain the specification of the filter (resonance frequency f_r , Bandwidth (Bw), reflection loss (L_R)).
2. Choose the appropriate topology of the filter.
3. Generate the coupling matrix of the filter.
4. Extract the coupling values.
5. Realization of the dimensions.

The next subsections will show all the coupling techniques and associated calculations.

5.3.1 External Coupling

In order to achieve the external coupling for the dual-mode dielectric resonator filter that has been proposed, a coaxial probe was oriented in the middle of the side hole through ceramic. E-field can be used for the coupling because it is maximum around the hole and perpendicular to the Z-axis direction, as presented in Figure 5.3. The radius of the hole is 0.75 mm, which gave a resonant frequency of 1.96 GHz and Q_u of 3850. The external coupling can be calculated by the one-port method. Figure 5.4 illustrates the external quality factors Q_e , against the length of I/O probe (L_f).

It can be observed that the L_f has a significant effect on the Q_e , which decreased with a rise in the L_f . A wide range of bandwidth can be achieved by adjusting the probe coupling.

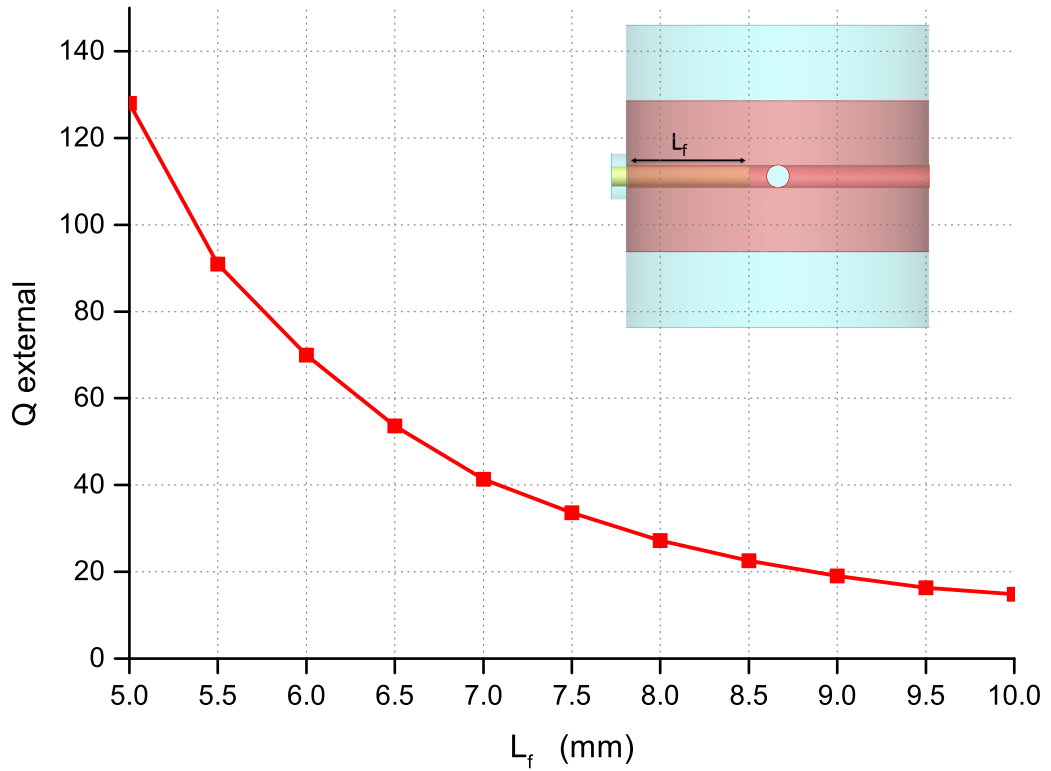


Figure 5.4: Variation of external quality factor (Q_e) against L_f .

5.3.2 Inter-Resonator Coupling

The inter-resonator coupling was implemented through the circular hole which is at 45° with respect to modes one and two. A circular hole acts as an impedance inverter over a broad bandwidth of the filter [5]. Lossy coupling probes were used to calculate the coupling bandwidth in the HFSS. Figure 5.5 shows coupling bandwidth against the distance between the centre of the DR and the hole (X_f) with variations in the hole radius (r_e), measured in mm. It is observed that there are two distinct regions in the graph, below 6mm and over 8mm for X_f . The coupling bandwidths increased significantly when X_f increased for all of region one. However, the opposite is observed in region 2, where the coupling bandwidth decreased slowly with X_f . The maximum coupling bandwidth occurred at $X_f=7$ mm, which is increase with r_e with maximum value of 110 MHz at $r_e=3.6$ mm. Therefore, this coupling technique can be implemented as a filter with a variety of bandwidth from narrow to wideband.

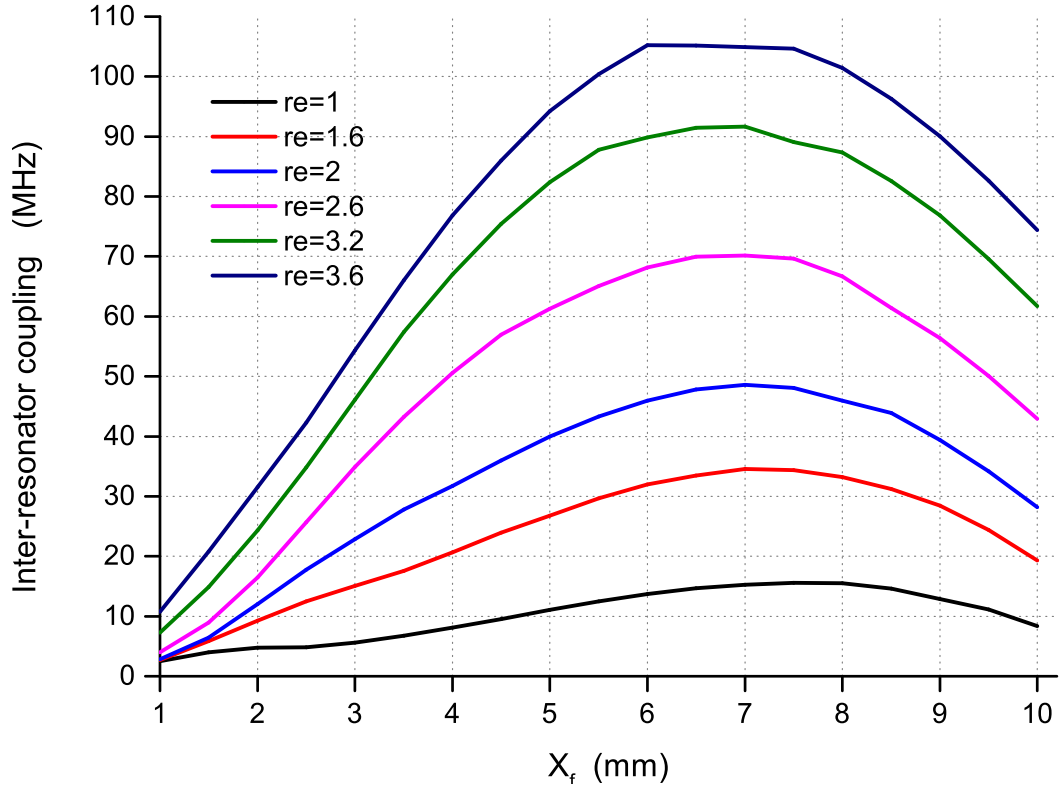


Figure 5.5: Inter-resonator coupling bandwidth varying with radius (re) and etching hole position (X_f).

5.3.3 Inter-Cavity Coupling

Connecting two cavities together entails an efficient and suitable configuration. In this filter, a coaxial probe was utilised in coupling the two cavities with a planar configuration, as shown in Figure 5.7. A probe was placed in the centre of both DRs through the metallic wall. Figure 5.6 illustrates the inter-cavity coupling bandwidth against the length of the probe in each cavity (L_{f1}). It is noted that the L_{f1} has a significant effect on the coupling bandwidth. The coupling rose steadily in the range of L_{f1} (4 mm to 6 mm), increasing from 8 MHz to 32 MHz. It rapidly increased from 6 mm to 8 mm with about a 34 MHz/mm slope. Therefore, high accuracy is required to fabricate this filter.

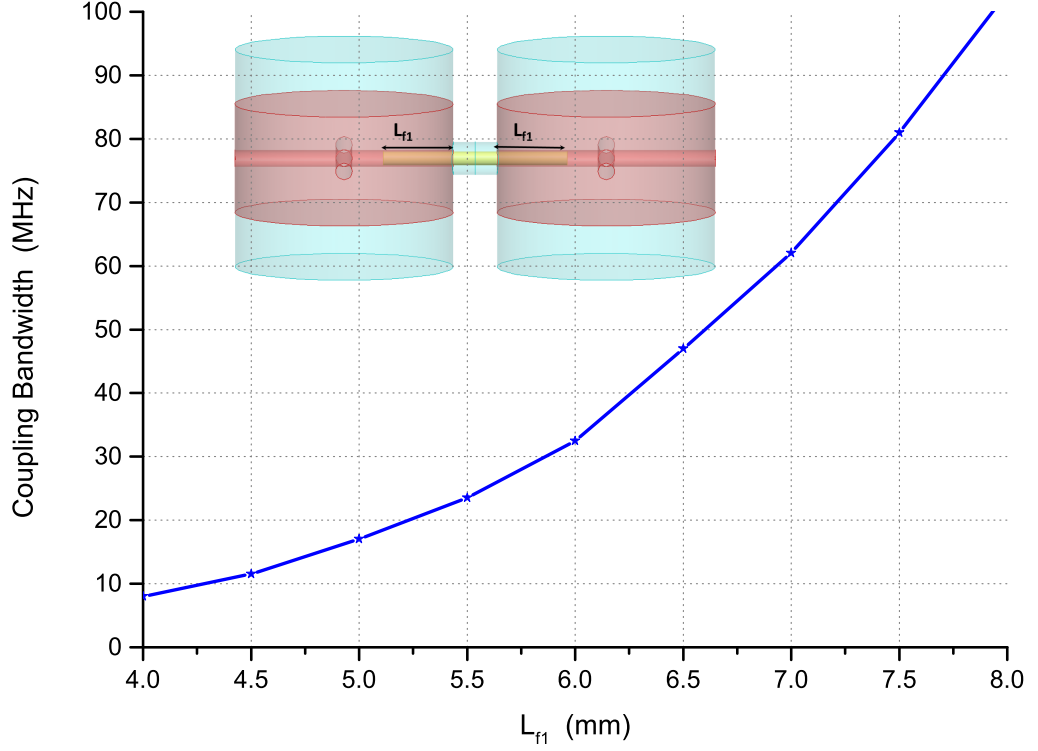


Figure 5.6: Variation of inter-cavity coupling bandwidth (M_{23}) against L_{f1} .

5.3.4 Simulation Results

The configuration of the 4th order dual-mode filter in HFSS software is shown in Figure 5.7. Two metallic cavities were used to present the filter with two pieces of ceramic ($\epsilon_r=43$ and $\tan \delta = 4 \times 10^{-5}$) placed in the middle and shorted by the side wall with conductivity= $4 \times 10^7 S/m$. The coaxial probe L_f was used for I/O coupling and L_{f1} controlled the inter-cavities coupling. The notch through the DR was used to present the inter-resonator coupling. To obtain the proper dimensions for all parameters as indicated in Figure 5.7, it is essential to propose the topology of the filter and calculate the coupling matrix. The 4th order Chebyshev dual-mode filter was designed with a centre frequency of 1.961 GHz, bandwidth (Bw) of 52 MHz and return loss (L_R) of 20 dB at the passband. We used the coupling matrix as mentioned in Chapter 4. The input and output external quality factors and the coupling coefficients were computed for fractional bandwidth (FBW)=2.65%, and found to be $M_{12}=M_{34}= 47.35$ MHz, and $Q_e=35.19$. Referring to Figure 5.4, the length of the I/O probe required to obtain the exact external quality factor

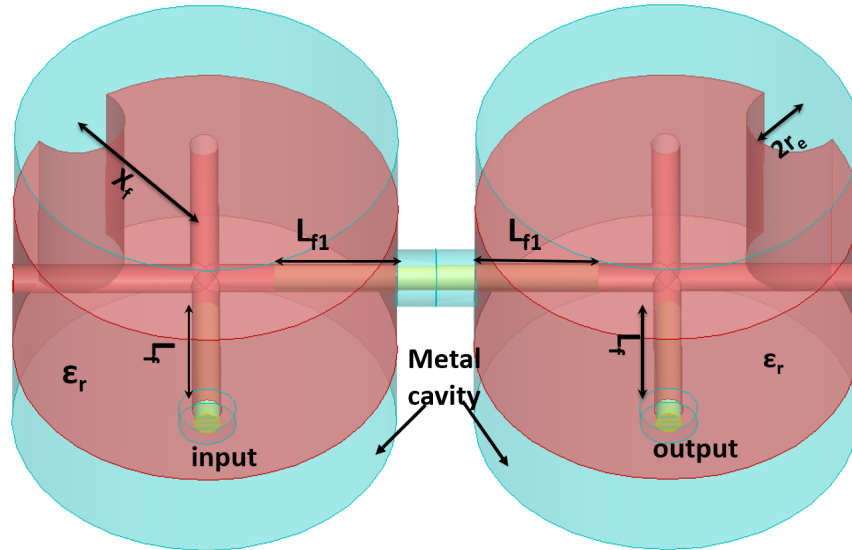


Figure 5.7: Configuration of 4th order filter dual-mode in HFSS.

was 7.4 mm; the internal coupling is shown in Figure 5.5. The dimension of the hole is 2.5 mm for the diameter and it was placed at 9.4 mm from the centre of the dielectric rod and the $M_{23}=36.4$ MHz with $L_{f1}=6.4$ mm. Figure 5.8 presents the S parameter response for the 4th order filter at the designed values. It can be observed that the bandwidth of the filter at -19 dB was equal to 54 MHz, and the worse case return loss was 14 dB. The insertion loss at the resonant frequency (1.961GHz) is less than 0.25 dB and the extracted unloaded Q factor was slightly more than 3900. It is clear that the losses are much smaller than the filter with the direct contact coupling technique, because the tangential E-field at the probe is smaller. The maximum out-of-band rejection in the upper side is about 42 dB, which occurred at 2.125 GHz. The wideband response of the filter is shown in Figure 5.9. It can be seen that the lower spurious mode is about 2.67 GHz, which agrees with the eigen-mode analysis. Additionally, a second-order filter response has appeared at the first spurious frequency, with a bandwidth about 110 MHz. It may be caused by the high coupling from I/O to the first spurious mode, which is the dual-mode $TE_{21\delta}$ type. The coupling to the $TM_{01\delta}$ mode seems to be very weak, as shown at the frequency 2.85 GHz. The overall free spurious-free window was about 600 MHz, if it was calculated from the 3 dB point of the first spurious band.

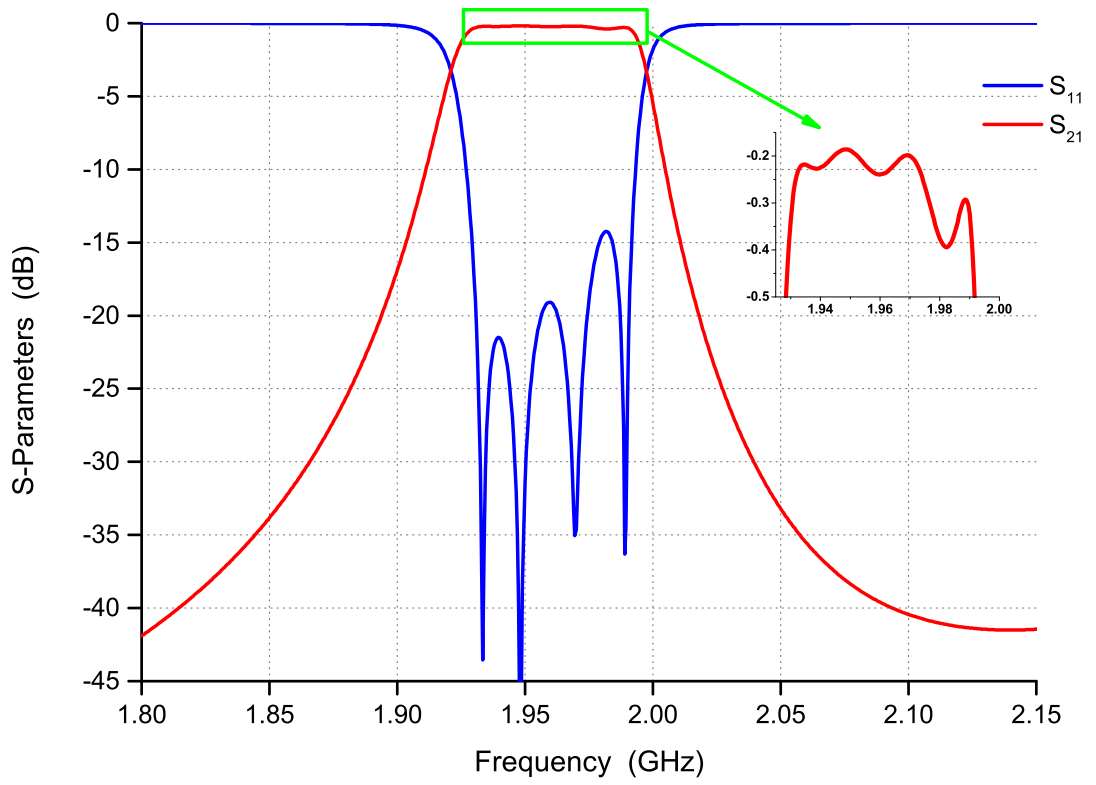


Figure 5.8: Simulated response of 4th order planar filter.

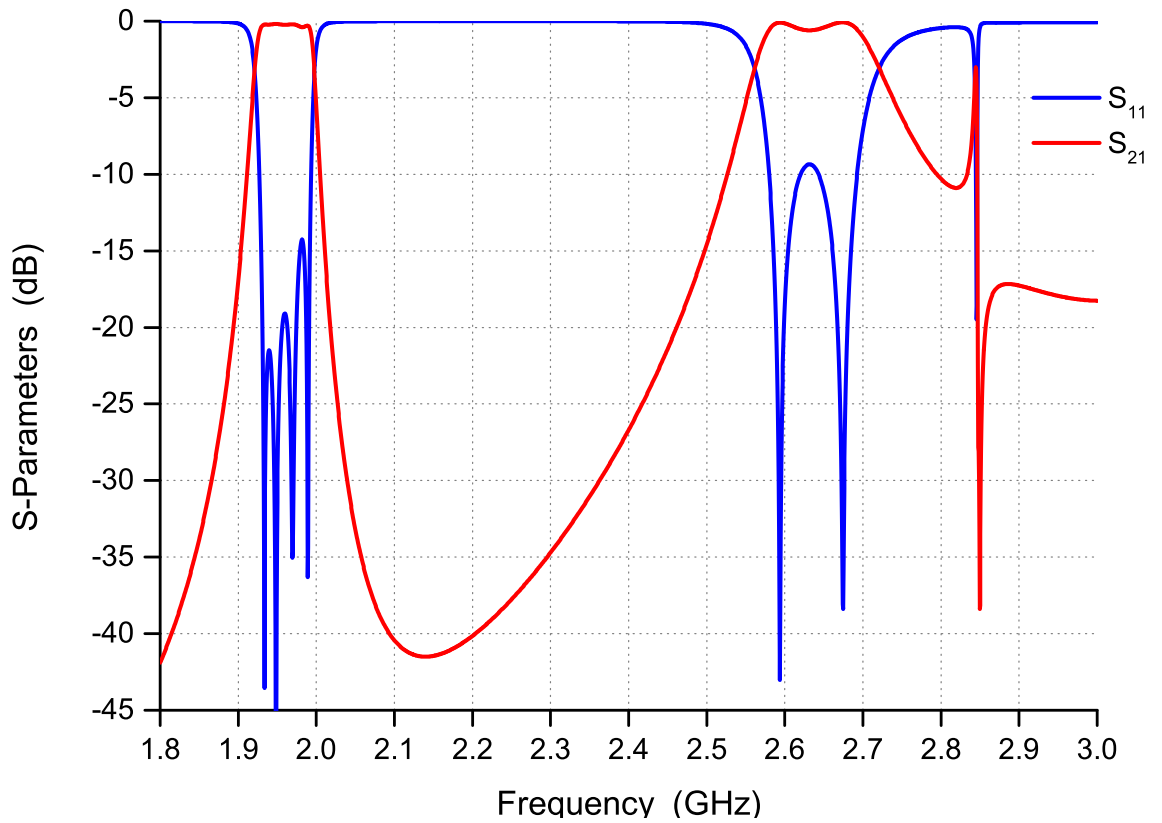


Figure 5.9: Simulated wideband response of 4th order planar filter.

5.4 Design of the Dual-Mode Filter Inline Configuration

Inter-cavity couplings by using the iris plate between the two cavities are commonly used in waveguide and coaxial filters. The 4th order dual-mode filter with iris plate was proposed as shown in Figure 5.10. It consisted of two pieces of ceramic puck

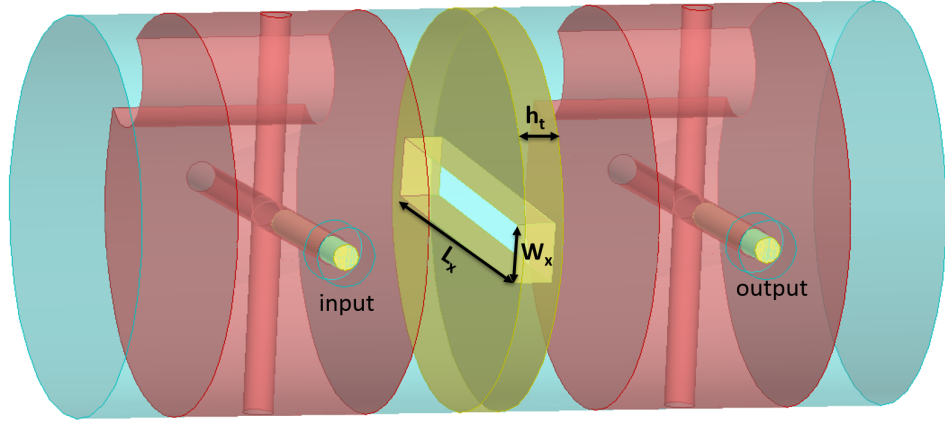


Figure 5.10: Inline configuration of 4th order filter dual-mode in HFSS .

with $\epsilon_r=43$ and $\tan \delta = 4 \times 10^{-5}$ placed in the middle and shorted by the side wall of the copper cavity $\sigma = 4 \times 10^7 S/m$. The hole through the ceramic was used for inter-resonator coupling. The iris plate was used for the inter-cavity coupling with thickness (h_t) of about 2 mm. The length L_x and width W_x of the iris controlled the coupling bandwidth between the two cavities. Figure 5.11 illustrates the coupling bandwidth against L_x with varying values of W_x . It is clear that a linear proportion relationship exists between the coupling bandwidth and the L_x either W_x . Also, the slope increased further with W_x which are 13, 19, 20 and 22 MHz/mm, when W_x changed from 1 mm to 4 mm. Furthermore, a good diversity of bandwidth can be achieved by using the iris technique, for example, as shown in Figure 5.11, from 8 MHz to 50 MHz. The specification of the filter is similar to the 4th order Chebyshev planar structure. In this case, $f_0=1.961$ GHz, Bw=52 MHz and $L_R=20$ dB. Additionally, the filter topology, coupling matrix, I/O coupling length and inter-resonator coupling are exactly the same as the previous case: the

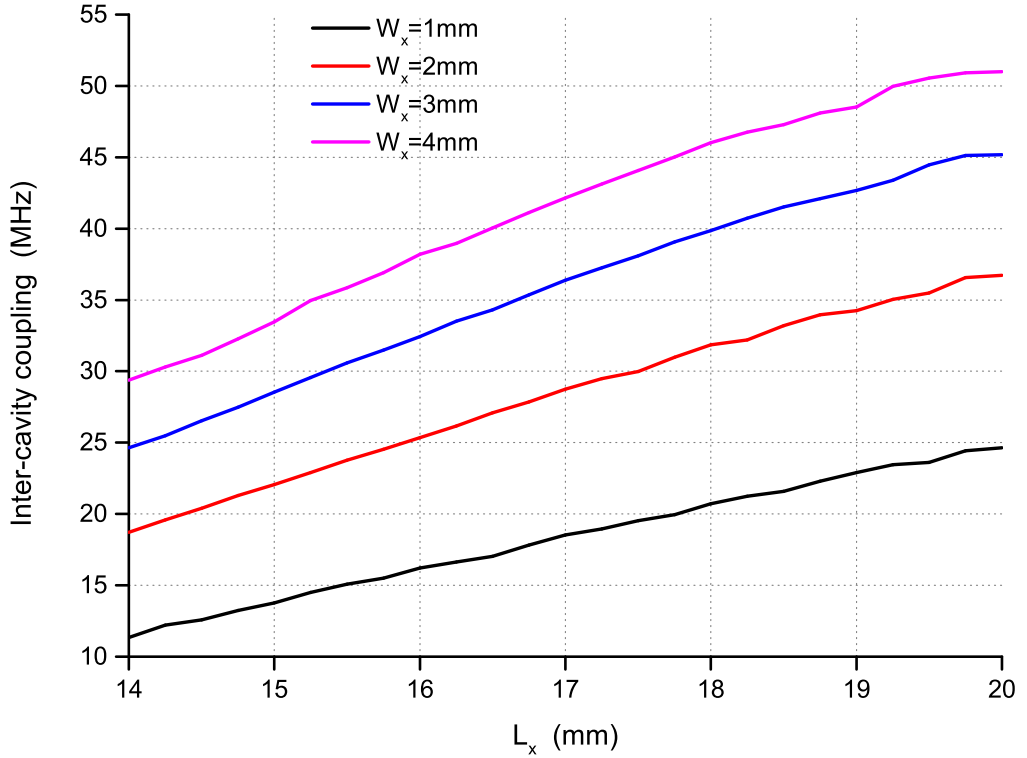


Figure 5.11: Coupling bandwidth for two cavities against L_x and W_x .

L_f , X_f and re are 7.4 mm, 2.5 mm and 9.4 mm respectively. $M_{23}=36.4$ MHz was realized from Figure 5.11, where L_x is 17 mm and W_x is 3 mm.

Figure 5.12 shows the S-parameter response for the 4th order Chebyshev inline filter. It can be seen that the maximum return loss was -15 dB in the lower side of f_0 , two peaks were on the upper side and under -25 dB, and the bandwidth of the filter at -19 dB was equal to 54 MHz. The insertion loss at the resonant frequency 1.961 GHz is about 0.2 dB and the extracted unloaded Q factor is about 3800. It is clear that the losses are slightly higher than in the filter with planar configuration; this may be caused by the tangential H-field crossing through the iris which has a thickness of 2 mm.

Figure 5.13 presents the wideband response of the 4th order Chebyshev dual-mode DR filter with iris structure coupling. It is observed that the maximum out-of-band rejection in the upper side is about 72 dB, which occurred at 2.4 GHz. The performance of the filter has a clean window of about 800 MHz under -40 dB. Moreover, the first spurious frequency at 2.67 has been suppressed because the

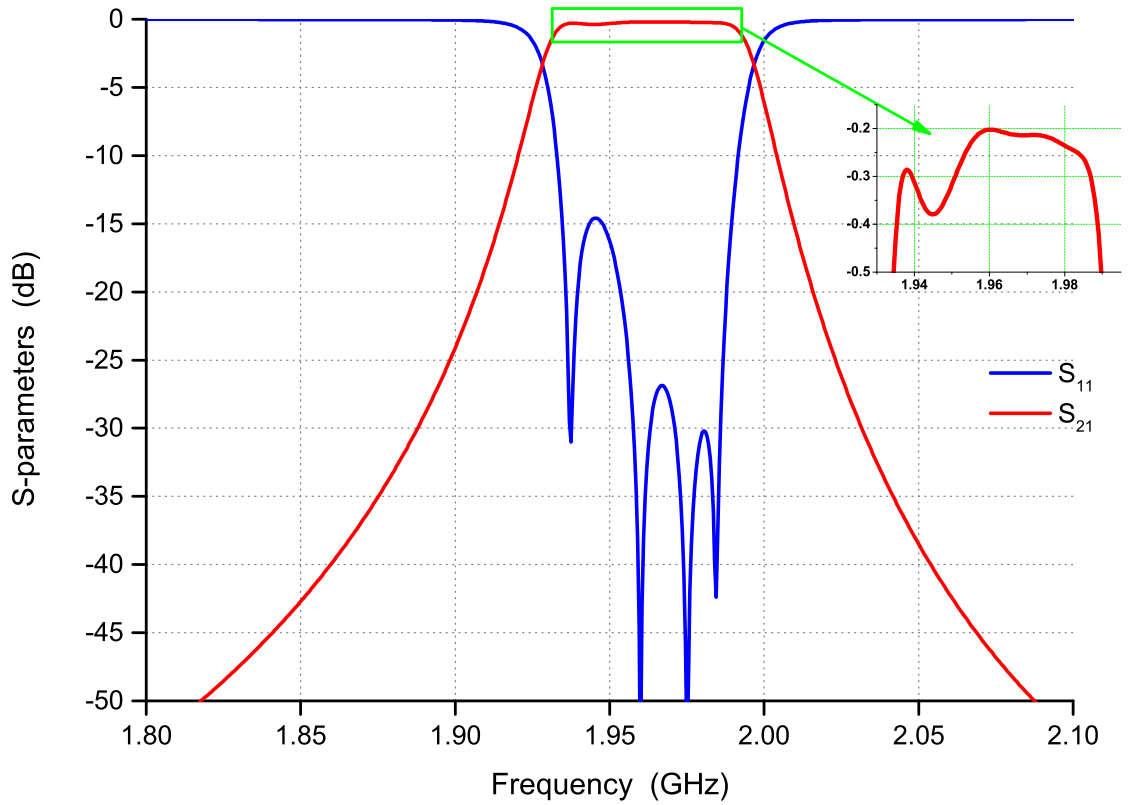


Figure 5.12: Simulated response of 4th order inline filter..

mode $TE_{21\delta}$ has a weak H-field in the middle of the iris and it is perpendicular to the direction of the iris in this structure. The third mode, $TM_{01\delta}$, is a weak coupling of about -8 dB with very narrow bandwidth at 2.83 GHz. This may be caused by the maximum E-field in the middle of the whole cavity and a decline in distance in the direction of the side wall, especially in the centre of the DR. Another reason could be because the probe length is short, not much energy coupling could be collected.

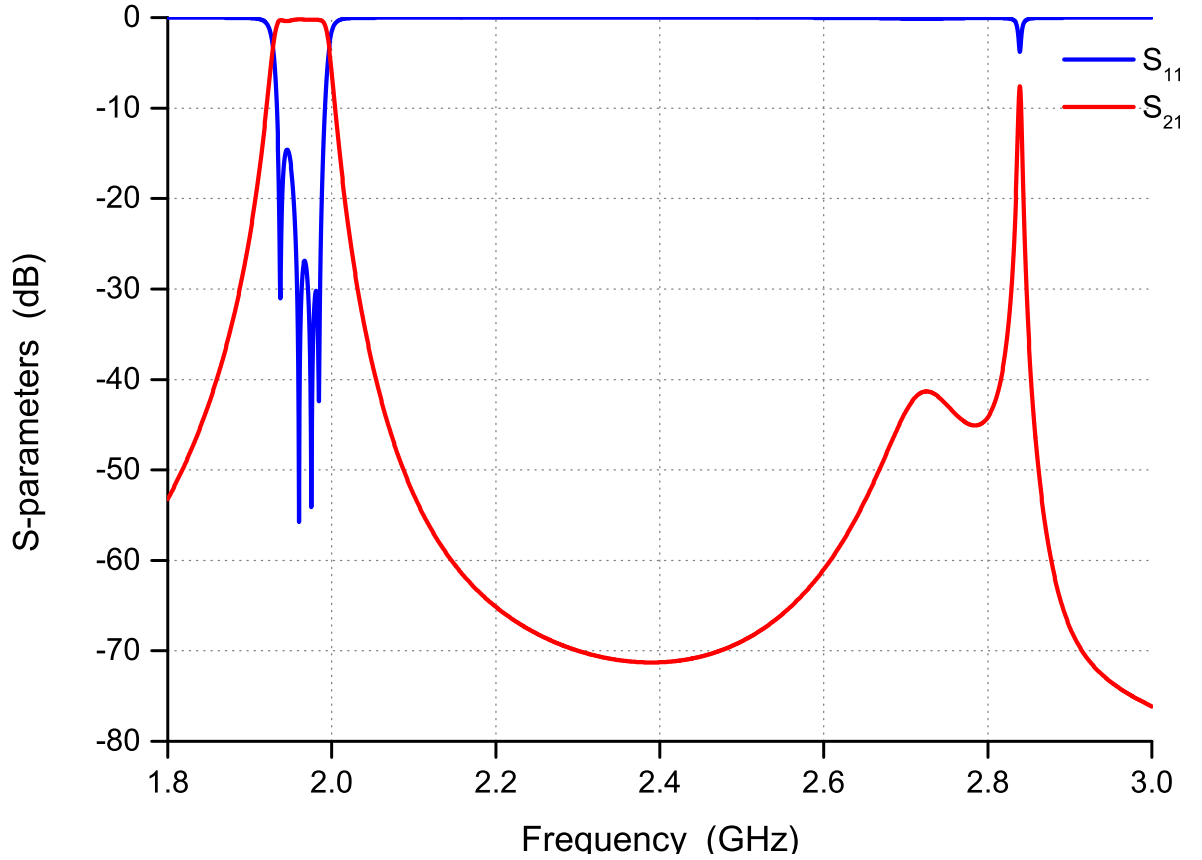


Figure 5.13: Simulated wideband response of 4th order inline filter.

5.5 Dual-Mode Loaded Cavity Filter with T-shape Coupling

The fundamental mode in the proposed cavity was $TE_{11\delta}$, the majority of the E-field was concentrated in the middle of the ceramic puck, while the maximum H-field was near to the sidewall of the metal cavity. Cutting the ceramic is an important way to improve the coupling technique.

Figure 5.14 shows the configuration of the dual-mode DR with a cross section of the dielectric structure. The resonator consists of a thick ceramic disc with a high dielectric constant suspended in the middle of a cylindrical metallic cavity and short-circuited along the side wall. D and L are the diameter and length of the DR respectively, while L_a is the vertical size of the air gap above and below the rod. The vertically-etched slots and holes through the dielectric puck are implemented with dimensions r_0 , d_x and d_y to improve the Q factor and make a

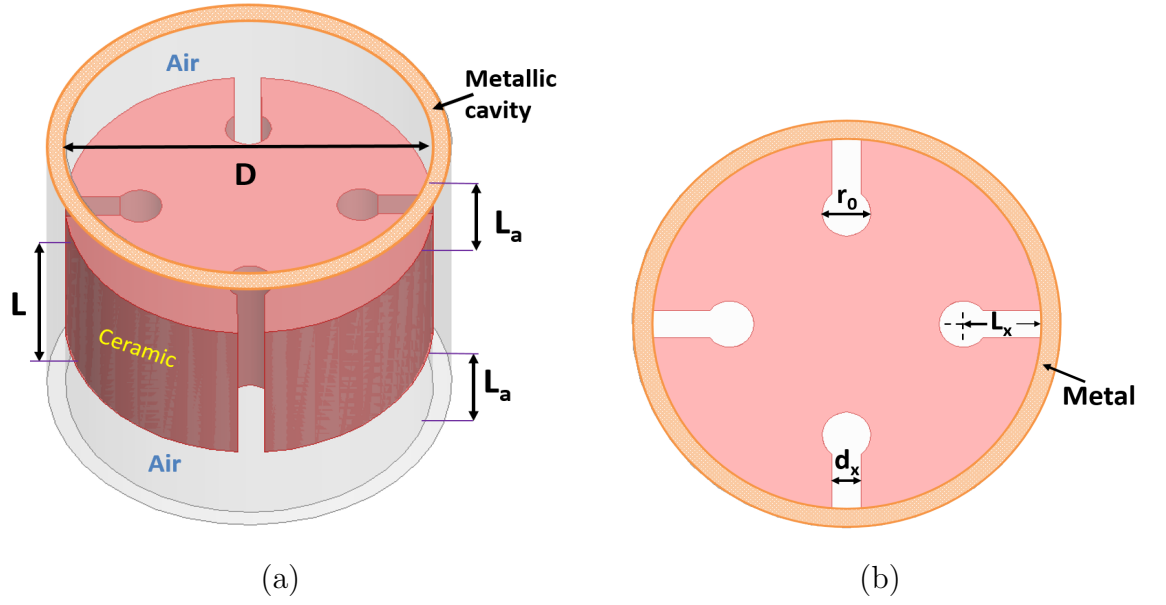


Figure 5.14: Configuration of dual-mode dielectric resonator (a) 3D-View and (b) Top view.

good space for effective I/O coupling. The ceramic material used in this work is barium titanate with a relative permittivity of 43 and loss tangent of 4×10^{-5} . The metal cylindrical cavity is made from copper with conductivity 4×10^7 S/m. In order to choose the optimum dimensions, HFSS software was used to calculate the resonance frequency and unloaded Q factors for DR. The optimum dimensions were $D=20$ mm and $L=10$ mm. The notching dimensions r_0 and d_x have been chosen to be 1.25 mm and 1.48 respectively. Figure 5.15 illustrates the variation of the resonant frequency and the Q_u of the first three modes against length of notch L_x . From the plot, the resonant frequencies for TE modes have gradually increased with L_x while the Q_u of the TM mode decreased. Choosing L_x equal to 4 mm provides a good trade-off between the spurious-free frequency and Q_u because the spurious-free window slightly changed after this dimension. Table 5.1 illustrates the figure-of-merit comparison between unpatterned (UNP) and vertically-etched (V-E) DRs based on the simulated resonant frequency(f_r), unloaded Q-factor (Q_u) and the type of mode for the first three modes. From the table, the $TE_{21\delta}$ is in single-mode while it was dual-mode in the UNP dielectric puck design caused by the 4 V-E and holes in the design structure which improve the spurious-free window when two or more cavity filters are used. The overall spurious suppression is 880

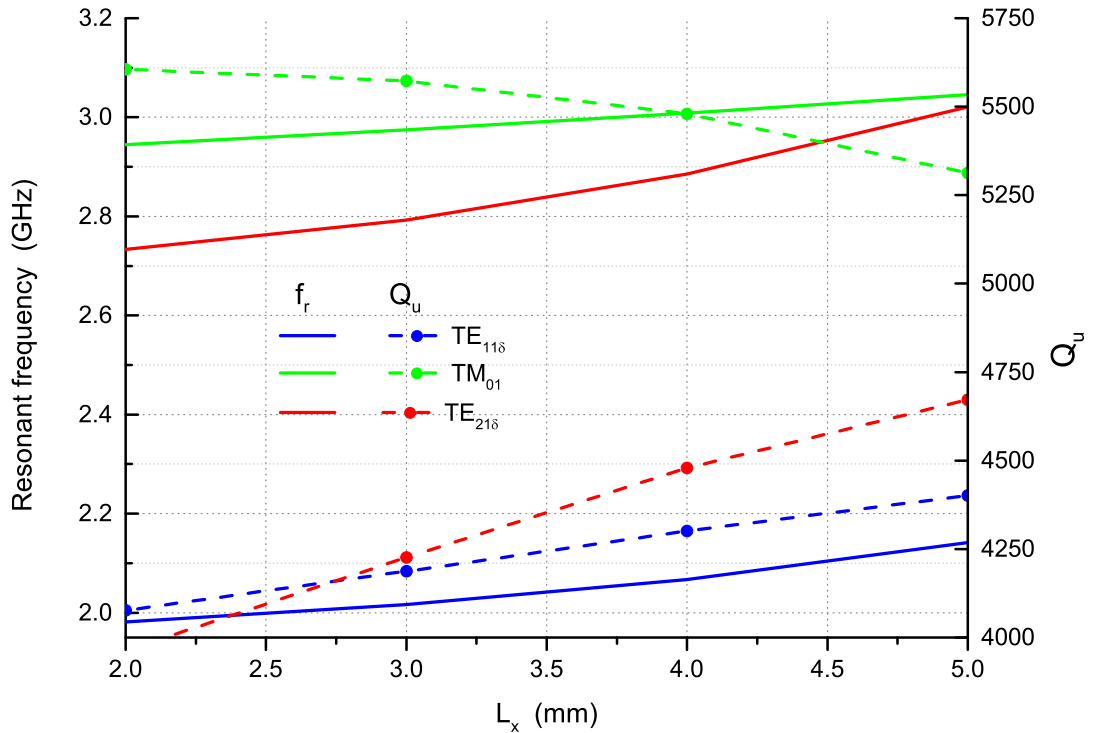


Figure 5.15: Resonance frequencies and Q_u with varying radius of hole (L_x).

MHz from the fundamental frequency, achieving a larger spurious-free window and Q -factor compared to the UNP DR. The electric and magnetic field patterns of the $TE_{11\delta}$ mode at 2.066 GHz are shown in Figure 5.16. It is clear that high E-field concentration around the vertically etched holes and slots can be used for efficient I/O coupling and the section $A - A'$ in Figure 5.16a shows the direction of E-field is cutting vertical holes while maintaining constant concentration in the middle. However, the behaviour of the H-field pattern is similar in both the top view and the $A - A'$ section as illustrated in 5.16, when it is compared to the UNP DR design.

Table 5.1: Comparison of simulated resonance frequency, mode type and Q_u for the cavity resonator with unpatterned and vertically-etched structures

Mode	f_r (GHz)		Q_u -factor		Type	
	V-E	UNP	V-E	UNP	V-E	UNP
$TE_{11\delta}$	2.066	1.92	4300	3800	Dual	Dual
$TE_{21\delta}$	2.885	2.69	4480	3500	Dual	Single
TM_{01}	3	2.85	5480	5000	Single	Single

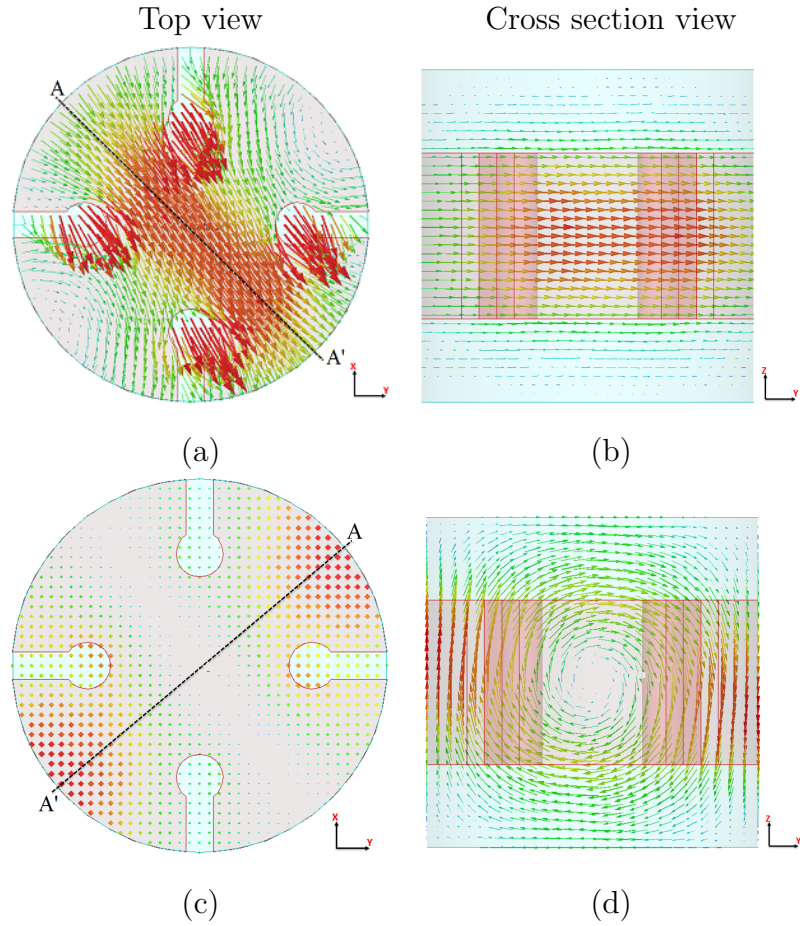


Figure 5.16: Field patterns (a) and (b) Electric field, (c) and (d) Magnetic field.

5.6 Filter Design with T-shaped I/O Coupling

As mentioned in section 5.3, to design filter we need to know the coupling value for external, internal and the inter-cavity. The next section will discuss the methods and the shape required to achieve the filter specification to be implemented.

5.6.1 External Q factor

A T-shaped probe is employed to provide the efficient EM-signal coupling for the input and output ports, as depicted in Figure 5.17. The probe length L_m was used to control the EM coupling by varying the diameter of the probe. A diameter of 2 mm has been chosen to obtain a proper gap between the side of the DR and the probe to avoid over-coupling when there is a direct contact between them. The

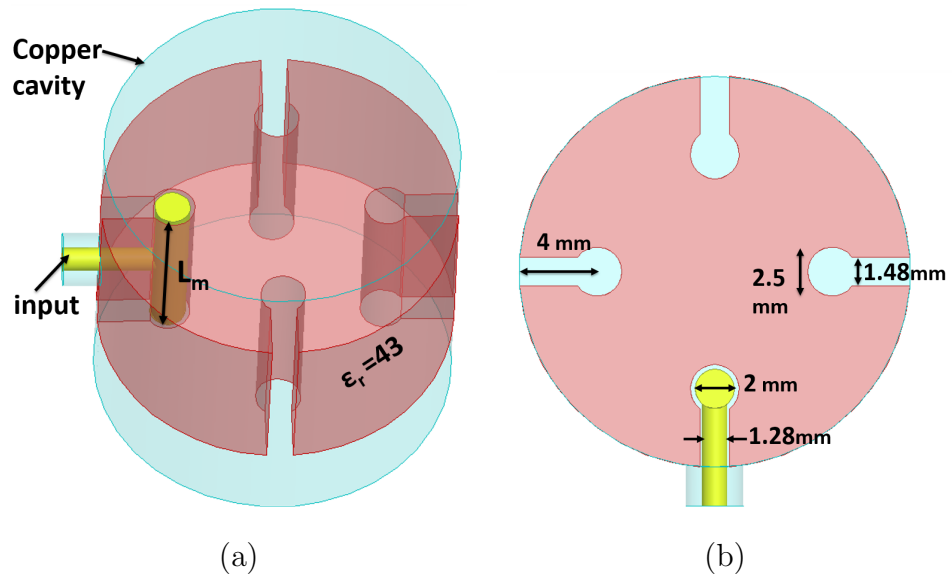


Figure 5.17: Configuration of input/output coupling in HFSS (a) 3D view and (b) Top view.

group delay method is used to calculate Q_e . Figure 5.18 illustrates the Q_e for various length of L_m . From the graph, an inversely proportional relationship is discovered between the external coupling and the probe lengths.

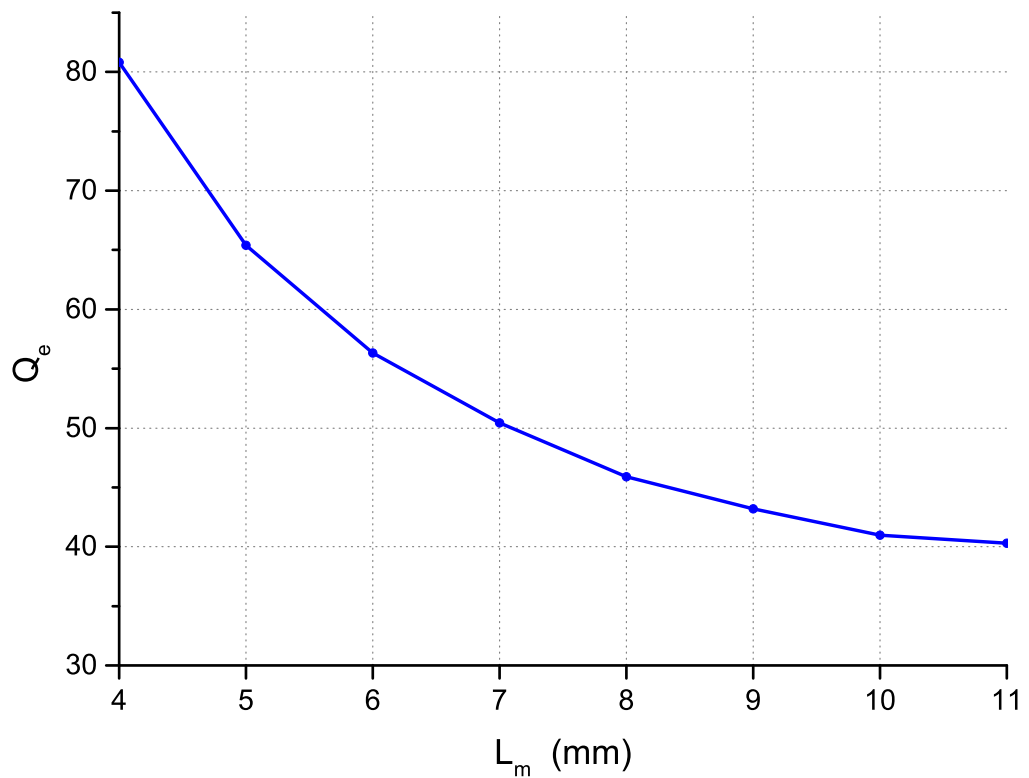


Figure 5.18: The external quality factor (Q_e) against L_m .

5.6.2 Inter-Resonator Coupling

A vertically etched hole at 45° w.r.t degenerate modes is employed to achieve efficient EM inter-resonator mechanism coupling. Eigen-mode simulation has been used to determine and synthesize the inter-resonator coupling in the DR cavity. Figure 5.19 shows the coupling bandwidth against distance between the centre of the DR and the coupling hole (X_f) with variations in the vertically-etched hole radius (r_e). From the plot, there are two distinct and contradictory regions of behaviour in the graph converging at $X_f=5$ mm . The coupling bandwidths increase significantly as X_f increases in region one ($X_f < 5\text{mm}$) but gradually decrease in area two. Furthermore, a maximum coupling bandwidth occurs at X_f is 5 mm, which is caused by a maximum E-field close to the I/O coupling etched holes.

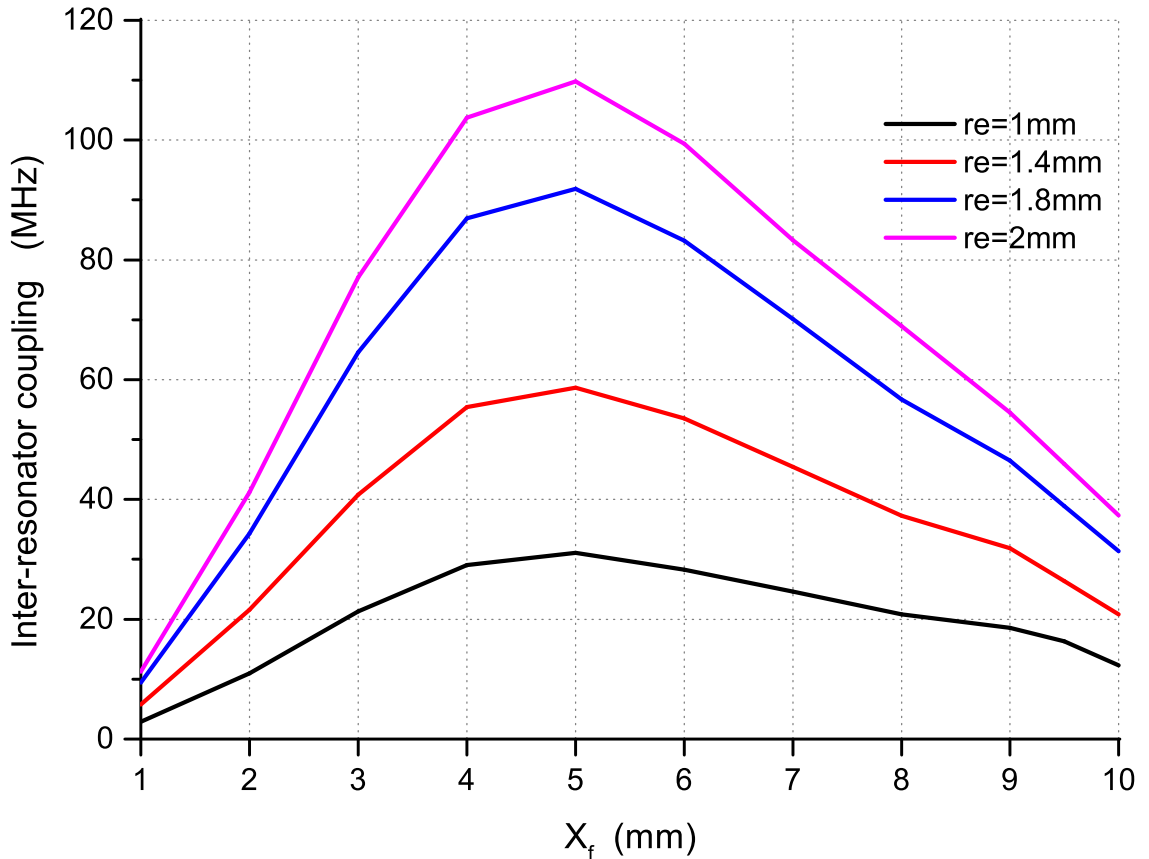


Figure 5.19: Inter-resonator coupling bandwidth against X_f .

5.6.3 Inter-Cavity Coupling

Figure 5.20 presents the configuration of the inter-cavity coupling. This was achieved by changing the length of probe L_n to obtain the specific value of the coupling. In order to connect the two cavities, the probe was placed in a rectan-

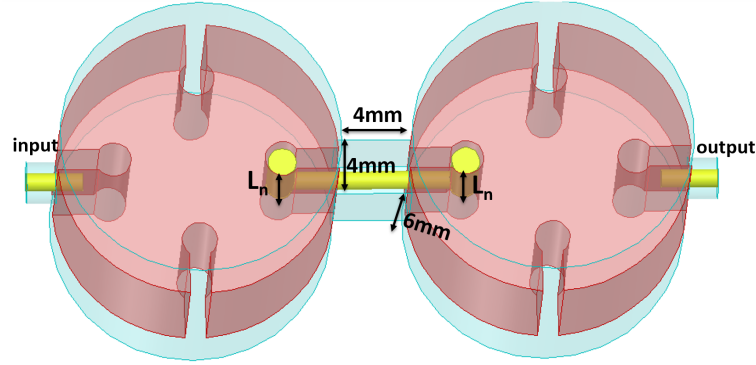


Figure 5.20: Configuration of inter-cavity coupling in HFSS.

gular air-filled cavity with dimensions of $4mm \times 4mm \times 6mm$. Figure 5.21 shows the inter-cavity coupling bandwidth against L_n . From the plot, L_n has a strong effect on the coupling bandwidth and it is a linearly proportional relationship. A positive slope of 10 MHz/mm is observed.

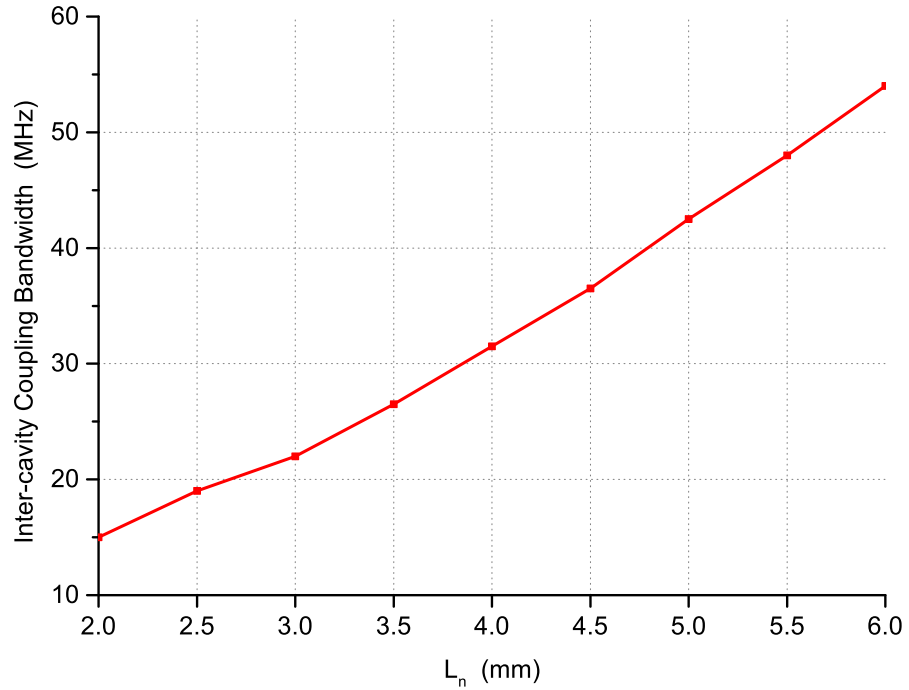


Figure 5.21: Inter-cavity coupling bandwidth against L_n .

5.6.4 Filter Design with T-shaped Probe

Following the above coupling calculations, the filter is designed and fabricated. Figure 5.22 displays the physical configuration of the dual-mode 4th order filter with T shape coupling. The metallic cavity and all the probes were fabricated from copper with conductivity about $4 \times 10^7 S/m$. The two ceramic pieces with $\epsilon_r=43$ and $\tan \delta = 4 \times 10^{-5}$ were placed in the middle of the copper cavity and short-circuited along the side wall. The coaxial probe L_m was used for I/O coupling and L_n control the inter-cavity coupling. The vertically-etched hole through the DR was used to introduce the inter-resonator coupling and was fabricated out of copper metal. A fourth-order Chebyshev dual-mode filter was designed at cen-

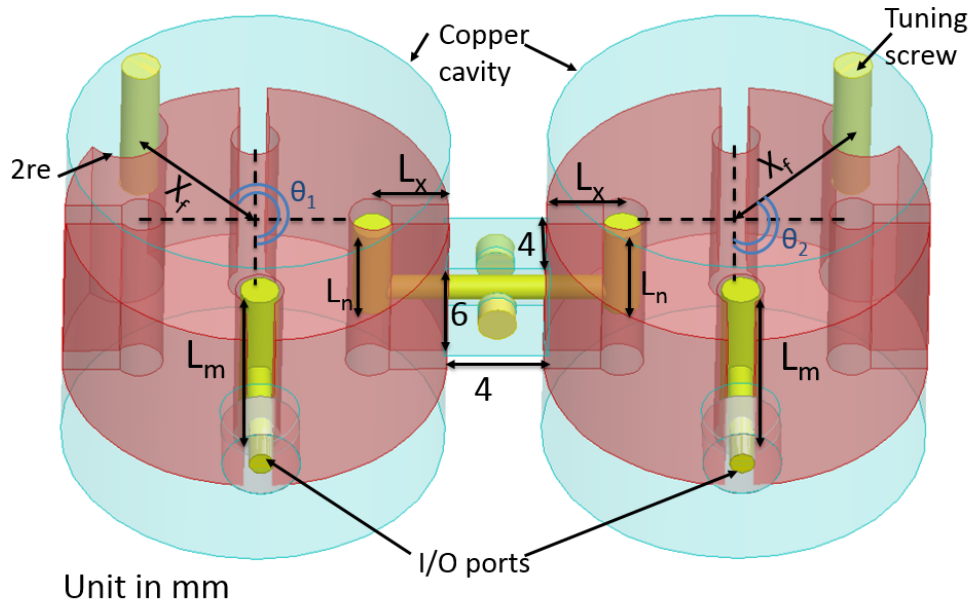


Figure 5.22: T shape coupling configuration of 4th order filter dual-mode in HFSS.

tre frequency of 2.08 GHz, with operational bandwidth of 66 MHz and return loss (RL) of better than 20 dB. The normalized coupling matrix (M) was generated as mentioned in Chapter 4. The input and output external quality factors and coupling coefficients were computed for fractional bandwidth (FBW)=2.173% , and found to be $M_{12}=M_{34}= 60.1$ MHz, and $Q_e=30$. From Figure 5.18, the length of the L_m probe required to obtain the exact external quality factor is 10 mm, where the

internal coupling is depicted in Figure 5.19. The diameter of the vertically etched hole is 4.4 mm and it is located at 9.5 mm from the centre of the dielectric puck, and the $M_{23}=46.2$ MHz, L_n is 5.2 mm. The orientations of the inter-resonator coupling holes were $\theta_1 = 225^\circ$ and $\theta_2 = 135^\circ$, as shown in Figure 5.22.

Figure 5.23 shows the simulated S parameter response for the 4th-order T-shape coupling filter. From the plot, the bandwidth of the filter measured at RL=14 dB was equal to 66.5 MHz. The insertion (IL) loss at the operational frequency 2.08 GHz is less than 0.375 dB and the extracted unloaded Q factor is more than 3700 with losses in the Q_u of approximately 500. The maximum out-of-band rejection in the upper side is approximately 47 dB which is found at 2.239 GHz.

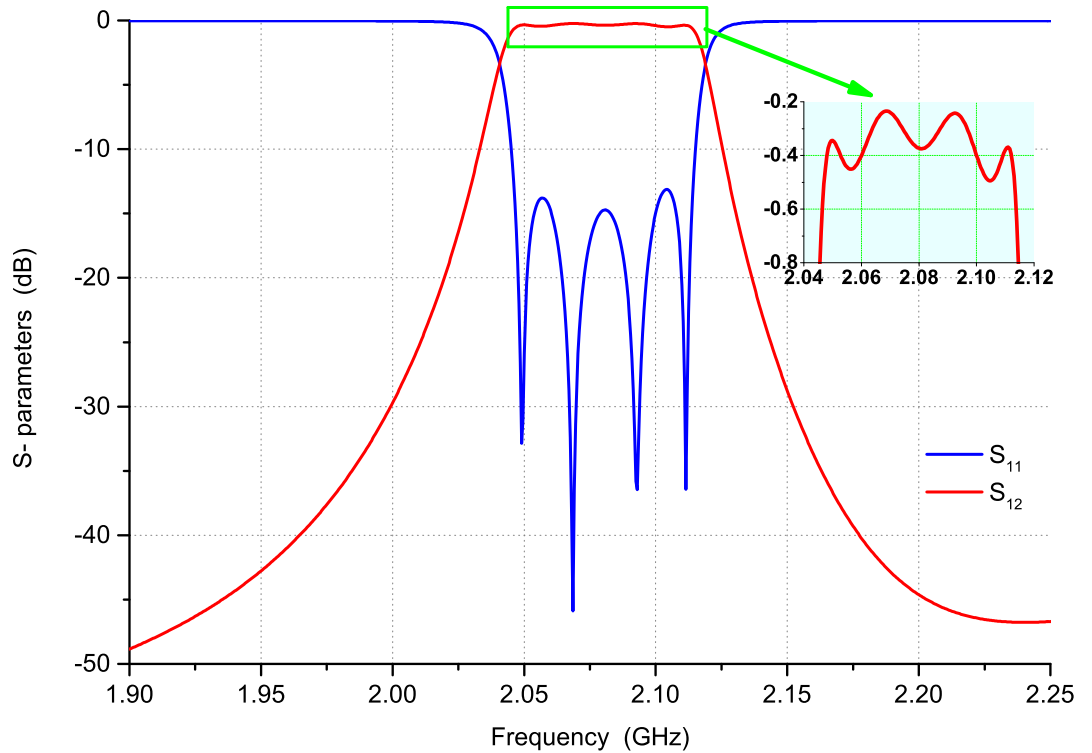


Figure 5.23: Simulated response of 4th order T-shape coupling filter.

Figure 5.24 shows the spurious response of the T- shaped coupling filter. The first spurious mode is at approximately 2.8 GHz and in a good agreement with the eigen-mode analysis. Furthermore, the third spurious mode is at 3 GHz. The overall spurious-free window is at approximately 720 MHz, which is a superior suppression compared with the conventional dual-mode DR filter.

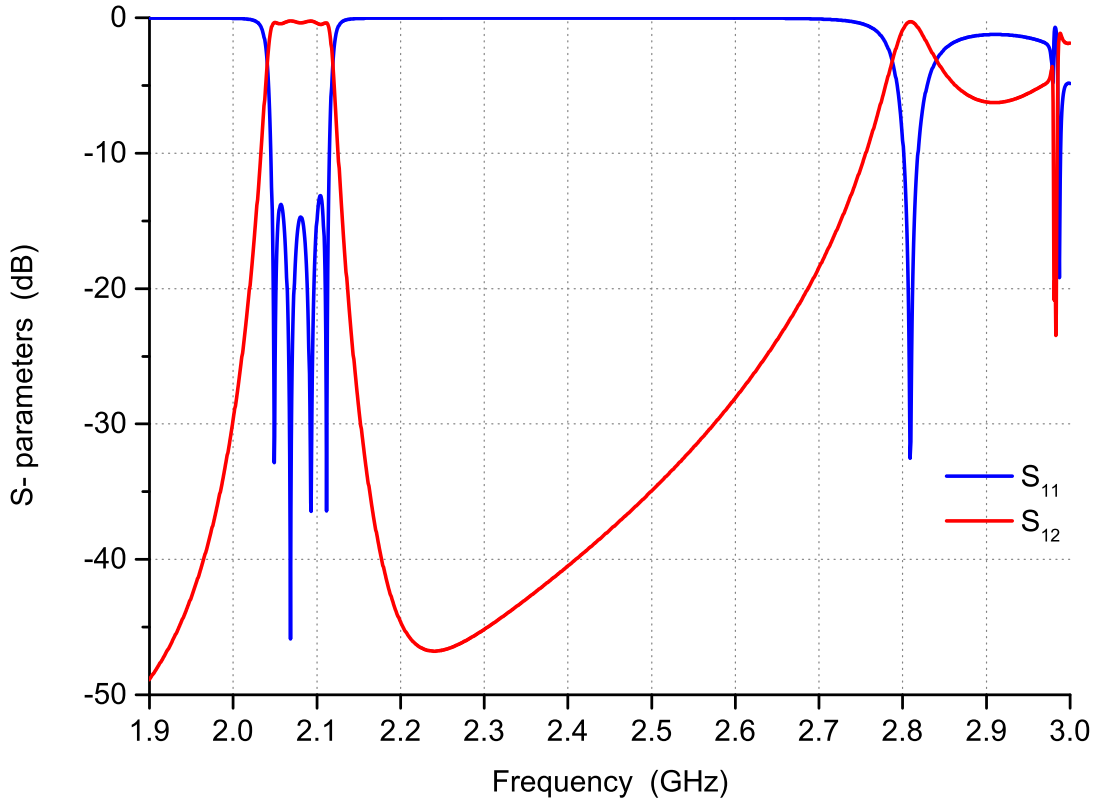


Figure 5.24: Simulated wideband response of 4th order T-shape coupling filter.

5.7 Experimental Results

Figure 5.25 provides a photograph illustrating the fabrication of the 4th-order T-shaped coupling filter. The dimensions of the rectangular filter are $56\text{mm} \times 28\text{mm} \times 25\text{mm}$, while the other cavity dimensions and the properties of the material are exactly the same as mentioned in section 5.6.4. Six tuning screws of 2 mm in diameter were positioned on the top lid of the cavity to fine-tune the coupling coefficients and all probes were fabricated out of copper. The probes were covered by plastic foil to avoid over-coupling when the probe touches the DR. S-parameter measurement is achieved by using an Agilent E5071C Network Analyzer. Two-port calibration is performed by using the Agilent N4431-60006 Electronic Calibration Module prior to the measurement. Figure 5.26 shows the measured results of the filter at the inband response. From the measurements, the insertion loss is approximately 0.42 dB at the operational frequency of 2.18 GHz with the operational bandwidth of 77 MHz at the RL=15 dB. The extracted

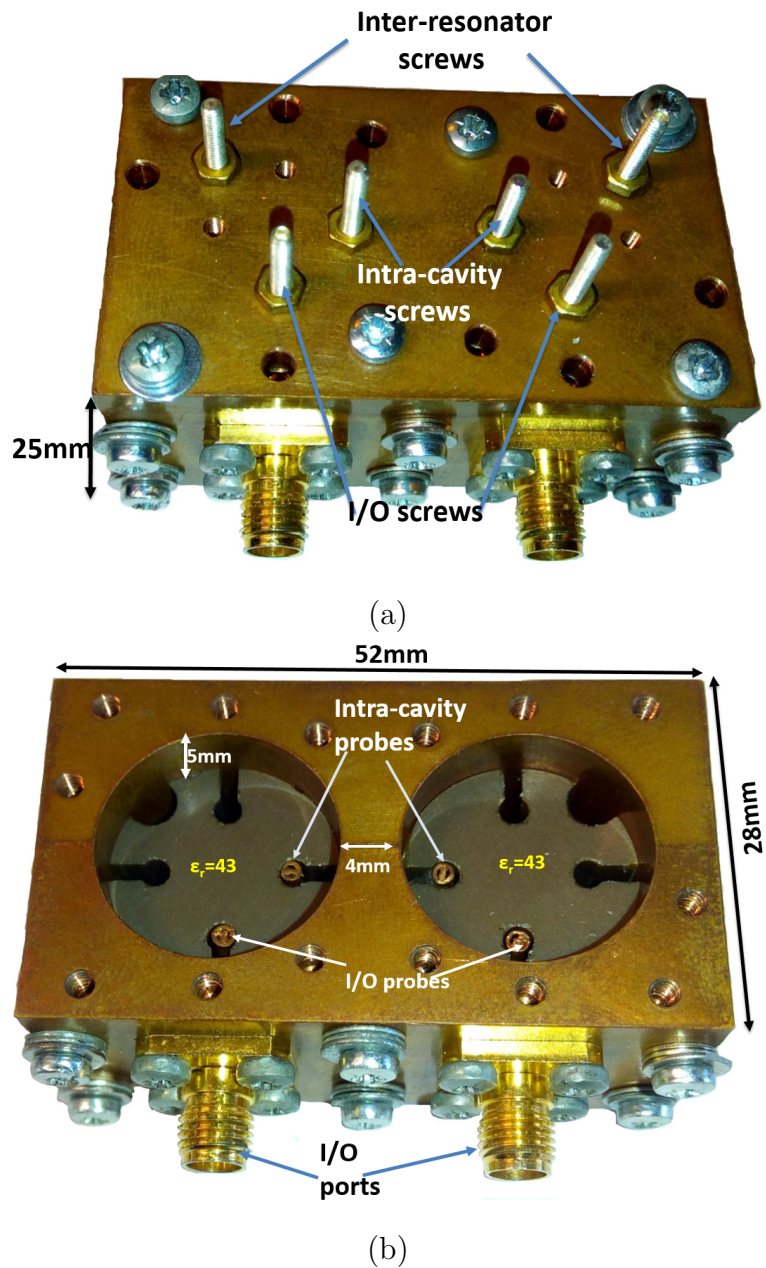


Figure 5.25: Fabricated of 4th -order T-shaped coupling dual-mode bandpass filter (a) with top lid, (b) without lid.

Q_u from the response, based on the measurement results, is approximately 2200. There were frequency shifts of 100 MHz and 11 MHz in the operational frequency and bandwidth, respectively, compared with the simulation results. The frequency shifts are caused by the gap between the ceramic and the wall of the copper cavity due to the tolerance of the fabrication. Moreover, the bandwidth shifting is caused because of the tolerance of the fabrication in X_f and r_e for the vertically etched hole for the inter-resonator coupling. There are many reasons for the loss in the fabricated filter prototype. Firstly, the non-uniform gap between the ceramic and

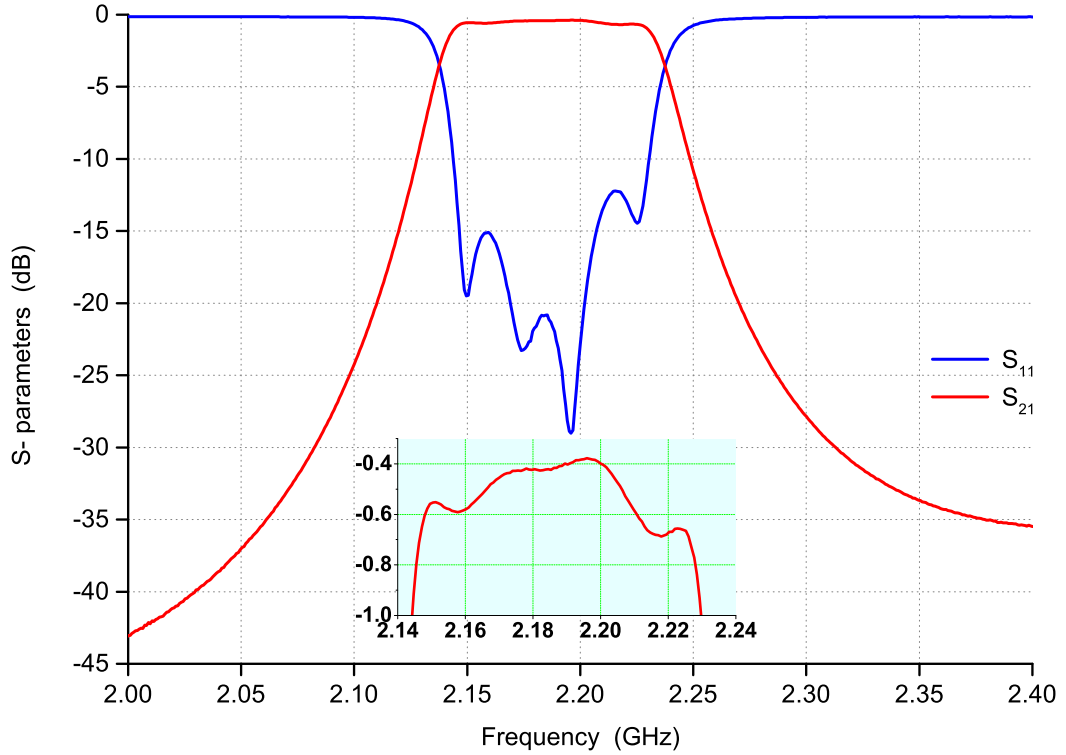


Figure 5.26: Measured response of the 4th order T-shaped coupling filter.

the cavity wall. Secondly, the plastic foil that has been used to insulate the probes to avoid contact with the DR.

Figure 5.27 presents the spurious response of the T-shaped 4th-order filter for the measured results. From the plot, the spurious signal occurs at 3 GHz. The TE_{216} shifted up to about 150 MHz and the overall spurious-free window remained at 820 MHz.

Figure 5.28 shows the S-parameter for the T-shaped 4th-order when the ceramic is covered and not covered by aluminium foil. From the plot, the resonance frequency shifted down to 50 MHz compared with the uncovered ceramic while the Bw remained the same. The IL at the resonance frequency was -2.8 dB, which means, the losses are larger than in the first case. The losses increased because of the non-smooth layer between the ceramic and the cavity wall, which may create an air gap.

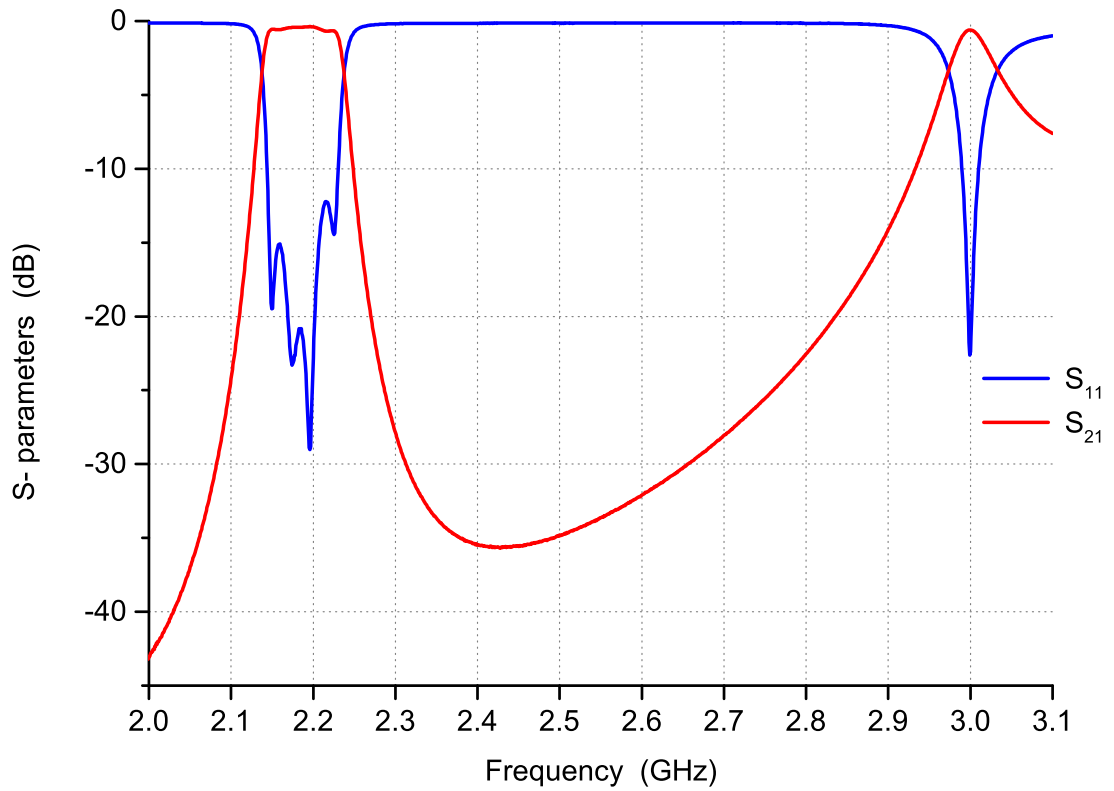


Figure 5.27: Wideband response of the measured 4th order T-shaped coupling filter.

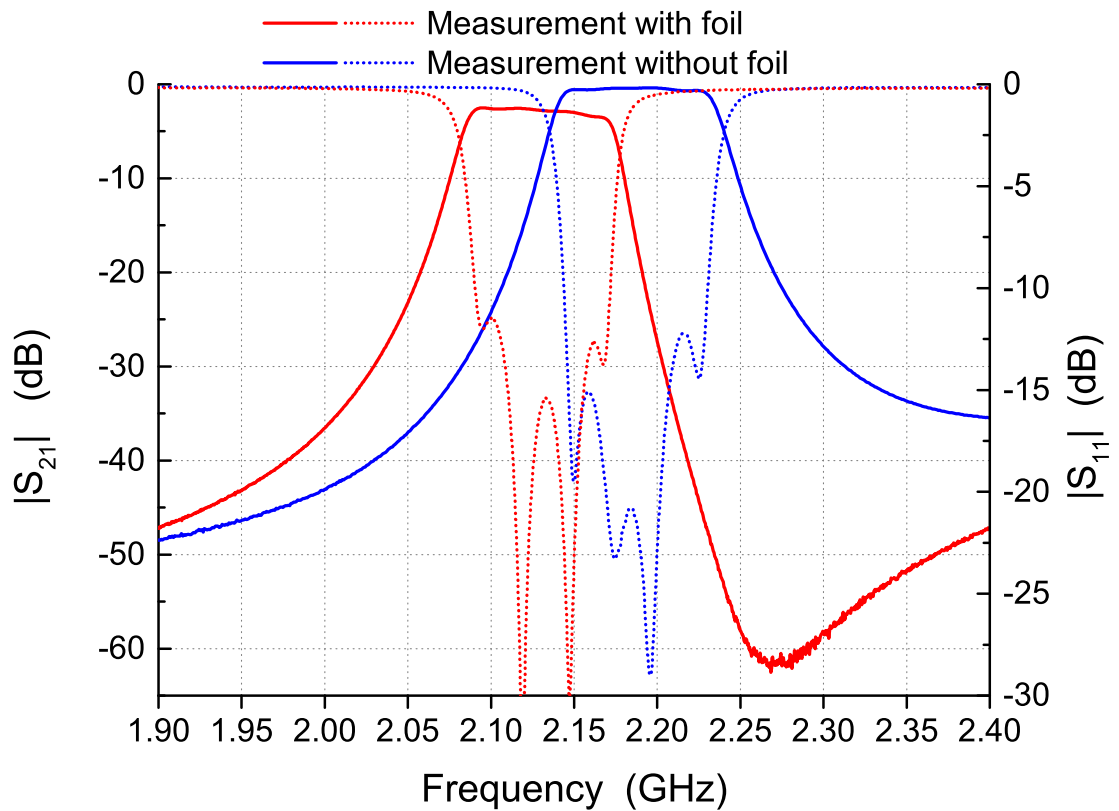


Figure 5.28: Comparison of wideband response of measured T-shaped coupling filter

5.8 Summary

Cutting holes through the ceramic in the middle of the cylindrical face does not affect the sequence of the modes in the DR and the fundamental mode is $TE_{11\delta}$. The inter-resonator coupling was achieved by cutting a hole in the ceramic puck at 45° with respect to modes. Two 4th order Chebyshev dual-mode filters were designed by using the planar and inline structures. The I/O coupling was implemented by a probe connected with a 50 Ω SMA connector. The planar configuration filter result provides a high Q-factor and good spurious-free window of 600 MHz and the inter-cavity coupling was achieved by a probe connected between the two cavities. The inline structure shows a high suppression isolation which was 800 MHz under -40 dB and the iris was used for inter-cavity coupling. T-shaped coupling filter with the ceramic puck cut from the top to the bottom was simulated and fabricated. The practical result shows an upward shift in the resonant frequency because of the small gap between the metallic cavity and the ceramic.

Chapter 6

HE_{11} Dual-Mode DR Filters

6.1 Introduction

The miniaturisation of filters is essential for the application of 4G because the MIMO systems applied in these technology. Dielectric resonators are one of the ways to reduce filter volume and keep the electrical performance the same. Generally, there are two main practical issues a with dual-mode filter shorted to the side wall of the cavity: (1) it is very hard to achieve a perfect contact between the puck and the metal,(2) the length of the probe significantly affects the response of the filter. Dual-mode dielectric resonator (DR) loaded filters, operating in the HE_{11} mode, are attracting attention due to the lower loss, smaller volume, relative ease of fabrication, and an elliptical function response that can be realized when using them. This chapter will discuss a new HE_{11} dual-mode bandpass filter which offers the optimum volume and a highly miniaturisation ratio compared with those in the previous literature. The DR structure is composed of a dielectric puck placed in the middle of a metallic cavity and shorted by the bottom side. The fundamental resonance for the dual-degenerate mode is HE_{11} . HFSS software has been used to calculate the resonant frequencies, Q-factor and the performance of the filter. Parametric study has been applied to choose the optimum dimensions of the resonator. Moreover, fourth degree Chebyshev filters were designed with a current

loop probe for the input and output coupling. An etching hole from the DR which is located at 45° with respect to the modes is employed for the inter-resonator coupling.

6.2 Configuration of the Proposed Resonator

Mode charts are important in the design of microwave bandpass filters, especially in the prerequisite stage design which features the behaviour of the resonant frequency in the proposed DR configuration. A suspension of the dielectric disc in a metallic cavity is very common in DR filters, but the fundamental mode in such a structure is $TE_{01\delta}$. Figure 6.1 provides a diagram of a DR suspended in the middle of the perfect conductor cavity. The dimensions of the perfect conductor cavity are

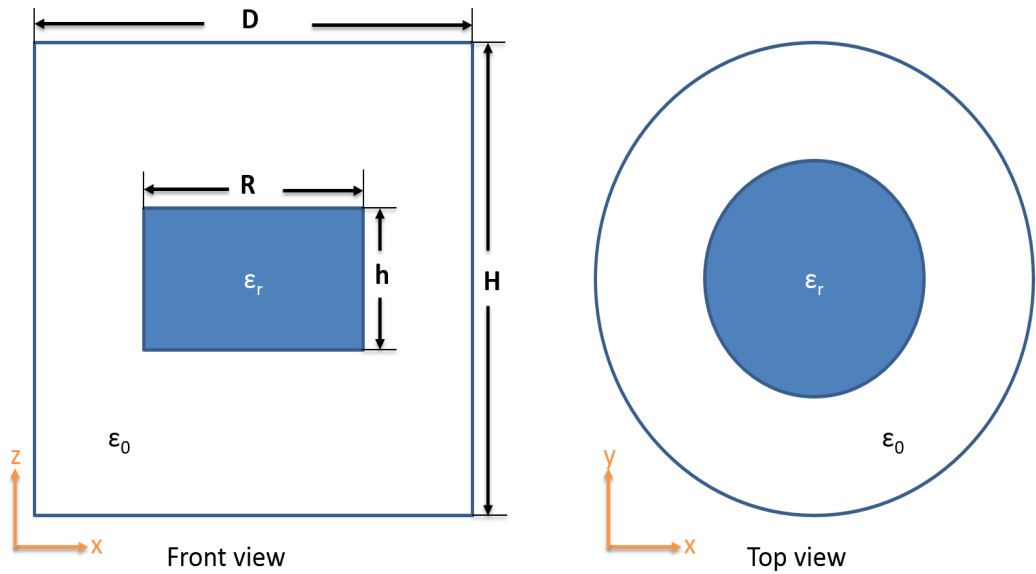


Figure 6.1: Diagram of DR in conducting cavity.

40 mm for the height H and the diameter D , while the relative permittivity of the puck is 43. An eigenmode solver was used to calculate the resonant frequency for different mode types by varying the spacing between the top face of the dielectric puck and the metallic cavity, as shown in Figure 6.2. In the range $H/h < 1.2$, the fundamental mode is TM_{01} but it is rapidly increased with the decrease in the height of the dielectric puck and HE_{11} becomes the fundamental mode until the ratio is equal to two. At this stage, the $TE_{01\delta}$ became the fundamental mode for

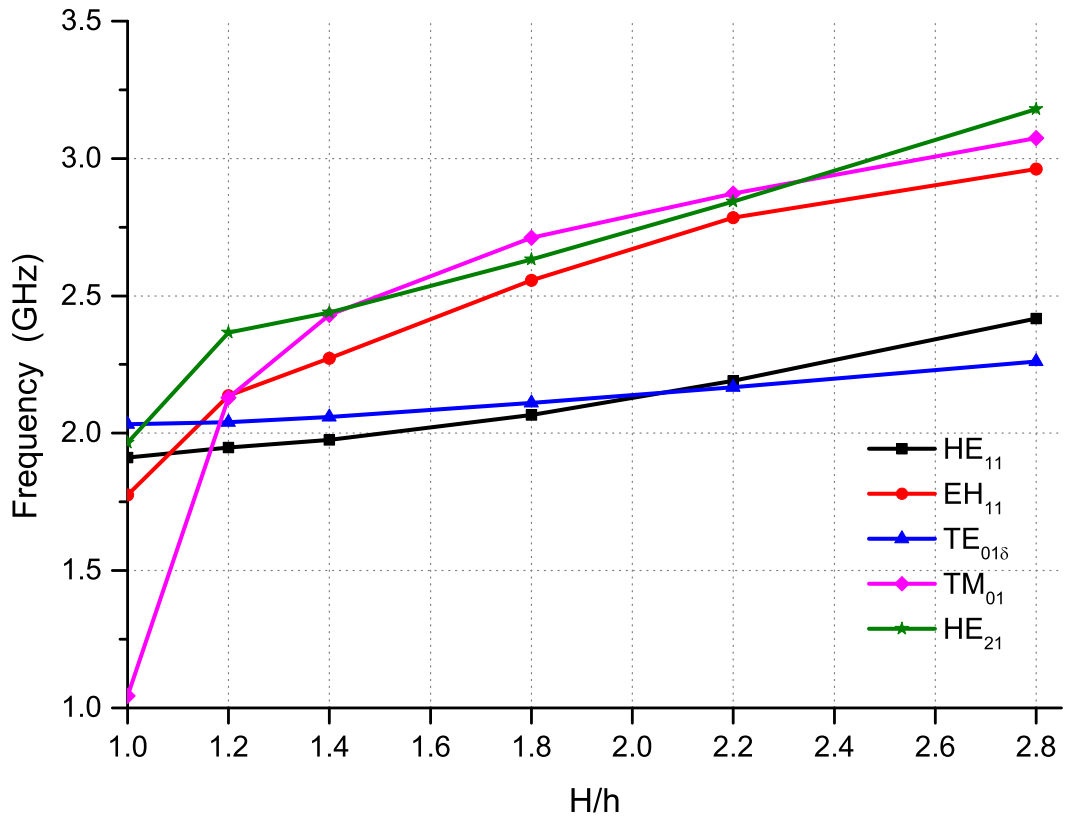


Figure 6.2: Mode chart against of H/h with frequency.

$H/h > 2$. The spurious-free window at this range is very poor and could not be used in microwave application. A way to force the HE_{11} to be in first mode is by shorting the dielectric puck from the bottom, as shown in Figure 6.3. It can be seen that the fundamental mode is HE_{11} for $H/h > 1.3$, which is slightly increased with H/h ratio. Moreover, the second mode $TE_{01\delta}$ rises gradually.

From the mode chart in Figure 6.3, HE_{11} becomes the fundamental frequency with a good spurious-free window. This is due to contact made between the ceramic and either the top or bottom face of the cavity. However, the resonator is large in size and needs optimization to achieve a small size and high Q-factor. By varying all the dimensions of the DR to obtain a dual-mode, it should operate at 2 GHz with the HE_{11} mode. Table 6.1 illustrates Q_u , the spurious-free window and the volume of the resonator. It is clear that the variation of Q_u was between 5500 and 6100 and the volume in cm^3 was in the range of 18-28 while the spurious-free window was about 300-455 MHz. In order to obtain the optimum resonator, the resonator specifications should provide a high value for Q_u and a spurious-free

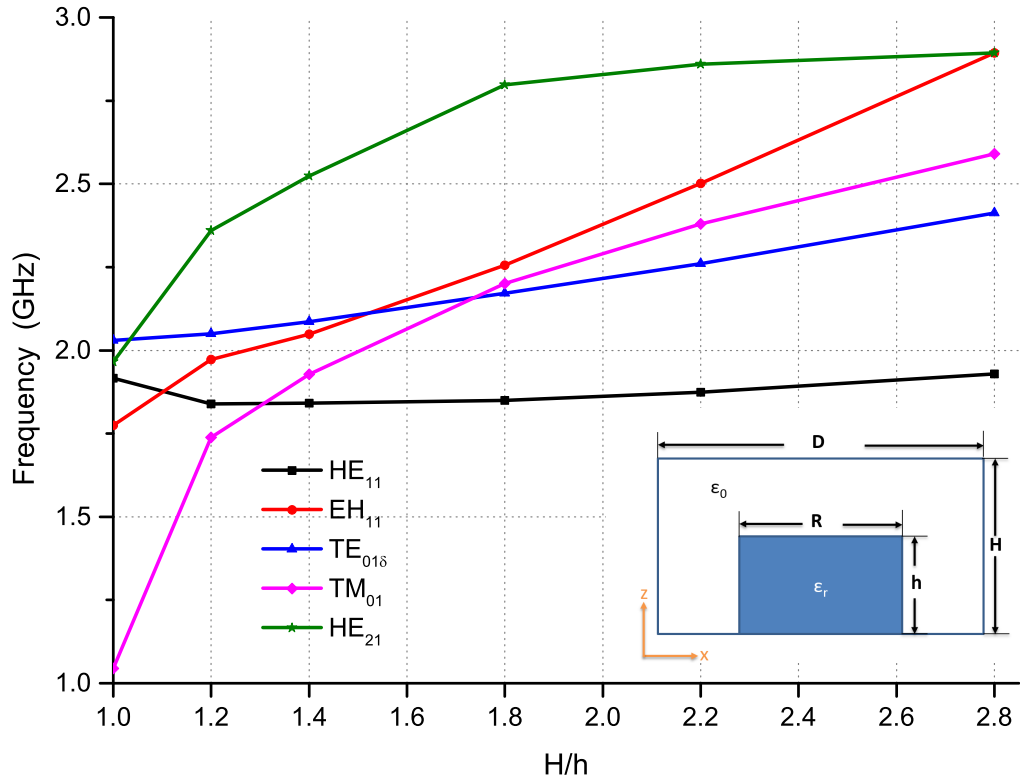


Figure 6.3: Mode chart for shorted dielectric against of H/h .

Table 6.1: Q_u , the spurious-free window and the volume of HE_{11} dual-mode resonator with different dimension at resonant frequency equal 2 GHz.

Height of DR (mm)	Diameter of DR (mm)	Height of cavity (mm)	Diameter of cavity (mm)	Volume (cm^3)	Q factor	spurious-free window (MHz)
15	20	19.5	38	22.11	5599	361.7
15	20	19.5	40	24.50	5665	339.48
15	20	21	36	21.37	5651	443.54
15	20	21	38	23.81	5716	448.36
15	20	22.5	36	22.90	57561	450.09
20	20	30	30	21.20	6028	300.18
14	20	20	34	18.5	5500	451.57
20	20	32	30	22.61	6060	308.03
15	20	25.5	34	23.15	5782	451.92
20	20	34	30	24.03	6084	312.05
15	20	27	34	24.51	5815	455.32
20	20	36	30	25.44	6097	314.18
15	20	28.5	34	25.87	5842	461.36
20	20	38	30	26.86	6094	308.72
15	20	30	34	27.23	5865	457.22

window and small volume. The optimum dimensions are 34 mm, 20 mm, 20 mm and 14 mm for the diameter of the cavity, diameter of the dielectric puck, height of the cavity and height of the ceramic respectively. The fundamental frequency, Q_u and spurious-free window at the optimum dimensions were 2.05 GHz, 5500 and 455 MHz respectively. The resonator offers a size reduction ratio of about 14% compared with air-filled coaxial filters. Normally, the E-field of HE_{11} is circular around the ceramic puck if it is placed in the middle of the metallic cavity, but shorting from one side caused the removal of the semi-circle of the E-field near to the ground. Figure 6.4 shows the E and H-field patterns of the HE_{11} mode for the proposed cavity. E-field was recorded around the DR which is at some places perpendicular to the side wall of the cavity, while the high field remained concentrated inside the ceramic near to the ground. Moreover, the magnetic field is almost entirely in the ceramic, which has a poor intensity outside, but which could be used for input coupling despite being weak.

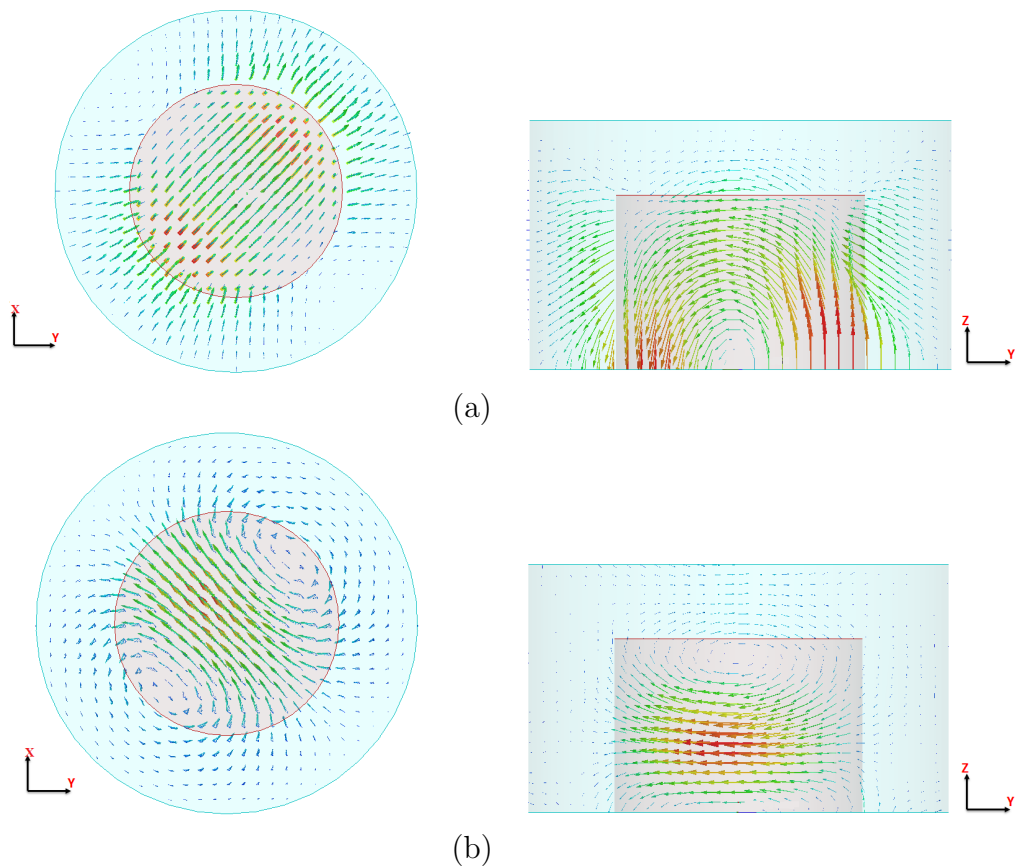


Figure 6.4: Field distributions of HE_{11} dual-mode (a) E-field plot (b) H-field plot.

6.2.1 Effect of the Resonator Dimensions

A parametric study was conducted to demonstrate the effect of the change of dimensions on the resonant frequency, Q_u and the spurious-free window. Firstly, assume there is a gap (ga) between the bottom of the DR and the face of the copper cavity which has a conductivity of about $4 \times 10^7 S/m$. The gap was varied followed by calculation of the parameters to see the effect on the resonator, as presented in Figure 6.5. It can be seen that the gap has an enormous effect on the fundamental frequency of the resonator, which increased by about 150 MHz when the gap increased by $50 \mu m$. There is no change in the second mode ($TE_{01\delta}$) and the Q_u is directly proportional to the gap size. In practical work, there should be a perfect contact between the ceramic and the base metal cavity by solder or by use of a plastic screw on the top of the DR to eliminate any gap between them. Secondly, it was assumed that paint solder was applied to coat the base of the dielectric puck.

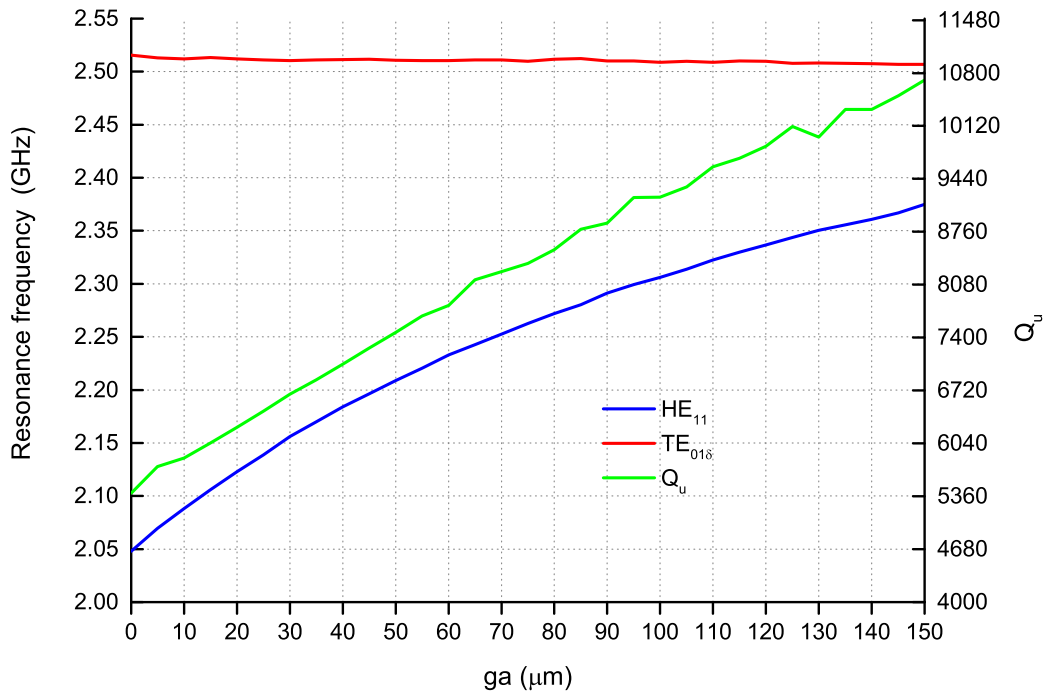


Figure 6.5: Resonant frequencies and Q_u against the varying ga .

Figure 6.6 illustrates the first two modes of the proposed cavity with unloaded Q -factor plotted against the gap size where the ceramic was soldered at conductivity

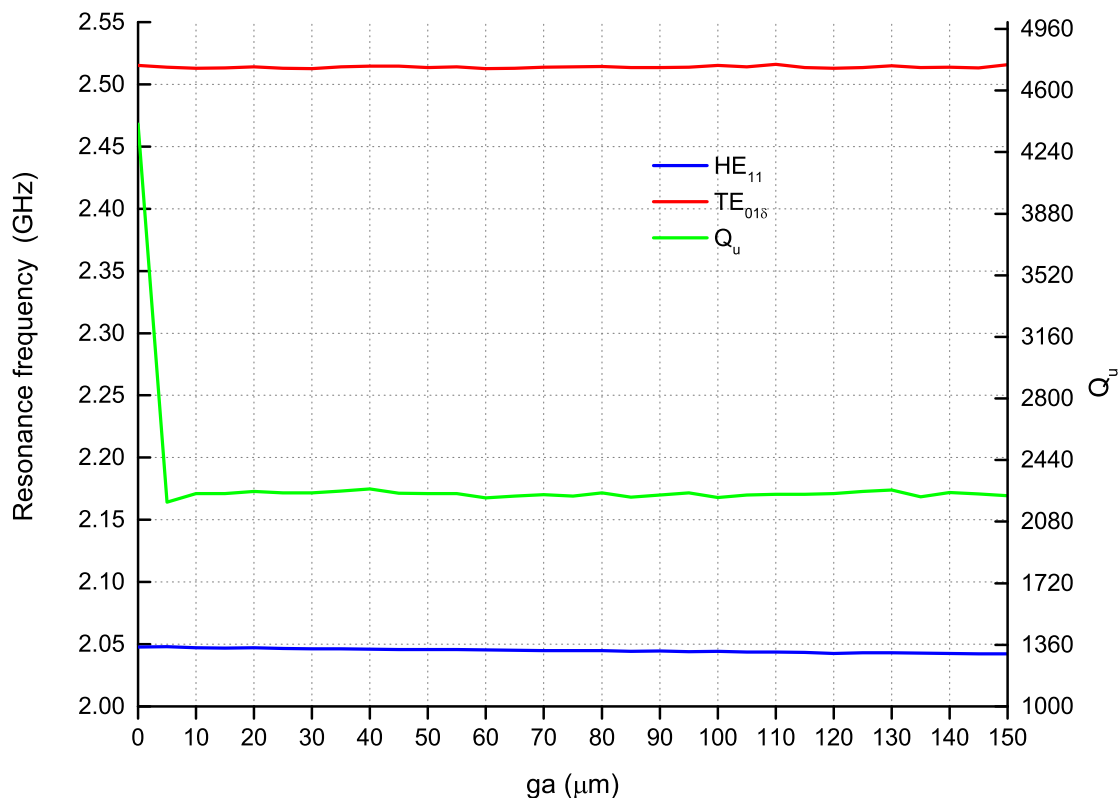


Figure 6.6: Resonant frequencies and Q_u against the varying ga with ceramic solder.

2×10^7 S/m. It was observed that the dual-mode HE_{11} and $TE_{01\delta}$ were not affected by a change in gap distance. However, the Q_u is significantly affected and is reduced from 4200-2200 at $5 \mu\text{m}$ compared with when there is no gap. This happened due to the high quantity of the tangential H-field inside the puck and near the bottom of the ground and, with a gap, there were two plates of loss-inducing metal instead of one. Furthermore, the solder coating is lossy even when it is in perfect contact; the drop in Q_u was about 1100 when the copper under the dielectric was replaced by solder. The behaviour of the resonator as the position of the dielectric puck changes in the horizontal direction was investigated. Figure 6.7 shows the resonance frequencies and Q_u against the shifting of DR in the x-direction (b_a). It is clear that a 2 mm shift in x-y direction does not have any effect on the resonance frequency and the Q_u , both of which remain of similar values, giving good tolerance for filter fabrication.

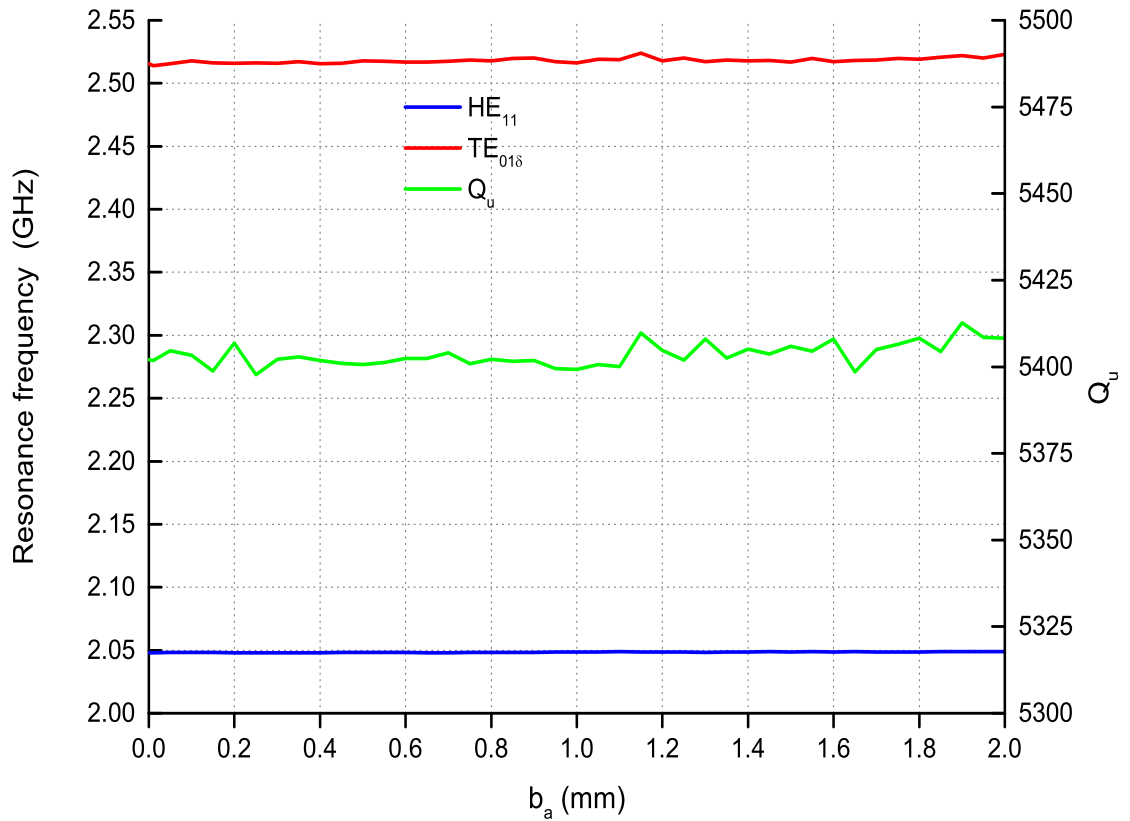


Figure 6.7: Resonant frequencies and Q_u against the varying b_a .

6.3 Coupling Technique

As mentioned in the previous section, 6.2, the E and H-fields can be utilised for coupling technique. Therefore, a coaxial probe was attached to a metal ground post designed for I/O coupling, as shown in Figure 6.8. A tuning screw element above the metal post was used to tune the capacitance of the probe and correct any imperfections in the realised design. In order to have good control of the coupling, a hollow space was provided inside the post. Figure 6.9 illustrates the external Q-factor against the distance between the dielectric puck, the inductive post (t) and the length of the tuning screw (ts). Clearly, the relationship between the Q_e and the (t) is directly proportional. The maximum bandwidth can be achieved at $t=0.3$ mm, which is not a wide bandwidth. As shown in the Figure 6.9(top-X Y-right), when $t=0.5$ mm the screw can be incorporated to increase the coupling that changes from about 60 to 32, when the length of the screw changes by about 2 mm.

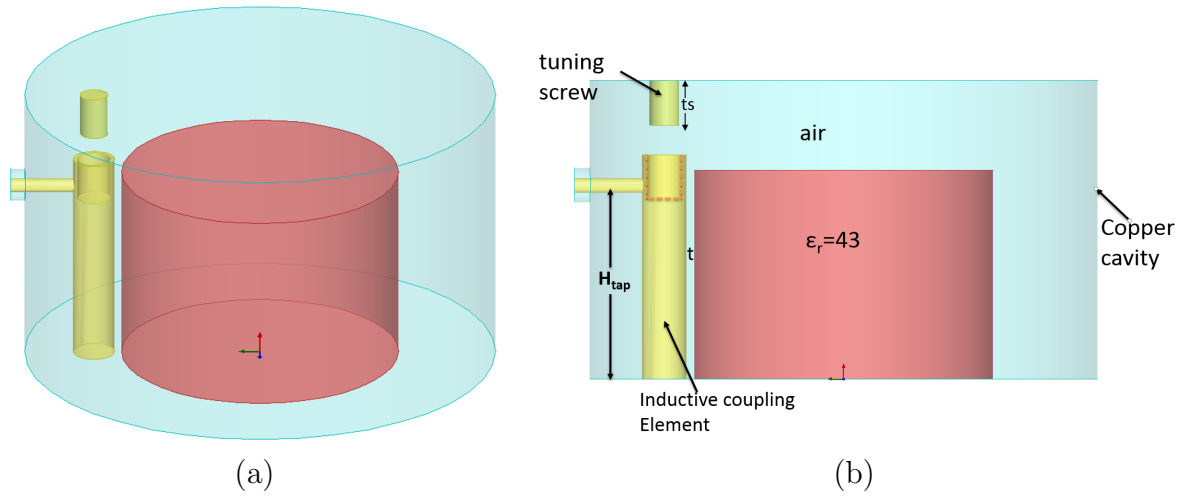


Figure 6.8: Coupling mechanism for HE_{11} dual-mode (a) 3D view (b) side view.

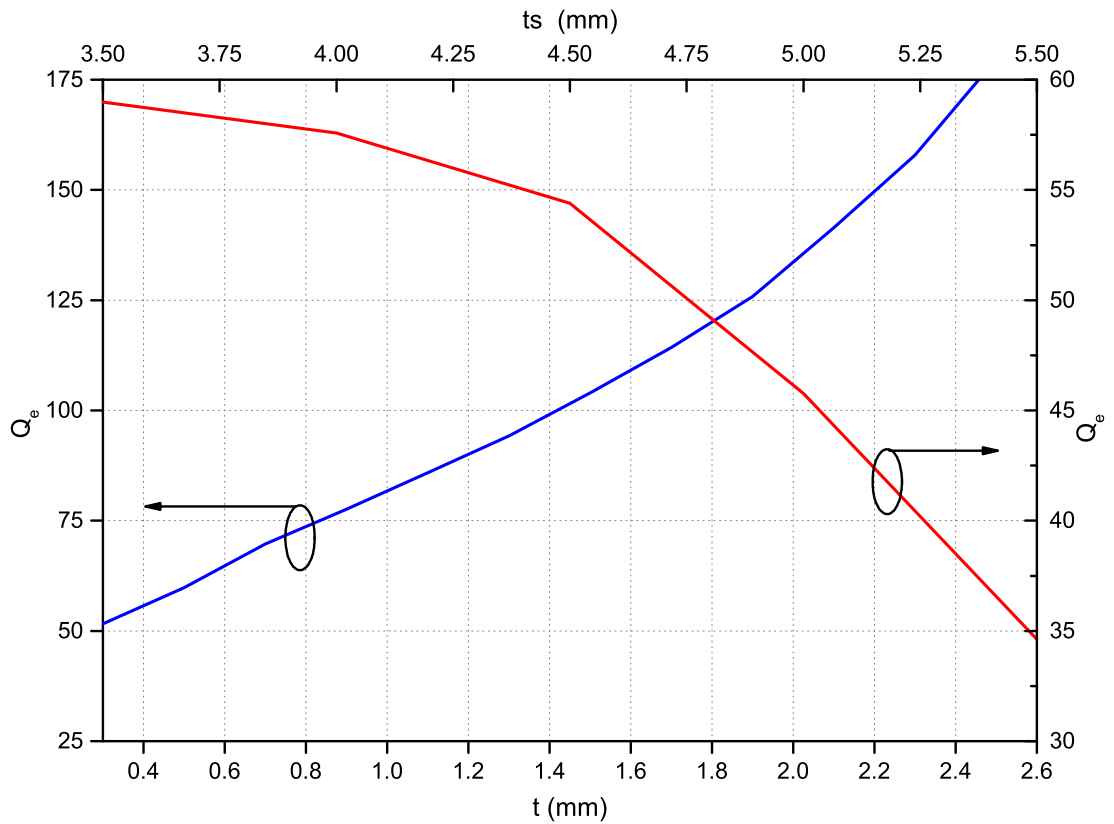


Figure 6.9: External quality factor (Q_e) against t and ts .

There are two methods to implement the inter-resonator coupling for the HE_{11} dual-mode filter. The first method is by use of a circular metal tuning screw from the base side placed at 45° with respect to modes one and two, with length (L_{c1}) and diameter (D_e), while X_{f1} is the distance from the centre of the DR, as shown in Figure 6.10a. The inter-resonator coupling bandwidth and the Q_u are plotted against L_{c1} in Figure 6.11. It is clear that the two main factors having a

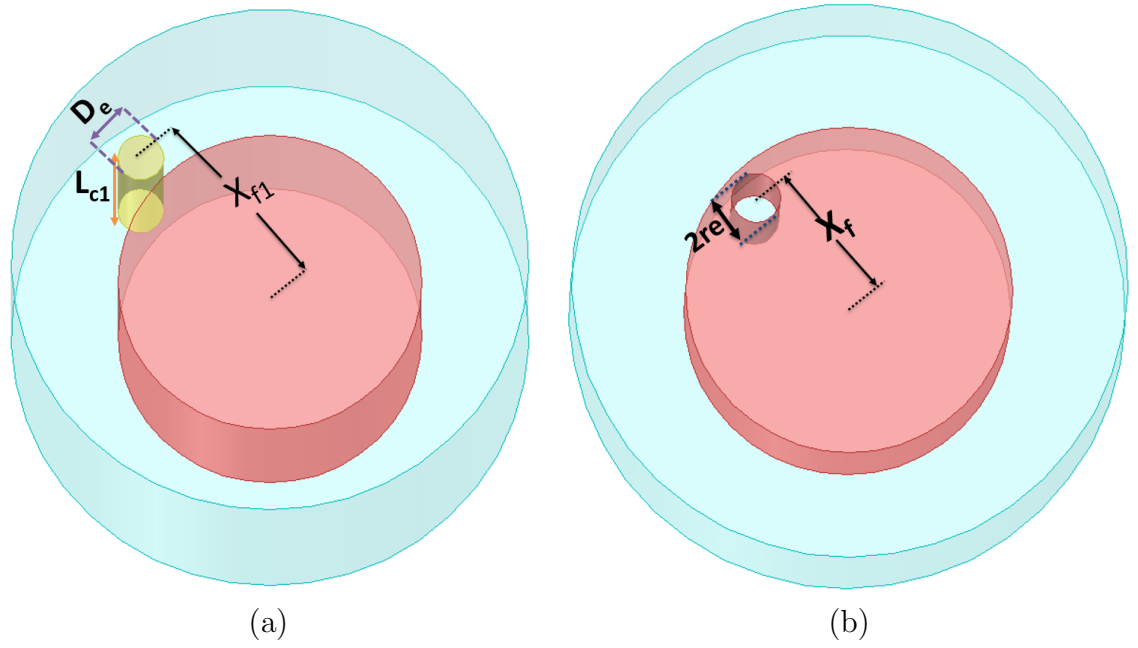


Figure 6.10: Inter-resonator coupling for HE_{11} (a) metallic screw (b) circular hole.

significant influence on the coupling bandwidth are the diameter D_e and the height of the tuning coupling screw L_{c1} , which are directly proportional to the coupling bandwidth. The maximum coupling bandwidth can be achieved at L_{c1} equal to 18 mm for 35 MHz and 55 MHz when D_e is 1 mm and 1.5 mm respectively. However, the drawbacks of this technique include: increasing the losses to about 1000 by reducing the Q_u and the tuning complexity since the filter has to be on the side of the cavity. The second method of etching a vertical circular hole in the dielectric puck placed at 45° with respect to modes one and two is shown in Figure 6.10b. The coupling bandwidth against the distance between the centre of the DR and the hole (X_f) with varying the hole radius (re), which is measured in mm, is presented in Figure 6.12. Bell-shaped behaviour was observed for the coupling at 7 mm of X_f which gives the maximum coupling for all the recorded values for re . A good diversity of bandwidth can be achieved by this technique which ranges up to 90 MHz at 2.6 mm. Furthermore, the Q_u could be improved when we use the cutting strategy indicated in the previous chapters for the TE_{11} dual-mode.

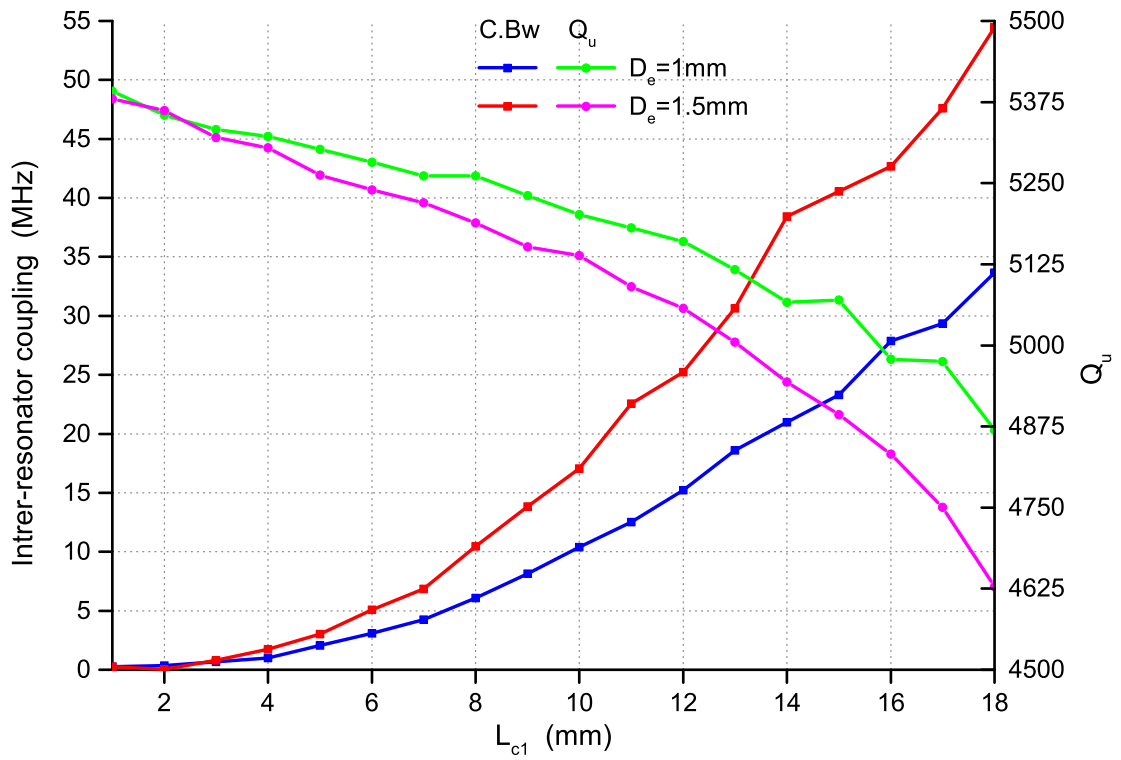


Figure 6.11: Inter resonator coupling bandwidth against L_{c1} .

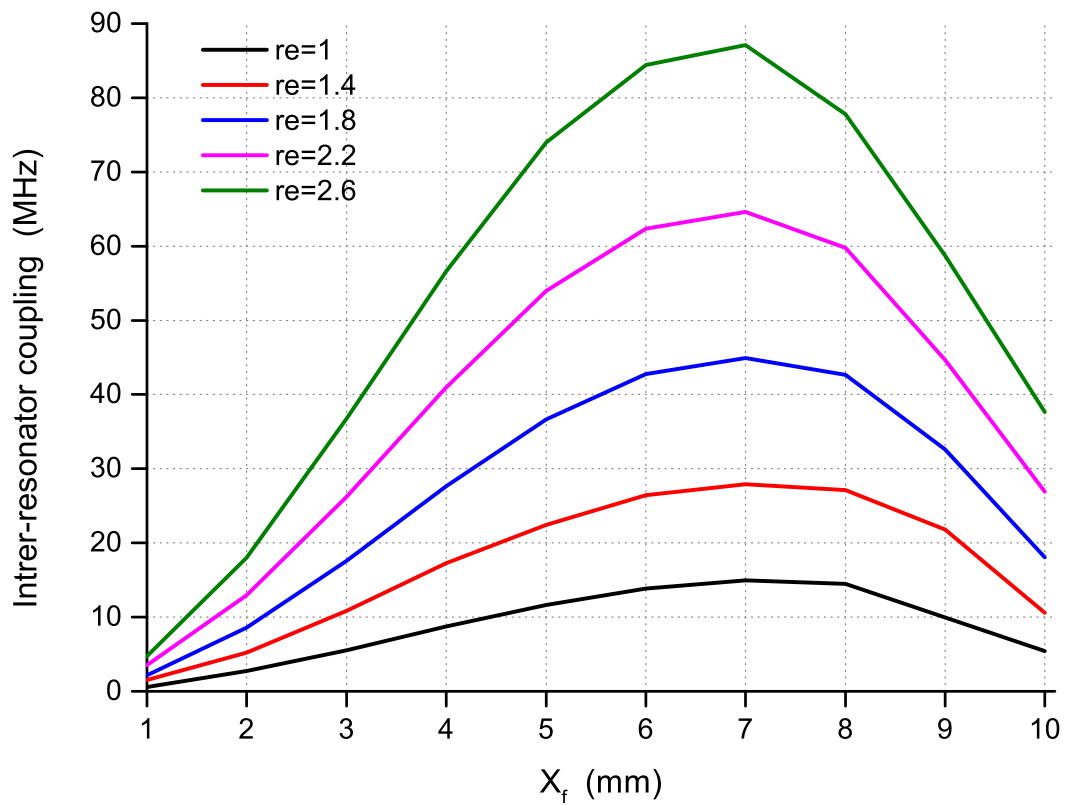


Figure 6.12: Inter resonator coupling bandwidth varying with radius (re) and (X_f).

6.4 Design of the 4th-order Dual-Mode HE_{11} Filter

The 4th order Chebyshev dual-mode filter was designed with a centre frequency of 2.05 GHz, bandwidth of 50 MHz and reflection loss (IL) of 20 dB at the pass-band. The coupling matrix and Chebyshev topology at FBW=2.439% are shown in Figure 6.13. The I/O external quality factors and the coupling coefficients are computed by coupling matrix synthesis (CMS) software.

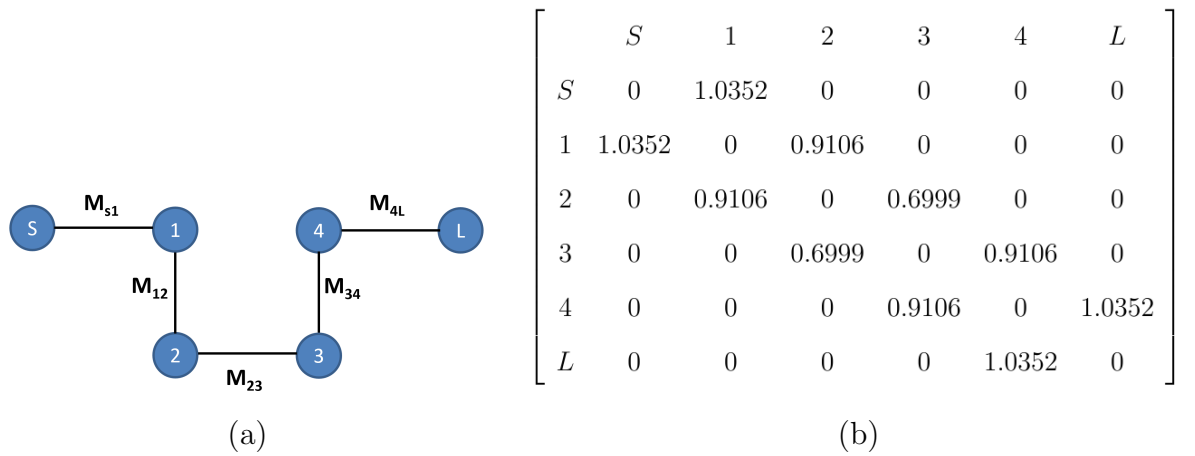


Figure 6.13: 4th order filter (a) Filter topology, (b) Normalized coupling matrix.

Figure 6.14 presents the configuration of the 4th order filter in HFSS which consists of two copper cavities and two ceramic pieces which were short-circuited from the backside. All intra-cavity couplings were implemented by an inductive grounded post with a tuning screw on each post to control the coupling bandwidth. To realize the filter, all coupling coefficients from the coupling matrix(CM) need to be converted to physical dimensions by using the coupling equivalence values in Figures 6.11 and 6.12, as provided in Table 6.2.

Figure 6.15 shows the S-parameter for the 4th-order Chebyshev filter around the in-band response at $\theta_1 = 315^\circ$ and $\theta_2 = 225^\circ$. It can be observed that the bandwidth of the filter at -16 dB was 50 MHz it meets the requirements of cellular systems. The insertion loss at the resonant frequency 2.065 GHz is less than 0.3 dB and the extracted unloaded Q-factor is slightly more than 4800, while the losses

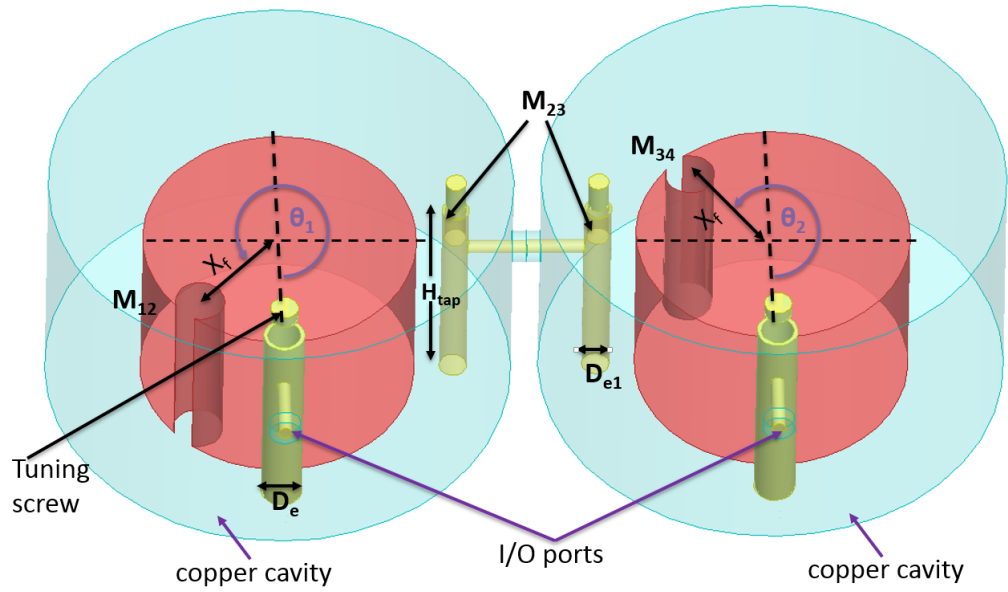


Figure 6.14: Configuration of HE_{11} dual-mode 4^{th} order filter in HFSS.

Table 6.2: Typical dimensions of 4^{th} order filter HE_{11} dual-mode.

Coefficient No.	Distance from the centre (mm)	Diameter of element (mm)	Length of element (mm)	H_{tap} (mm)
$M_{S1}=M_{4L}$	12	3	14	13
M_{23}	12.8	2	14	10
$M_{12} = M_{34}$	9	4.4	14	-

in Q are about 500 compared with eigen-mode analysis.

Figure 6.16 shows the broadband response of the 4^{th} order Chebyshev filter. It can be seen that the lower spurious mode is about 2.55 GHz, which means the spurious-free window is about 500 MHz instead of 444 MHz as shown in eigen-mode analysis; also, the maximum isolation was 60 dB and 75 dB for the upper and lower band respectively. The position of high isolation seems to be a complex transmission zero (TZ), which will be discussed in section 6.5.

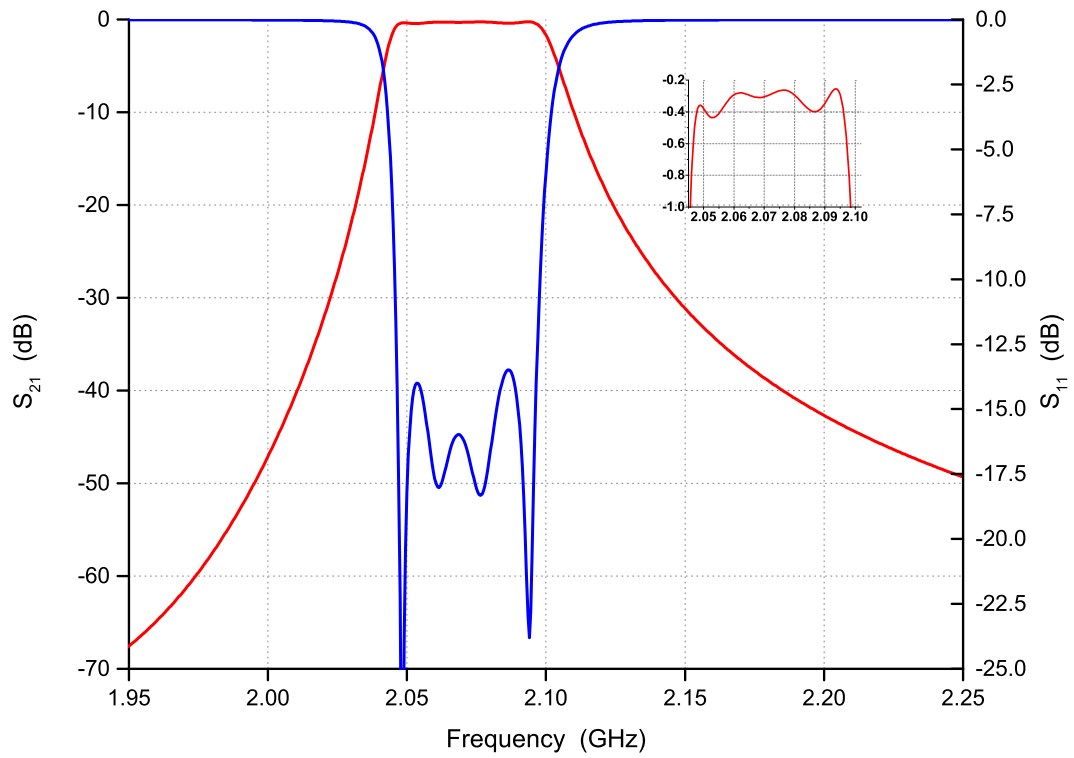


Figure 6.15: Simulated response of 4th order HE_{11} dual-mode filter.

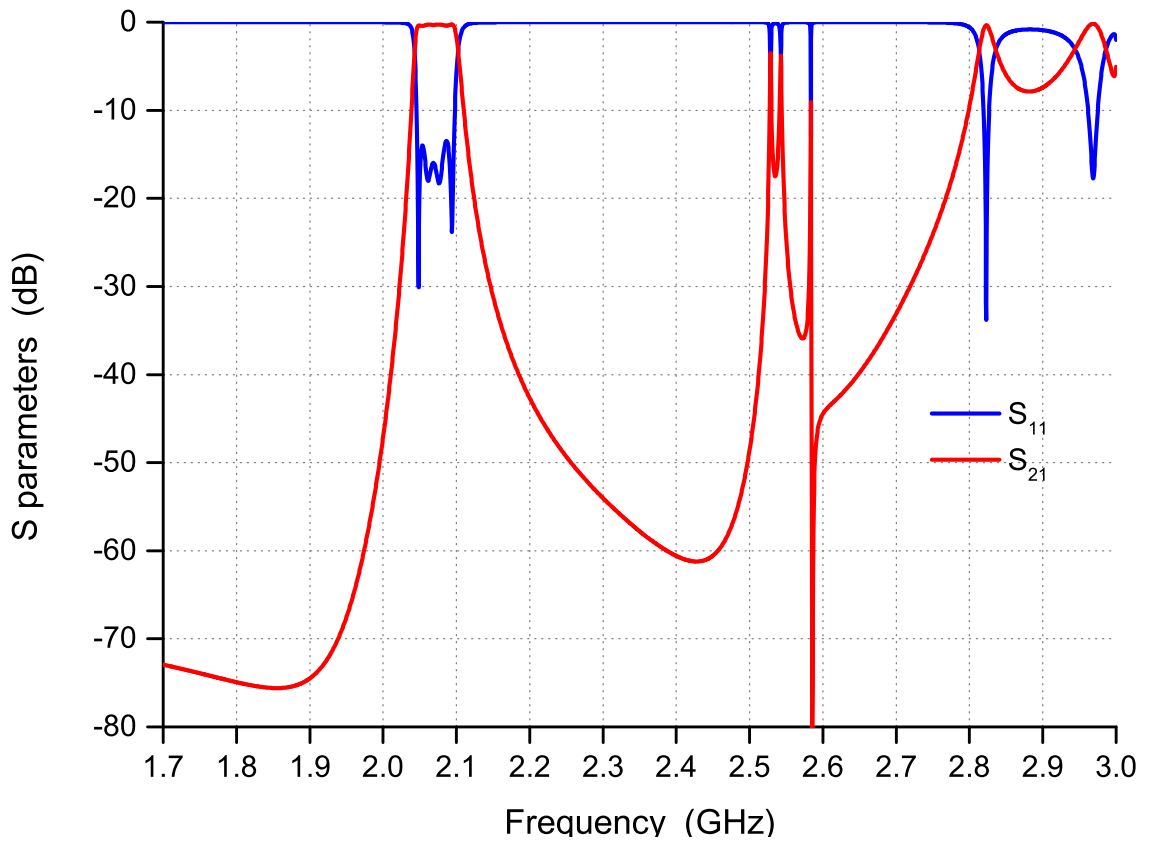


Figure 6.16: Broadband response simulated of 4th order HE_{11} dual-mode filter.

6.5 Circuit Model for HE_{11} Dual-mode Resonator Filter

To understand the behaviour of transmission zeros that had appeared in Figure 6.16, we need to study and analysis the field patten of the resonator for suggesting a mathematical model of the filter. Figure 6.17 presents the E-field pattern of HE_{11} mode close to the top of the DR at 2.05 GHz. The E-field pattern of HE_{11} dual-mode is similar to the suspended ring resonator dual-mode, especially at the area around the DR where the TZs may be generated. In this case, it is possible to present the transmission line ring resonator as mathematical approach for HE_{11} dual-mode resonator.

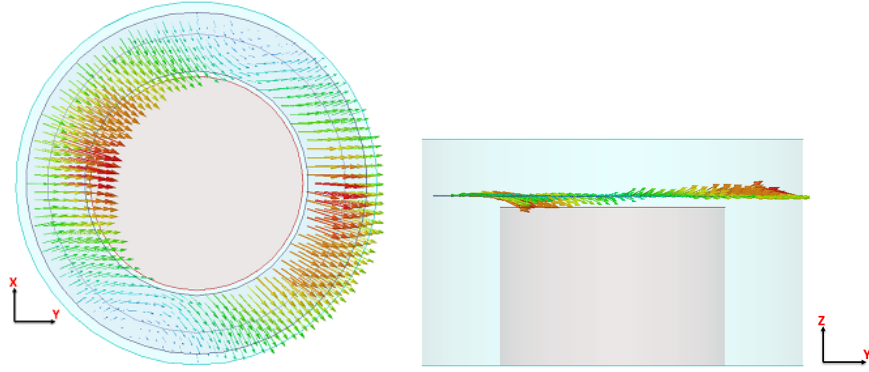


Figure 6.17: E-field distributions of HE_{11} dual-mode.

Figure 6.18 presents the ring resonator with frequency invariant reactance (FIR) that displays the coupling between two modes (jC) and the resonant frequency (jB); θ_1 is the electrical length between the input and output, and θ_2 and θ_3 are the electrical length of input/output notch coupling respectively. To analyse the circuit, it was assumed that the ring resonator operates in two paths that are connected in parallel. Path one is a transmission line with electrical length θ_1 and has the following transfer matrix:

$$T_1 = \begin{bmatrix} \cos(\theta_1) & jZ_0 \sin(\theta_1) \\ jY_0 \sin(\theta_1) & \cos(\theta_1) \end{bmatrix} \quad (6.1)$$

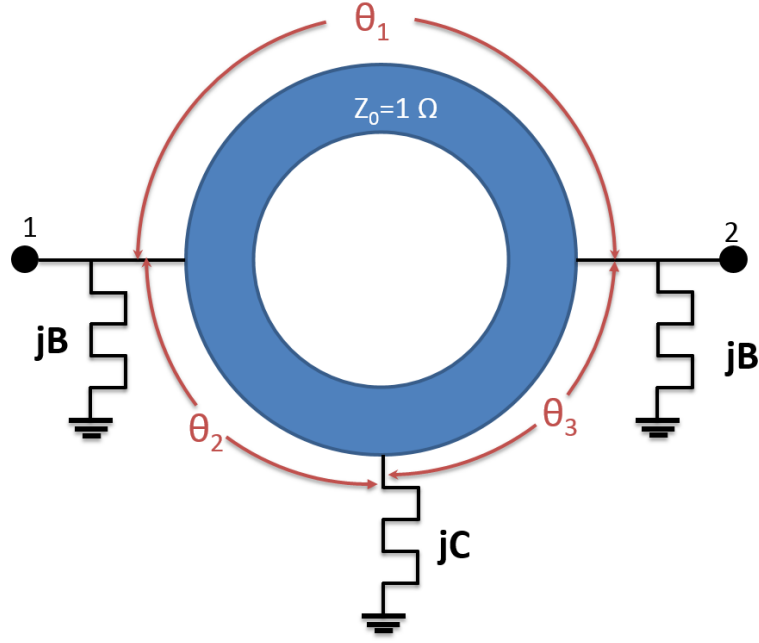


Figure 6.18: Ring resonator with FIR coupling elements.

where Z_0 is equal to 1, the equation is simplified as:

$$T_1 = \begin{bmatrix} \cos(\theta_1) & j \sin(\theta_1) \\ j \sin(\theta_1) & \cos(\theta_1) \end{bmatrix} \quad (6.2)$$

To obtain the admittance for path one the following formula is applied [55]:

$$Y_1 = \begin{bmatrix} \frac{D}{B} & \frac{-(AD - BC)}{B} \\ -\frac{1}{B} & \frac{A}{B} \end{bmatrix} \Rightarrow Y_1 = \begin{bmatrix} \frac{-j}{\tan(\theta_1)} & \frac{j}{\sin(\theta_1)} \\ \frac{j}{\sin(\theta_1)} & \frac{-j}{\tan(\theta_1)} \end{bmatrix} \quad (6.3)$$

Path two can be divided into three parts: two transmission lines with electrical length θ_2 and θ_3 respectively and one as FIR.

$$T_2 = \begin{bmatrix} \cos(\theta_2) & j \sin(\theta_2) \\ j \sin(\theta_2) & \cos(\theta_2) \end{bmatrix} \begin{bmatrix} 1 & 0 \\ jC & 1 \end{bmatrix} \begin{bmatrix} \cos(\theta_3) & j \sin(\theta_3) \\ j \sin(\theta_3) & \cos(\theta_3) \end{bmatrix} \quad (6.4)$$

$$T_2 = \begin{bmatrix} \cos(\theta_2 + \theta_3) - C \sin(\theta_2) \cos(\theta_3) & j [\sin(\theta_2 + \theta_3) - C \sin(\theta_2) \sin(\theta_3)] \\ j [\sin(\theta_2 + \theta_3) + C \cos(\theta_2) \cos(\theta_3)] & \cos(\theta_2 + \theta_3) - C \sin(\theta_3) \cos(\theta_2) \end{bmatrix}$$

(6.5)

Convert T matrix to Y matrix as shown below:

$$Y_2 = \begin{bmatrix} \frac{\cos(\theta_2 + \theta_3) - C \sin \theta_3 \cos \theta_2}{j [\sin(\theta_2 + \theta_3) - C \sin \theta_2 \sin \theta_3]} & \frac{j}{\sin(\theta_2 + \theta_3) - C \sin \theta_2 \sin \theta_3} \\ \frac{j}{\sin(\theta_2 + \theta_3) - C \sin \theta_2 \sin \theta_3} & \frac{\cos(\theta_2 + \theta_3) - C \sin \theta_2 \cos \theta_3}{j [\sin(\theta_2 + \theta_3) - C \sin \theta_2 \sin \theta_3]} \end{bmatrix} \quad (6.6)$$

The two Y admittances are on a parallel, so the total will be:

$$Y = Y_1 + Y_2 \quad (6.7)$$

$$Y = \begin{bmatrix} \frac{\cos(\theta_2 + \theta_3) - C \sin \theta_3 \cos \theta_2}{j [\sin(\theta_2 + \theta_3) - C \sin \theta_2 \sin \theta_3]} + \frac{-j}{\tan(\theta_1)} & \frac{j}{\sin(\theta_2 + \theta_3) - C \sin \theta_2 \sin \theta_3} + \frac{j}{\sin(\theta_1)} \\ \frac{j}{\sin(\theta_2 + \theta_3) - C \sin \theta_2 \sin \theta_3} + \frac{j}{\sin(\theta_1)} & \frac{\cos(\theta_2 + \theta_3) - C \sin \theta_2 \cos \theta_3}{j [\sin(\theta_2 + \theta_3) - C \sin \theta_2 \sin \theta_3]} + \frac{-j}{\tan(\theta_1)} \end{bmatrix} \quad (6.8)$$

The Y matrix is converted to a π equivalent circuit, as shown in Figure 6.19.

The circuit is simplified to feature an inverter and two resonators, as presented in

Figure 6.20. When the admittance, Y_{12} , is equal to zero, solving the root using

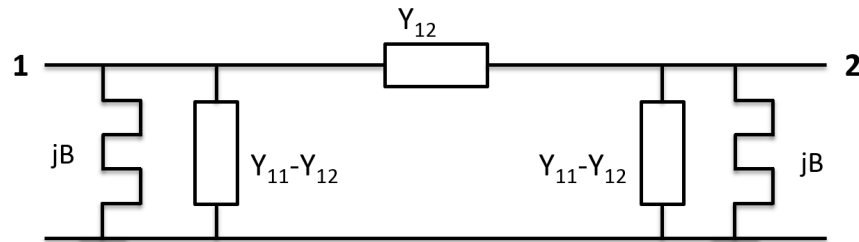


Figure 6.19: Equivalent circuit for ring resonator.

the Newton-Raphson method gives the position of the transmission zero.

$$Y_{12} = \frac{j [\sin(\theta_1) + \sin(\theta_2 + \theta_3) - C \sin(\theta_2) \sin(\theta_3)]}{\sin(\theta_1) (\sin(\theta_2 + \theta_3) - C \sin(\theta_2) \sin(\theta_3))} \quad (6.9)$$

Substitute the θ_3 as a dependant variable in θ_1 and θ_2 .

$$\theta_3 = 2\pi - (\theta_1 + \theta_2) \quad (6.10)$$

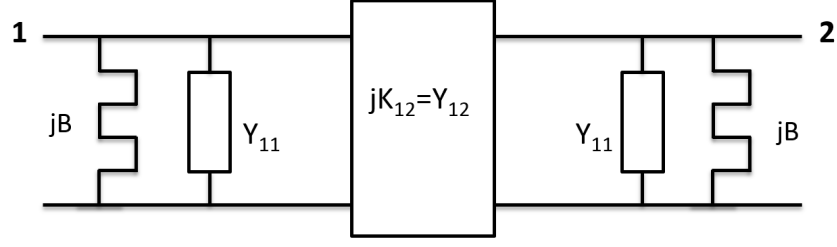


Figure 6.20: Equivalent circuit representation for the two-port network.

$$Y_{12} = \frac{j [\sin(\theta_{a1}\omega) + \sin(\theta_{a2}\omega + \theta_{a3}\omega) - C \sin(\theta_{a2}\omega) \sin(\theta_{a3}\omega)]}{\sin(\theta_{a1}\omega) (\sin(\theta_{a2}\omega + \theta_{a3}\omega) - C \sin(\theta_{a2}\omega) \sin(\theta_{a3}\omega))} \quad (6.11)$$

Table 6.3 shows the TZs position after substituting each θ by $\theta_{a\omega}$ at 1 Hz to obtain the value of ω when the Y_{12} is equal to zero. It was observed that two types of

Table 6.3: TZs position at resonant frequency 1 Hz.

Coupling coefficient (C)	θ_{a1}	θ_{a2}	θ_{a3}	Roots
1	90 ⁰	135 ⁰	135 ⁰	j0.634, j1.142
		45 ⁰	225 ⁰	0.187+j0.865, -0.187+j0.865
4		135 ⁰	135 ⁰	j0.263 , j1.202
		45 ⁰	225 ⁰	j0.5 , j0.722
0		45 ⁰	0	j , j
-1		135 ⁰	135 ⁰	-j0.634 , -j1.142

roots were recorded imaginary and complex number. When C=1, the position of notch (θ_{a2}) was a significant term to control the type and the value of TZ, and the imaginary roots are placed on each side band of the resonant frequency. Changing the sign of C can put the TZs into the lower band. The increase in C caused one type of TZ. TZs can be generated in a planar structure even though there is no coupling notch connected, and will occur at the same resonant frequency. In this case, by changing the item (B), the f_r will be shifted down and the TZs are found in the upper side band. To calculate the reflection zero (RZ), the resonance value in equation 6.12 should be zero.

$$jB + Y_{11} = 0 \quad (6.12)$$

$$RZ = \frac{\cos(\theta_2 + \theta_3) - C \sin \theta_3 \cos \theta_2}{j [\sin(\theta_2 + \theta_3) - C \sin \theta_2 \sin \theta_3]} - \frac{j}{\tan \theta_1} + jB \quad (6.13)$$

6.6 Filter with Transmission Zeros

The dual-mode mathematical model shows there are pairs of TZs available in all orientations of notch cases which may sometimes appear in the imaginary axis or the complex axis.

Figure 6.21 presents the simulation response of a 4th order filter with variable position of the first coupling notch. At $\theta_1 = 225^\circ, \theta_2 = 135^\circ$ gave a pair of TZs on the upper and lower side bands which occurred at 2.187 GHz and 1.84 GHz respectively. The $\theta_1 = 45^\circ$ breaks the symmetry of the path field and also gave pairs of TZs in each side but at different frequencies. The maximum isolation between the centre frequency and 2.5 GHz in the upper side is about 80 dB and 90 dB in cases one and two respectively. The complex TZ at 2.4 GHz comes from the second mode ($TE_{01\delta}$) which is coupled by the same I/O coupling and the inter-resonator coupling but it is less effective than the first mode. Varying the position of the two notch couplings, as shown in Figure 6.22, improved the isolation without changing the number of TZs, where the isolation is about 110 dB in the upper side

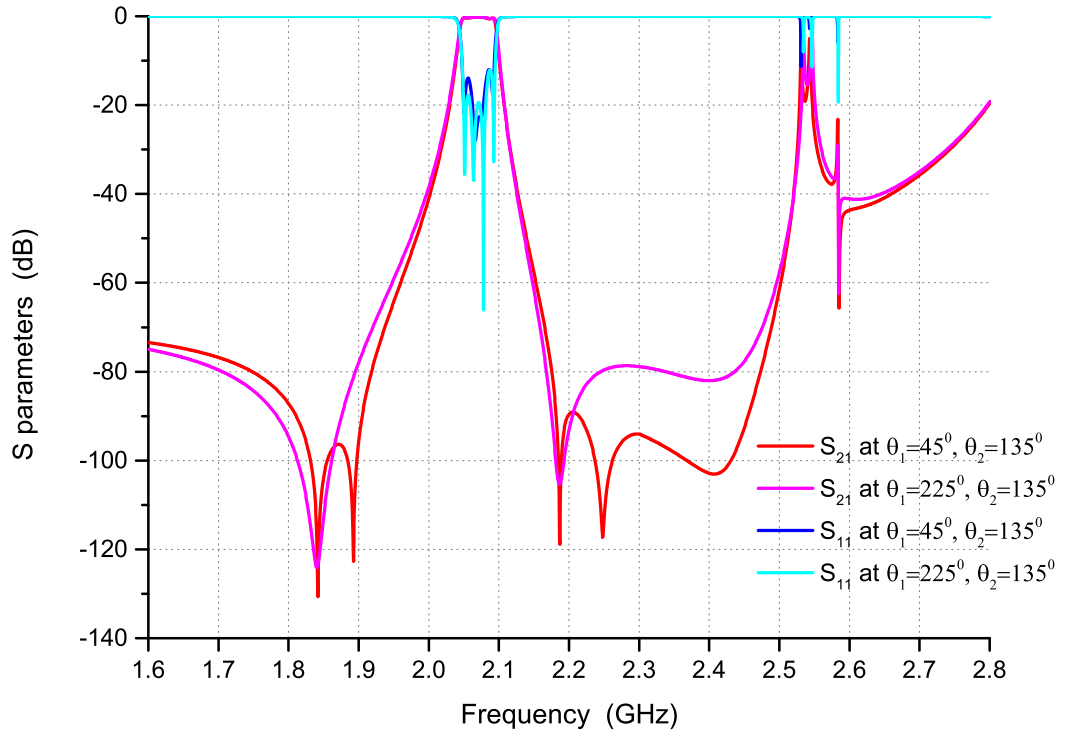


Figure 6.21: Simulation of 4th order HE_{11} dual-mode filter with TZs.

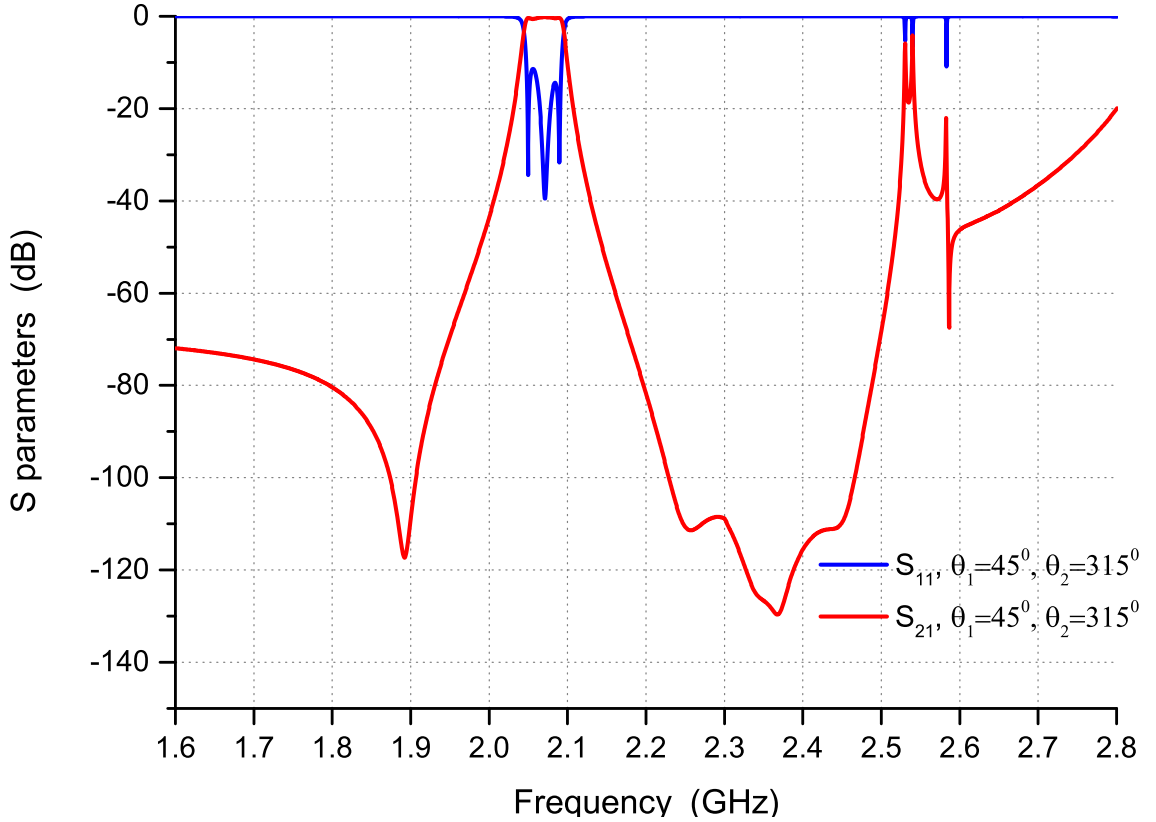


Figure 6.22: Simulation of 4th order HE_{11} dual-mode filter with TZs.

band. There are other ways to control the position of TZs instead of changing the notch coupling orientation. One method is by inserting a tuning screw at 45° w.r.t where the I/O coupling and intra-coupling probes are placed. Figure 6.23 shows the performance of the filter using varying tuning screws of 3 mm diameter. The position of the TZ in the upper side band was varied by 35 MHz in the direction of the resonant frequency while the down side band was shifted by about 50 MHz in the same direction. Additionally, the TZ from the $TE_{01\delta}$ disappeared and was isolated by about 30 dB at 2.44 GHz. Figure 6.24 presents the performance of the filter with two tuning screw of 3 mm diameter. It can be seen that the pair of TZs had the same behaviour as seen in Figure 6.23 and the resonant frequency in this case shifted down by about 80 MHz. The TZs around the $TE_{01\delta}$ were converted from the imaginary axis to the complex axis along the H_T , which changed from 0 to 18 mm.

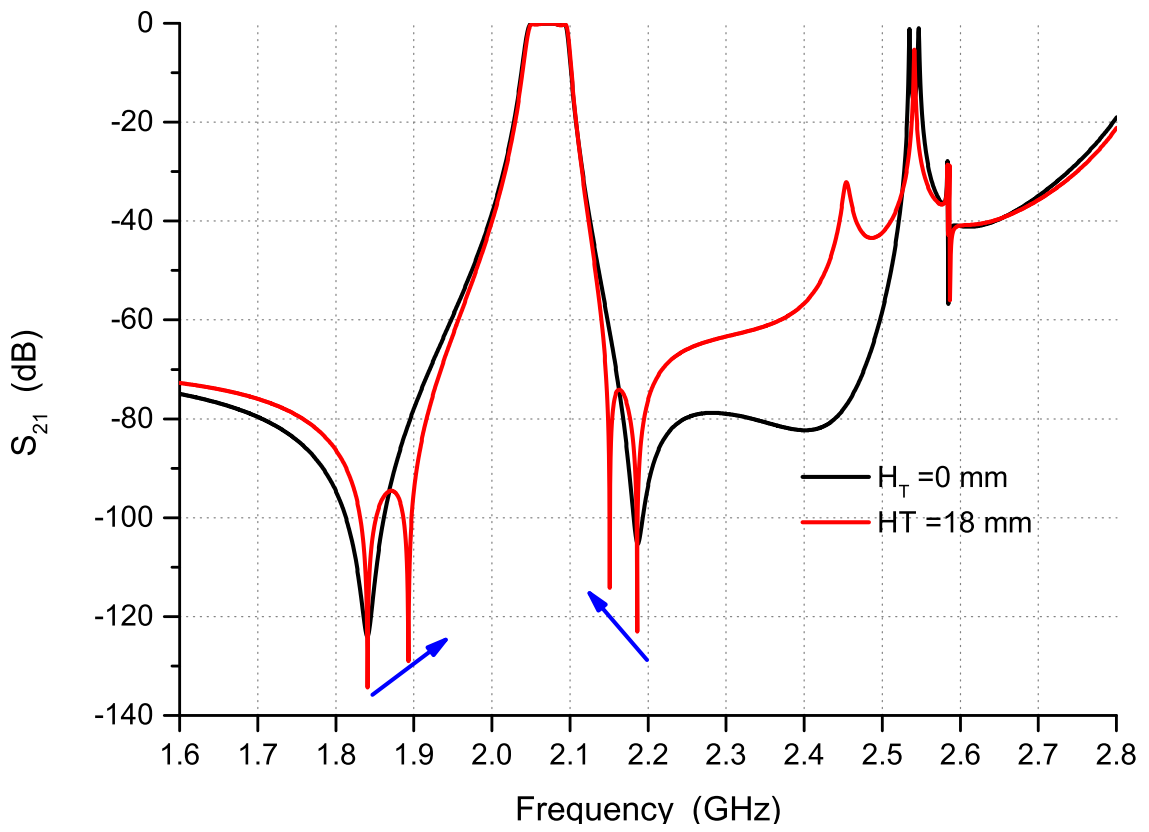


Figure 6.23: Control the TZs position by one tuning screw.

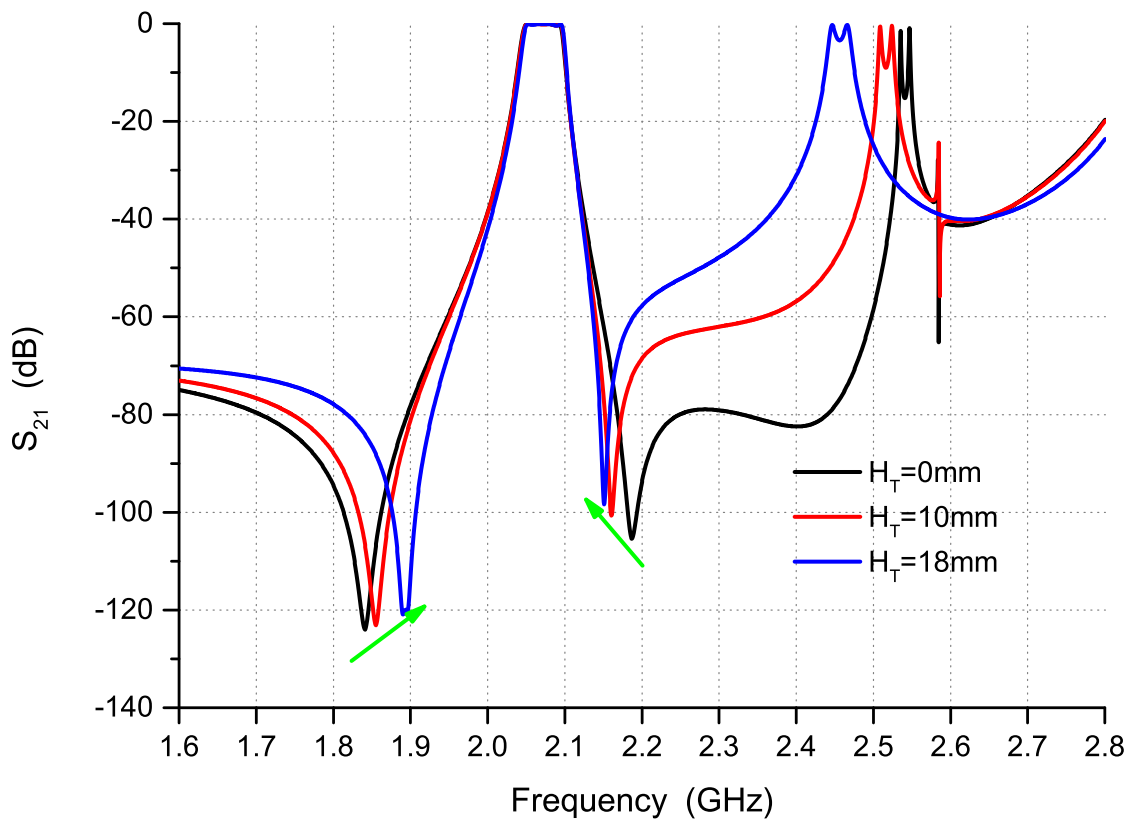


Figure 6.24: Control the TZs position by two tuning screws.

6.7 Implementation of the HE_{11} dual-mode filter

Figure 6.25 shows a photograph of the fabrication of a 4th order HE_{11} dual-mode filter. The rectangular filter has dimensions of 80 mm x 44 mm x 30 mm while the other cavity dimensions and the properties of the material were the same as those mentioned in section 6.4. Six tuning screws 3 mm in diameter were

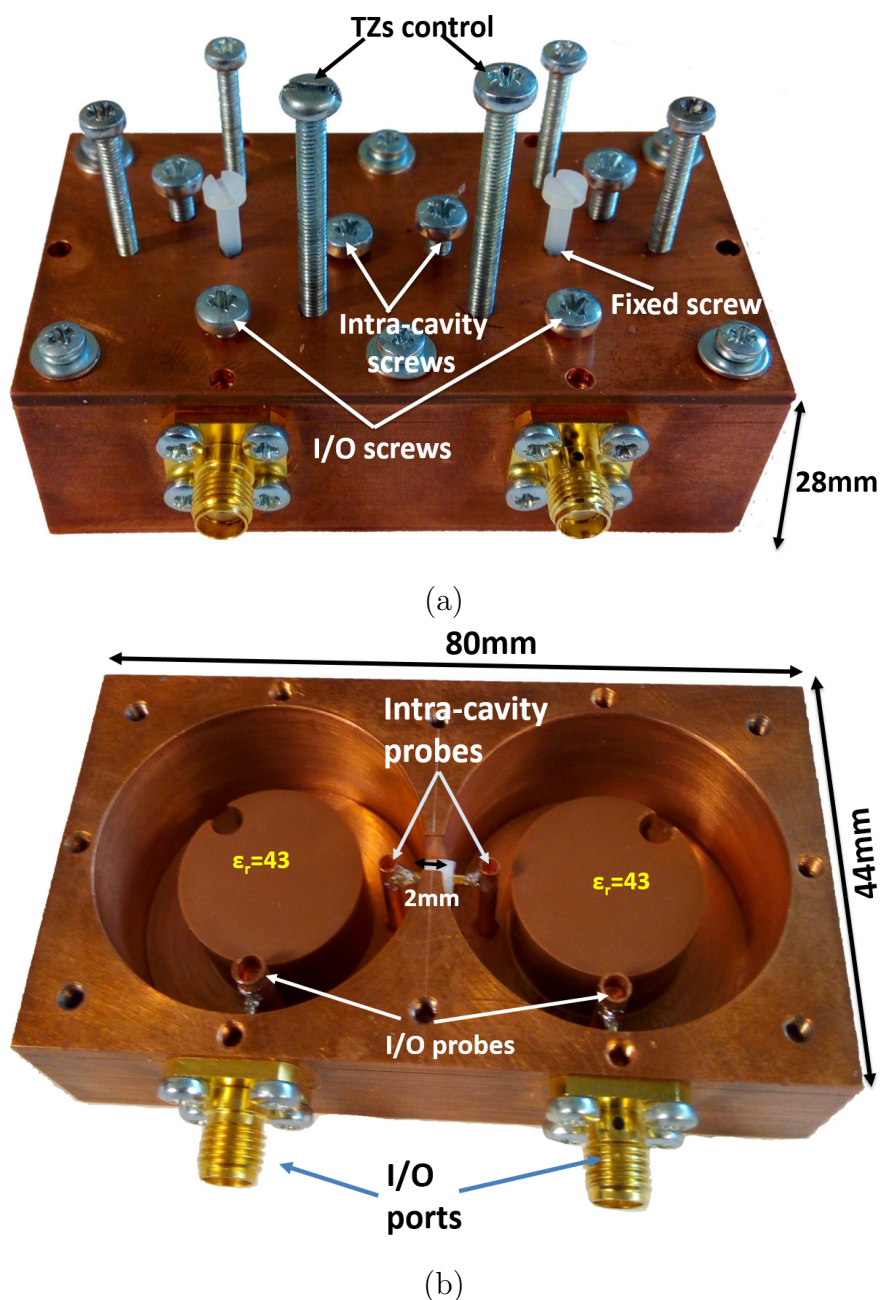


Figure 6.25: Fabricated 4th degree HE_{11} dual-mode bandpass filter.

positioned on the top lid of the cavity to fine-tune the coupling coefficients and all probes were fabricated of copper. A Teflon probe with 2 mm diameter provided a good contact between the ceramic and the base of the copper cavity. S-parameter measurement is achieved by using an Agilent E5071C Network Analyzer. Two-port calibration was performed by using an Agilent N4431-60006 Electronic Calibration Module prior to the measurement. Figure 6.26 shows the S-parameters found experimentally and modelled for a 4th order Chebyshev filter around the in-band response at $\theta_1 = 225^\circ$ and $\theta_2 = 135^\circ$. It can be observed that the measured bandwidth of the filter at -10 dB was equal to 56 MHz, which increased to about 6 MHz compared with the simulation results. The insertion loss at the resonant frequency 2.069 GHz is approximately 0.71 dB and the extracted unloaded Q-factor from the group delay in Figure 6.27 is slightly more than 3800 where the Q_u is equal to the simulation result. There is a difference in the simulation result in this figure and that mentioned in Figure 6.21 because of the changes in the hole diameter and Teflon filling for I/O and intra-cavity coupling. Figure 6.28 shows

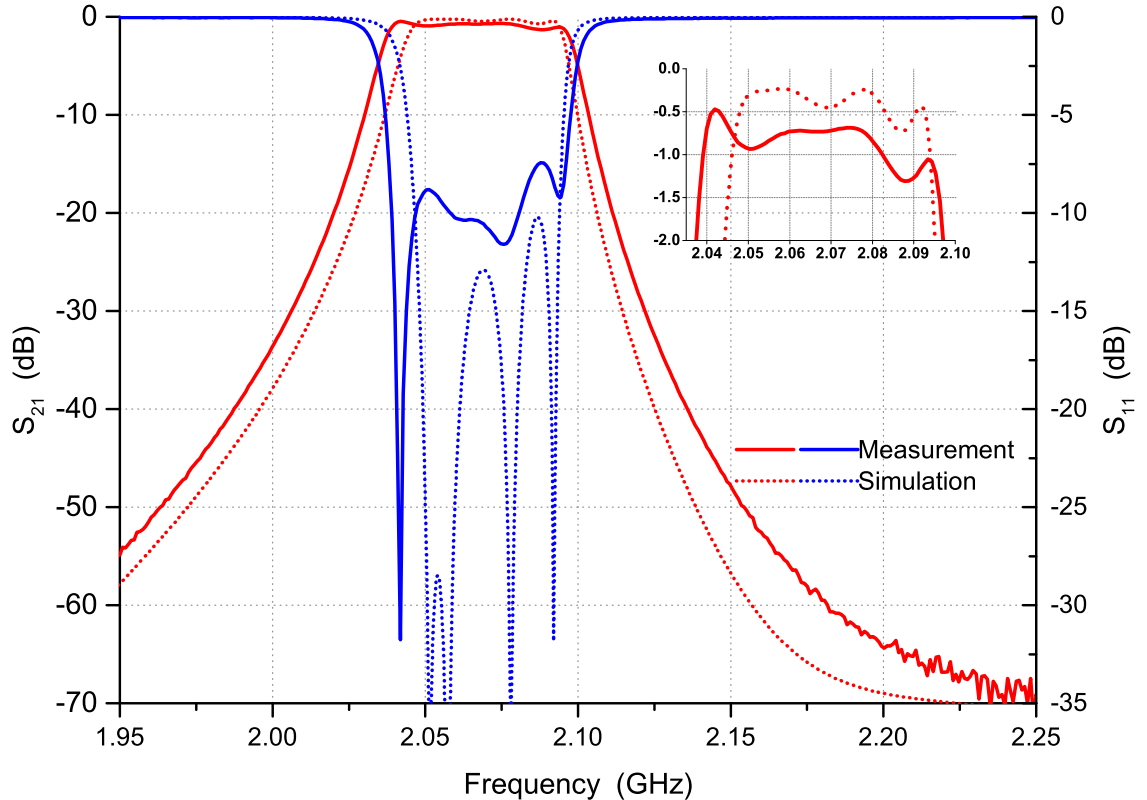


Figure 6.26: Simulated and measured response of 4th order HE_{11} dual-mode filter at $\theta_1 = 225^\circ$ and $\theta_2 = 135^\circ$.

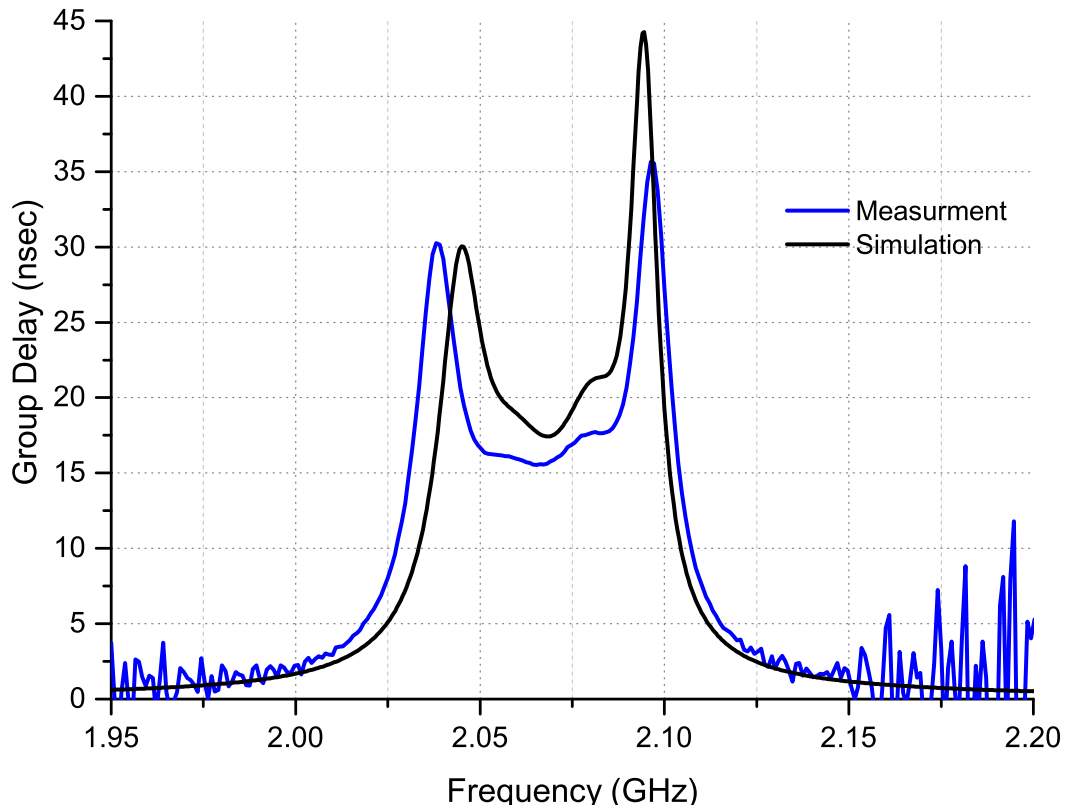


Figure 6.27: Measured and simulation group delay for 4th order HE_{11} dual-mode.

the measured and simulated broadband response of a 4th order Chebyshev filter. It can be seen that the lower spurious mode is about 2.55 GHz, which means the spurious-free window is about 500 MHz instead of 444 MHz as shown in the eigenmode analysis. Also, the maximum isolation was 80 dB for both the upper and lower bands. There is a good agreement between the measurement and simulation results. Figure 6.29 presents the performance of the practical filter with varying two tuning screws (H_T) that have a diameter of 3 mm. It can be seen that the TZs in the lower band shifted up by 61 MHz. The TZs around the $TE_{01\delta}$ were converted from the imaginary axis to a complex axis along the H_T , which changed from 0 to 18 mm. Figure 6.30 presents the simulated and measured response of the 4th order HE_{11} dual-mode filter at $\theta_1 = 315^\circ$ and $\theta_2 = 135^\circ$. From the figure, it can be seen that the measurement result has a good agreement with the simulation result. The IL in the resonance frequency was similar in both cases while the measured Bw was increased by 6 MHz. The performance of the broadband response in Figure 6.31 is similar to the simulation, which has a pair of imaginary TZs in each side

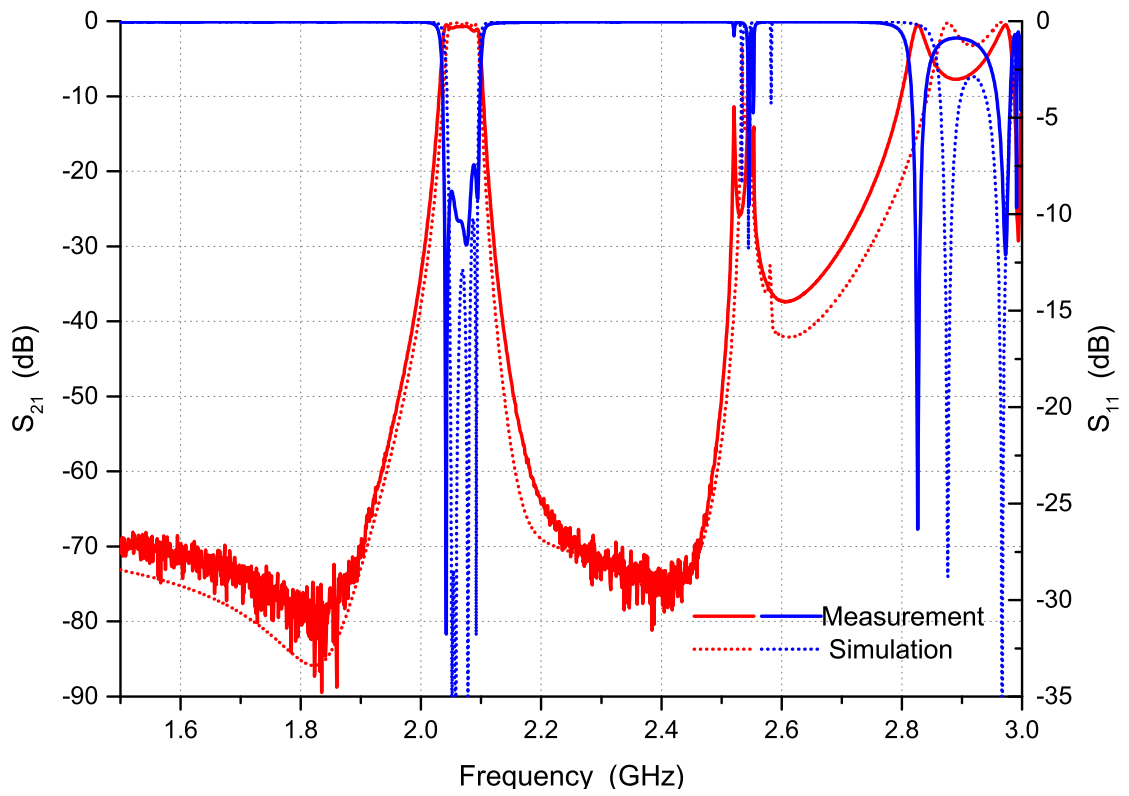


Figure 6.28: Broadband response simulated and measured for 4th order HE_{11} dual-mode filter at $\theta_1 = 225^\circ$ and $\theta_2 = 135^\circ$.

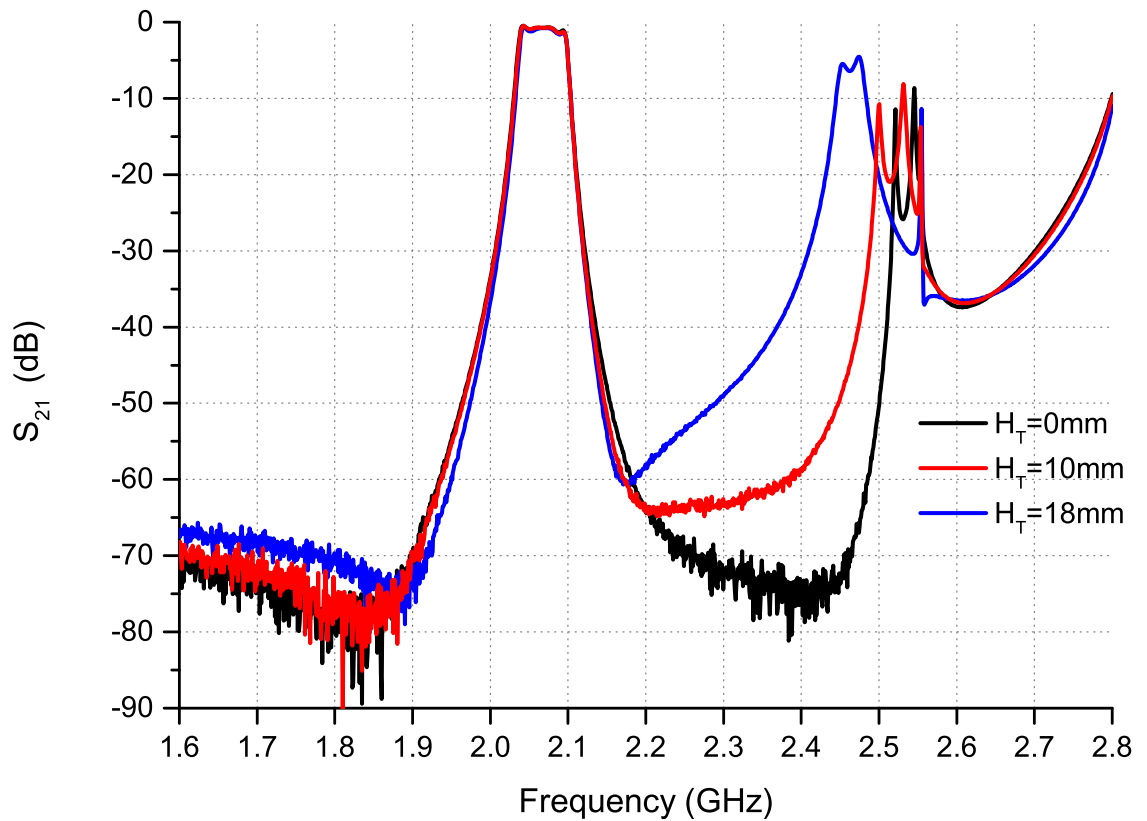


Figure 6.29: Control the TZ position by two tuning screws in measurement at $\theta_1 = 225^\circ$ and $\theta_2 = 135^\circ$.

of the resonance frequency. The TZs occurred at 2.21 GHz and 1.928 GHz.

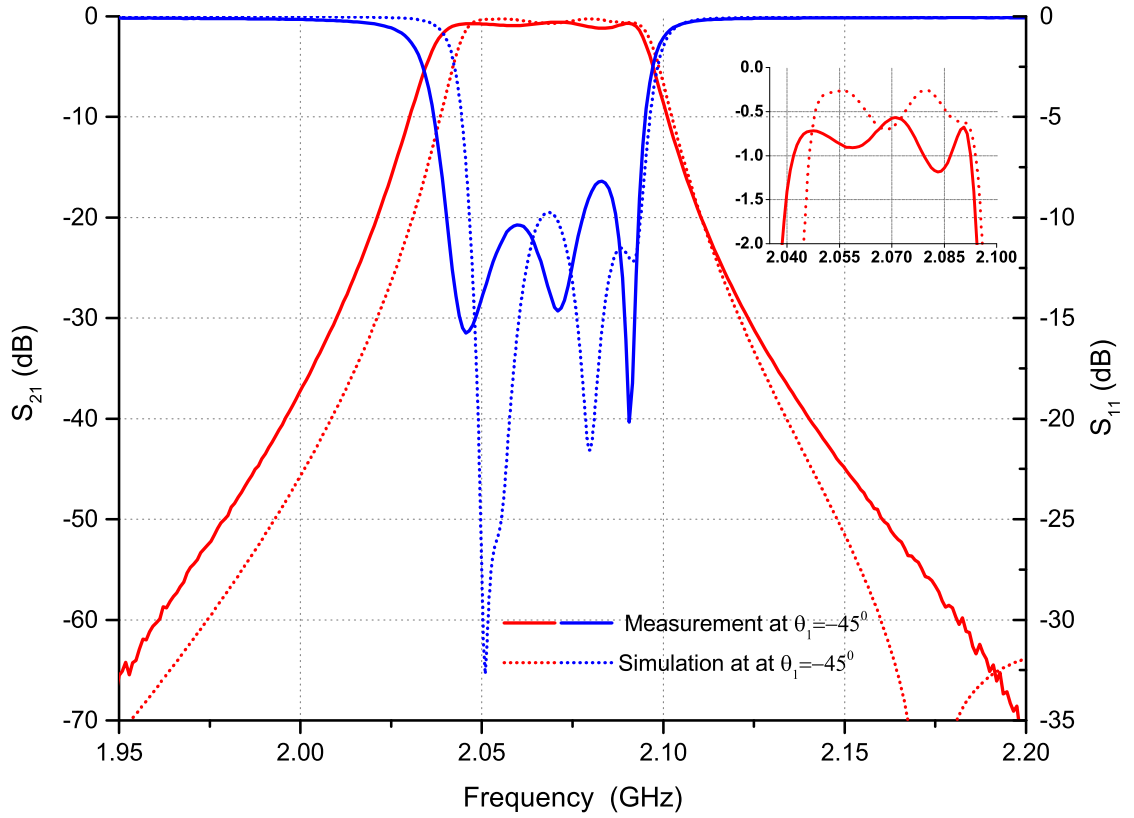


Figure 6.30: Simulated and measured response of 4th order HE_{11} dual-mode filter at $\theta_1 = 315^\circ$ and $\theta_2 = 135^\circ$.

Table 6.4 illustrates the figure-of-merits and extensive comparisons between the novel HE_{11} dual-mode resonator designs and the published research works with the same dual-mode.

Table 6.4: Comparison of HE_{11} dual-mode filter with the state-of-the arts.

Ref.	Resonant frequency (GHz)	Size (cm^3)	Q_u	spurious-free window (MHz)	ϵ_r
[39]	3.949	24.29	8000	300	37.25
[51]	1.857	250.4	6000	820	metal
[53]	0.942	274.6	6300	480	45
This work	2.05	18.15	5500	500	43

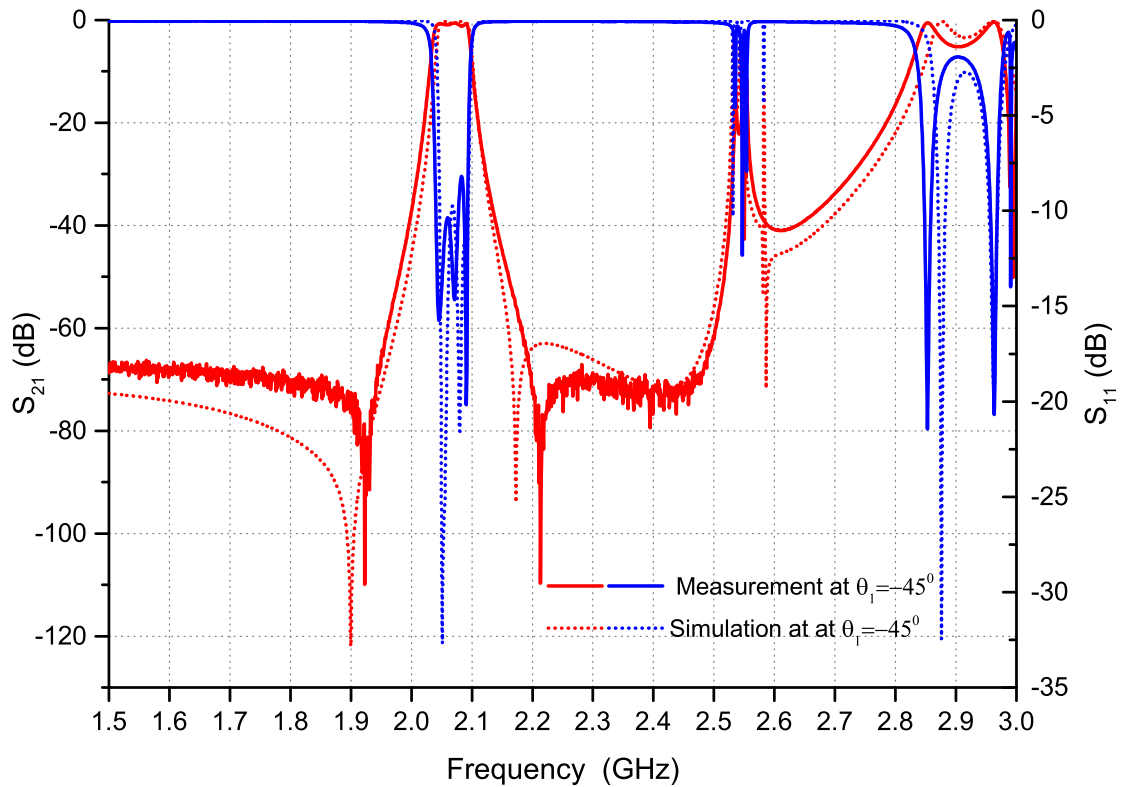


Figure 6.31: Simulated and measured broadband response of 4th order HE_{11} dual-mode filter at $\theta_1 = 315^\circ$ and $\theta_2 = 135^\circ$.

6.8 Summary

A HE_{11} dual-mode 4th order filter with high Q-factor has been designed. The ceramic was shorted from the bottom side to the base of the copper cavity. The filter offers a significant reduction in volume compared to the air-filled coaxial filter which is at the same frequency and Q-factor. The I/O and the intra-cavity coupling were implemented by connecting the coaxial probe to the grounded post. The simulation result showed that the filter has low losses when under loaded and the suppression was constant compared with eigen-mode analysis. The position of the inter-resonator hole had a significant effect on the position of TZs as proven by the simulation and the mathematical model. A TZ was observed no matter where the hole was oriented. The number of TZs above the inband is equal to that of the lower band. A good agreement between the measurement and simulation results has been demonstrated.

Chapter 7

Triple-Mode Filter with Splitted Dielectric Resonator Pucks

7.1 Introduction

A high-performance compact size bandpass filter is required in cellular base stations. Triple-mode is a possible way to miniaturise the filter. Researchers are becoming interested in how to bring about reduction in size of filter. This chapter discusses a new triple-mode dielectric resonator filter using two piece of ceramic puck. A triple-mode resonator can be achieved by a dual-mode of EH_{11} with a different mode that has the same resonant frequency. The filter presented in this work offers a high Q factor for the dual-mode and is different from the other modes. A high reduction volume ratio is offered with an easy coupling structure compared to the existing concept. The I/O coupling was achieved by a $50\ \Omega$ coaxial probe and the inter-resonator was made by etching a vertical hole through the two of ceramic pucks and also the length of the I/O probes. Tuning screws were used to adjust the coupling values. One cavity was simulated by HFSS and a good spurious-free window was obtained.

7.2 Triple-Mode Resonator Cavity

Figure 7.1 depicts the configuration of a triple-mode dielectric resonator. It consists of a two-piece of dielectric puck with a high permittivity suspended in the middle of a cylindrical metallic cavity. D_{res} and L_{res} are the diameter and length of the DR while D_{cav} and L_{cav} are the diameter and length of the metallic cavity. t_{rg} , t_g are the gap between the ceramic pucks and the cavity side wall. The

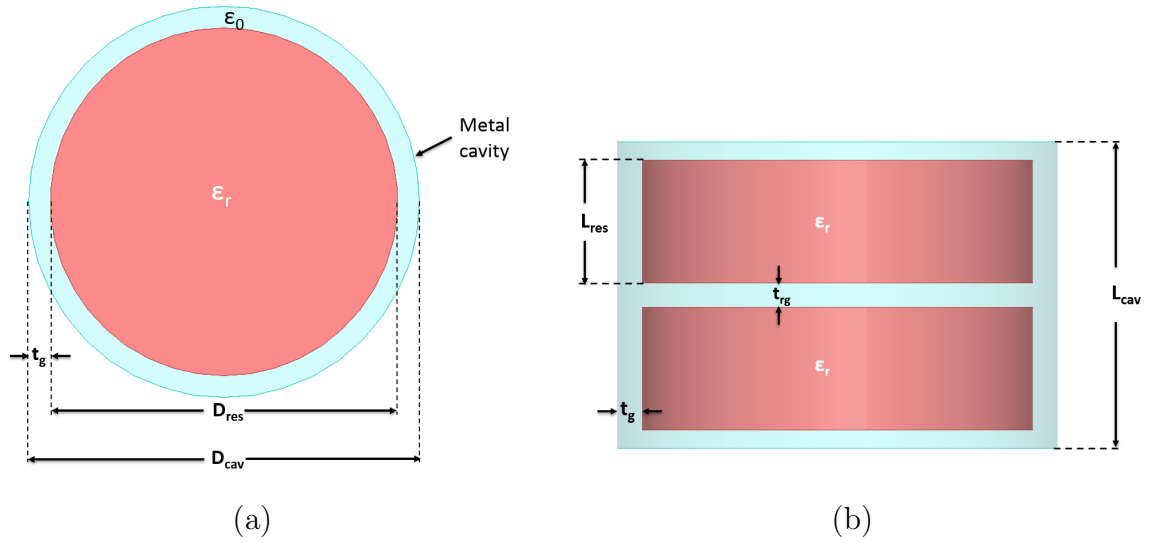


Figure 7.1: Configuration of triple-mode DR (a) Top view, (b) Side view.

ceramic material used in this work is barium titanate with a relative permittivity of 43 and loss tangent of 4×10^{-5} . The metal cylindrical cavity is made from copper with conductivity 4×10^7 S/m. In order to choose the optimum dimensions, HFSS software was used to calculate the resonance frequency and unloaded Q factors for the DR. Table 7.1 illustrates the resonance frequencies, Q_u and the mode type. From the column unpatterned ceramic(UNP) the triple-mode was produced by EH_{11} dual-mode, $TE_{01\delta}$ mode at resonance frequency of 1.96 GHz. The dimensions of the resonator at this frequency were $D_{cav}=36$ mm, $D_{res}=32$, $L_{cav}=25$ mm, $L_{res}=10$ mm and $t_{rg}=2$ mm. Parametric study has been applied to show the effect of parameters on the f_r , Q_u and the spurious-free window. Figure 7.2 shows the resonant frequencies against the variation in the gap between the ceramic pucks (t_{rg}). It was observed that the dominant mode is $TE_{01\delta}$ at $t_{rg} < 1.75$

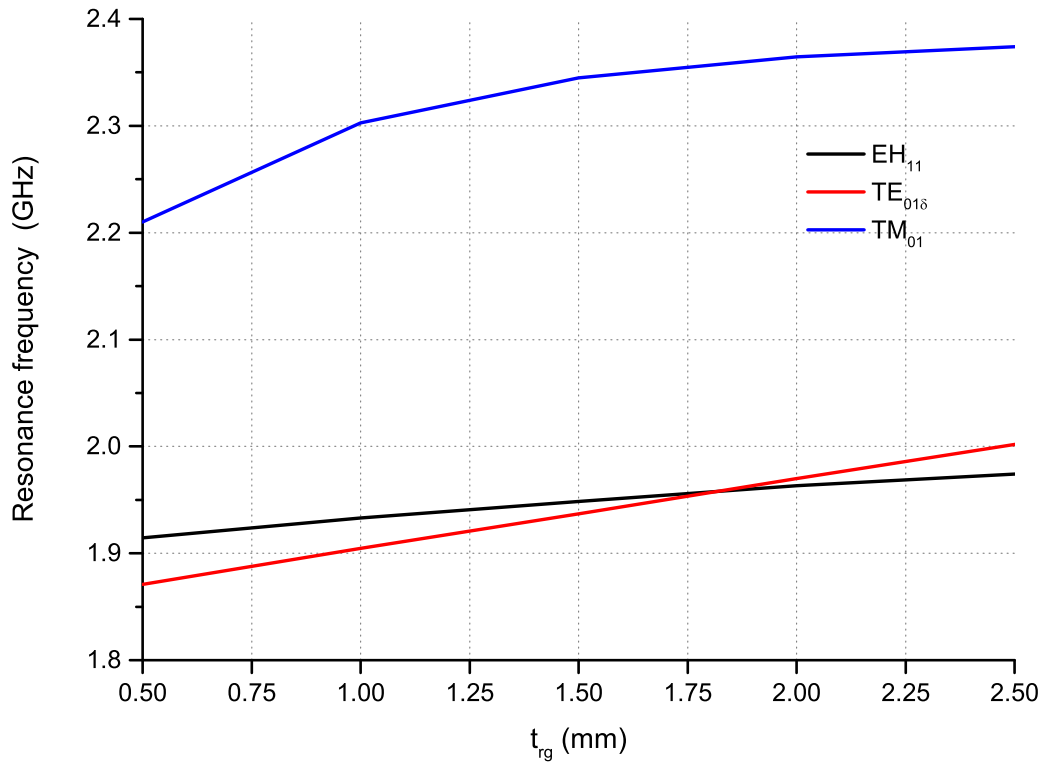


Figure 7.2: Resonant frequencies against t_{rg} .

mm and the second mode is a EH_{11} that occurred at 1.9 GHz. TM_{01} increased to about 200 MHz when t_{rg} increased to 2 mm while the second mode rose gradually and converge at the former. At t_{rg} 1.75 mm, the triple-mode was achieved and the maximum spurious-free window was recorded at 2 mm. The gap between the dielectric pieces and from the side wall was 2 mm and from the top and bottom faces it was about 1.5 mm. The spurious-free window is about 400 MHz, which offers good suppression in multi-mode dielectric resonator filters. The reduction volume ratio is 15.6% compared with an air-filled coaxial filter at $\sqrt{\epsilon_r}Z_0$ equal 77 Ω .

The E and H-field pattern at the operation resonant frequency of 1.95 GHz is shown in Figure 7.3. It can be seen that the E field for the dual-mode EH_{11} varies and is concentrated between the dielectric puck and the side wall of the cavity. A weak E field was seen around the top and bottom, while $TE_{01\delta}$ varies by θ and was concentrated in the middle of the metal cavity. The maximum H field was in the middle of each dielectric pieces for the EH_{11} dual-mode, while it cuts across both pieces for the other mode. From the field pattern, a good method to couple

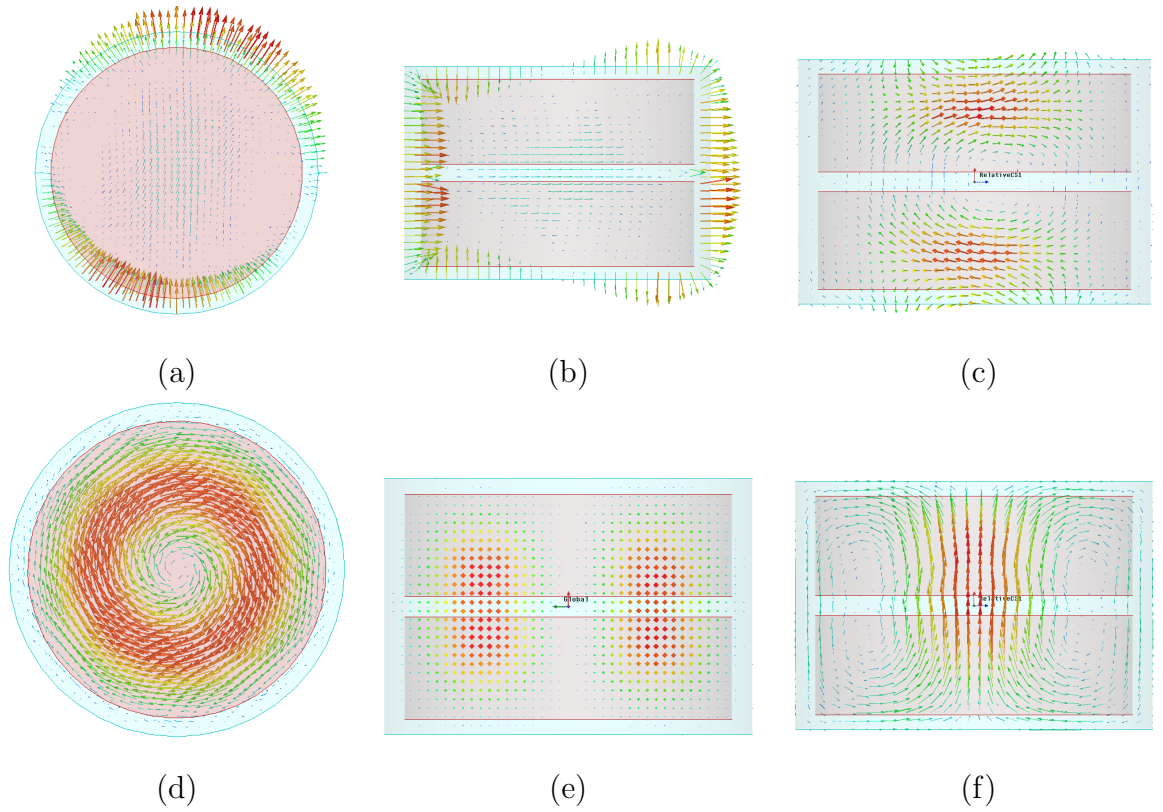


Figure 7.3: E and H field pattern (a) and (b) E-field for EH_{11} (c) H-field for EH_{11} (d) and (e) E-field for $TE_{01\delta}$ (c) H-field for $TE_{01\delta}$.

this cavity is by using an E field. Because the distance between the dielectric puck and the wall cavity is small and so it is difficult to couple the probes, the vertical etching through the ceramic puck allows for the probe to be positioned from the top or bottom of the cavity. Figure 7.4 illustrates the triple-mode resonator with cut-out rectangular cubic shapes from each dielectric in four positions. The cubic has dimensions L_i, W_i, L_{res} . The result for $W_i = L_i = 3$ mm is shown in Table 7.1. There is no effect on the sequence of modes which were increased by 28 MHz and the TM_{01} mode rose by 16 MHz. The Q_u was the same as for the UNP ceramic puck in which $TE_{01\delta}$ was increased by 585.

The coupling mechanism in the triple-mode resonator is similar to that in the dual-mode if these modes are perpendicular. The challenge of using different-type modes is that any discontinuity inserted into the cavity will cause changes in both frequency and sequence. To design a coupling technique, there is a need to factor in the effect of change in the probe properties (length, diameter, orientation), the

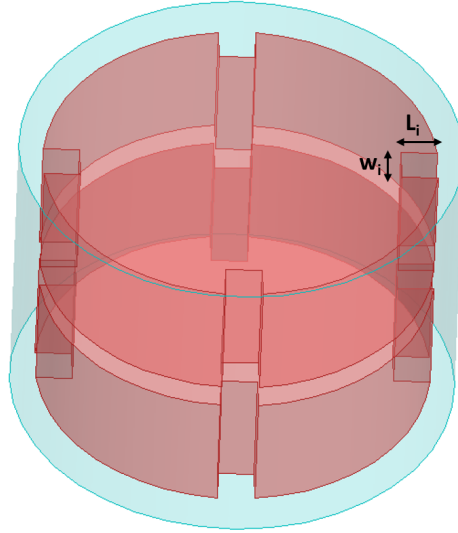


Figure 7.4: Triple-mode resonator with vertical etching from the side of the DRs.

Table 7.1: Comparison of simulated resonance frequency (f_r), mode type and Q_u for the cavity resonator with unpatterned (UNP) and vertically-etched(V-E) structures in triple-mode cavity.

Mode	f_r (GHz)		Q_u -factor		Type	
	UNP	V-E	UNP	V-E	UNP	V-E
EH_{11}	1.96	1.989	11200	11195	Dual	Dual
$TE_{01\delta}$	1.97	2.005	7000	7585	single	single
TM_{01}	2.36	2.376	14700	14587	single	single

hole size on the three modes and also their sequence.

7.3 The Coupling Mechanism

As displayed in the field pattern in Figure 7.3, the best way to couple the triple-mode is by connecting the probe from the top to bottom by inserting it through the vertical etch. Figure 7.5 presents the coupling structure for the proposed triple-mode DR filter.

Figure 7.6 illustrates the external Q- factor against the length of the probe (L_{fh}) at the diameter of the copper probe (d_f) which is equal to 2 mm. It can be seen that the Q_e is rapidly decreased when L_{fh} increases from 5 mm to 15 mm while

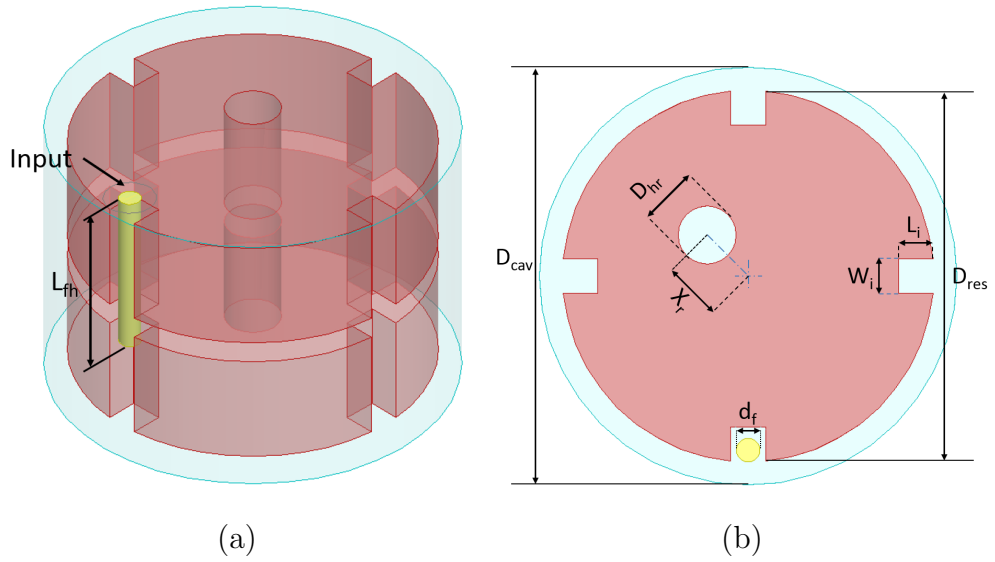


Figure 7.5: I/O and inter-resonator coupling for triple-mode cavity (a) 3D view (b) top view.

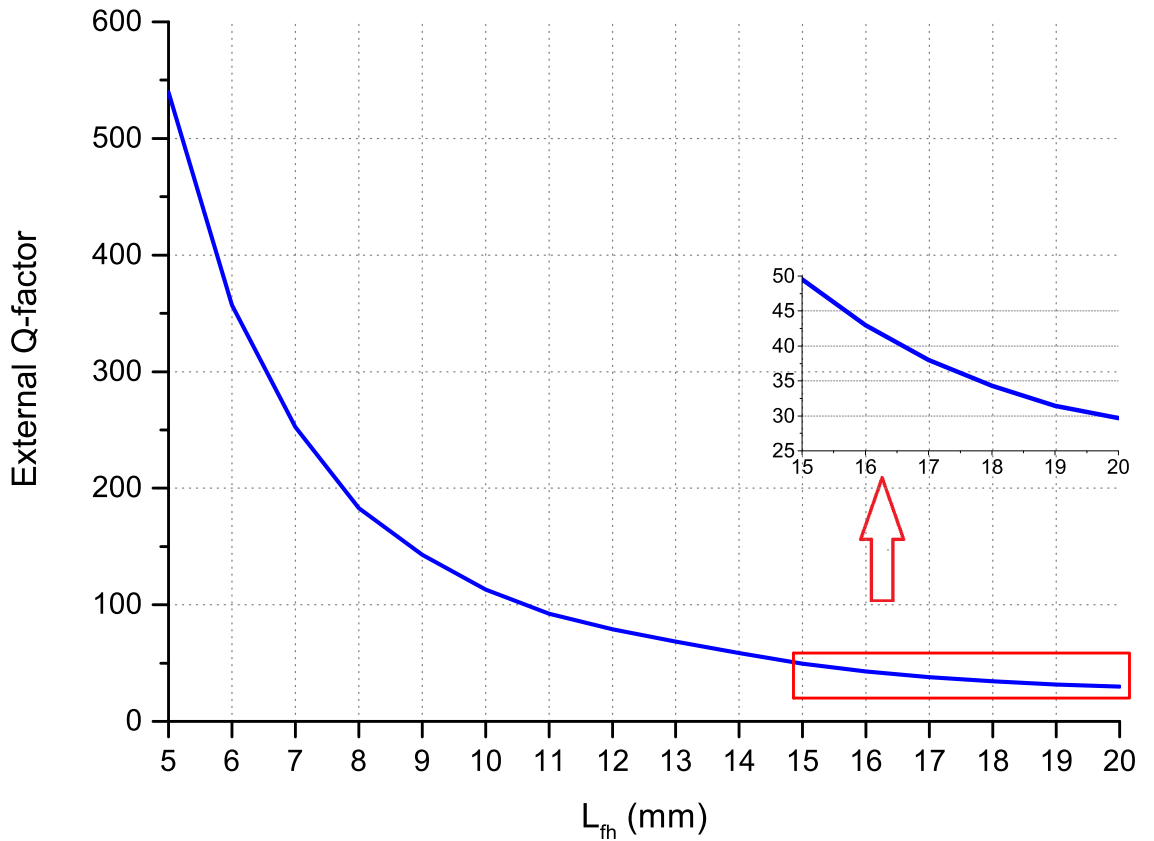


Figure 7.6: External Q-factor varying with length of I/O coupling probe.

it gradually decreased when $L_{fh} > 15$ mm. A narrow bandwidth can be achieved by this technique. The resonant frequencies of the modes can be affected by the variation of L_{fh} , as provided in Figure 7.7. It was observed that, when L_{fh} increased, the EH_{11} dual-mode decreased while the $TE_{01\delta}$ remained constant. From

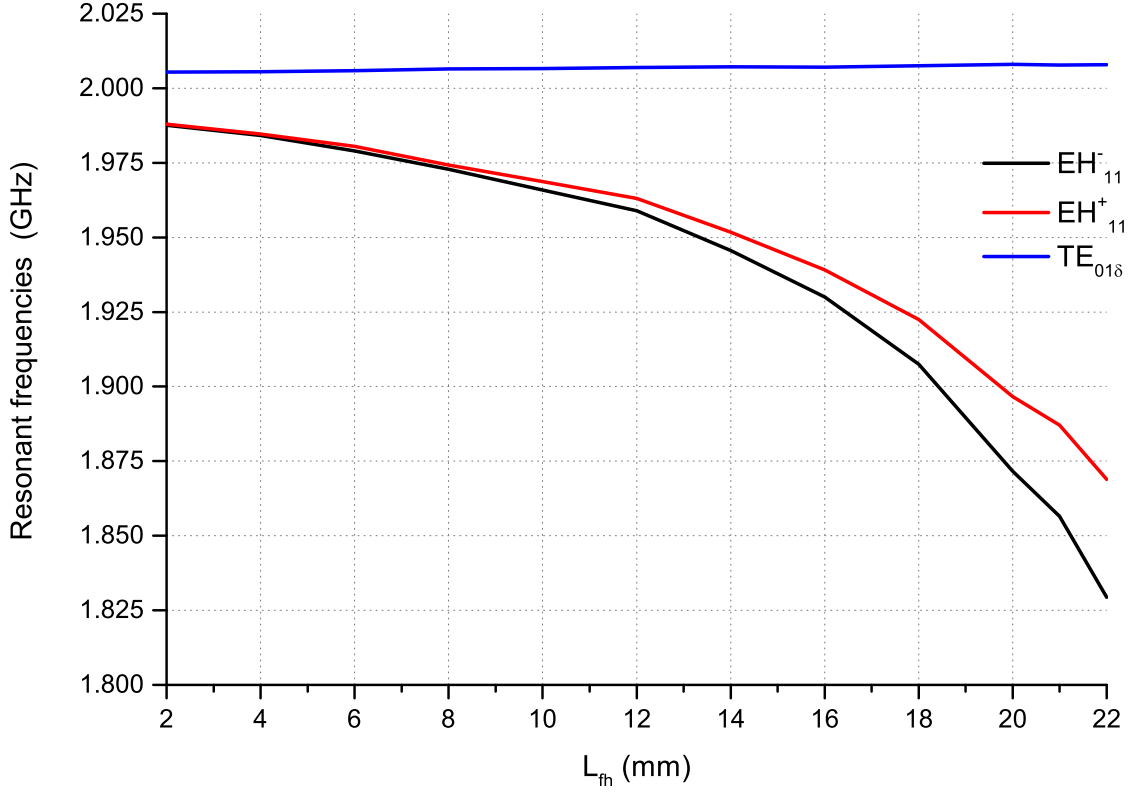


Figure 7.7: Resonant frequencies varying with length of I/O coupling probe.

8 mm, the EH_{11} dual-mode started to separate from each other and coupling sets between them.

Positioning an etching hole at 45° with respect to EH_{11}^- on each DR has a significant effect on the resonant frequencies as displayed in Figure 7.8. The plotted figure was at the diameter of the vertical etching hole (D_{hr}), which is equal to 4 mm. The $TE_{01\delta}$ increased to about 70 MHz when the distance between the centres of the DR and etching hole (X_r) changed from 0 to 9 mm. The decrease was of 30 MHz in other modes at the same range of X_r . The effect of having tuning screws through the vertical etching hole and from the side wall of the metallic cavity has been investigated.

Figure 7.9 shows the relationship between the resonant frequencies for the triple-mode and the length of the tuning screw (L_{TT}) which was connected at the top of the cavity. The screw diameter is 4 mm while the X_r and D_{hr} are 5 mm. The resonance frequency of the EH_{11}^- mode was increased to about 15 MHz and the EH_{11}^+ mode decreased to about 40 MHz while the $TE_{01\delta}$ mode was slightly increased. The frequency difference between the modes at L_{TT} equal to zero is caused by the

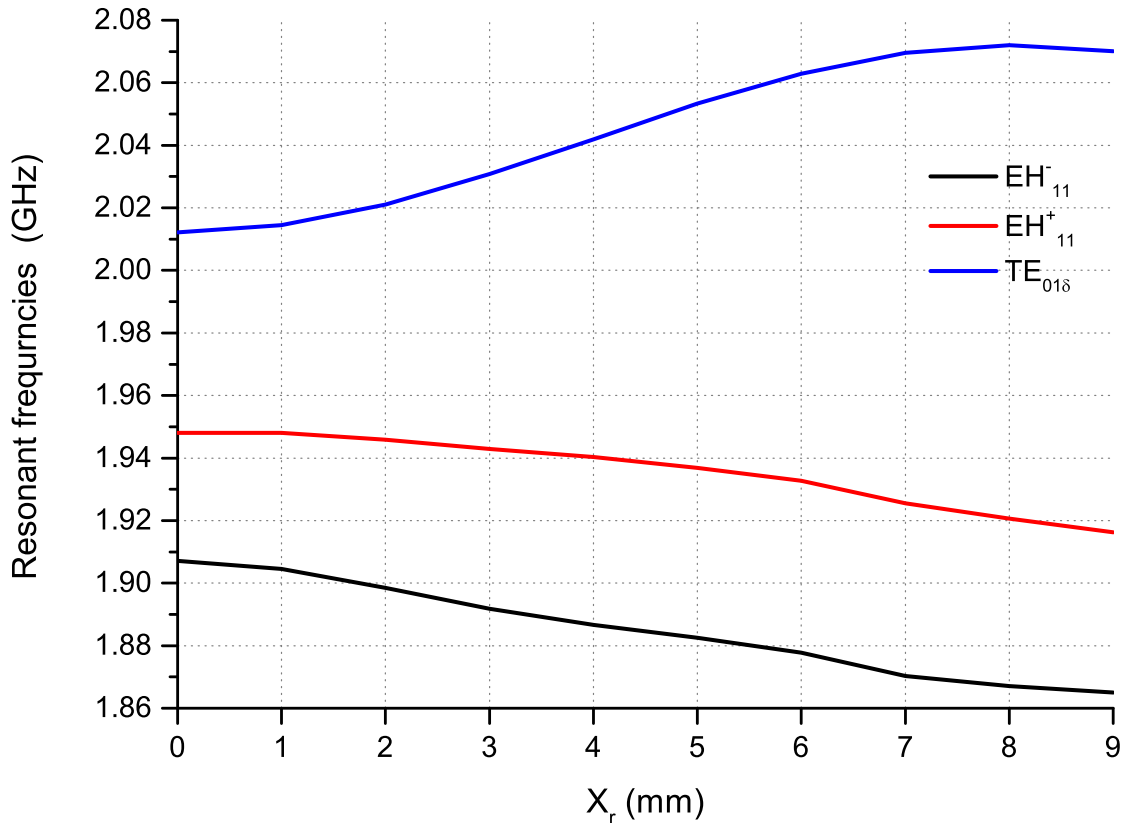


Figure 7.8: Resonant frequencies varying with offset of hole (X_r).

vertical etching hole coupling.

Figure 7.10 presents results for the variation of the resonant frequencies of the triple-mode with the length of screw (L_{TS}) from the side wall of the cavity. The screw diameter was adjusted to 1.5 mm to achieve a proper fit into the gap between the two ceramic pieces. It was observed that the lower mode was significantly affected by L_{TS} , which decreased to about 90 MHz when the L_{TS} increased by 10 mm. The other mode remained at the same value during the changes in L_{TS} . This screw can be used as an inter-resonator coupling between the EH_{11} modes.

7.4 Simulation Result for One Cavity

In order to design a 3rd-order filter based on the triple-mode DR cavity, there is the need to use a parametric sweep in HFSS to obtain a satisfactory result. Figure 7.11 presents the configuration of the 3rd order filter by the triple-mode resonator cavity. The length of I/O coupling probe L_{fh} , distance from the centre of DR and

hole X_r and all parameters have been discussed in the previous section and are key in designing a triple-mode filter.

Table 7.2 displays the dimensions of all parameters that affect the coupling, which are calculated based on the typical performance.

Figure 7.12 shows the S-parameters response for a 3^{rd} order triple-mode DR filter without any tuning screws. A non-equal ripple of return loss at the inband region was observed and all values are less than 19 dB. The resonant frequency is 2.04 GHz, the Bw is 56 MHz under 19 dB and the maximum insertion loss in-band was about 0.1 dB. The first spurious frequency appeared at 2.426 GHz and the overall suppression window from the resonant frequency is about 382 MHz. Three TZs can be observed in the response: a pair of TZs occurred at 2.11 GHz and the other at 2.318 GHz. The pair of TZs are produced by the topology of the triple-mode filter at the resonance frequency, while the final one comes from the spurious band coupling topology.

Figure 7.13 shows the S-parameters response of the 3^{rd} order filter triple-mode

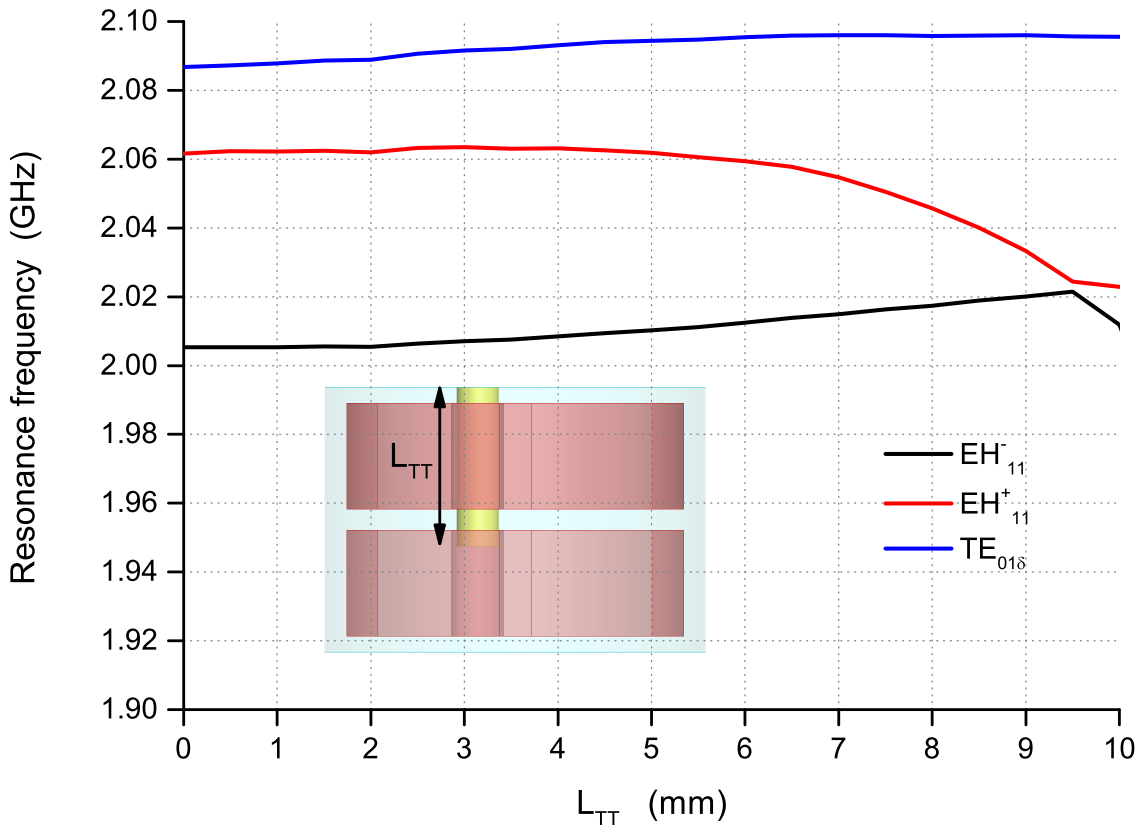


Figure 7.9: Resonant frequencies varying with L_{TT} .

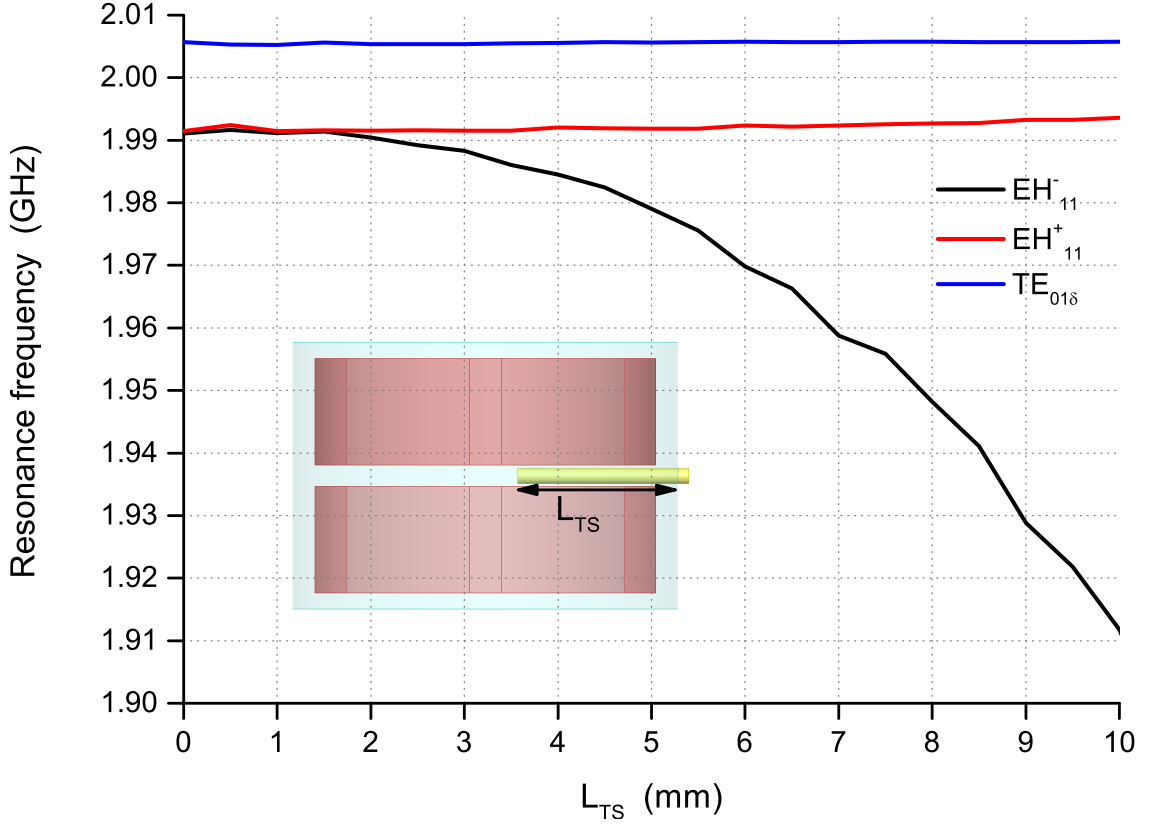


Figure 7.10: Resonant frequencies varying against L_{TS} .

Table 7.2: Typical dimensions of 3rd order filter triple-mode.

Typical dimensions		Typical performance
$L_{fh}=18$ mm	$D_{rh}=5$ mm	$f_0 = 2.044$ GHz
$W_i= 3$ mm	$L_i= 3$ mm	$\epsilon_r=43$
T1=4 mm	$L_{TS}= 4$ mm	$\tan \delta = 4 \times 10^{-5}$
diameter of $L_{fh}=2$ mm		$\sigma = 4 \times 10^7 S/m$
diameter of $L_{TS} = 1.5$ mm		

DR with tuning screws. It can be seen that the the inband ripples were equal and below 22 dB. The resonant frequency and bandwidth were the same as that shown in Figure 7.12. The second TZ and first spurious frequency were shifted backward to about 28 MHz and 36 MHz respectively, while the pair of TZs were increased to about 11 MHz. The extraction of Q-factor from the IL and group delay was about 8500, which is more than value of $TE_{01\delta}$. Table 7.3 illustrates the figure-of-merits and extensive comparisons between the novel proposed triple-mode resonator designs and the published research works with the same triple-mode. This design offers a significant improvements base on size and spurious-free

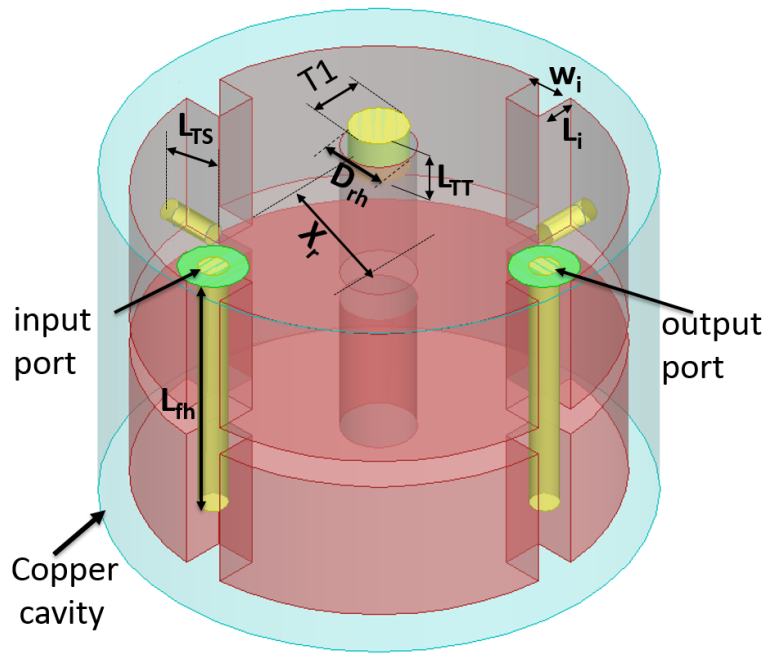


Figure 7.11: Structure of triple-mode 3rd order filter in HFSS.

window compared with other references.

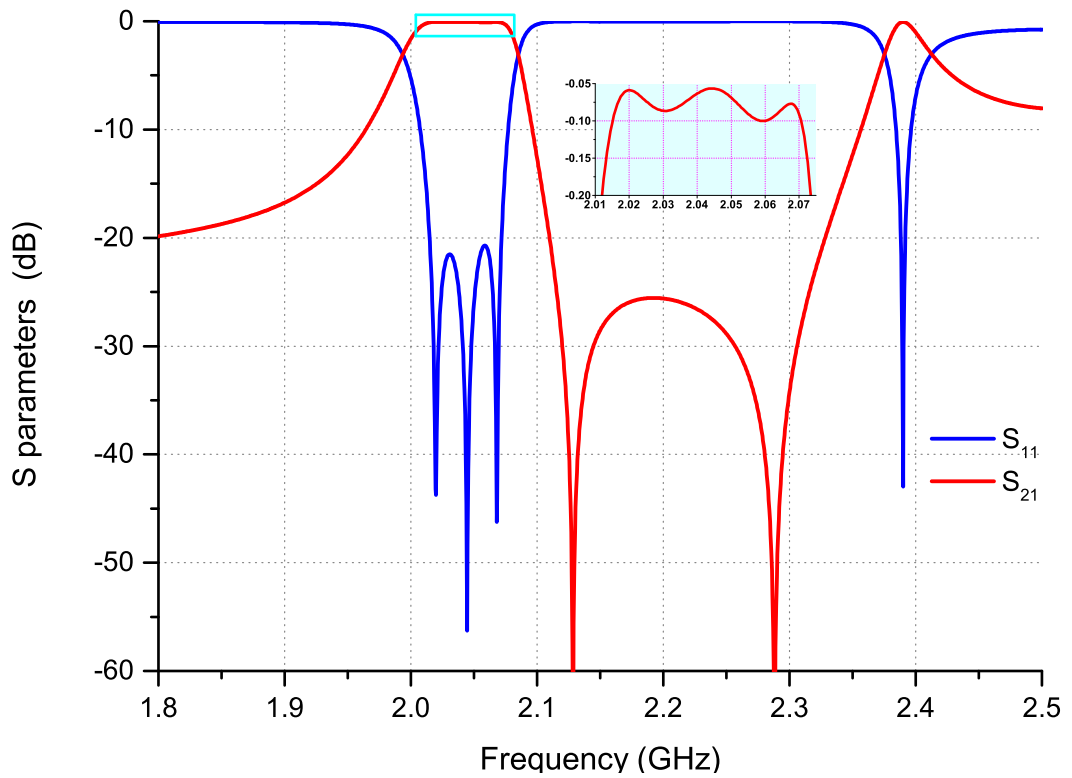


Figure 7.13: Frequency response of triple-mode filter with tuning screws.

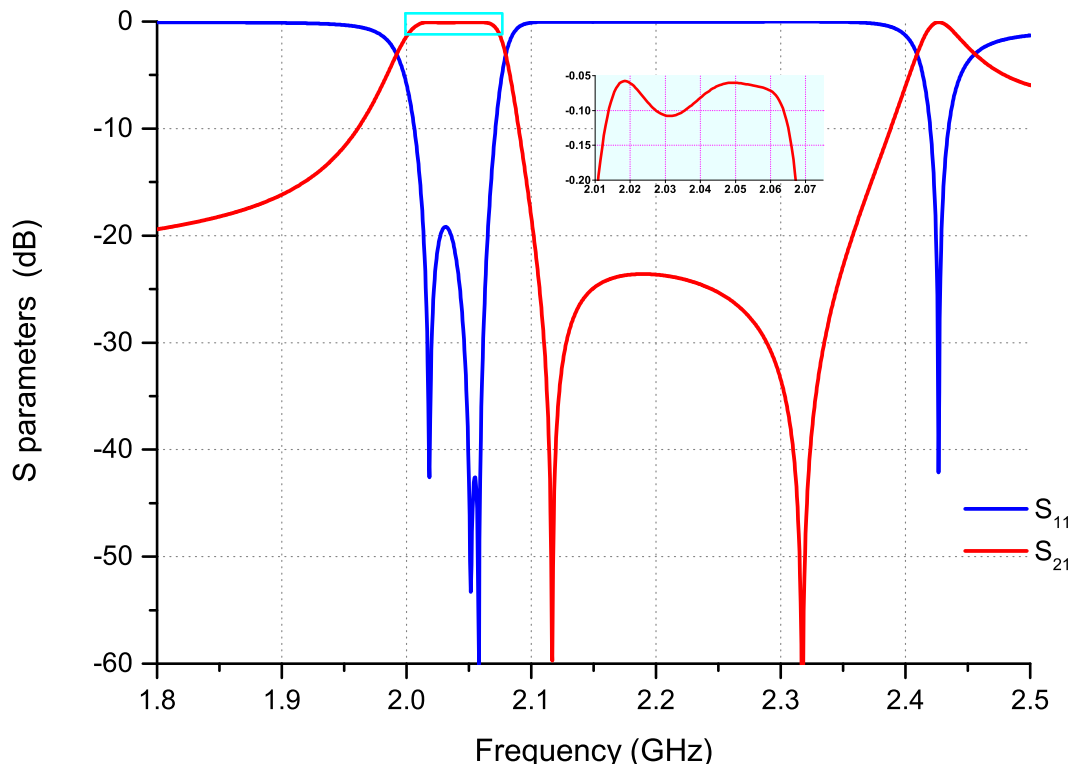


Figure 7.12: Frequency response of triple-mode filter without tuning screws.

Table 7.3: Comparison of the proposed triple-mode filter with other references.

Ref.	Resonant frequency (GHz)	Size (cm^3)	Q_u	spurious-free window (MHz)	ϵ_r
[69]	2.55	86.4	6000	230 down/340 up	40
[64]	2	260	18000	500	44
[80]	2	112.5	12000	-	38
This work	2.04	22.7	8500	500	43

7.5 Summary

A Novel triple-mode two piece of DR filter has been simulated with different mode types. It offers a high Q factor and 15.6% volume reduction ratio compared to an air coaxial filter and a good improvements compared with other references. The gap between the ceramic pieces has a significant effect on the resonant frequency and the sequence of the modes. The filter was operated at the cellular base station specification based on the resonant frequency and bandwidth. Two TZs appeared at the upper band region and the suppression under 20 dB was about 230 MHz.

Chapter 8

Conclusions and future work

8.1 Conclusions

Miniaturisation of microwave filters is important in cellular base stations as the filter consumes a big portion in an RF system. To reduce the losses power in the coaxial cable, filters should be connected to the antenna directly in top of mast. The aim of this thesis was to design a small filter unit without compromising the electrical performance. A dielectric resonator (DR) filter is one of the ways to reduce filter size. This thesis proposed two methods to miniaturise the filter volume: dual-mode DR filter and triple-mode DR. HFSS software can be used to simulate the filter in any 3D shape.

The novel $TE_{11\delta}$ dual-mode DR filter offers a significant volume reduction of about 11% compared to the air-filled coaxial filter. The resonator consists of a dielectric puck material with relative permittivity 43 and tangent loss of about 4×10^{-5} placed in the middle of the metallic cavity and grounded from the cylindrical face. The inter-resonator coupling for all types of filters was achieved by etching a hole through the ceramic puck at 45° with respect to the mode.

$TE_{11\delta}$ dual-mode DR filter planar structure was designed and fabricated with two different coupling techniques. The I/O and intra-cavity coupling were achieved by

placing the coaxial probe into the top or bottom face of the ceramic puck while the length of probe controls the amount of coupling. The measurement results of the 4th order Chebyshev filter indicate high losses in the filter with a 15 MHz shift in the resonant frequency, and the spurious-free window was reduced by about 400 MHz compared with eigen-mode analysis. The gap between the metallic cavity and the dielectric puck was responsible for the forward shift in the resonance frequency. The gap between the probe and ceramic puck significantly affected the coupling magnitude. The filter with a silver-painted strip line coupling technique provides high sensitivity when its dimensions are changed; the Q factor and the spurious-free window were worse compared with the probe coupling filter.

$TE_{11\delta}$ dual-mode filter entails etching two perpendicular holes through the ceramic puck in the centre of the cylindrical face was suggested to improve the spurious-free window. The result for the planar configuration of the 4th order filter features a high Q-factor and good spurious-free window of about 600 MHz from the fundamental frequency 1.96 GHz, while the inline structure shows a high suppression isolation which was about 800 MHz under -40 dB and the iris was used for intra-cavity coupling. Etching the ceramic puck by holes or slots from the top to the bottom does not affect the sequence of the modes in the DR and the fundamental mode is $TE_{11\delta}$. I/O coupling with T shape can be used to excite the filter. The practical result shows an upward shift in the resonant frequency of about 100 MHz due to the small gap between the metallic cavity and the ceramic puck. The spurious-free window was 820 MHz from the fundamental frequency 2.1 GHz .

Another new type of dual-mode DR filter is to shorten the base of the ceramic puck to the bottom side of the metallic cavity and have some space around the puck. HE_{11} dual-mode is the fundamental mode in this structure. The volume reduction ratio was 14% compared to the air-filled coaxial filter. Additionally, This design offers a significant improvements base on size and spurious-free window compared with other references. The I/O and the intra-cavity coupling were implemented by connecting the coaxial probe to the grounded post. A 4th order HE_{11} dual-mode

filter was simulated to obtain a potential result. To explain the position of the TZs, a new mathematical model for the dual-mode has been suggested. It shows that the filter still has a TZ in all cases of orientation of the hole for inter-resonator coupling. Two type of TZs can be classified in this model, complex and imaginary. The number of TZs above the inband is equal to the lower band.

An novel triple-mode splitted DR filter has been simulated with different mode types. It offers a high Q factor and 15.6% volume reduction ratio compared to the air coaxial filter and a good improvements compared with other references. The gap between the ceramic pieces has a significant effect on the resonant frequency and the sequence of the modes. A pair of TZs emerged at the upper band region and the suppression under 20 dB was about 230 MHz.

8.2 Future Work

Minimization of bandpass filter by multi-mode DR is introduced in this work. The work can be extended in several aspects. For example, a $TE_{11\delta}$ dual-mode with multi cavities could be designed. The DR could be designed with different aspects of D/L to improve the spurious-free window for the planner and inline configuration.

In term of the technical problem, the metallic cavity could be replaced by a thin ceramic layer coated in silver paint to avoid the perfect contact problem between the DR and the wall of the metallic cavity. Also, it is possible to connect single and multi-mode DRs as mono-block filter fabrication.

Another possible extension is discovering the multi-mode DR filter with different resonator mode (TEM mode and the TE or TH mode) and investigating that in respect of the Q-factor, size and the spurious-free window.

Base on improving the spurious-free window term, a cascaded BPF implemented by multi-mode DR with BSF can be investigated to remove the spurious band close

to the fundamental band. Furthermore, an LPF with a high clean spurious-free window cascaded connection can be interested, when the LPF is realized by a DR or any type is compatible with a multi-mode DR.

References

- [1] G. Matthaei, L. Young, and E. Jones, *Microwave Filters, Impedance-matching Networks, and Coupling Structures*. Artech House microwave library, Artech House Books, 1980.
- [2] I. C. Hunter, L. Billonet, B. Jarry, and P. Guillon, “Microwave filters-applications and technology,” *IEEE Transactions on Microwave Theory and Techniques*, vol. 50, pp. 794–805, Mar 2002.
- [3] R. Cameron, R. Mansour, and C. Kudsia, *Microwave Filters for Communication Systems: Fundamentals, Design and Applications*. Wiley, 2007.
- [4] I. Hunter, *Theory and Design of Microwave Filters*. Electromagnetics and Radar Series, Institution of Engineering and Technology, 2001.
- [5] G. Zhang, M. J. Lancaster, and F. Huang, “Realization of four transmission zeros in a four-pole superconducting microstrip filter using cross-shaped spiral resonators,” *IEEE Transactions on Applied Superconductivity*, vol. 15, pp. 3927–3931, Dec 2005.
- [6] T. Yu, C. Li, F. Li, Q. Zhang, L. Sun, X. Zhang, A. He, H. Li, Q. Luo, C. Gu, H. Tian, D. Zheng, C. Gao, and Y. He, “A novel quasi-elliptic hts filter with group-delay equalization using compact quasi-lumped element resonators in vhf band,” *IEEE Transactions on Applied Superconductivity*, vol. 19, pp. 69–75, April 2009.

- [7] C. Montgomery, *Technique of Microwave Measurements. Edited by C.G. Montgomery, Etc.* [Massachusetts Institute of Technology. Radiation Laboratory Series. no. 11.], McGraw-Hill Book Company, 1947.
- [8] R. D. Richtmyer, "Dielectric Resonators," *Journal of Applied Physics*, vol. 10, pp. 391–398, June 1939.
- [9] A. Okaya and L. F. Barash, "The dielectric microwave resonator," *Proceedings of the IRE*, vol. 50, pp. 2081–2092, Oct 1962.
- [10] S. B. Cohn, "Microwave bandpass filters containing high-q dielectric resonators," *IEEE Transactions on Microwave Theory and Techniques*, vol. 16, pp. 218–227, Apr 1968.
- [11] E. Snitzer, "Cylindrical dielectric waveguide modes," *JOSA*, vol. 51, no. 5, pp. 491–498, 1961.
- [12] D. L. Rebsch, D. C. Webb, R. A. Moore, and J. D. Cowlishaw, "A mode chart for accurate design of cylindrical dielectric resonators (correspondence)," *IEEE Transactions on Microwave Theory and Techniques*, vol. 13, pp. 468–469, Jul 1965.
- [13] Y. Kobayashi and S. Tanaka, "Resonant modes of a dielectric rod resonator short-circuited at both ends by parallel conducting plates," *IEEE Transactions on Microwave Theory and Techniques*, vol. 28, pp. 1077–1085, Oct 1980.
- [14] K. A. Zaki and C. Chen, "New results in dielectric-loaded resonators," *IEEE Transactions on Microwave Theory and Techniques*, vol. 34, pp. 815–824, Jul 1986.
- [15] W. H. Harrison, "A miniature high-q bandpass filter employing dielectric resonators," *IEEE Transactions on Microwave Theory and Techniques*, vol. 16, pp. 210–218, Apr 1968.

- [16] D. J. Masse, R. A. Pucel, D. W. Readey, E. A. Maguire, and C. P. Hartwig, "A new low-loss high-k temperature-compensated dielectric for microwave applications," *Proceedings of the IEEE*, vol. 59, pp. 1628–1629, Nov 1971.
- [17] K. Wakino, T. Nishikawa, S. Tamura, and Y. Ishikawa, "Microwave bandpass filters containing dielectric resonators with improved temperature stability and spurious response," in *1975 IEEE-MTT-S International Microwave Symposium*, pp. 63–66, May 1975.
- [18] K. A. Zaki and A. E. Atia, "Modes in dielectric-loaded waveguides and resonators," *IEEE Transactions on Microwave Theory and Techniques*, vol. 31, pp. 1039–1045, Dec 1983.
- [19] R. R. Mansour, "High- q tunable dielectric resonator filters," *IEEE Microwave Magazine*, vol. 10, pp. 84–98, Oct 2009.
- [20] R. R. Mansour, "Filter technologies for wireless base stations," *IEEE Microwave Magazine*, vol. 5, pp. 68–74, Mar 2004.
- [21] L. Matthaei, "Comb-line bandpass filters of narrow or moderate bandwidth," *Microwave Journal*, vol. 5, pp. 82–91, August 1963.
- [22] M. E. Sabbagh, K. A. Zaki, H.-W. Yao, and M. Yu, "Full-wave analysis of coupling between combline resonators and its application to combline filters with canonical configurations," *IEEE Transactions on Microwave Theory and Techniques*, vol. 49, pp. 2384–2393, Dec 2001.
- [23] M. Höft and S. Burger, "Q-factor improvement of combline resonators," in *2005 German Microwave Conference (GeMiC)*, 2005.
- [24] G. Shen and D. Budimir, "Novel resonator structures for combline filter applications," in *2002 32nd European Microwave Conference*, pp. 1–3, Sept 2002.
- [25] C. Wang, K. A. Zaki, A. E. Atia, and T. G. Dolan, "Dielectric combline resonators and filters," *IEEE Transactions on Microwave Theory and Techniques*, vol. 46, pp. 2501–2506, Dec 1998.

- [26] N. E. A. Rashid, M. T. Ali, and N. Hamzah, "Properties of dielectric combine resonator for base station filters," in *2004 RF and Microwave Conference (IEEE Cat. No.04EX924)*, pp. 76–79, Oct 2004.
- [27] D. Pozar, *Microwave Engineering*. Wiley, 2004.
- [28] D. Kajfez and P. Guillon, *Dielectric Resonators*. Artech House microwave library, Noble Publishing Corporation, 1998.
- [29] C. Wang and K. A. Zaki, "Dielectric resonators and filters," *IEEE Microwave Magazine*, vol. 8, pp. 115–127, Oct 2007.
- [30] J. Hong and J. Lancaster, *Microstrip Filters for RF/Microwave Applications*. Wiley, 2001.
- [31] J. S. Hong and M. J. Lancaster, "Realisation of quasielliptic function filter using dual-mode microstrip square loop resonators," *Electronics Letters*, vol. 31, pp. 2085–2086, Nov 1995.
- [32] A. C. Kundu and I. Awai, "Control of attenuation pole frequency of a dual-mode microstrip ring resonator bandpass filter," *IEEE Transactions on Microwave Theory and Techniques*, vol. 49, pp. 1113–1117, Jun 2001.
- [33] J. S. Hong, H. Shaman, and Y. H. Chun, "Dual-mode microstrip open-loop resonators and filters," *IEEE Transactions on Microwave Theory and Techniques*, vol. 55, pp. 1764–1770, Aug 2007.
- [34] J.-S. Hong and S. Li, "Theory and experiment of dual-mode microstrip triangular patch resonators and filters," *IEEE Transactions on Microwave Theory and Techniques*, vol. 52, pp. 1237–1243, April 2004.
- [35] M. Sagawa, M. Makimoto, and S. Yamashita, "Geometrical structures and fundamental characteristics of microwave stepped-impedance resonators," *IEEE Transactions on Microwave Theory and Techniques*, vol. 45, pp. 1078–1085, Jul 1997.

- [36] H.-W. Wu, S.-K. Liu, M.-H. Weng, and C.-H. Hung, "Compact microstrip bandpass filter with multispurious suppression," *Progress In Electromagnetics Research*, vol. 107, pp. 21–30, 2010.
- [37] C. Wilker, Z.-Y. Shen, P. Pang, W. L. Holstein, and D. W. Face, "Nonlinear effects in high temperature superconductors: 3rd order intercept from harmonic generation," *IEEE Transactions on Applied Superconductivity*, vol. 5, pp. 1665–1670, June 1995.
- [38] R. R. Mansour, B. Jolley, S. Ye, F. S. Thomson, and V. Dokas, "On the power handling capability of high temperature superconductive filters," *IEEE Transactions on Microwave Theory and Techniques*, vol. 44, pp. 1322–1338, Jul 1996.
- [39] S. J. Fiedziuszko, "Corrections to "dual mode dielectric resonator loaded cavity filters"," *IEEE Transactions on Microwave Theory and Techniques*, vol. 31, pp. 315–315, Mar 1983.
- [40] K. A. Zaki, C. Chen, and A. E. Atia, "Canonical and longitudinal dual-mode dielectric resonator filters without iris," *IEEE Transactions on Microwave Theory and Techniques*, vol. 35, pp. 1130–1135, Dec 1987.
- [41] Y. Kobayashi and K. Kubo, "Canonical bandpass filters using dual-mode dielectric resonators," in *1987 IEEE MTT-S International Microwave Symposium Digest*, vol. 1, pp. 137–140, May 1987.
- [42] S. W. Chen and K. A. Zaki, "A novel coupled method for dual-mode dielectric resonators and waveguide filters," *IEEE Transactions on Microwave Theory and Techniques*, vol. 38, pp. 1885–1893, Dec 1990.
- [43] K. A. Zaki, C. Chen, and A. E. Atia, "A new realization of dual mode dielectric resonator filters," in *1987 17th European Microwave Conference*, pp. 169–174, Sept 1987.

- [44] D. Mirshekar-Syahakal, C. W. Sim, and J. M. Chuma, "Stacked and planar dual-mode filters using dielectric loaded rectangular cavity resonator," in *ICMMT 2000. 2000 2nd International Conference on Microwave and Millimeter Wave Technology Proceedings (Cat. No.00EX364)*, pp. 100–103, 2000.
- [45] G. Macchiarella, M. Fumagalli, and S. C. D'Oro, "A new coupling structure for dual mode dielectric resonators," *IEEE Microwave and Guided Wave Letters*, vol. 10, pp. 523–525, Dec 2000.
- [46] M. Fumagalli, G. Macchiarella, and G. Resnati, "Dual-mode filters for cellular base stations using metallized dielectric resonators," in *2001 IEEE MTT-S International Microwave Symposium Digest (Cat. No.01CH37157)*, vol. 3, pp. 1799–1802 vol.3, May 2001.
- [47] D. Baillargeat, S. Verdeyme, and P. Guillon, "Slotted dielectric resonators for rigorous design of a four-poles dual mode filter," *IEEE Microwave and Guided Wave Letters*, vol. 4, pp. 332–334, Oct 1994.
- [48] L. Accatino, G. Bertin, M. Mongiardo, and G. Resnati, "Dual-mode filters with grooved/splitted dielectric resonators for cellular-radio base stations," *IEEE Transactions on Microwave Theory and Techniques*, vol. 50, pp. 2882–2889, Dec 2002.
- [49] L. Ji-Fuh and W. D. Blair, "High- Q TE_{01} mode DR filters for PCS wireless base stations," *Microwave Theory and Techniques, IEEE Transactions on*, vol. 46, no. 12, pp. 2493–2500, 1998.
- [50] T. Nishikawa, K. Wakino, K. Tsunoda, and Y. Ishikawa, "Dielectric high-power bandpass filter using quarter-cut $TE_{01\delta}$ image resonator for cellular base stations," in *Microwave Symposium Digest, 1987 IEEE MTT-S International*, vol. 1, pp. 133–136.
- [51] W. Chi, K. A. Zaki, A. E. Atia, and T. G. Dolan, "Conductor loaded resonator filters with wide spurious-free stopbands," *Microwave Theory and Techniques, IEEE Transactions on*, vol. 45, no. 12, pp. 2387–2392, 1997.

- [52] S. J. Fiedziuszko, “‘engine-block’, dual mode dielectric resonator loaded cavity filter with nonadjacent cavity couplings,” in *Microwave Symposium Digest, 1984 IEEE MTT-S International*, pp. 285–287.
- [53] I. C. Hunter, J. Rhodes, and V. Dassonville, “Dual-mode filters with conductor-loaded dielectric resonators,” *Microwave Theory and Techniques, IEEE Transactions on*, vol. 47, no. 12, pp. 2304–2311, 1999.
- [54] H. Hai and W. Ke-Li, “A TM_{11} dual-mode dielectric resonator filter with planar coupling configuration,” *Microwave Theory and Techniques, IEEE Transactions on*, vol. 61, no. 1, pp. 131–138, 2013.
- [55] A. Panariello, Y. Ming, and C. Ernst, “Ku-band high power dielectric resonator filters,” *Microwave Theory and Techniques, IEEE Transactions on*, vol. 61, no. 1, pp. 382–392, 2013.
- [56] M. Höft, “Y-shape dielectric dual-mode resonator,” *Microwave Theory and Techniques, IEEE Transactions on*, vol. 56, no. 12, pp. 3066–3071, 2008.
- [57] W. Chi, K. A. Zaki, and A. E. Atia, “Dual mode combined dielectric and conductor loaded cavity filters,” in *Microwave Symposium Digest, 1997., IEEE MTT-S International*, vol. 2, pp. 1103–1107 vol.2.
- [58] R. R. Mansour, “Dual-mode dielectric resonator filters with improved spurious performance,” in *Microwave Symposium Digest, 1993., IEEE MTT-S International*, pp. 439–442 vol.1.
- [59] S. W. Chen and K. A. Zaki, “Dielectric ring resonators loaded in waveguide and on substrate,” *Microwave Theory and Techniques, IEEE Transactions on*, vol. 39, no. 12, pp. 2069–2076, 1991.
- [60] D. D. Fernando, I. C. Hunter, and V. Postoyalko, “A novel dual-mode $TE_{11\delta}$ dielectric resonator,” in *High Frequency Postgraduate Student Colloquium, 1999*, pp. 48–53.

- [61] M. Höft, “Dielectric TE dual-mode resonator filters,” in *Microwave Conference, 2010 German*, pp. 206–209.
- [62] L. Ji-Fuh, K. A. Zaki, and A. E. Atia, “Mixed modes dielectric resonator filters,” *Microwave Theory and Techniques, IEEE Transactions on*, vol. 42, no. 12, pp. 2449–2454, 1994.
- [63] M. Memarian and R. R. Mansour, “Dual-mode half-cut dielectric resonator filters,” in *Microwave Symposium Digest, 2009. MTT '09. IEEE MTT-S International*, pp. 1465–1468.
- [64] V. Walker and I. C. Hunter, “Design of triple mode TE_{01δ} resonator transmission filters,” *IEEE Microwave and Wireless Components Letters*, vol. 12, pp. 215–217, June 2002.
- [65] L. H. Chua and D. Mirshekar-Syahkal, “Analysis and design of three transmission zeros bandpass filter utilizing triple-mode dielectric loaded cubical cavity,” in *IEEE MTT-S International Microwave Symposium Digest, 2003*, vol. 2, pp. 937–940 vol.2, June 2003.
- [66] H. Matsumoto, T. Tsujiguchi, and T. Nishikawa, “A miniaturized dielectric monoblock duplexer matched by the buried impedance transforming circuit,” in *Proceedings of 1995 IEEE MTT-S International Microwave Symposium*, pp. 1539–1542 vol.3, May 1995.
- [67] D. R. Hendry and A. M. Abbosh, “Analysis of compact triple-mode ceramic cavity filters using parallel-coupled resonators approach,” *IEEE Transactions on Microwave Theory and Techniques*, vol. 64, pp. 2529–2537, Aug 2016.
- [68] N. S. Park, D. Y. Lee, B. C. Kim, J. H. Won, I. H. Na, G. H. Jang, Y. H. Cho, X. G. Wang, and S. W. Yun, “Compact triple-mode bandpass filter using spherical dielectric resonator,” in *2013 European Microwave Conference*, pp. 810–813, Oct 2013.

- [69] S. W. Wong, Z. C. Zhang, S. F. Feng, F. C. Chen, L. Zhu, and Q. X. Chu, "Triple-mode dielectric resonator diplexer for base-station applications," *IEEE Transactions on Microwave Theory and Techniques*, vol. 63, pp. 3947–3953, Dec 2015.
- [70] R. J. Cameron, "General coupling matrix synthesis methods for Chebyshev filtering functions," *Microwave Theory and Techniques, IEEE Transactions on*, vol. 47, no. 4, pp. 433–442, 1999.
- [71] S. Amari, "Synthesis of cross-coupled resonator filters using an analytical gradient-based optimization technique," *Microwave Theory and Techniques, IEEE Transactions on*, vol. 48, no. 9, pp. 1559–1564, 2000.
- [72] I. Hunter, R. Ranson, A. Guyette, and A. Abunjaileh, "Microwave filter design from a systems perspective," *IEEE Microwave Magazine*, vol. 8, pp. 71–77, Oct 2007.
- [73] A. Atia and A. Williams, "New types of waveguide bandpass filters for satellite transponders," *Comsat Tech. Review*, vol. 1, no. 1, pp. 20–43, 1971.
- [74] A. E. Atia and A. E. Williams, "Narrow-bandpass waveguide filters," *IEEE Transactions on Microwave Theory and Techniques*, vol. 20, no. 4, pp. 258–265, 1972.
- [75] A. Atia, A. Williams, and R. Newcomb, "Narrow-band multiple-coupled cavity synthesis," *IEEE Transactions on circuits and systems*, vol. 21, no. 5, pp. 649–655, 1974.
- [76] H. U. Manual, "Ansoft corp," *Pittsburgh, PA, USA*, 2005.
- [77] J. Hayashi and Y. Nikawa, "Waveguide filter using LTCC," in *APMC 2001. 2001 Asia-Pacific Microwave Conference (Cat. No.01TH8577)*, vol. 3, pp. 1012–1015 vol.3, 2001.

- [78] J. S. Hong, "Couplings of asynchronously tuned coupled microwave resonators," *IEE Proceedings - Microwaves, Antennas and Propagation*, vol. 147, pp. 354–358, Oct 2000.
- [79] J. B. Ness, "A unified approach to the design, measurement, and tuning of coupled-resonator filters," *IEEE Transactions on Microwave Theory and Techniques*, vol. 46, pp. 343–351, Apr 1998.
- [80] J. Hattori, H. Wakamatsu, H. Kubo, and Y. Ishikawa, "2 GHz band triple mode dielectric resonator duplexer for digital cellular base station," in *2000 Asia-Pacific Microwave Conference. Proceedings (Cat. No.00TH8522)*, pp. 1315–1318, 2000.